Advanced numerical modeling in geophysics

Dimitri Komatitsch

Université de Pau et des Pays de l'Adour
Laboratoire d'Imagerie Géophysique

Habilitation à Diriger des Recherches

présentée par

Dimitri KOMATITSCH

Modélisation Numérique Avancée pour la Géophysique

———

Advanced Numerical Modeling in Geophysics

Soutenue le vendredi 19 septembre 2003 à 10h30 devant le jury composé de

Prof. Jean-Louis GOUT (Univ. Pau) :	**Président**
Dr. Eric DE BAZELAIRE, Docteur d'État (Univ. Pau) :	**Rapporteur**
Prof. Yvon MADAY (Univ. Paris VI) :	**Rapporteur**
Prof. Jean-Paul MONTAGNER (IPG Paris) :	**Rapporteur**
Prof. Rémi ABGRALL (Univ. Bordeaux) :	**Examinateur**
Prof. Franck BARBIER (Univ. Pau) :	**Examinateur**
Prof. Jeroen TROMP (Caltech, USA) :	**Examinateur**

Dimitri Komatitsch
Laboratoire d'Imagerie Géophysique
Université de Pau et des Pays de l'Adour
Boîte Postale 1155 – Avenue de l'Université
64013 Pau Cedex, France
Email : dimitri.komatitsch@univ-pau.fr

Table des matières

Première partie

Résumé du travail de recherche effectué

Chapitre 1

Résumé des activités de recherche effectuées

1.1 Introduction

La géophysique est une science fondamentalement liée aux observations, et son évolution rapide dans de nombreux domaines au cours des deux dernières décennies est due en grande partie à des avancées métrologiques importantes qui améliorent la qualité et la quantité des observations recueillies. Par exemple, dans le domaine de la sismologie, le réseau global (Global Seismographic Network - GSN) contient plus de 120 sismomètres, le premier instrument permanent de fond de mer (ocean-bottom seismometer - H2O) a été installé, et dans un futur proche des projets ambitieux tels que le réseau ultra-dense américain de sismomètres 'USArray' permettront d'obtenir des quantités très importantes de données à l'échelle d'un continent ou d'une région, enregistrées par des réseaux haute-résolution de stations large bande. Dans le domaine de la géodésie satellitaire, que l'on peut aussi considérer en un sens comme la sismologie ultra-longue période, les progrès métrologiques de positionnement GPS et l'interférométrie radar ont permis de mesurer les déformations et d'en déduire les contraintes à l'échelle régionale pendant et après de grands séismes (par exemple en Californie du Sud, Landers en 1992 ou Hector Mine en 1999), et d'étudier l'évolution de ces régions liée aux phénomènes post-sismiques.

Bien évidemment, les progrès réalisés en instrumentation et acquisition de données doivent être accompagnés d'une meilleure compréhension théorique des phénomènes mis en jeu, ainsi que d'une meilleure modélisation de ceux-ci, au moyen de techniques de calcul numérique tridimensionnelles. Si nous comparons à l'évolution d'autres domaines tels que la mécanique des fluides, la météorologie ou encore l'astrophysique, dans lesquels les progrès en calcul scientifique ont suivi de près les progrès en instrumentation (cas des souffleries numériques, étude numérique de phénomènes climatiques tels que les ouragans etc.), le domaine de la sismologie n'a pas encore bénéficié pleinement des progrès rapides de l'analyse numérique, du calcul scientifique et de la technologie des ordinateurs modernes (calcul parallèle et vectoriel).

Le présent mémoire résume les recherches que j'ai effectuées jusqu'à présent pour faire le lien entre différents domaines de la géophysique et les progrès du calcul scientifique. Nous avons d'une part développé des outils sophistiqués de calcul, nous les avons validés de manière rigoureuse, et nous les avons ensuite appliqués à des cas concrets intéressant la sismologie locale, régionale et globale. Dans la conclusion de ce document, nous exposons également quelques thèmes de recherche que nous souhaitons développer dans le futur.

1.2 Recherches menées jusqu'à présent

Jusqu'à présent, je me suis intéressé principalement à quatre thèmes scientifiques :

- étude de la propagation des ondes sismiques dans des modèles géologiques complexes tels que les bassins sédimentaires ou la terre globale (mon thème de recherche principal),
- étude de nouvelles conditions de frontière parfaitement absorbantes pour les méthodes numériques de type éléments finis,
- approximation de surfaces géologiques complexes par des méthodes non-oscillantes,

– algorithmique proprement dite : optimisation de méthodes de calcul variationnel sur des supercalculateurs parallèles et/ou vectoriels, et des réseaux d'ordinateurs PCs à faible coût, dans le but de rendre le calcul tridimensionnel (3-D) complexe plus accessible à la communauté géophysique, plus particulièrement dans le domaine de la sismologie.

Nous détaillons ci-dessous les principaux résultats obtenus dans le cadre de chacun de ces quatre sujets. Ces thèmes seront ensuite développés de manière détaillée dans les différents chapitres du présent mémoire.

1.2.1 Méthode des éléments spectraux pour la propagation des ondes sismiques

Au cours des 20 dernières années, différentes méthodes ont été utilisées pour le calcul de sismogrammes synthétiques dans des modèles géologiques complexes, au départ bidimensionnels, puis ensuite dans des modèles 3-D. La technique des différences finies (e.g., Virieux 1986; Ohminato & Chouet 1997) est la plus populaire, et a été appliquée avec succès à des modèles locaux ou régionaux (e.g., Olsen & Archuleta 1996; Wald & Graves 1998; Peyrat et al. 2001). Une autre technique largement utilisée est la méthode pseudo-spectrale, utilisant des bases globales de polynômes de Chebyshev ou de Legendre (e.g., Carcione 1996). Cependant, dans de nombreux cas d'intérêt pratique, les méthodes traditionnelles mentionnées ci-dessus souffrent de limitations telles que la dispersion ou l'anisotropie numérique, par exemple lorsque l'on s'intéresse de manière précise aux ondes de surface, qui sont importantes dans les problèmes de résonance et de risque sismique dans les bassins sédimentaires, et pour l'étude de la structure de la croûte et du manteau supérieur à l'échelle régionale ou globale.

Dans le cadre de mes travaux de recherche, j'ai donc développé une nouvelle méthode, appelée la méthode des éléments spectraux, qui avait été introduite initialement pour la mécanique des fluides (Patera 1984; Maday & Patera 1989; Maday et al. 1993; Fischer & Rønquist 1994), et que j'ai appliquée pour la première fois à la propagation d'ondes dans des structures 3-D (voir par exemple pour le 2-D Cohen et al. (1993); Priolo et al. (1994); Komatitsch (1997); Komatitsch & Vilotte (1998) et pour le 3-D Komatitsch (1997); Faccioli et al. (1997); Komatitsch & Vilotte (1998); Komatitsch & Tromp (1999)). La conclusion principale de ce travail a été de démontrer la supériorité de la méthode des éléments spectraux sur les méthodes numériques plus classiques en termes de précision, de faible dispersion numérique, et de flexibilité géométrique permettant de l'adapter à des modèles complexes 3-D de grande taille (e.g., Komatitsch & Vilotte 1998; Komatitsch & Tromp 2002a,b; Komatitsch et al. 2003; Tsuboi et al. 2003). Un tel gain de précision est un avantage important dans le cadre de la résolution de problèmes de modélisation sismologique directs ou inverses.

1.2.2 Étude de l'amplification sismique dans le bassin de Los Angeles

Lors de mes années de recherche aux Etats-Unis (à Harvard et Caltech), j'ai travaillé sur l'étude des mouvements forts du sol dans la région du bassin de Los Angeles. Cette région est constituée d'un bassin de grande dimension (plus de 100 km $\times$ 100 km) dont la structure en fait l'un des bassins sédimentaires les plus profonds (la couche sédimentaire a une épaisseur de 8.5 km au maximum sous la ville) et les plus dangereux du monde en raison de l'amplification des ondes sismiques. Si l'on ajoute à cela la présence de zones montagneuses entourant le bassin (jouant le rôle de piège d'énergie), la proximité de nombreuses failles actives (dont la faille majeure de San Andreas), la présence de plus de 15 millions d'habitants dans la région, et l'existence d'un second bassin (vallée de San Fernando) également très peuplé et entouré de montagnes, on comprend aisément l'intérêt d'étudier de la manière la plus précise possible la propagation des ondes sismiques dans cette région tectoniquement très active et géologiquement très complexe.

À mon arrivée à Harvard en 1998, mes collègues (John Shaw et al.) étaient en train de construire un modèle précis de la géologie de l'ensemble du bassin. Par rapport aux modèles antérieurs (Magistrale et al. 1996, 2000), leur idée était d'utiliser les nombreux profils de sismique active et les forages (well logs) réalisés par les compagnies pétrolières dans la région pour mieux contraindre la structure du sous-sol. Le modèle final a ainsi été contraint à partir de plus de 20000 km de profils sismiques bidimensionnels et de 300 logs de vitesse des ondes de compression dans des puits de forage (Süss & Shaw 2003). De mon côté, j'ai tiré avantage de la souplesse de la technique des éléments spectraux pour créer un maillage haute-résolution du nouveau modèle de bassin, et faire des calculs dans ce modèle en collaboration avec mes collègues de Caltech, Qinya Liu et Jeroen Tromp. Nous avons sélectionné deux tremblements de terre récents ayant eu lieu à l'intérieur du bassin, bien enregistrés par plus de 140 stations du réseau TriNet de Californie du Sud, et de magnitude suffisamment petite pour pouvoir être considérés comme des sources ponctuelles nous donnant ainsi une mesure expérimentale directe de la fonction de Green du bassin. Notre choix s'est porté sur le tremblement de terre de Hollywood (9 septembre 2001, $M_w = 4.2$) et celui de Yorba Linda (3 septembre 2002, $M_w = 4.3$). Pour la première fois, nous avons pu ajuster les trois composantes du vecteur déplacement, la plupart des études antérieures se concentrant sur la seule composante verticale (e.g., Olsen et al. 1997; Wald & Graves 1998; Olsen 2000), et ceci en obtenant un bon accord jusqu'à des périodes

relativement courtes (2 secondes). Cette étude a confirmé que des effets 3-D importants peuvent amplifier les mouvements forts du sol dans les bassins sédimentaires, et a illustré de façon claire l'utilité de techniques de calcul numérique 3-D sophistiquées dans un tel cadre (Komatitsch et al. 2004).

1.2.3 Étude de grands tremblements de terre à l'échelle de la Terre globale

Si nous souhaitons à présent nous intéresser à des simulations numériques de la propagation des ondes sismiques à l'échelle de la Terre globale, la difficulté principale consiste à prendre en compte les caractéristiques spécifiques du problème global : géométrie sphérique, fort contraste de propriétés élastiques entre l'ensemble formé par la croûte et le manteau supérieur et le reste du modèle, effet de la gravité à longue période. Ces problèmes complexes ont été résolus de manière élégante dans le travail de thèse d'Emmanuel Chaljub (Chaljub 2000) en collaboration avec Jean-Pierre Vilotte et Jean-Paul Montagner à l'Institut de Physique du Globe de Paris (Chaljub et al. 2003). Le travail de thèse de Yann Capdeville (Capdeville 2000), à nouveau à l'Institut de Physique du Globe de Paris (Capdeville et al. 2003), a par ailleurs permis de coupler la méthode des éléments spectraux dans le manteau et la croûte avec une solution quasi-analytique de sommation de modes normaux pour un modèle à symétrie sphérique du noyau de la Terre. De mon côté, j'ai entrepris d'améliorer la méthode des éléments spectraux à l'échelle globale en résolvant des problèmes additionnels importants, tels que la paramétrisation du fluide dans le noyau externe de la Terre (en se basant sur l'utilisation d'un potentiel de vitesse généralisé), l'introduction de l'anisotropie du manteau supérieur, la prise en compte de la rotation de la Terre, la prise en compte d'un modèle 3-D du manteau (Ritsema et al. 1999), de la croûte (Bassin et al. 2000), de la topographie et l'ellipticité de la terre, ainsi que la prise en compte de l'effet des océans (essentiellement pour modéliser leur effet sur la dispersion des ondes de surface trans-océaniques et sur le coefficient de réflexion des ondes PP) (Komatitsch & Tromp 2002a,b; Komatitsch et al. 2002, 2003; Tsuboi et al. 2003).

Dans le cadre de ce projet de recherche, j'ai étudié plusieurs tremblements de terre réels pour lesquels nous souhaitions comprendre des effets observés dans les données qui étaient mal expliqués par les modèles unidimensionnels à symétrie sphérique tels que PREM (Dziewonski & Anderson 1981). Par exemple, dans le cas d'un tremblement de terre à faible profondeur (15 km) en novembre 1999 à Vanuatu ($M_w = 7.4$) enregistré au Japon et en Californie, les données montraient des ondes de surface avec des propriétés très différentes du comportement suggéré par un calcul dans PREM. Un calcul 3-D complet avec prise en compte du modèle crustal et de l'effet des océans nous a permis de beaucoup mieux reproduire les données. Ceci suggère qu'il faudra un jour utiliser de tels calculs 3-D précis pour analyser les données d'ondes de surface et mieux contraindre les modèles crustaux, dont la connaissance reste actuellement approximative.

1.2.4 Conditions parfaitement absorbantes pour les méthodes numériques

Nous avons montré ci-dessus que les techniques de calcul 3-D constituent un outil précieux dans l'analyse des données sismologiques. Cependant, un obstacle important à cet égard reste le coût de calcul élevé de ces techniques (même si l'évolution rapide des ordinateurs rend chaque jour ce problème technologique moins gênant). Dans le cas de modélisations locales ou régionales (bassins sédimentaires fortement peuplés par exemple), c'est-à-dire en domaine non borné, il est nécessaire de définir des frontières artificielles délimitant le modèle à étudier. Pour calculer le modèle réel, les ondes doivent être absorbées sur ces bords fictifs pour simuler leur 'sortie' du domaine. Ce problème est classique en simulation numérique, et faisait jusqu'à récemment l'objet de traitements approchés tels que les équations paraxiales (Clayton & Engquist 1977) ou les zones d'amortissement de type éponges (Cerjan et al. 1985), peu satisfaisantes car renvoyant de fortes phases parasites à l'intérieur du modèle, en particulier à incidence rasante dans le cas des conditions paraxiales, et à basse fréquence dans le cas des zones de type éponge.

Bérenger (1994) a introduit une condition novatrice pour les équations de Maxwell, ayant la propriété d'être mathématiquement parfaitement adaptée au modèle, c'est-à-dire de ne renvoyer aucune phase parasite dans la région à étudier d'un point de vue mathématique avant discrétisation par un schéma numérique. Cette condition a de ce fait été baptisée couche parfaitement adaptée PML (Perfectly Matched Layer). En raison de son efficacité très significativement supérieure aux conditions utilisées précédemment, cette condition PML a connu un succès rapide dans le domaine de l'électromagnétisme. En exploitant une analogie entre les équations de Maxwell et l'équation des ondes élastiques écrite comme un système du premier ordre en vitesse et contraintes, plusieurs auteurs ont adapté cette condition au cas de l'absorption des ondes élastiques (e.g., Hastings et al. 1996; Qi & Geers 1998; Collino & Tsogka 2001). Ces formulations sont idéales pour certaines techniques numériques telles que les différences finies, mais ne peuvent malheureusement pas être utilisées directement dans le cadre de méthodes comme les éléments finis classiques ou les éléments spectraux, car celles-ci sont basées sur l'équation des ondes écrite comme un système du deuxième ordre en déplacement. Pour pallier cet inconvénient majeur, j'ai entrepris avec mon collègue Jeroen Tromp (de Caltech) une étude de la condition PML au deuxième ordre,

qui nous a permis de trouver une solution efficace pour l'adapter aux méthodes d'éléments finis ou spectraux classiques (Komatitsch & Tromp 2003). Ce travail est important car, comme nous avons augmenté drastiquement l'efficacité des bords absorbants, nous pouvons mettre ces bords beaucoup plus près de la zone du modèle que nous cherchons à étudier, ce qui réduit dans de grandes proportions le coût de calcul, en particulier à 3-D.

1.2.5 Calcul parallèle, vectoriel et optimisation

Au cours des années 90, des techniques de calcul numérique permettant d'aborder des problèmes 3-D de grande taille ont commencé à émerger. Cependant, de nombreux auteurs ont continué à effectuer des calculs bidimensionnels en raison du coût de calcul de ces méthodes à 3-D, et de la difficulté de les implémenter (nécessité de calculer sur de grosses machines multiprocesseurs, avec des techniques de calcul spécifiques telles que la programmation multi-tâches). Plus récemment cependant, des informaticiens ont commencé à tirer parti de l'augmentation phénoménale de la puissance de calcul des ordinateurs personnels (PCs) pour essayer de les transformer en machines de calcul parallèle en réseau. De telles machines sont connues sous le nom de 'clusters de PCs' ou 'Beowulfs', et utilisent souvent des composants informatiques standard afin de réduire le coût de construction (Taubes 1996; Sterling et al. 1999). L'avantage de ces machines est de rendre possible le calcul 3-D haute résolution à faible coût, mais le désavantage est qu'il faut modifier explicitement les algorithmes de calcul existants, car chaque PC a son propre processeur et sa propre mémoire. De ce fait il faut diviser le maillage en autant de blocs que de PCs, et programmer des envois de messages entre PCs pour échanger les informations aux interfaces communes des blocs (ceci se fait ordinairement à l'aide une bibliothèque d'envoi de messages appelée MPI, pour 'Message Passing Interface') (Gropp et al. 1996).

Dans le but de pouvoir augmenter autant que possible la résolution de nos calculs 3-D (pour pouvoir par exemple ajuster les données du bassin de Los Angeles à une fréquence élevée sans être trop limité par le coût de calcul, comme dans la section 1.2.2 ci-dessus), nous avons décidé d'étudier l'optimisation des algorithmes d'éléments spectraux sur de tels réseaux de calculateurs. Dans une première étape, nous avons entrepris la construction d'un cluster de grande taille. J'ai coordonné l'ensemble de ce projet (d'un montant total de $400.000), c'est-à-dire l'étude de faisabilité, le choix des pièces, l'assemblage matériel, l'installation logicielle et la phase de tests. La machine a été construite sur le site de Caltech au cours de l'été 2000, l'assemblage étant réalisé en 15 jours avec l'aide de trois étudiants. L'ensemble comporte un total de 320 processeurs et 160 gigaoctets de mémoire. La machine a depuis démontré une très bonne fiabilité, elle est toujours en 2003 l'ordinateur principal de calcul utilisé par le groupe de modélisation sismologique de Caltech.

Dans une deuxième étape, nous avons optimisé notre algorithme de calcul de propagation d'ondes sismiques par éléments spectraux pour ce type de calculateur. J'ai à nouveau coordonné cet effort. L'idée principale était d'arriver à une méthode de calcul optimale et fiable qui puisse être ensuite mise à disposition de l'ensemble de la communauté scientifique. Ce but a été atteint, cet outil (avec son code source complet) étant maintenant disponible pour toute recherche académique non-commerciale sur simple demande auprès des auteurs (moi-même et Jeroen Tromp, Caltech).

Au cours de l'année 2002, un large consortium universitaire et gouvernemental au Japon a mis en service un supercalculateur de très grande taille, dédié au calcul scientifique pour les sciences de la Terre, appelé le 'Earth Simulator'. Il s'agit d'un projet de plusieurs années, démarré en 1997. Cette machine est actuellement (début 2003) l'ordinateur le plus rapide et le plus gros du monde, avec 5120 processeurs et 10000 gigaoctets de mémoire. Ayant des contacts avec le Prof. Seiji Tsuboi du centre de prévision JAMSTEC au Japon, nous avons saisi cette opportunité pour réaliser des calculs à très haute résolution sur cette machine. La machine ayant une structure sophistiquée (machine essentiellement parallèle, mais dotée de processeurs vectoriels), j'ai dû optimiser mon algorithme pour tirer parti de la structure vectorielle. Nous avons alors pu calculer des sismogrammes dans la terre 3-D jusqu'à des périodes de 5 secondes, ce qui n'avait jamais été atteint auparavant. À titre de référence, la plupart des calculs de sommation de modes normaux pour des modèles sphériques unidimensionnels s'arrêtent à 8 secondes, certains à 6 secondes, c'est-à-dire que nos calculs 3-D sont maintenant plus précis que ces catalogues de référence 1-D (Komatitsch et al. 2003; Tsuboi et al. 2003).

1.2.6 Approximation de surface par des méthodes non-oscillantes

Au cours de certaines études dans le domaine de la géophysique, comme par exemple l'analyse du risque volcanique, il est nécessaire de décrire précisément la topographie d'un modèle complexe. Les données de topographie brutes sont souvent connues avec une excellente précision grâce aux Modèles Numériques de Terrain (MNT), mais les décrire mathématiquement comme une surface (et non un simple ensemble de points) présentant une régularité suffisante pour pouvoir être utilisée dans des algorithmes de maillage de la structure est un problème plus difficile (on a souvent besoin d'imposer une régularité de classe C^1 au minimum, parfois plus). Ceci est crucial dans le cadre de l'étude de certains problèmes géophysiques, car une description adéquate de la surface permettra d'utiliser des méthodes de calcul numérique pour

mieux comprendre par exemple le risque volcanique, c'est-à-dire la propagation de coulées pyroclastiques (comme dans le cas de la Montagne Pelée ou du Vésuve) ou la formation de panaches. Un autre exemple est celui de la description d'interfaces géologiques complexes, comme dans le cadre du calcul de l'évolution de bassins sédimentaires soumis à de fortes contraintes tectoniques. Des outils d'approximation de surface sont disponibles pour cela (par exemple le logiciel standard GoCad dans l'industrie pétrolière et en géologie (Mallet 1997)). Cependant, dans le cas de surfaces irrégulières présentant de fortes variations locales (failles dans le cas d'une interface, vallées aux parois abruptes dans le cas d'un volcan), ces algorithmes ont tendance à osciller localement en raison de la difficulté à approximer une 'marche d'escalier' correspondant au changement rapide d'élévation par une fonction régulière (phénomène des oscillations de Gibbs).

Pour pallier ce problème, avec mes collègues Christian Gout et Dominique Apprato du Département d'Analyse Numérique de l'Université de Pau et des Pays de l'Adour, nous avons étudié de nouvelles techniques non-oscillantes d'approximation de surface (Gout 1997; Gout & Komatitsch 2000; Apprato et al. 2002). L'idée est d'introduire des fonctions d'échelle non linéaires pour 'aplatir' la surface avant de l'approximer par une fonction spline, puis appliquer la fonction non linéaire inverse au spline pour restaurer la vraie surface. La surface aplatie peut alors être approximée par un spline avec le degré de régularité souhaité sans générer d'oscillations significatives.

Deuxième partie

Modélisation sismologique à l'échelle de la Terre globale

Chapitre 2

Modélisation dans la Terre globale 1-D

Résumé

Dans ce premier chapitre, nous introduisons une méthode d'éléments spectraux pour simuler la propagation des ondes sismiques dans la Terre globale décrite comme un modèle unidimensionnel (1-D) à symétrie sphérique. La méthode est basée sur une formulation faible des équations du mouvement et combine la flexibilité d'une méthode d'éléments finis avec la précision d'une méthode pseudospectrale globale. Le maillage d'éléments finis est adapté à toutes les discontinuités de premier et de second ordre du modèle. Afin de maintenir une résolution relativement constante dans tout le modèle en termes de nombre de points de grille par longueur d'onde, la taille des éléments augmente avec la profondeur de façon conforme, de ce fait nous conservons une matrice de masse exactement diagonale dans la méthode des éléments spectraux. Dans le manteau et la graine nous résolvons l'équation des ondes écrite en déplacement, tandis que dans le noyau externe liquide nous utilisons une formulation basée sur un potentiel scalaire. Les trois domaines sont couplés à la surface de la graine et à l'interface noyau-manteau en imposant la continuité de la traction et de la composante normale de la vitesse. Les effets de l'atténuation et de l'anisotropie sont incorporés. La méthode est implémentée sur un ordinateur parallèle en utilisant une technique informatique de passage de messages. Nous la validons en comparant les sismogrammes synthétiques calculés par la méthode des éléments spectraux à des sismogrammes synthétiques quasi-analytiques de référence calculés par une méthode de sommation de modes normaux pour le modèle à symétrie sphérique de référence PREM. Les deux méthodes sont en excellent accord pour toutes les ondes de surface et de volume jusqu'à des périodes de 20 secondes.

Abstract

In this first chapter, we introduce a spectral-element method to simulate seismic wave propagation throughout the entire Earth described as a one-dimensional (1-D) spherically-symmetric model. The method is based upon a weak formulation of the equations of motion and combines the flexibility of a finite-element method with the accuracy of a global pseudospectral method. The finite-element mesh honors all first- and second-order discontinuities in the Earth model. To maintain a relatively constant resolution throughout the model in terms of the number of grid points per wavelength, the size of the elements is increased with depth in a conforming fashion, thus retaining a diagonal mass matrix. In the Earth's mantle and inner core we solve the wave equation in terms of displacement, whereas in the liquid outer core we use a formulation based upon a scalar potential. The three domains are matched at the inner-core and core-mantle boundaries, honoring the continuity of traction and the normal component of velocity. The effects of attenuation and anisotropy are fully incorporated. The method is implemented on a parallel computer using a message-passing technique. We benchmark spectral-element synthetic seismograms against normal-mode synthetic seismograms for spherically symmetric reference model PREM. The two methods are in excellent agreement for all body- and surface-wave arrivals with periods greater than about 20 s.

2.1 Introduction

The calculation of accurate synthetic seismograms for three-dimensional (3-D) full Earth models poses a formidable challenge. The effects of an anisotropic asthenosphere, a slow crust with highly variable thickness, sharp fluid-solid discontinuities at the inner-core (ICB) and core-mantle (CMB) boundaries, ellipticity, free-surface topography, and attenuation must all be accounted for. In this first chapter we demonstrate that the spectral-element method (SEM), introduced

more than 15 years ago in computational fluid mechanics (Patera 1984; Maday & Patera 1989; Fischer & Rønquist 1994), can meet this challenge. The method has been used to accurately model wave propagation on local and regional scales, both in 2-D (Priolo et al. 1994; Komatitsch 1997; Faccioli et al. 1997; Komatitsch & Vilotte 1998) and in 3-D (Komatitsch 1997; Faccioli et al. 1997; Komatitsch & Vilotte 1998; Seriani 1998; Komatitsch & Tromp 1999; Paolucci et al. 1999). Previous publications have documented that the more specific aspects of global wave propagation can be dealt with by the SEM: Komatitsch & Vilotte (1998), Komatitsch & Tromp (1999) and Paolucci et al. (1999) demonstrate that the effects of free-surface topography can be accommodated, Komatitsch et al. (2000a) show that fluid-solid boundaries can be accurately modeled, Seriani et al. (1995) and Komatitsch et al. (2000b) incorporate effects due to anisotropy, and Komatitsch & Tromp (1999) implement attenuation. In this first chapter we summarize the main properties of the method and combine all these ingredients to tackle the problem of global wave propagation.

For spherically symmetric Earth models, normal-mode summation is the preferred method for the calculation of synthetic seismograms (e.g., Dahlen & Tromp 1998). Typically, normal-mode synthetic seismograms are accurate for periods greater than about 8 s (i.e., just above the micro-seismic noise band), and involve the summation of a few hundred thousand modes. The effects of fluid-solid boundaries, transverse isotropy with a radial symmetry axis, and radial models of attenuation can all be accommodated. In this chapter we benchmark our SEM synthetic seismograms against reference normal-mode synthetic seismograms calculated for the Preliminary Reference Earth Model (PREM) (Dziewonski & Anderson 1981).

The SEM has been previously applied to the problem of 3-D global wave propagation in innovative work by Chaljub (2000), Chaljub et al. (2003) and Capdeville et al. (2003). They use a so-called 'mortar' version of the SEM (Bernardi et al. 1990, 1994; Lahaye et al. 1997), which allows for non-conforming meshes in which each side of every element does not have to match up exactly with the side of a neighboring element. This makes mesh design more flexible, since it allows one to use smaller elements in the upper part of the model where wave speeds are slowest, but comes at a significant increase in the complexity and cost of the implementation because the mass matrix is no longer diagonal on the non-conforming interfaces. As a result, an iterative solver has to be used to solve the non-diagonal system. Here we use a classical SEM based upon a conforming mesh that retains a diagonal mass matrix. Chaljub (2000) and Capdeville et al. (2003) incorporate the effects of self-gravitation, which are not considered in this study, but they do not incorporate anisotropy or attenuation, which we do consider, nor the crust at short periods. Capdeville et al. (2003) deal with problems posed by the fluid outer core by introducing an efficient coupling technique, which matches a normal-mode solution in the core to a SEM in the mantle. This allows one to reduce the cost of the method by assuming a spherically symmetric solution in the core and using spectral elements only in the upper part of the model. However, the requirement that the matching surface be strictly spherically symmetric precludes the incorporation of effects due to CMB topography or the Earth's ellipticity. Tromp & Komatitsch (2000) used a SEM to simulate wave propagation in a portion of the globe. In this chapter we extend the simulations to the entire globe and incorporate effects due to anisotropy, attenuation, and the solid inner core. We implement the fluid-solid matching conditions using a simple and efficient domain decomposition technique.

Other researchers have attempted to simulate 3-D global wave propagation based upon a coupled-mode approach, in which the modes of a 3-D Earth model are expressed as a sum over the modes of a spherically symmetric Earth model (e.g., Park 1986; Park & Yu 1992; Lognonné & Romanowicz 1990; Capdeville et al. 2000), or direct-solution methods, which use more general basis functions (e.g., Hara et al. 1991; Geller & Ohminato 1994; Takeuchi et al. 2000). Coupled-mode and direct-solution synthetic seismograms are expensive to calculate, in particular for models with strong lateral variations which require a wide coupling bandwidth. Effects due to boundary undulations are linearized, which makes it difficult to accommodate significant variations in crustal thickness. The finite-difference technique (e.g., Igel & Weber 1996; Chaljub & Tarantola 1997; Thomas et al. 2000) provides an alternative approach to the calculation of global synthetic seismograms. It is well-known, however, that finite-difference methods are inaccurate for surface waves because of numerical dispersion (e.g., Robertsson 1996). Furthermore, the design of a grid for the globe poses geometrical difficulties because of the decrease in grid spacing with depth. In addition, diffracted phases are hard to model accurately, in particular at the CMB, because of the staggered nature of the grid. Finally, pseudospectral methods have been used to address the problem (e.g., Tessmer et al. 1992; Carcione & Wang 1993; Furumura et al. 1998; Igel 1999). As in finite-difference methods, gridding the entire globe has not yet been accomplished because of difficulties related to the spherical geometry, and the accurate implementation of the free surface boundary condition is problematic. In addition, major velocity discontinuities in the model are difficult to take into account because of the global polynomial nature of the solution. In practice, coupled-mode, direct-solution, finite-difference, and pseudospectral methods often have to assume that Earth models are 2-D axisymmetric to reduce the computational burden. The COSY project (Igel & Geller 2000) brought together several research groups in an attempt to benchmark numerical algorithms for 1-D and 3-D Earth models. The results are summarized in a special issue of *Physics of the Earth and Planetary Interiors* (Volume 119, 2000) which illustrates many of the difficulties associated with the problem.

2.2 Meshing the globe

As in any finite-element method, a first crucial step towards the accurate simulation of 3-D seismic wave propagation is the design of a mesh: the model volume Ω needs to be subdivided into a number of non-overlapping elements Ω_e, $e = 1, \ldots, n_e$, such that $\Omega = \cup_{e=1}^{n_e} \Omega_e$. In this section we highlight some of the basic ingredients of mesh design, which are classical finite-element results. For a detailed introduction to finite-element methods the reader is referred to Zienkiewicz (1977) and Hughes (1987).

A classical spectral-element method relies upon a mesh of hexahedral finite elements Ω_e that are isomorphous to the cube. Tetrahedra that are classical in finite element methods are excluded in the SEM because of the tensorization of the polynomial basis that is required to obtain an exactly diagonal mass matrix, as will be explained in Section 2.3. The six sides of each hexahedral element must match up exactly with the sides of neighboring elements. Such a mesh is traditionally called a conforming mesh in the finite-element literature. For reasons of accuracy, a good mesh should honor all the major first- and second-order discontinuities in the model, and the size of the elements should reflect the distribution of wave speeds, such that one maintains a relatively similar number of grid points per wavelength throughout the model. Since wave speed generally increases with depth, this implies that the elements should become gradually larger with depth. These requirements make the design of a mesh for the globe challenging.

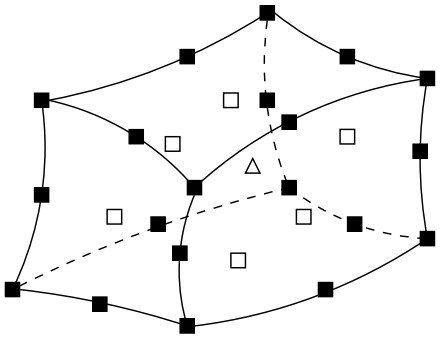

Figure 2.1 *The geometry of each of the curved hexahedra is defined by 27 control nodes. This is a schematic example of a curved element and its anchors.*

The mapping between Cartesian points $\mathbf{x} = (x, y, z)$ within a deformed, hexahedral element Ω_e and the reference cube may be written in the form

$$\mathbf{x}(\boldsymbol{\xi}) = \sum_{a=1}^{n_a} N_a(\boldsymbol{\xi}) \mathbf{x}_a. \tag{2.1}$$

Points within the reference cube are denoted by the vector $\boldsymbol{\xi} = (\xi, \eta, \zeta)$, where $-1 \leq \xi \leq 1$, $-1 \leq \eta \leq 1$ and $-1 \leq \zeta \leq 1$. The geometry of our finite elements is defined in terms of $n_a = 27$ control points, or anchors, $\mathbf{x}_a$, as shown in Figure 2.1. The n_a shape functions N_a are triple products of degree-2 Lagrange polynomials. The three Lagrange polynomials of degree 2 with three control points $\xi_0 = -1$, $\xi_1 = 0$, and $\xi_2 = 1$ are $\ell_0^2(\xi) = \frac{1}{2}\xi(\xi - 1)$, $\ell_1^2(\xi) = 1 - \xi^2$ and $\ell_2^2(\xi) = \frac{1}{2}\xi(\xi + 1)$. Given the choice of anchors $\mathbf{x}_a$, the shape functions N_a determine the geometry of the element.

A small volume $\mathrm{d}x\,\mathrm{d}y\,\mathrm{d}z$ within a given finite element is related to a volume $\mathrm{d}\xi\,\mathrm{d}\eta\,\mathrm{d}\zeta$ in the reference cube by $\mathrm{d}x\,\mathrm{d}y\,\mathrm{d}z = J\,\mathrm{d}\xi\,\mathrm{d}\eta\,\mathrm{d}\zeta$, where the Jacobian J of the mapping is given by $J = |\partial(x, y, z)/\partial(\xi, \eta, \zeta)|$. The partial derivative matrix $\partial\mathbf{x}/\partial\boldsymbol{\xi}$ needed for the calculation of J is obtained by analytically differentiating the mapping (2.1). Partial derivatives of the shape functions N_a are defined in terms of Lagrange polynomials of degree 2 and their derivatives. One needs to ensure that the mapping (2.1) is unique and invertible, i.e., $\boldsymbol{\xi}(\mathbf{x})$ should be well-defined and the Jacobian J should never vanish. As in any finite-element method (e.g., Hughes 1987), the behavior of the Jacobian J is controlled by the geometry of the mesh, and is a measure of its quality.

We will see that modeling interaction between the fluid and solid parts of the model at the CMB and ICB requires the evaluation of surface integrals. The mesh on a fluid-solid discontinuity Γ consists of boundary elements Γ_b, $b = 1, \ldots, n_b$, such that $\Gamma = \cup_{b=1}^{n_b} \Gamma_b$. The quadrilateral boundary elements Γ_b are simply the bottom or top sides of hexahedral volume elements Ω_e that border the CMB or ICB. They are isomorphous to the square. Let $-1 \leq \xi \leq 1$, $-1 \leq \eta \leq 1$ denote points in the square, and let $\mathbf{x}$ denote points in a boundary element Γ_b. The mapping between points in a quadrilateral boundary element and the reference cube may be written in the form

$$\mathbf{x}(\xi, \eta) = \sum_{a=1}^{n_a} N_a(\xi, \eta) \mathbf{x}_a. \tag{2.2}$$

We use 9 anchors $\mathbf{x}_a$ to describe the geometry of a boundary element Γ_b, which is the number of anchors that lie on one face of a hexahedral volume element Ω_e shown in Figure 2.1. The 9 shape functions $N_a(\xi, \eta)$ are double products of Lagrange polynomials of degree 2.

The orientation of the reference square is chosen such that the unit outward normal $\hat{\mathbf{n}}$ to a boundary element Γ_b is given by

$$\hat{\mathbf{n}} = \frac{1}{J_b} \frac{\partial \mathbf{x}}{\partial \xi} \times \frac{\partial \mathbf{x}}{\partial \eta}, \tag{2.3}$$

where J_b denotes the Jacobian of the transformation:

$$J_b = \left\| \frac{\partial \mathbf{x}}{\partial \xi} \times \frac{\partial \mathbf{x}}{\partial \eta} \right\|. \tag{2.4}$$

To calculate the Jacobian J_b and the unit outward normal $\hat{\mathbf{n}}$ one needs to determine the six partial derivatives $\partial \mathbf{x}/\partial \xi$ and $\partial \mathbf{x}/\partial \eta$. This is accomplished by analytically differentiating the mapping (2.2).

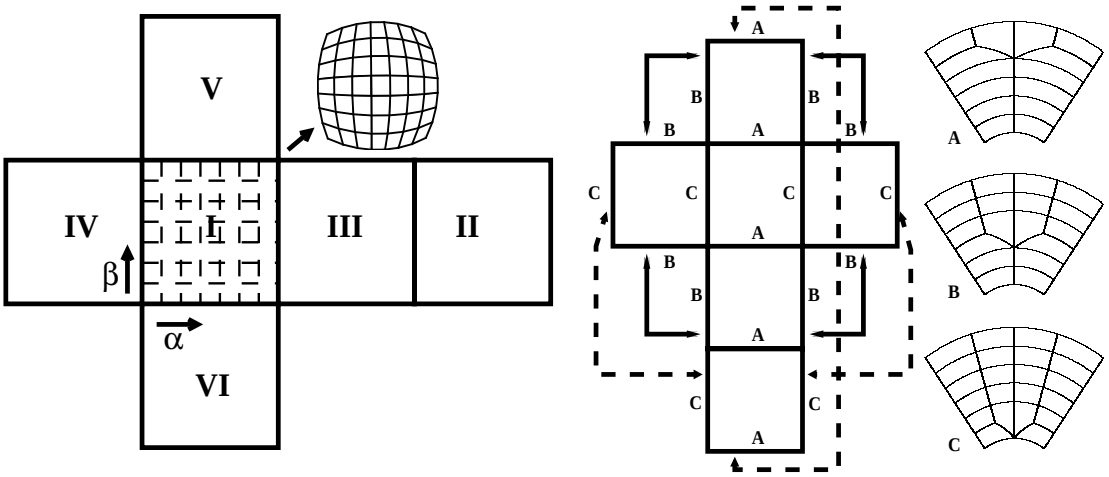

Figure 2.2 *(Left) View of the six building blocks that constitute the cubed sphere. Each of the six faces I–VI of the cube is represented by an equidistant mesh in terms of surface coordinates $-\pi/4 \leq \alpha \leq \pi/4$ and $-\pi/4 \leq \beta \leq \pi/4$. The analytical relations (2.2) map the six faces of the cube to the surface of the sphere, resulting in the angularly equidistant mesh shown to the top right for one of the six faces. (Right) Mesh size needs to be increased in the globe as a function of depth to maintain a similar number of grid points per wavelength throughout the model. This is accomplished in three stages. Besides a top and bottom, each of the six building blocks that constitute the cubed sphere has four sides that need to match up exactly with four other blocks to complete the cube, as indicated by the arrows. Schematically, these four sides have one of three designs: A, B, or C. When the six blocks are fitted together to make the entire globe, they match perfectly.*

The mesh we use is based upon the concept of the 'quasi-uniform gnomonic projection', or 'cubed sphere' (Sadourny 1972; Ronchi et al. 1996; Taylor et al. 1997), which was introduced for global wave propagation problems by Taylor et al. (1997) and Chaljub (2000). The key idea is to map each of the six sides of the cube to the surface of the sphere. Labeling the six faces of the cube by Roman numerals I–VI, on each individual face we introduce Cartesian coordinates (α, β) such that $-\pi/4 \leq \alpha \leq \pi/4$ and $-\pi/4 \leq \beta \leq \pi/4$ map out the face, as shown in Figure 2.2. Next, let the Cartesian coordinates (x, y, z) denote points on the surface of a sphere with radius r, such that $r = (x^2 + y^2 + z^2)^{1/2}$, and define the auxiliary variables $X = \tan\alpha$, $Y = \tan\beta$, and $Z = r(1 + X^2 + Y^2)^{-1/2}$. Then the mapping from each of the six faces of the cube to the surface of a sphere with radius r is defined by (e.g., Ronchi et al. 1996; Chaljub 2000):

Face I:	$x = Z$,	$y = XZ$,	$z = YZ$,	Face II:	$x = -Z$,	$y = -XZ$	$z = YZ$,
Face III:	$x = -XZ$,	$y = Z$,	$z = YZ$,	Face IV:	$x = XZ$,	$y = -Z$,	$z = YZ$,
Face V:	$x = -YZ$,	$y = XZ$,	$z = Z$,	Face VI:	$x = YZ$,	$y = XZ$,	$z = -Z$.

In this fashion an equidistant grid in α and β on each face of the cube is mapped to an angularly equidistant grid on the surface of the sphere with radius r. As underlined by Ronchi et al. (1996), this gives a mesh on the surface of the sphere with smooth variations of the Jacobian, which is a requirement for good mesh design.

Unfortunately, a regular mesh is not suitable for numerical simulations of 3-D wave propagation, because the elements naturally decrease in size with depth due to the spherical geometry. To maintain a relatively similar number of grid points per wavelength the elements should instead increase in size, because seismic velocities in PREM generally increase with depth. An increase in element size can be obtained by first doubling the mesh in one lateral direction, and, subsequently, at a greater depth, increasing its size in the other lateral dimension (e.g., Komatitsch & Tromp 1999). Increasing the mesh size with depth in a single chunk in this fashion is therefore straightforward. However, accomplishing this for more than

one chunk in such a manner that each element on the side of one chunk matches up perfectly with an element on the side of a neighboring chunk, in order to obtain a geometrically conforming mesh for the entire sphere, is less straightforward. Figure 2.2 illustrates schematically how this may be accomplished based upon a three-stage doubling as a function of depth. Note that there are three types of chunks: AB, AC, and BC. In each of the types the doubling is performed at different levels, such that the final six chunks fit together perfectly to make the entire globe based upon the cubed-sphere mapping. The main drawbacks of this mesh are the transition regions in which the doublings are implemented, because some resolution is lost due to the irregular shape of the elements. As mentioned earlier, an alternative is the use of a non-conforming mesh in the context of the 'mortar' method (Chaljub 2000), with the related complexity of implementation and the loss of a diagonal matrix system.

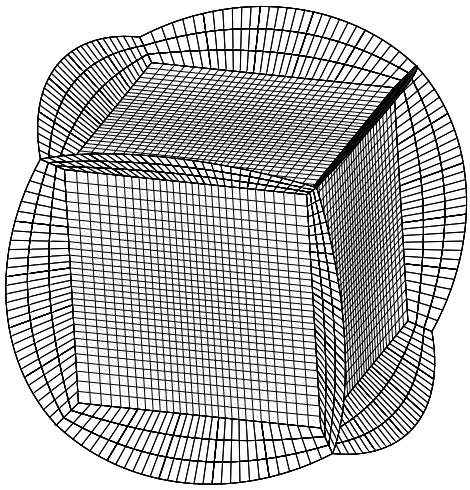

Figure 2.3 *To avoid a mesh singularity associated with the Earth's center, we place a cube at the center of the solid inner core. We use a simple linear interpolation to create the mesh between the surface of the central cube and the cubed sphere mesh at the ICB. This figure shows the actual mesh used within the solid inner core. Note that there is a layer of three elements between the ICB and the central cube. Note also that element size within the central cube is not constant; this reflects a match-up with the angularly equidistant mesh at the ICB.*

To avoid singularities at the Earth's center, Chaljub (2000) introduced the idea of placing a cube around the center of the inner core. The mesh within this cube needs to match up with the cubed sphere mesh at the ICB. The mapping between this spherical surface and the surface of the cube in the inner core is obtained by simple linear interpolation between the two surfaces. Figure 2.3 shows the actual mesh used in the simulations for the inner core. Note that the mesh at the surface of the cube is not regular, but rather is a flat version of the cubed sphere mapping.

The mesh used in the 3-D simulations is shown in Figure 2.4 and is designed to honor all first-order discontinuities in the Preliminary Reference Earth Model (PREM) (Dziewonski & Anderson 1981), which are the Moho at a depth of 24.4 km, the upper mantle discontinuities at depths of 220 km, 400 km, and 670 km, the CMB, and the ICB; it also honors second-order discontinuities at 600 km, 771 km, and at the top of D". The mesh is doubled in size once below the Moho, a second time below the 670 km discontinuity, and a third time just above the ICB. Each of the six chunks has 240×240 elements at the free surface and, as a result of the three doublings, 30×30 elements at the ICB.

The radial density and velocity profiles of the model are determined by PREM. The 3-km thick water layer and the lower crust of PREM have been replaced by PREM upper crust, such that our model has a homogeneous crust with a thickness of 24.4 km and the constant properties of the PREM upper crust. The reason for this simplification is that the exact location of the boundary between the upper and lower crust can only be honored by using at least two layers of finite elements in the crust, which would increase the computer memory requirements too dramatically. Of course the Earth's real crust is very different from that in PREM, which uses an arbitrary average of the oceanic and continental crust, and the depth of the associated upper/lower crust boundary therefore has little meaning at the global scale. PREM has a transversely isotropic asthenosphere between 24.4 km and 220 km, which is incorporated in our SEM simulations. We will consider wave propagation in PREM with and without incorporating attenuation. Normal-mode catalogs with a shortest period of 8 s were calculated for identical versions of PREM to obtain elastic and anelastic reference solutions.

2.3 The Spectral-Element Method

In this chapter we ignore the effects of self-gravitation and rotation on global wave propagation. Self-gravitation and rotation are only relevant in the context of long-period surface waves and will be considered in the next chapter.

2.3.1 Mantle and Crust

The wave equation for the Earth's mantle and crust may be written in the form

$$\rho\,\partial_t^2\mathbf{s} = \boldsymbol{\nabla}\cdot\mathbf{T} + \mathbf{f}, \tag{2.5}$$

where ρ denotes the 3-D distribution of density and $\mathbf{T}$ the stress tensor which is linearly related to the displacement gradient $\boldsymbol{\nabla}\mathbf{s}$ by Hooke's law:

$$\mathbf{T} = \mathbf{c} : \boldsymbol{\nabla}\mathbf{s}. \tag{2.6}$$

In a transversely isotropic Earth model, such as PREM, the elastic tensor $\mathbf{c}$ is determined in terms of the five elastic parameters A, C, L, N, and F (Love 1911).

In an attenuating medium, Hooke's law (2.6) needs to be modified such that the stress is determined by the entire strain history:

$$\mathbf{T}(t) = \int_{-\infty}^{t} \partial_t\mathbf{c}(t-t') : \boldsymbol{\nabla}\mathbf{s}(t')\,\mathrm{d}t'. \tag{2.7}$$

In seismology, the quality factor Q is observed to be constant over a wide range of frequencies. Such an absorption-band solid may be mimicked by a series of L standard linear solids (Liu et al. 1976; Carcione et al. 1988; Moczo et al. 1997). In practice, two or three linear solids usually suffice to obtain an almost constant Q (Emmerich & Korn 1987). Attenuation in the Earth is mainly controlled by the shear quality factor, such that only the time dependence of the isotropic shear modulus needs to be accommodated (the bulk quality factor is several hundred times larger than the shear quality factor throughout the Earth). In a transversely isotropic Earth model one keeps track of the time dependence of the effective shear modulus. The shear modulus of such a standard linear solid may be written in the form (Liu et al. 1976)

$$\mu(t) = \mu_R\left[1 - \sum_{\ell=1}^{L}(1-\tau_\ell^\epsilon/\tau_\ell^\sigma)e^{-t/\tau_\ell^\sigma}\right]H(t). \tag{2.8}$$

Here μ_R denotes the relaxed modulus, $H(t)$ is the Heaviside function, and τ_ℓ^σ and τ_ℓ^ϵ denote the stress and strain relaxation times, respectively, of the ℓth standard linear solid. Using the absorption-band shear modulus (2.8), the constitutive relation (2.7) may be rewritten in the form

$$\mathbf{T} = \mathbf{c}_U : \boldsymbol{\nabla}\mathbf{s} - \sum_{\ell=1}^{L}\mathbf{R}_\ell, \tag{2.9}$$

where $\mathbf{c}_U$ is the unrelaxed elastic tensor determined by the unrelaxed shear modulus

$$\mu_U = \mu_R\left[1 - \sum_{\ell=1}^{L}(1-\tau_\ell^\epsilon/\tau_\ell^\sigma)\right]. \tag{2.10}$$

For each standard linear solid one needs to solve the memory-variable equation

$$\partial_t\mathbf{R}_\ell = -(\mathbf{R}_\ell - \delta\mu_\ell\mathbf{D})/\tau_\ell^\sigma, \tag{2.11}$$

where $\mathbf{D}$ is the strain deviator:

$$\mathbf{D} = \tfrac{1}{2}[\boldsymbol{\nabla}\mathbf{s} + (\boldsymbol{\nabla}\mathbf{s})^T] - \tfrac{1}{3}(\boldsymbol{\nabla}\cdot\mathbf{s})\mathbf{I}. \tag{2.12}$$

Here a superscript T denotes the transpose and $\mathbf{I}$ is the identity tensor. The memory-variable tensors $\mathbf{R}_\ell$ are symmetric and have zero trace, such that each standard linear solid introduces five additional unknowns. The modulus defect $\delta\mu_\ell$ associated with each individual standard linear solid is determined by

$$\delta\mu_\ell = -\mu_R(1-\tau_\ell^\epsilon/\tau_\ell^\sigma). \tag{2.13}$$

The earthquake source is represented by a point force $\mathbf{f}$, which may be written in terms of the moment tensor $\mathbf{M}$ as

$$\mathbf{f} = -\mathbf{M}\cdot\boldsymbol{\nabla}\delta(\mathbf{r}-\mathbf{r}_\mathrm{s})S(t). \tag{2.14}$$

The location of the point source is denoted by $\mathbf{r}_\mathrm{s}$, $\delta(\mathbf{r}-\mathbf{r}_\mathrm{s})$ denotes the Dirac delta distribution located at $\mathbf{r}_\mathrm{s}$, and the source-time function is given by $S(t)$.

Two types of boundary conditions must be considered: on the free surface the traction $\hat{\mathbf{n}}\cdot\mathbf{T}$, where $\hat{\mathbf{n}}$ denotes the unit outward normal on the free surface, vanishes, and on the CMB the normal component of velocity $\hat{\mathbf{n}}\cdot\mathbf{v}$ and the traction $\hat{\mathbf{n}}\cdot\mathbf{T}$ are continuous.

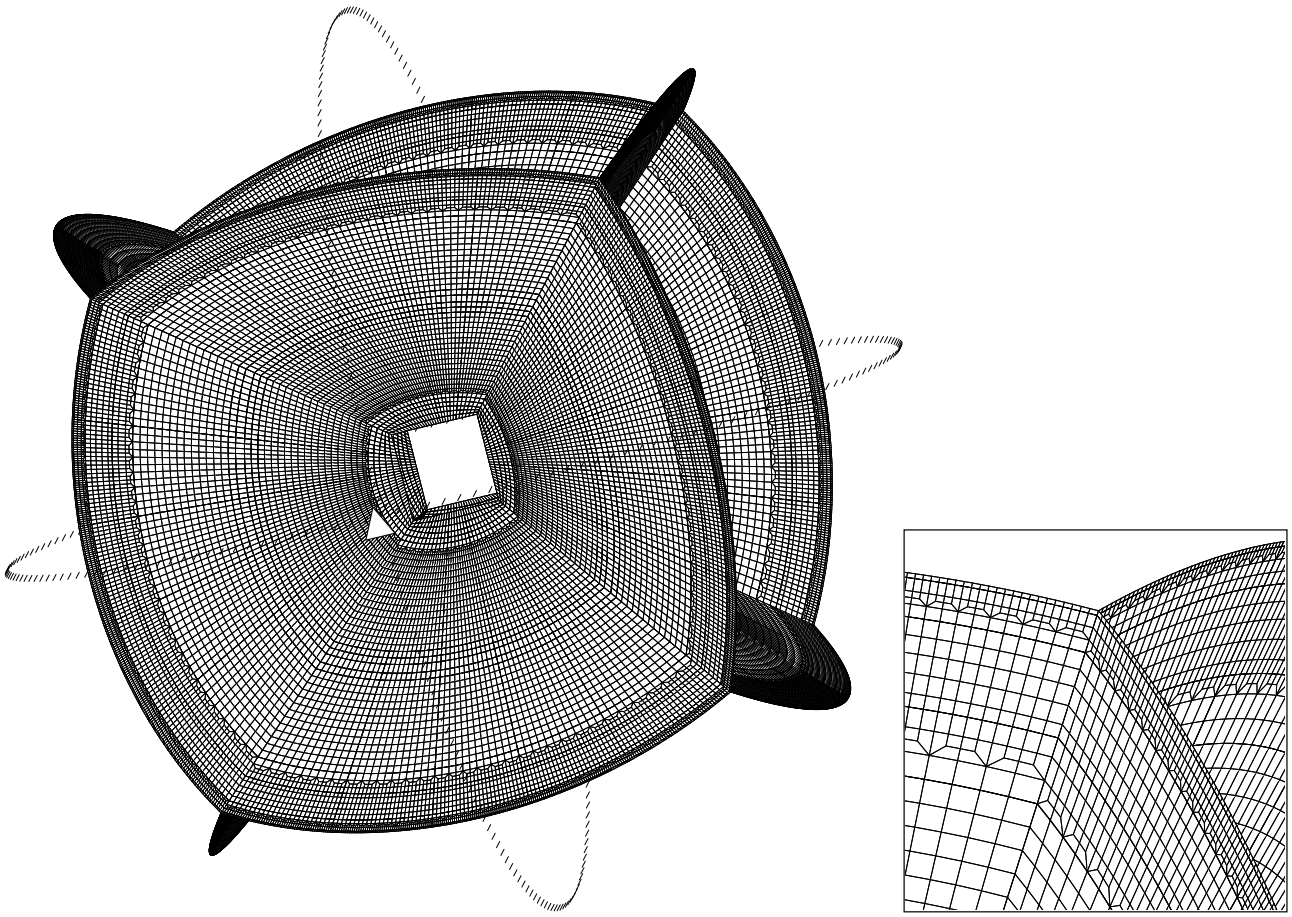

Figure 2.4 *Mesh used for the simulations presented in this study. It honors first-order discontinuities at depths of 24.4 km, 220 km, 400 km, and 670 km, the CMB, and the ICB; it also honors second-order discontinuities at 600 km, 771 km, and at the top of D". The mesh is doubled in size once below the Moho, a second time below the 670 km discontinuity, and a third time just above the ICB. Each of the six chunks has 240 × 240 elements at the free surface and 30 × 30 elements at the ICB. The triangle indicates the location of the source, situated on the equator and the Greenwich meridian. Rings of receivers with a 2° spacing along the equator and the Greenwich meridian are shown by the dashes. We also show a close-up of the two mesh doublings in the mantle.*

Finite-difference and pseudospectral methods are based upon the equation of motion (2.5) subject to the appropriate boundary conditions, which is a differential or 'strong' formulation of the problem. Spectral-element methods, like finite-element, coupled-mode, and direct-solution methods, are based upon an integral or 'weak' formulation of the problem. This formulation is obtained by taking the dot product of the momentum equation (2.5) with an arbitrary vector $\mathbf{w}$, called a test vector in the finite-element literature, integrating by parts over the volume M of the mantle and crust, and imposing the stress-free boundary condition. This gives

$$\int_{\mathrm{M}} \rho\, \mathbf{w} \cdot \partial_t^2 \mathbf{s}\, \mathrm{d}^3\mathbf{r} = -\int_{\mathrm{M}} \boldsymbol{\nabla}\mathbf{w} : \mathbf{T}\, \mathrm{d}^3\mathbf{r} \;+\; \mathbf{M} : \boldsymbol{\nabla}\mathbf{w}(\mathbf{r}_{\mathrm{s}})\, S(t) - \int_{\mathrm{CMB}} \mathbf{w} \cdot \mathbf{T} \cdot \hat{\mathbf{n}}\, \mathrm{d}^2\mathbf{r}, \tag{2.15}$$

where $\hat{\mathbf{n}}$ is the unit outward normal on the CMB. Equation (2.15) is equivalent to the strong formulation (2.5) subject to the appropriate boundary conditions because it holds for any test vector $\mathbf{w}$.

The weak formulation (2.15) is valid for a completely general, anelastic, anisotropic model. To correctly model interactions between the solid mantle and the fluid core, we need to impose the continuity of traction and of the normal velocity at the CMB. Coupling fluid and solid finite elements is not an easy problem numerically (e.g., Thompson & Pinsky 1996; Bermúdez et al. 1999). In this study we implement the fluid-solid interactions based upon a domain decomposition method: in the mantle we impose the continuity of traction and in the next section on the fluid outer core we will impose the continuity of normal velocity. To impose continuity of traction, we replace the traction term $\hat{\mathbf{n}} \cdot \mathbf{T}$ in the integral over the CMB by the traction $-p\,\hat{\mathbf{n}}$ in the fluid, where p denotes the fluid pressure. We find

$$\int_{\mathrm{M}} \rho\, \mathbf{w} \cdot \partial_t^2 \mathbf{s}\, \mathrm{d}^3\mathbf{r} = -\int_{\mathrm{M}} \boldsymbol{\nabla}\mathbf{w} : \mathbf{T}\, \mathrm{d}^3\mathbf{r} \;+\; \mathbf{M} : \boldsymbol{\nabla}\mathbf{w}(\mathbf{r}_{\mathrm{s}})\, S(t) + \int_{\mathrm{CMB}} p\, \hat{\mathbf{n}} \cdot \mathbf{w}\, \mathrm{d}^2\mathbf{r}. \tag{2.16}$$

2.3.2 Outer core

In the fluid outer core, the equation of motion is

$$\rho\,\partial_t \mathbf{v} = -\boldsymbol{\nabla} p, \tag{2.17}$$

where $\mathbf{v}$ denotes the velocity in the fluid and the pressure p is determined by

$$\partial_t p = -\kappa\,\boldsymbol{\nabla}\cdot\mathbf{v}, \tag{2.18}$$

where κ is the bulk modulus of the fluid. On the CMB and the ICB the traction $-p\,\hat{\mathbf{n}}$ and the normal component of velocity $\hat{\mathbf{n}}\cdot\mathbf{v}$ must be continuous.

To solve the system of equations (2.17) and (2.18), we introduce a scalar potential χ (e.g., Everstine 1981; Kallivokas & Bielak 1993; Lesieur 1997) such that

$$p = -\partial_t \chi. \tag{2.19}$$

From (2.17) and the initial conditions ($\mathbf{v} = \mathbf{0}$ at $t = 0$), we find that

$$\mathbf{v} = \rho^{-1}\boldsymbol{\nabla}\chi. \tag{2.20}$$

Upon substituting (2.19) and (2.20) into (2.18) we obtain a scalar equation for χ:

$$\kappa^{-1}\partial_t^2\chi = \boldsymbol{\nabla}\cdot(\rho^{-1}\boldsymbol{\nabla}\chi). \tag{2.21}$$

The weak form of this equation is obtained by multiplying it by a scalar test function w and integrating by parts over the volume OC of the outer core:

$$\int_{\mathrm{OC}} \kappa^{-1} w\partial_t^2\chi\,\mathrm{d}^3\mathbf{r} = -\int_{\mathrm{OC}} \rho^{-1}\boldsymbol{\nabla}w\cdot\boldsymbol{\nabla}\chi\,\mathrm{d}^3\mathbf{r} + \int_{\mathrm{CMB}} w\,\hat{\mathbf{n}}\cdot\mathbf{v}\,\mathrm{d}^2\mathbf{r} - \int_{\mathrm{ICB}} w\,\hat{\mathbf{n}}\cdot\mathbf{v}\,\mathrm{d}^2\mathbf{r}, \tag{2.22}$$

where we used (2.20) in the surface integrals over the CMB and ICB. Again $\hat{\mathbf{n}}$ is the unit outward normal on either the CMB or the ICB.

Komatitsch et al. (2000a) used a fluid-solid domain decomposition approach that is valid for homogeneous fluids. The weak formulation (2.22) is valid for general, inhomogeneous fluids. At the CMB and the ICB we need to implement the second step of our domain decomposition technique by imposing the continuity of normal velocity. The continuity of traction has already been imposed in equation (2.16). At this point we replace the normal component of velocity $\hat{\mathbf{n}}\cdot\mathbf{v}$ in the integrals over the CMB and ICB with the normal component of velocity $\hat{\mathbf{n}}\cdot\partial_t\mathbf{s}$ in the mantle or inner core to correctly represent the interactions:

$$\int_{\mathrm{OC}} \kappa^{-1} w\partial_t^2\chi\,\mathrm{d}^3\mathbf{r} = -\int_{\mathrm{OC}} \rho^{-1}\boldsymbol{\nabla}w\cdot\boldsymbol{\nabla}\chi\,\mathrm{d}^3\mathbf{r} + \int_{\mathrm{CMB}} w\,\hat{\mathbf{n}}\cdot\partial_t\mathbf{s}\,\mathrm{d}^2\mathbf{r} - \int_{\mathrm{ICB}} w\,\hat{\mathbf{n}}\cdot\partial_t\mathbf{s}\,\mathrm{d}^2\mathbf{r}. \tag{2.23}$$

Note that the system of equations (2.16) and (2.23) honors both the continuity of traction and of the normal component of velocity and therefore correctly represents the fluid-solid interactions. This is the key motivation behind our domain decomposition approach.

2.3.3 Inner core

The weak form of the equation of motion in the solid inner core is similar to (2.16):

$$\int_{\mathrm{IC}} \rho\,\mathbf{w}\cdot\partial_t^2\mathbf{s}\,\mathrm{d}^3\mathbf{r} = -\int_{\mathrm{IC}} \boldsymbol{\nabla}\mathbf{w} : \mathbf{T}\,\mathrm{d}^3\mathbf{r} - \int_{\mathrm{ICB}} p\,\hat{\mathbf{n}}\cdot\mathbf{w}\,\mathrm{d}^2\mathbf{r}. \tag{2.24}$$

Note that the inner core-outer core interactions, represented by the surface integrals over the ICB in (2.23) and (2.24), also honor continuity in traction and continuity of the normal component of velocity. The normal follows the same convention as in previous sections.

2.3.4 Interpolation on an element

The next step is to represent the displacement field on an element, which requires the introduction of grid points in each element. In traditional finite-element methods the same low-degree polynomials used to describe the geometry of an element are also used to represent functions, such as the displacement field $\mathbf{s}$, on an element. Spectral-element methods also use a low-degree polynomial to describe the shape of an element, but employ a higher-degree polynomial to represent functions. In this regard, SEMs are related to so-called *h-p* finite-element methods, which also use polynomials of higher degree (e.g., Guo & Babuška 1986). Typically, a SEM uses Lagrange polynomials of degree 4 to 10 for the interpolation of functions (Seriani & Priolo 1994). The $n+1$ Lagrange polynomials of degree n are defined in terms of $n+1$ control points $-1 \leq \xi_\alpha \leq 1$, $\alpha = 0, \ldots, n$, by

$$\ell_\alpha^n(\xi) = \frac{(\xi-\xi_0)\cdots(\xi-\xi_{\alpha-1})(\xi-\xi_{\alpha+1})\cdots(\xi-\xi_n)}{(\xi_\alpha-\xi_0)\cdots(\xi_\alpha-\xi_{\alpha-1})(\xi_\alpha-\xi_{\alpha+1})\cdots(\xi_\alpha-\xi_n)}\,. \tag{2.25}$$

As a result of this definition, the Lagrange polynomials return a value of either zero or one when evaluated at a control point:

$$\ell_\alpha^n(\xi_\beta) = \delta_{\alpha\beta}, \tag{2.26}$$

where δ denotes the Kronecker delta. In a SEM, the control points ξ_α, $\alpha = 0, \ldots, n$, needed in the definition (2.25) are chosen to be the $n+1$ Gauss-Lobatto-Legendre points, which are the roots of $(1-\xi^2)P_n'(\xi) = 0$, where P_n' denotes the derivative of the Legendre polynomial of degree n (Canuto et al. 1988, p. 61). The reason for this choice is that, as we shall see, the combination of Lagrange interpolants with Gauss-Lobatto-Legendre quadrature greatly simplifies the algorithm, in particular regarding time-marching, since it leads to a diagonal mass matrix and therefore to fully explicit time schemes.

Functions f on an element are interpolated in terms of triple products of Lagrange polynomials as

$$f(\mathbf{x}(\xi,\eta,\zeta)) \approx \sum_{\alpha,\beta,\gamma=0}^{n_\alpha,n_\beta,n_\gamma} f^{\alpha\beta\gamma}\ell_\alpha(\xi)\ell_\beta(\eta)\ell_\gamma(\zeta), \tag{2.27}$$

where $f^{\alpha\beta\gamma} = f(\mathbf{x}(\xi_\alpha,\eta_\beta,\zeta_\gamma))$ denotes the value of the function f at the Gauss-Lobatto-Legendre point $\mathbf{x}(\xi_\alpha,\eta_\beta,\zeta_\gamma)$. We have dropped the superscript n on the Lagrange polynomials to avoid clutter in the notation. Note that, in principle, the method allows for different polynomial degrees, n_α, n_β, n_γ, in each of the three directions ξ, η, ζ. This enables one to use elements with high/low aspect ratios.

Using the polynomial representation (2.27), the gradient of a function, $\boldsymbol{\nabla} f = \sum_{i=1}^3 \hat{\mathbf{x}}_i \partial_i f$, evaluated at the Gauss-Lobatto-Legendre point $\mathbf{x}(\xi_{\alpha'},\eta_{\beta'},\zeta_{\gamma'})$, may be written in the form

$$\begin{aligned}\boldsymbol{\nabla} f(\mathbf{x}(\xi_{\alpha'},\eta_{\beta'},\zeta_{\gamma'})) \approx \sum_{i=1}^3 \hat{\mathbf{x}}_i \Bigg[&(\partial_i\xi)^{\alpha'\beta'\gamma'} \sum_{\alpha=0}^{n_\alpha} f^{\alpha\beta'\gamma'}\ell_\alpha'(\xi_{\alpha'}) \quad + \quad (\partial_i\eta)^{\alpha'\beta'\gamma'} \sum_{\beta=0}^{n_\beta} f^{\alpha'\beta\gamma'}\ell_\beta'(\eta_{\beta'}) \\ &+ \quad (\partial_i\zeta)^{\alpha'\beta'\gamma'} \sum_{\gamma=0}^{n_\gamma} f^{\alpha'\beta'\gamma}\ell_\gamma'(\zeta_{\gamma'}) \Bigg].\end{aligned} \tag{2.28}$$

Here $\hat{\mathbf{x}}_i$, $i = 1, 2, 3$, denote unit vectors in the directions of increasing x, y, and z, respectively, and ∂_i, $i = 1, 2, 3$, denote partial derivatives in those directions. We use a prime to denote derivatives of the Lagrange polynomials, as in ℓ_α'. The matrix $\partial\boldsymbol{\xi}/\partial\mathbf{x}$ is obtained by inverting the matrix $\partial\mathbf{x}/\partial\boldsymbol{\xi}$. This inverse exists provided the Jacobian J is non-singular, which is a requirement for the proper design of the mesh, as mentioned earlier.

2.3.5 Integration over an element

To solve the weak form of the equations of motion (2.16), (2.23), and (2.24), numerical integrations over the elements need to be performed. In classical finite-element methods, one frequently uses Gauss quadrature for this purpose. In a spectral-element method, one uses the Gauss-Lobatto-Legendre integration rule, because it leads to a diagonal mass matrix when used in conjunction with the Gauss-Lobatto-Legendre interpolation points, which greatly simplifies the algorithm. Using Gauss-Lobatto-Legendre quadrature, integrations over elements with volume Ω_e may be expressed as

$$\int_{\Omega_e} f(\mathbf{x})\,\mathrm{d}^3\mathbf{x} = \int_{-1}^1\int_{-1}^1\int_{-1}^1 f(\mathbf{x}(\xi,\eta,\zeta))\,J(\xi,\eta,\zeta)\,\mathrm{d}\xi\,\mathrm{d}\eta\,\mathrm{d}\zeta \approx \sum_{\alpha,\beta,\gamma=0}^{n_\alpha,n_\beta,n_\gamma} \omega_\alpha\omega_\beta\omega_\gamma f^{\alpha\beta\gamma}J^{\alpha\beta\gamma}, \tag{2.29}$$

where $J^{\alpha\beta\gamma} = J(\xi_\alpha, \eta_\beta, \zeta_\gamma)$, and $\omega_\alpha > 0$, for $\alpha = 0, \ldots, n$, denote the weights associated with the Gauss-Lobatto-Legendre quadrature (Canuto et al. 1988, p. 61). To perform this integration of functions and their partial derivatives over the elements, the values of the inverse Jacobian matrix $\partial\boldsymbol{\xi}/\partial\mathbf{x}$ need to be computed at the $(n+1)^3$ Gauss-Lobatto-Legendre integration points.

On the fluid-solid boundaries in the model we need to evaluate surface integrals in order to implement the coupling based upon domain decomposition. At the elemental level, using Gauss-Lobatto-Legendre quadrature, these surface integrations may be written in the form

$$\int_{\Gamma_b} f(\mathbf{x})\,\mathrm{d}^2\mathbf{x} = \int_{-1}^{1}\int_{-1}^{1} f(\mathbf{x}(\xi,\eta))\,J_b(\xi,\eta)\,\mathrm{d}\xi\,\mathrm{d}\eta \approx \sum_{\alpha,\beta=0}^{n_\alpha,n_\beta} \omega_\alpha\omega_\beta f^{\alpha\beta} J_b^{\alpha\beta}, \tag{2.30}$$

where Γ_b denotes the surface element, and $J_b^{\alpha\beta} = J_b(\xi_\alpha, \eta_\beta)$ is the Jacobian (2.4) evaluated at the Gauss-Lobatto-Legendre points of integration.

2.3.6 Discretization of the weak formulation

To obtain explicit expressions for the weak formulation of the problem, we first expand the displacement field $\mathbf{s}$ and the test vector $\mathbf{w}$ in terms of Lagrange polynomials:

$$\mathbf{s}(\mathbf{x}(\xi,\eta,\zeta),t) \approx \sum_{i=1}^{3} \hat{\mathbf{x}}_i \sum_{\sigma,\tau,\nu=0}^{n_\sigma,n_\tau,n_\nu} s_i^{\sigma\tau\nu}(t)\ell_\sigma(\xi)\ell_\tau(\eta)\ell_\nu(\zeta), \tag{2.31}$$

$$\mathbf{w}(\mathbf{x}(\xi,\eta,\zeta)) = \sum_{i=1}^{3} \hat{\mathbf{x}}_i \sum_{\alpha,\beta,\gamma=0}^{n_\sigma,n_\tau,n_\nu} w_i^{\alpha\beta\gamma}\ell_\alpha(\xi)\ell_\beta(\eta)\ell_\gamma(\zeta). \tag{2.32}$$

This choice of test vector makes the SEM a Galerkin method, because the basis functions used are the same as those used to represent the displacement. We evaluate the integrals in (2.16), (2.23), and (2.24) at the elemental level based upon Gauss-Lobatto-Legendre quadrature. The term on the left hand side of the weak form of the equation of motion (2.16) is traditionally called the mass matrix in finite-element modeling. At the elemental level, this integration may be written as

$$\int_{\Omega_e} \rho\,\mathbf{w}\cdot\partial_t^2\mathbf{s}\,\mathrm{d}^3\mathbf{x} = \int_{-1}^{1}\int_{-1}^{1}\int_{-1}^{1} \rho(\mathbf{x}(\boldsymbol{\xi}))\,\mathbf{w}(\mathbf{x}(\boldsymbol{\xi}))\cdot\partial_t^2\mathbf{s}(\mathbf{x}(\boldsymbol{\xi}),t)\,J(\boldsymbol{\xi})\,\mathrm{d}^3\boldsymbol{\xi}. \tag{2.33}$$

Upon substituting the interpolations (2.31) and (2.32) in (2.33), using the quadrature (2.29), we obtain

$$\int_{\Omega_e} \rho\,\mathbf{w}\cdot\partial_t^2\mathbf{s}\,\mathrm{d}^3\mathbf{x} \approx \sum_{\alpha,\beta,\gamma=0}^{n_\alpha,n_\beta,n_\gamma} \omega_\alpha\omega_\beta\omega_\gamma J^{\alpha\beta\gamma}\rho^{\alpha\beta\gamma} \sum_{i=1}^{3} w_i^{\alpha\beta\gamma}\ddot{s}_i^{\alpha\beta\gamma}(t), \tag{2.34}$$

where $\rho^{\alpha\beta\gamma} = \rho(\mathbf{x}(\xi_\alpha,\eta_\beta,\zeta_\gamma))$, and where a dot denotes differentiation with respect to time. By independently setting factors of $w_1^{\alpha\beta\gamma}$, $w_2^{\alpha\beta\gamma}$ and $w_3^{\alpha\beta\gamma}$ equal to zero, since the weak formulation (2.15) must hold for any test vector $\mathbf{w}$, we obtain independent equations for each component of acceleration $\ddot{s}_i^{\alpha\beta\gamma}(t)$ at grid point $(\xi_\alpha,\xi_\beta,\xi_\gamma)$. The remarkable property of (2.34) is that the value of acceleration at each point of a given element, $\ddot{s}_i^{\alpha\beta\gamma}(t)$, is simply multiplied by the factor $\omega_\alpha\omega_\beta\omega_\gamma\rho^{\alpha\beta\gamma}J^{\alpha\beta\gamma}$. In finite-element parlance one says that the elemental mass matrix is diagonal. It is this desirable property that has motivated the use of Lagrange interpolants together with Gauss-Lobatto-Legendre quadrature. Unlike in traditional finite-element methods, no linear system of equations needs to be inverted, and one can take full advantage of this property by using an explicit time-marching algorithm, as we will see later in this section. This is similar to the key idea used in finite element methods with mass lumping (e.g., Cohen et al. 1993; Bao et al. 1998).

The next integral that needs to be evaluated at the elemental level is the first term on the right hand side of (2.16), which is called the stiffness matrix in finite-element modeling. We find

$$\begin{aligned}\int_{\Omega_e} \boldsymbol{\nabla}\mathbf{w} : \mathbf{T}\,\mathrm{d}^3\mathbf{x} \;\approx\; & \sum_{\alpha,\beta,\gamma=0}^{n_\alpha,n_\beta,n_\gamma}\sum_{i=1}^{3} w_i^{\alpha\beta\gamma}\Bigg[\omega_\beta\omega_\gamma\sum_{\alpha'=0}^{n_{\alpha'}}\omega_{\alpha'}J_e^{\alpha'\beta\gamma}F_{i1}^{\alpha'\beta\gamma}\ell'_\alpha(\xi_{\alpha'}) \\ & + \omega_\alpha\omega_\gamma\sum_{\beta'=0}^{n_{\beta'}}\omega_{\beta'}J_e^{\alpha\beta'\gamma}F_{i2}^{\alpha\beta'\gamma}\ell'_\beta(\eta_{\beta'}) + \omega_\alpha\omega_\beta\sum_{\gamma'=0}^{n_{\gamma'}}\omega_{\gamma'}J_e^{\alpha\beta\gamma'}F_{i3}^{\alpha\beta\gamma'}\ell'_\gamma(\zeta_{\gamma'})\Bigg].\end{aligned} \tag{2.35}$$

where

$$F_{ik} = \sum_{j=1}^{3} T_{ij}\, \partial_j \xi_k, \tag{2.36}$$

and $F_{ik}^{\sigma\tau\nu} = F_{ik}(\mathbf{x}(\xi_\sigma, \eta_\tau, \zeta_\nu))$ denotes the value of F_{ik} at the Gauss-Lobatto-Legendre integration point $\mathbf{x}(\xi_\sigma, \eta_\tau, \zeta_\nu)$. For brevity, we have introduced index notation ξ_i, $i = 1, 2, 3$, where $\xi_1 = \xi$, $\xi_2 = \eta$, and $\xi_3 = \zeta$. In index notation, the elements of the mapping matrix $\partial\boldsymbol{\xi}/\partial\mathbf{x}$ may be written as $\partial_i \xi_j$. The value of the stress tensor $\mathbf{T}$ at the integration points is determined by

$$\mathbf{T}(\mathbf{x}(\xi_\alpha, \eta_\beta, \zeta_\gamma), t) = \mathbf{c}(\mathbf{x}(\xi_\alpha, \eta_\beta, \zeta_\gamma)) : \boldsymbol{\nabla}\mathbf{s}(\mathbf{x}(\xi_\alpha, \eta_\beta, \zeta_\gamma), t). \tag{2.37}$$

This calculation requires knowledge of the gradient of displacement $\boldsymbol{\nabla}\mathbf{s}$ at the Gauss-Lobatto-Legendre integration points. Upon differentiating (2.31) we obtain

$$\begin{aligned} \partial_i s_j(\mathbf{x}(\xi_\alpha, \eta_\beta, \zeta_\gamma), t) \;&=\; \left[\sum_{\sigma=0}^{n_\sigma} s_j^{\sigma\beta\gamma}(t) \ell'_\sigma(\xi_\alpha)\right] \partial_i \xi(\xi_\alpha, \eta_\beta, \zeta_\gamma) + \left[\sum_{\sigma=0}^{n_\sigma} s_j^{\alpha\sigma\gamma}(t) \ell'_\sigma(\eta_\beta)\right] \partial_i \eta(\xi_\alpha, \eta_\beta, \zeta_\gamma) \\ &+\; \left[\sum_{\sigma=0}^{n_\sigma} s_j^{\alpha\beta\sigma}(t) \ell'_\sigma(\zeta_\gamma)\right] \partial_i \zeta(\xi_\alpha, \eta_\beta, \zeta_\gamma). \end{aligned} \tag{2.38}$$

In an anelastic medium, the stiffness matrix is still given by (2.35), except that the stress tensor (2.37) needs to be replaced by

$$\mathbf{T}(\mathbf{x}(\xi_\alpha, \eta_\beta, \zeta_\gamma), t) = \mathbf{c}(\mathbf{x}(\xi_\alpha, \eta_\beta, \zeta_\gamma)) : \boldsymbol{\nabla}\mathbf{s}(\mathbf{x}(\xi_\alpha, \eta_\beta, \zeta_\gamma), t) - \sum_{\ell=1}^{L} \mathbf{R}_\ell(\mathbf{x}(\xi_\alpha, \eta_\beta, \zeta_\gamma), t), \tag{2.39}$$

in accordance with (2.9). The implication is that the five independent components of the symmetric, zero-trace memory tensor $\mathbf{R}_\ell$ need to be stored on the grid for each standard linear solid. For this reason, the memory requirements for an anelastic simulation increase substantially over those for purely elastic simulations. It is worth mentioning that to alleviate this burden, memory variables could be spread across an element, such that one carries only one memory variable at each grid point, obtaining the expected anelastic behavior in average (Zeng 1996; Day 1998).

The second term on the right hand side of the weak form of the equation of motion in the mantle (2.16) is the source term, which may be expressed as (Komatitsch & Tromp 1999)

$$\begin{aligned} \mathbf{M} : \boldsymbol{\nabla}\mathbf{w}(\mathbf{x}_\mathrm{s}) \;&\approx\; \sum_{\alpha,\beta,\gamma=0}^{n_\alpha,n_\beta,n_\gamma} \sum_{i=1}^{3} w_i^{\alpha\beta\gamma} \Bigg\{ \sum_{\sigma,\tau,\nu=0}^{n_\sigma,n_\tau,n_\nu} \ell_\sigma(\xi_{\alpha_\mathrm{s}}) \ell_\tau(\eta_{\beta_\mathrm{s}}) \ell_\nu(\zeta_{\gamma_\mathrm{s}}) \\ &\times\; \left[G_{i1}^{\sigma\tau\nu} \ell'_\alpha(\xi_{\alpha_\mathrm{s}}) \ell_\beta(\eta_{\beta_\mathrm{s}}) \ell_\gamma(\zeta_{\gamma_\mathrm{s}}) + G_{i2}^{\sigma\tau\nu} \ell_\alpha(\xi_{\alpha_\mathrm{s}}) \ell'_\beta(\eta_{\beta_\mathrm{s}}) \ell_\gamma(\zeta_{\beta_\mathrm{s}}) + G_{i3}^{\sigma\tau\nu} \ell_\alpha(\xi_{\alpha_\mathrm{s}}) \ell_\beta(\eta_{\beta_\mathrm{s}}) \ell'_\gamma(\zeta_{\gamma_\mathrm{s}})\right] \Bigg\}, \end{aligned} \tag{2.40}$$

where

$$G_{ik} = \sum_{j=1}^{3} M_{ij}\, \partial_j \xi_k, \tag{2.41}$$

and where $G_{ik}^{\sigma\tau\nu} = G_{ik}(\mathbf{x}(\xi_\sigma, \eta_\tau, \zeta_\nu))$ and $\mathbf{x}(\xi_{\alpha_\mathrm{s}}, \eta_{\beta_\mathrm{s}}, \zeta_{\gamma_\mathrm{s}}) = \mathbf{x}_\mathrm{s}$. Note that, due to the polynomial expansion, a point moment-tensor source gets spread over the entire element that contains the point source. This is not a problem, since the expression is consistent with the polynomial basis, except if receivers are placed very close to the source, particularly within the same element (Faccioli et al. 1997). Note also that the location of the source does not need to correspond to a Gauss-Lobatto-Legendre grid point.

The final term on the right hand side of the weak form of the equation of motion in the mantle and crust (2.16) is the surface integral over the CMB that represents the interactions in traction between the solid mantle and the liquid core. A key ingredient of our domain decomposition technique is that, since we have a conforming mesh everywhere, i.e., the grid points on the CMB are common to the meshes in the mantle and in the outer core, we can take the value of pressure at a given grid point from the fluid side, and use it directly in the surface integral on the solid side. Therefore, no interpolation is needed at a fluid-solid interface. This type of matching is referred to as pointwise matching in the finite-element literature. At the elemental level on a boundary, the surface integral may therefore be expressed as

$$\int_{\Gamma_b} p\, \hat{\mathbf{n}} \cdot \mathbf{w}\, \mathrm{d}^2\mathbf{r} \approx \sum_{\alpha,\beta=0}^{n_\alpha,n_\beta} \omega_\alpha \omega_\beta J_b^{\alpha\beta} \dot{\chi}^{\alpha\beta}(t) \sum_{i=1}^{3} w_i^{\alpha\beta} \hat{n}_i^{\alpha\beta}, \tag{2.42}$$

where we have used (2.19).

In the fluid outer core, the left hand side of the weak form of the equation of motion (2.23) may be written at the elemental level in the form

$$\int_{\Omega_e} \kappa^{-1} w \partial_t^2 \chi \, \mathrm{d}^3\mathbf{r} \approx \sum_{\alpha,\beta,\gamma=0}^{n_\alpha,n_\beta,n_\gamma} \omega_\alpha \omega_\beta \omega_\gamma J^{\alpha\beta\gamma} (\kappa^{\alpha\beta\gamma})^{-1} w^{\alpha\beta\gamma} \ddot{\chi}^{\alpha\beta\gamma}(t). \tag{2.43}$$

As for the left hand side of the weak form in the solid regions (2.34), this elemental 'mass' matrix is diagonal. The first integral on the right side of the fluid weak formulation (2.23) becomes at the elemental level

$$\begin{aligned} \int_{\Omega_e} \rho^{-1} \boldsymbol{\nabla} w \cdot \boldsymbol{\nabla} \chi \, \mathrm{d}^3\mathbf{r} \quad \approx \quad & \sum_{\alpha,\beta,\gamma=0}^{n_\alpha,n_\beta,n_\gamma} w^{\alpha\beta\gamma} \Bigg[\omega_\beta \omega_\gamma \sum_{\alpha'=0}^{n_{\alpha'}} \omega_{\alpha'} J_e^{\alpha'\beta\gamma} (\rho^{\alpha'\beta\gamma})^{-1} (\partial_1 \chi)^{\alpha'\beta\gamma} \ell'_\alpha(\xi_{\alpha'}) \\ + \quad & \omega_\alpha \omega_\gamma \sum_{\beta'=0}^{n_{\beta'}} \omega_{\beta'} J_e^{\alpha\beta'\gamma} (\rho^{\alpha\beta'\gamma})^{-1} (\partial_2 \chi)^{\alpha\beta'\gamma} \ell'_\beta(\eta_{\beta'}) \\ + \quad & \omega_\alpha \omega_\beta \sum_{\gamma'=0}^{n_{\gamma'}} \omega_{\gamma'} J_e^{\alpha\beta\gamma'} (\rho^{\alpha\beta\gamma'})^{-1} (\partial_3 \chi)^{\alpha\beta\gamma'} \ell'_\gamma(\zeta_{\gamma'}) \Bigg], \end{aligned} \tag{2.44}$$

where

$$(\partial_i \chi)^{\alpha\beta\gamma} = \sum_{\alpha=0}^{n_\alpha} \chi^{\alpha\beta'\gamma'} \ell'_\alpha(\xi_{\alpha'}) \partial_i \xi + \sum_{\beta=0}^{n_\beta} \chi^{\alpha'\beta\gamma'} \ell'_\beta(\eta_{\beta'}) \partial_i \eta + \sum_{\gamma=0}^{n_\gamma} \chi^{\alpha'\beta'\gamma} \ell'_\gamma(\zeta_{\gamma'}) \partial_i \zeta. \tag{2.45}$$

The remaining volume and surface integrals in (2.23) and (2.24) are identical in form to other integrals already discussed in this section.

2.3.7 Assembly of the system and time marching

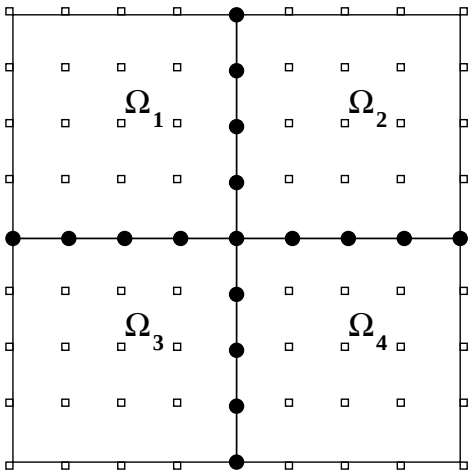

Figure 2.5 *Schematic illustration of the local and global meshes for a four-element 2-D spectral-element discretization with a polynomial degree of* $N = 4$. *Each element contains* $(N+1)^2 = 25$ *Gauss-Lobatto-Legendre points that constitute the local mesh for each element. These points are non-evenly spaced but have been drawn evenly spaced here for simplicity. In the global mesh, points lying on edges or corners (as well as on faces in 3-D) are shared between elements. The contributions to the global system of degrees of freedom, computed separately on each element, have to be summed at the common points represented by black dots. Exactly two elements share points on an edge in 2-D, while corners can be shared by any number of elements depending on the topology of the mesh, which may be non structured.*

In each individual spectral element, functions are sampled at the Gauss-Lobatto-Legendre points of integration. Grid points that lie on the sides, edges, or corners of an hexahedral element are shared amongst neighboring elements, as illustrated in Figure 2.5. Therefore, as in a classical finite-element method, we need to distinguish the local mesh of grid points that define an element from the global mesh of all the grid points in the model, many of which are shared amongst several spectral elements. A mapping between grid points in the local mesh and grid points in the global mesh needs to be defined; efficient routines are available for this purpose from finite-element modeling. Before the system can be marched forward in time, the contributions (the so-called internal forces) from all the elements that share a common global grid point need to be summed. In a traditional finite-element method this is referred to as assembling the system. This assembly stage is a costly part of the calculation on parallel computers, because information from individual elements needs to be shared with neighboring elements. From a computational point of view, this operation involves communications between distinct CPUs.

Let U denote the displacement vector of the global system in the solid regions, i.e., U contains the displacement vector at all the grid points in the global mesh, classically referred to as the global degrees of freedom of the system. The ordinary

differential equation that governs the time dependence of the global system may be written in the form

$$M\ddot{U} + KU + BU = F, \tag{2.46}$$

where M denotes the global diagonal mass matrix, K the global stiffness matrix, B the boundary interactions at the CMB or ICB, and F the source term, all of which have been described at the elemental level earlier in this section. To take full advantage of the fact that the global mass matrix is diagonal, time discretization of the second-order ordinary differential equation (2.46) is achieved based upon a classical explicit second-order finite-difference scheme, which is a particular case of the more general Newmark scheme (e.g., Hughes 1987), moving the stiffness and boundary terms to the right-hand side. Such a scheme is conditionally stable, and the Courant stability condition is governed by the maximum value of the ratio between the P-wave velocity and the size of the grid spacing. In the fluid regions of the model, we solve a system similar to (2.46) but written in terms of the generalized scalar potential χ. Because of the domain decomposition used to match the fluid and the solid regions of the model, we implement the scheme in a staggered predictor-multicorrector format (Park & Felippa 1980; Felippa & Deruntz 1984; Thompson & Pinsky 1996; Komatitsch et al. 2000a), iterating on the coupling conditions (i.e., the surface integrals over the CMB and the ICB). Such an iterative scheme converges very rapidly (Komatitsch et al. 2000a), after only two iterations in practice in the cases presented in this study. The iterations have a negligible impact on the cost of the method since we only need to iterate on the degrees of freedom that are coupled at the interface (i.e., only the layers of elements in contact with the CMB and the ICB, which represent a very small percentage of the total number of elements).

The memory-variable equation (2.11) is solved for $\mathbf{R}_\ell$ using a modified second-order Runge-Kutta scheme in time, since such schemes are known to be efficient for this problem (Carcione 1994). We do not spread the memory variables across the grid.

Figure 2.6 *The PC cluster that we built at Caltech in the summer of 2000. It is composed of 160 dual-processor PCs (Pentium III, 733 MHz) with 1 gigabyte of memory each, for a total of 320 processors and 160 gigabytes. The height of the shelves is approximately 2.40 m. The boxes are connected using a standard 100 Mbits/s Fast Ethernet network (the green and blue cables). In the back (left), one can see the 192-port CISCO switch.*

Two quantities that reflect the quality of the mesh are the number of grid points per wavelength, i.e., the resolution of the mesh in terms of how well it samples the wave field,

$$N = \tau_0 (v/\Delta h)_{\min}, \tag{2.47}$$

and the stability condition

$$C = \Delta t (v/\Delta h)_{\max}, \tag{2.48}$$

which illustrates how large the time step of the explicit time integration scheme can be while maintaining a stable simulation. Here τ_0 denotes the shortest period of the source, $(v/\Delta h)_{\min}$ denotes the minimum ratio of wave speed v and grid spacing Δh within a given element, and $(v/\Delta h)_{\max}$ denotes the maximum ratio of wave speed and grid spacing.

It is worth mentioning that the two time schemes used in this study are only second-order accurate, contrary to the high-order spatial accuracy provided by the spectral-element discretization. Therefore it might be of interest in the future to switch to higher-order time schemes, as proposed for instance by Tarnow & Simo (1994). However, this problem is not critical since the stability condition of the explicit time scheme imposes a reasonably small time step, which provides an accurate evolution in time, even with a simple second-order scheme.

2.4 Parallel implementation

The mesh designed for the Earth in Figure 2.4 is too large to fit in memory on a single computer. We therefore implement the method on a cluster of PCs using a message-passing programming methodology. Research on how to use large PC clusters for scientific purposes started in 1994 with NASA's Beowulf project, named after the famous Old English poem narrating the adventures of the Scandinavian prince *Beowulf* (e.g., Heaney 2000). The name of the initial project is now used as a generic name for this type of architecture: these PC cluster computers are referred to as 'Beowulf' machines. Their main advantage is that they provide an excellent price-performance ratio, i.e., impressive performance can be reached at relatively low cost compared to classical shared-memory computers.

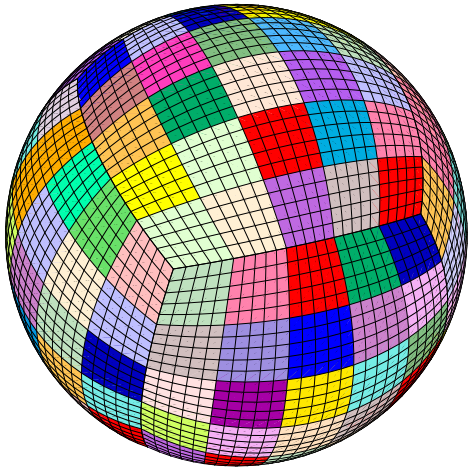

Figure 2.7 *Each of the six chunks that makes up the cubed sphere is subdivided in terms of 25 slices of elements. Each of these slices resides on a single CPU, such that the entire calculation involves 150 CPUs. The results on the edges of a slice need to be communicated to all its neighbors. Note that the communication patterns are different for slices inside a chunk, on the edges of a chunk, and on the corners of a chunk.*

The main drawback of the parallel approach is that one needs to use message-passing techniques, since memory is distributed over the different PCs, which makes implementation of algorithms usually more difficult. An important advantage, however, is the portability of codes written based upon this philosophy, because they can virtually run on any kind of machine, including shared-memory computers. The standard approach for programming clusters is to use a message-passing library called MPI (e.g., Gropp et al. 1994), an acronym for 'Message Passing Interface'. MPI has become a *de facto* standard in the parallel computing community, thus ensuring the portability of software. In our SEM, because we can use fully explicit time-marching schemes since the mass matrix is diagonal by construction, the PCs spend most of their time doing computations, and communications of results between PCs represent only a small fraction of the time of simulation. Therefore, clusters of PCs are ideal for this application in spite of the high latency of the inexpensive network connecting them.

The SEM calculations are performed on a PC cluster in the Seismological Laboratory at Caltech (Figure 2.6). This machine consists of 80 dual-processor PCs with 1 gigabyte of memory each. We built this cluster ourselves from scratch in the summer of 2000 using standard PC parts ('Commodity Off-The-Shelf' technology).

The simulations are distributed over 150 processors: each of the six chunks that constitute the globe is subdivided amongst 25 processors (corresponding to 25 mesh slices). Figure 2.7 shows how the slices are designed in the cubed-sphere mesh. Note that inside each of the six chunks the mesh of slices is derived from a regular Cartesian topology. However, the topology of the network of slices is different between chunks: each corner of each chunk is shared between three rather than two or four slices. This complicates the message-passing implementation since, as illustrated in Figure 2.5, in the assembly of the global system given by equation (2.46) one needs to sum all the contributions (i.e., the internal forces computed separately in each slice) between slices. This problem is solved using a three-step sequence of messages: we first assemble the contributions between slices inside each chunk; then between slices located on the edges of different chunks, excluding the corners of valence 3; then in a last step we assemble these corners separately.

The mesh shown in Figure 2.4 contains a total of approximately 2.6 million spectral elements. In each spectral element we use a polynomial degree $N = 4$ for the expansion of the Lagrange interpolants at the Gauss-Lobatto-Legendre points (as in equations (2.34) and (2.35) for instance), which means each spectral element contains $(N + 1)^3 = 125$ points, and the total global system of equation (2.46), counting common points on the edges only once, contains 180 million points (corresponding to approximately 483 million degrees of freedom since we solve for the three components of displacement at each grid point, except in the fluid outer core, where we solve for the scalar potential). Polynomial degrees around 4 or 5 have proven to be optimal for wave propagation problems using the SEM, since they provide the best tradeoff between accuracy and time-integration stability (Seriani & Priolo 1994). After division of the mesh into slices, each processor is responsible for 17,000 elements; with a polynomial degree $N = 4$, this corresponds to roughly 1.2 million grid points per

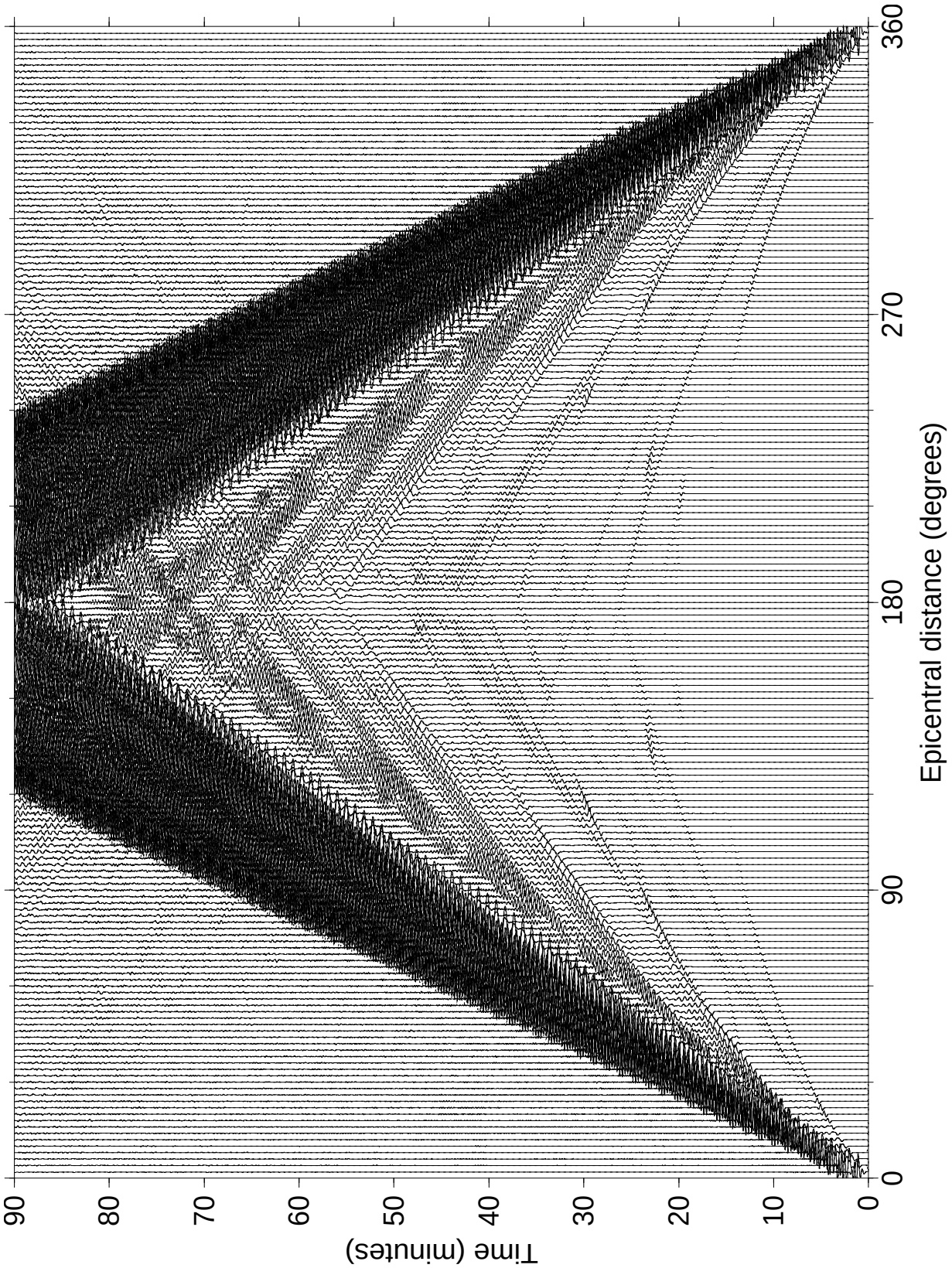

Figure 2.8 *SEM (solid lines) and normal-mode (dotted lines) record sections for elastic, anisotropic PREM. The event is the February 17, 1996, Irian Jaya earthquake which occurred at a depth of 15 km. Stations record ground displacement at* 2° *intervals along the equator. Each trace is individually scaled so that they all have the same maximum value. The vertical component of displacement is displayed. The SEM and normal-mode synthetic seismograms are in excellent agreement for all body- and surface-wave arrivals; they almost cannot be distinguished on the scale of this figure.*

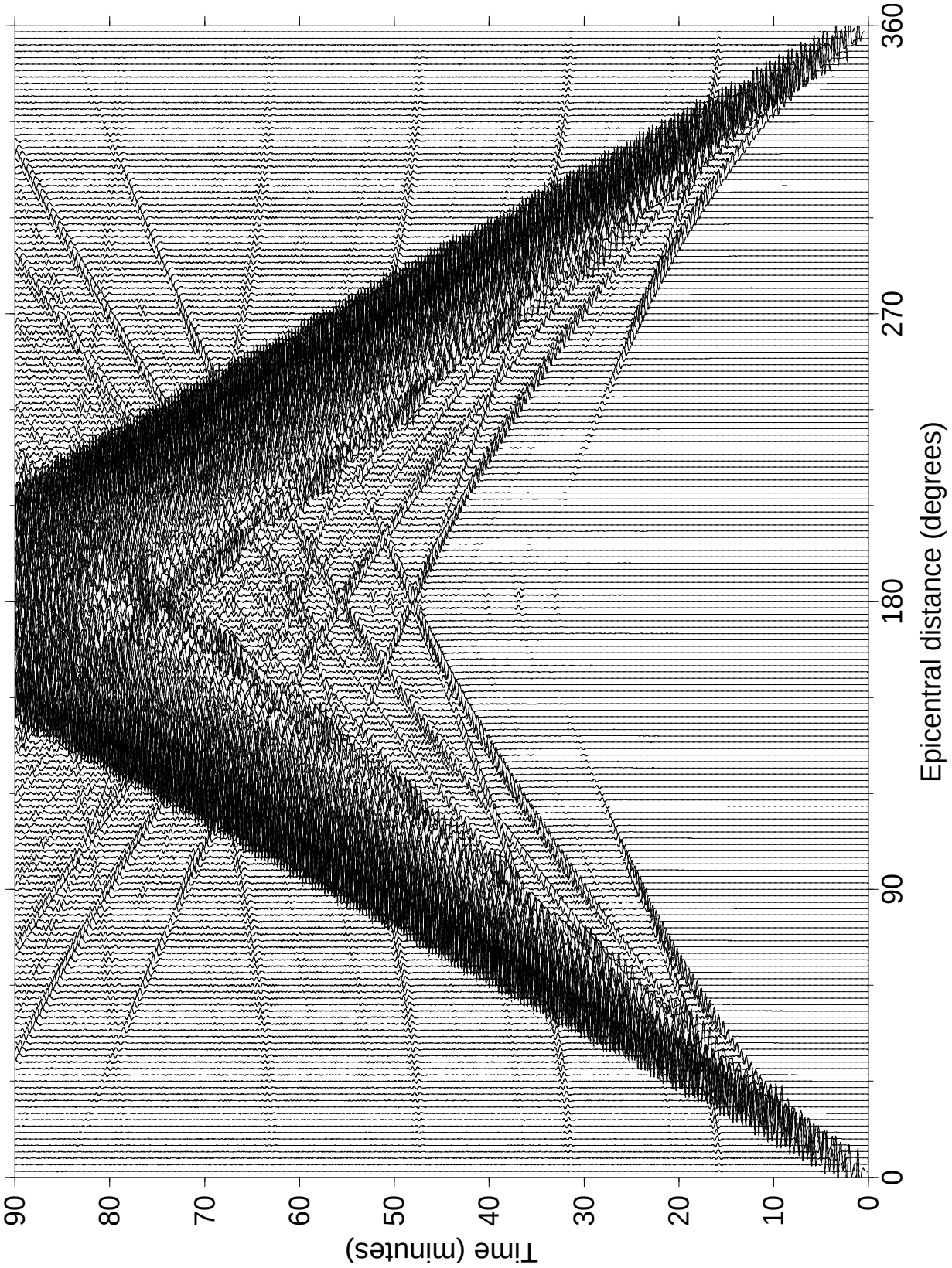

Figure 2.9 *Same as Figure 2.8 for the transverse component of displacement.*

processor. It is worth mentioning that, because of the mesh coarsening with depth, as shown in Figure 2.4, most of the elements are located in the upper part of the model, where the wave speeds are slowest: 13 % of the elements are in the crust, 70 % in the mantle, 16 % in the outer core, and 1 % in the inner core (the small central cube in excluded, since it is handled separately). Therefore, most of the cost of the calculations comes from the upper mantle, and the entire core is almost negligible in terms of CPU time (also because in the outer core we solve for a scalar potential instead of a vector, which therefore further reduces the amount of calculations).

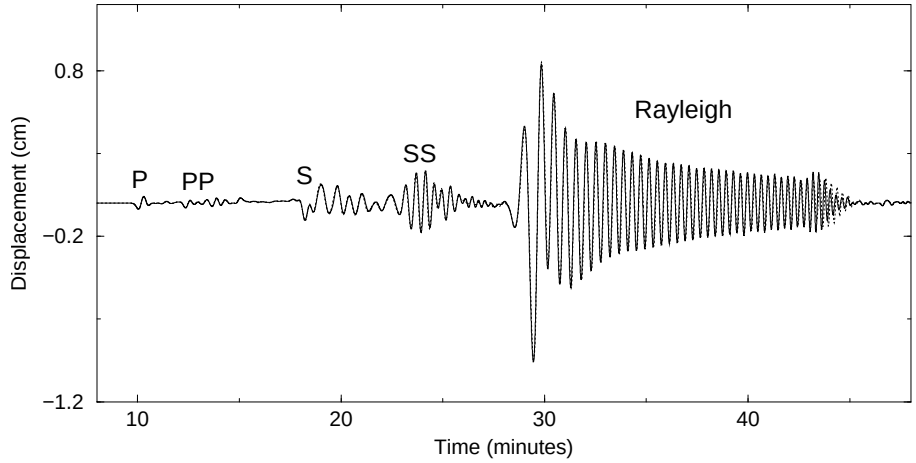

Figure 2.10 *Comparison between normal-mode and SEM synthetic seismograms at an epicentral distance of* 60° *for the shallow Irian Jaya event, for the vertical component of displacement. Note the strongly dispersed surface wave and the excellent match for the body-wave arrivals.*

2.5 Results

In this section we carefully benchmark the SEM against normal-mode synthetic seismograms for anisotropic PREM without the ocean layer. We use the mesh and source-receiver geometry shown in Figure 2.4. In each simulation the epicenter is located on the equator and the Greenwich meridian. Stations record ground displacement along the equator and the Greenwich meridian at 2-degree intervals. For reference, we used two normal-mode catalogs with a shortest period of 8 s: one without attenuation and another one with attenuation. No free-air, tilt, or gravitational potential corrections were applied (Dahlen & Tromp 1998).

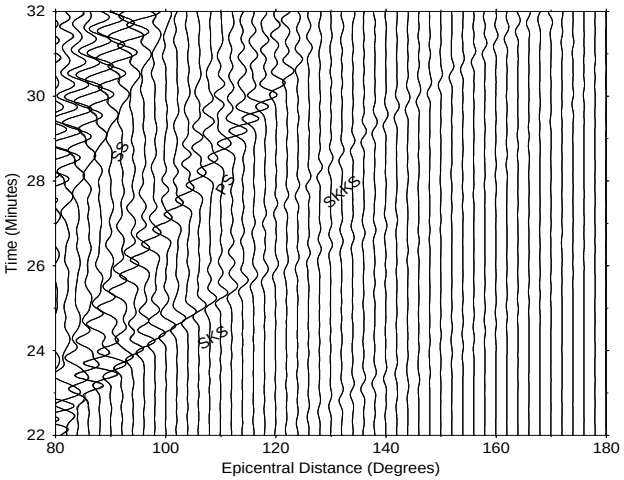

Figure 2.11 *Record section comparison between SEM (solid lines) and mode (dotted lines) synthetic seismograms for core-sensitive body-wave arrivals SKS and SKKS between* 80° *and* 180°*. At each epicentral distance we plot both the SEM and the mode solutions, which are basically indistinguishable. The accurate predictions for SKS and SKKS validate the domain decomposition between the fluid and solid regions of the model as well as the potential used to represent the inhomogeneous fluid discussed in Section 2.3.2. Note that the converted phase PS is also very well modeled.*

2.5.1 Validation for a shallow earthquake without attenuation

We simulate the February 17, 1996, Irian Jaya earthquake. This large $M_w = 8.2$ event had its hypocenter at a depth of 15 km. Because of its shallow depth, the event generates strong surface waves, which provide a difficult test for the SEM: the free surface boundary condition, the thin, slow crust, and the anisotropic asthenosphere all come into play. The event

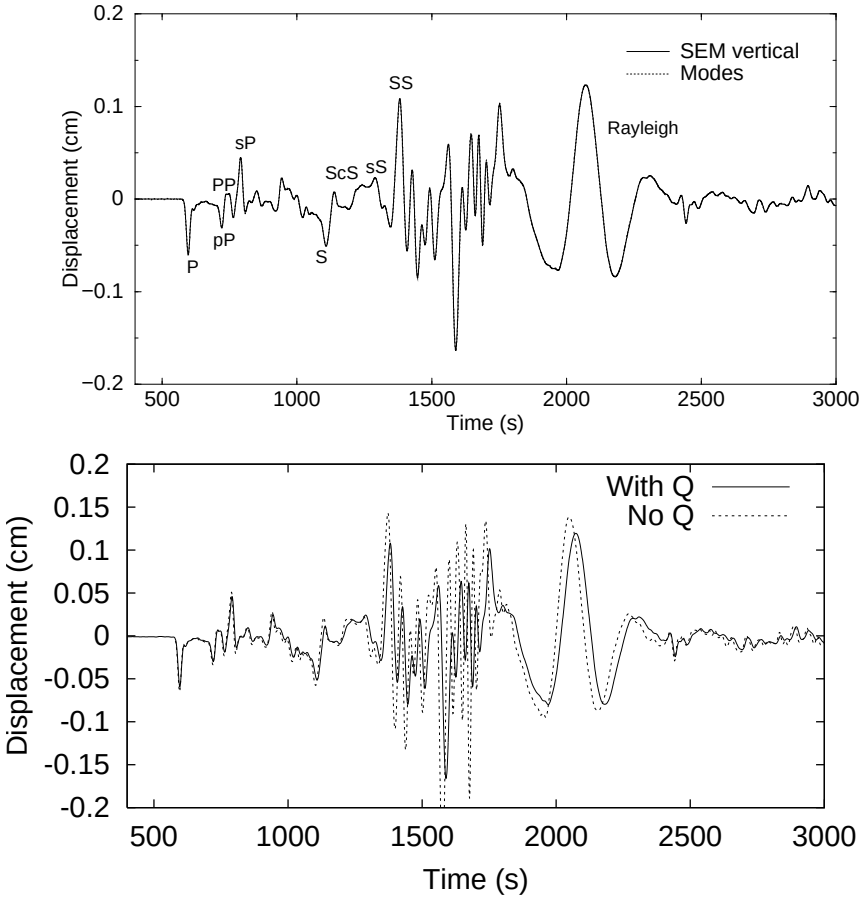

Figure 2.12 *(Top) SEM (solid line) and mode (dotted line) synthetic seismograms for the great magnitude 8.2 Bolivia earthquake of June 9, 1994, recorded at TriNet station PAS in Pasadena, California. The depth of the event is 647 km. Anisotropy and attenuation are both included in this simulation. The vertical component of displacement is displayed. The agreement is almost perfect. (Bottom) To illustrate the effects of attenuation and physical dispersion associated with anelastic PREM, we compare vertical component mode synthetic seismograms for PREM with (solid line) and without (dotted line) incorporating the effects of anelasticity. Note that elastic PREM is faster than anelastic PREM, and that in particular the S wave is significantly attenuated.*

has a half-duration of 18 s. Attenuation is turned off in this first simulation in order to validate the method and the code for purely elastic, anisotropic media.

In Figures 2.8 and 2.9 we show 90-minute-long vertical and transverse record sections for epicentral distances from 0° to 360° and stations along the equator, as shown in Figure 2.4. Each epicentral distance is associated with two traces: one calculated based upon normal-mode summation and the other based upon the SEM. The fact that the two synthetic seismograms are basically indistinguishable demonstrates that the SEM synthetic seismograms are very accurate. Many classical teleseismic body-wave arrivals can be easily distinguished. On the vertical component one can clearly see P, S and their surface bounces, as well as the strongly dispersed Rayleigh wave. On the transverse component, S, SS, SSS, and SSSS are very prominent, and so are ScS_{1-5}, and the Love wave. Note that near the antipode, where energy is arriving from all directions and the transverse component has little meaning, SKKS energy can be seen around 32 minutes in both the mode and the SEM solutions.

In Figure 2.10 we show a more detailed comparison between normal-mode and SEM synthetic seismograms at an epicentral distance of 60°. Because the mode synthetic seismograms are only quasi-analytical, and therefore also contain some numerical errors, we do not show the difference between the SEM and normal-mode synthetic seismograms since this is not an objective estimate of the accuracy of the SEM. The figure illustrates the level of accuracy for P, PP, S, and SS body waves as well as the Rayleigh wave on the vertical component.

The accuracy of the implementation of the inhomogeneous outer core based upon a scalar potential, as discussed in Section 2.3.2, is well illustrated by the SKS and SKKS arrivals in Figure 2.11. The fact that normal modes and the SEM agree very well both in phase and in amplitude also validates the implementation of the domain decomposition between the fluid and solid regions of the model and the associated boundary conditions.

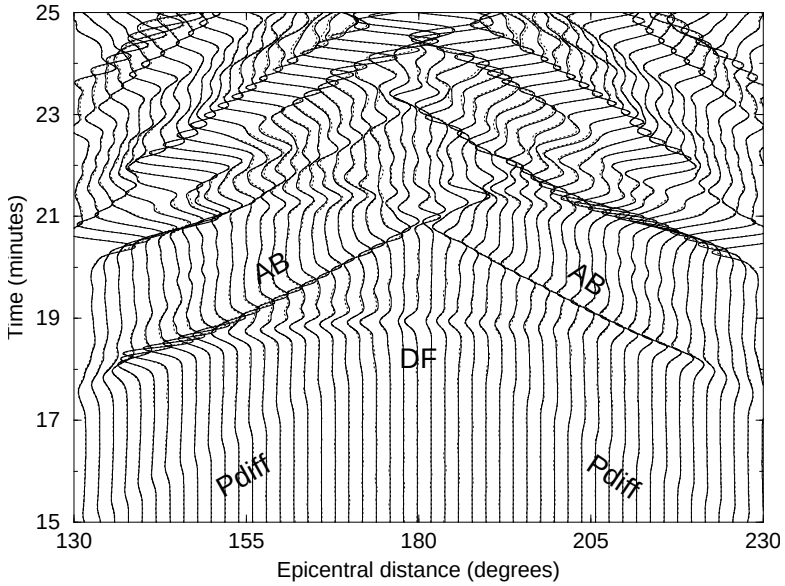

Figure 2.13 *Record section comparison of PKP phases calculated for anelastic, anisotropic PREM based upon the SEM (solid lines) and modes (dotted lines) between* 130° *and* 230° *along the Greenwich meridian. At each epicentral distance we plot both the SEM and the mode solution. All PKP arrivals, including PKIKP, which has traveled through the central cube in the mesh, are well reproduced. Note also a very weak* $P_{\rm diff}$ *arrival in both synthetics between* 130° *and* 170° *and between* 190° *and* 230°*. This demonstrates that we can correctly handle the unusually high value of Poisson's ratio in the inner core.*

2.5.2 Validation for a deep earthquake with attenuation

At this point we wish to validate our implementation of attenuation in the method. We simulate the June 9, 1994, Bolivia earthquake of magnitude $M_w = 8.2$, which occurred at a depth of 647 km. We use a moment-rate function similar to the one used for the Irian Jaya event, but with a slightly shorter half-duration of 15 s.

Associated with PREM is a five-layer attenuation model. As mentioned earlier, we only incorporate shear attenuation: bulk attenuation can be safely neglected because the bulk quality factor Q is several hundred times larger than the shear Q. The calculation of normal-mode seismograms for anelastic Earth models is based upon first-order perturbation theory, which is acceptable for the attenuation associated with PREM (e.g., Dahlen & Tromp 1998); however as a consequence the mode synthetic seismograms in this section are not as accurate as in the purely elastic case of the previous section. In the SEM, for each layer we determine stress and stain relaxation times τ_ℓ^σ and τ_ℓ^ϵ for an absorption-band model over the period range between 20 and 1000 s, based upon three standard linear solids. Because of the broad period range, a solution based upon two solids does not give a satisfactory result. We evenly space the three stress relaxation times τ_ℓ^σ in logarithmic frequency. Next, we determine the strain relaxation times τ_ℓ^ϵ by minimizing the difference between the desired constant Q and predictions based upon the series of three standard linear solids using a simple iterative inversion scheme. Associated with the absorption-band model is physical dispersion which affects the arrival times of the waves. To accommodate this, we take PREM, which has a reference frequency of one Hertz, i.e., $\omega_0 = 2\pi$, and determine the shear modulus appropriate for a frequency ω_c at the logarithmic center of the frequency range of interest (Liu et al. 1976):

$$\mu(\omega_c) = \mu(\omega_0)[1 + 2/(\pi Q_\mu)\ln(\omega_c/\omega_0)]. \tag{2.49}$$

Given $\mu(\omega_c)$ we can calculate the relaxed modulus μ_R, from which we obtain the time dependent modulus $\mu(t)$ and the unrelaxed modulus μ_U based upon equations (2.8) and (2.10), respectively.

We check the results of our simulation at teleseismic distance at the Pasadena, California, TriNet station PAS at an epicentral distance of 68°. Figure 2.12 shows the vertical component of displacement both for the modes and the SEM. Excellent agreement is obtained. To appreciate the effects of attenuation and how accurately it has been modeled by the SEM, the figure also shows the solution computed based upon normal modes with and without attenuation. One can see that the waveforms are significantly affected by attenuation, both in phase and amplitude.

We show in Figure 2.13 a close-up of PKP arrivals on the vertical component. The PKP waveforms are very sensitive to the very high value of Poisson's ratio, 0.44, in the inner core: if the shear-wave velocity is not correctly represented, the PKP waveforms change considerably. Numerically this poses a challenge, because if the mesh is not fine enough the very slow inner-core shear-wave velocity of about 3.6 km.s^{-1} is not sampled by enough points per wavelength. In our results, the PKP(AB) and PKP(BC) outer core branches as well as the PKP(DF) inner core branch are all very accurately modeled. A very weak $P_{\rm diff}$ arrival can be seen in the P shadow in both synthetics. The PKP(DF) arrival has traveled through the cube at the center of the inner core (Figure 2.3), which interacts with all the processors in the parallel implementation of the method, as explained previously. Note the very prominent depth phases, e.g., pPKP(DF), which arrive about 2 and a half minutes after the corresponding direct phases due to the large depth of the event.

Chapitre 3

Modélisation dans la Terre globale 3-D

Résumé

Dans le chapitre précédent, nous avons validé la méthode des éléments spectraux pour la propagation des ondes sismiques dans des modèles de Terre globaux 1-D. Dans ce chapitre, nous incluons la complexité des modèles de Terre 3-D, c'est-à-dire des variations transversales de la vitesse des ondes de compression, de cisaillement et de la densité, un modèle 3-D de la croûte, l'ellipticité de la Terre, ainsi que la topographie et la bathymétrie. Nous incluons l'effet des océans, de la rotation et de la gravité. Pour modéliser l'effet des océans, nous introduisons une formulation basée sur un chargement équivalent pour lequel il n'est pas nécessaire de mailler explicitement les océans. Certains de ces effets, qui sont souvent considérés comme négligeables en sismologie globale, peuvent en réalité jouer un rôle significatif pour certaines configurations de source et de récepteur. L'anisotropie et l'atténuation, qui ont été introduites dans le chapitre précédent, sont également incorporées dans ce chapitre. Tous ces phénomènes sont introduits de telle manière que nous préservons les principaux avantages de la méthode des éléments spectraux, c'est-à-dire une matrice de masse exactement diagonale et une efficacité de calcul élevée sur les ordinateurs parallèles. Pour valider l'implémentation de la gravité et des océans, nous comparons les sismogrammes synthétiques calculés par la méthode des éléments spectraux à des sismogrammes synthétiques quasi-analytiques calculés par une méthode de sommation de modes normaux pour le modèle à symétrie sphérique PREM. Les deux méthodes sont en excellent accord pour toutes les ondes de volume et de surface jusqu'à des périodes d'environ 20 secondes dans le cas de la gravité et 25 secondes dans le cas des océans. Nous présentons des résultats pour un tremblement de terre réel dans un modèle 3-D, pour lequel l'ajustement aux données est sensiblement amélioré par rapport à un calcul classique de modes normaux dans PREM. Nous montrons que pour des trajets trans-Pacifique l'onde de Rayleigh peut arriver plus d'une minute plus tôt que dans PREM, et que l'onde de Love a une durée beaucoup plus courte.

Abstract

In the previous chapter, we validated the spectral-element method for seismic wave propagation in spherically-symmetric global Earth models. In this chapter, we include the full complexity of 3-D Earth models, i.e., lateral variations in compressional-wave velocity, shear-wave velocity and density, a 3-D crustal model, ellipticity, as well as topography and bathymetry. We also include the effects of the oceans, rotation, and self-gravitation. For the oceans we introduce a formulation based upon an equivalent load, in which the oceans do not need to be meshed explicitly. Some of these effects, which are often considered negligible in global seismology, can in fact play a significant role for certain source-receiver configurations. Anisotropy and attenuation, which were introduced and validated in the previous chapter, are also incorporated in this study. The complex phenomena that are taken into account are introduced in such a way that we preserve the main advantages of the spectral-element method, which are an exactly diagonal mass matrix and very high computational efficiency on parallel computers. For self-gravitation and the oceans we benchmark the spectral-element synthetic seismograms against normal-mode synthetic seismograms for spherically-symmetric reference model PREM. The two methods are in excellent agreement for all body- and surface-wave arrivals with periods greater than about 20 s in the case of self-gravitation and 25 s in the case of the oceans. We subsequently present results of simulations for a real earthquake in a fully 3-D Earth model for which the fit to the data is significantly improved compared to classical normal-mode calculations based upon PREM. For example, we show that for trans-Pacific paths the Rayleigh wave can arrive more than a minute earlier than in PREM, and that the Love wave is much shorter in duration.

3.1 Introduction

Progress in global seismology is to a large extent due to the tremendous growth in seismic data acquisition, particularly with the worldwide deployment of digital broadband networks over the past two decades. Based upon this wealth of data, 3-D models of shear and compressional velocity heterogeneity, anisotropy, and attenuation have provided important constraints on the Earth's composition and physical processes (Montagner 1998; Romanowicz 1998; Becker & Boschi 2002). While data acquisition continues to be a priority, it is clear that improving seismic models will also require the development, implementation, and application of theories and numerical methods that accurately incorporate the effects of mantle and crustal heterogeneity on wave propagation.

For one-dimensional (1-D) Earth models, i.e., models that vary as a function of depth only, e.g., the Preliminary Reference Earth Model (PREM) (Dziewonski & Anderson 1981) shown in Figure 3.1, semi-analytical techniques, such as normal-mode summation (Gilbert 1970) and the reflectivity method (Fuchs & Muller 1971), are widely used to synthesize seismograms. To calculate seismograms in three-dimensional (3-D) Earth models, e.g., shear-velocity model S20RTS (Ritsema et al. 1999) shown in Figure 3.1, seismologists frequently resort to asymptotic techniques, such as ray theory (Cervený 2001), the path-average approximation (Woodhouse & Dziewonski 1984), or non-linear asymptotic coupling theory (Li & Tanimoto 1993).

All tomographic inversions for 3-D models of the mantle are rooted in perturbation theory. In travel-time tomography, the difference between the observed arrival time of a seismic wave and a prediction based upon a 1-D model, δT, may be related to 3-D perturbations in wave velocity, δv, through Fermat's principle:

$$\delta T = -\int_{\text{ray path}} \frac{\delta v}{v^2}\,\mathrm{d}s. \tag{3.1}$$

Here v denotes either compressional velocity α or shear velocity β in the 1-D reference model, and the integration is along the unperturbed ray path in this reference model. Surface-wave tomography involves an inversion of the difference between the observed and predicted phase, $\delta\Psi$, for lateral variations in Love or Rayleigh phase velocity, δc:

$$\delta\Psi = -\int_{\text{great circle}} \frac{\delta c}{c^2}\,\mathrm{d}s. \tag{3.2}$$

In this case the integration is along the great circle between a given earthquake and station, and c denotes the phase velocity in the 1-D reference model. Finally, in normal-mode seismology the difference between the observed and predicted mode eigenfrequency, $\delta\omega$, may be related to 3-D variations in compressional velocity $\delta\alpha$, shear velocity $\delta\beta$, and density $\delta\rho$, through Rayleigh's principle:

$$\delta\omega = \int_V (\delta\alpha K_\alpha + \delta\beta K_\beta + \delta\rho K_\rho)\,\mathrm{d}^3\mathbf{r}. \tag{3.3}$$

The integration is over the entire volume V of the Earth, and the sensitivity kernels K_α, K_β, and K_ρ are calculated based upon the modes and model parameters of the 1-D reference model.

These three popular approximations define simple linear inverse problems. However, it has recently been demonstrated that they may be of limited validity when we wish to recover velocity variations on length scales smaller than approximately 1000 km (Nolet & Dahlen 2000; Spetzler et al. 2001), close to the resolution provided by the most recent 3-D models.

To assess the quality of a 3-D model, i.e., to evaluate the misfit between the data and the synthetic seismograms, the same approximate methods that were used to construct the model are called upon. This means that there is a real danger that errors in the theory are mapped back into the model.

To overcome this dilemma, seismologists have begun to resort to numerical methods. Unfortunately, most of the current techniques come with severe restrictions, and furthermore they are frequently limited to 2-D axi-symmetric models to reduce the computational burden. Because of its simplicity and ease of implementation, the finite-difference technique has been introduced to simulate global seismic wave propagation (Igel & Weber 1996; Chaljub & Tarantola 1997). This technique is based upon a strong or differential formulation of the wave equation in its differential form, which makes the implementation of the free surface boundary condition as well as the accurate representation of sharp solid-solid (e.g., upper mantle discontinuities at depths of 410 km and 660 km) and, more importantly, fluid-solid boundaries (e.g., the core-mantle and inner-core boundary) problematic. The pseudospectral technique, in which the wave field is expanded in global basis functions, typically sines, cosines, or Chebyshev polynomials (Furumura et al. 1998; Cormier 1999), is associated with similar difficulties because it is also based upon a strong formulation. Nevertheless, this method has been used to simulate wave propagation in a portion of the mantle (Igel 1999). For both finite-difference and pseudospectral

techniques, gridding the entire globe remains an outstanding challenge (the main difficulty comes from the singularity of coordinates at the center of Earth). Alternative approaches, such as the direct-solution method (Hara et al. 1991; Geller & Ohminato 1994) and the coupled-mode method (Park 1986; Lognonné & Romanowicz 1990), which are based upon a weak or integral formulation of the equation of motion, are numerically expensive because of the wide coupling bandwidth required in the presence of strong lateral heterogeneity, and handling variations in crustal thickness is difficult because effects due to boundary undulations are linearized. Because direct-solution and coupled-mode methods involve the manipulation of large matrices, they are restricted to modeling long-period seismograms (typically periods greater than 80 seconds).

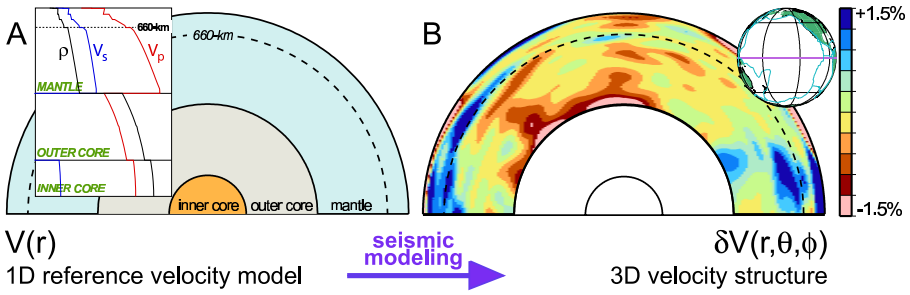

Figure 3.1 *Illustration of how seismic modeling is commonly conducted. (A) Cross section of the Earth with the mantle, outer core, and inner core shaded blue, gray, and yellow, respectively. Superimposed on the left are 1-D profiles of density (black), shear velocity (blue), and compressional velocity (red) for the Preliminary Reference Earth Model (PREM) (Dziewonski & Anderson 1981). The shear velocity is zero in the liquid outer core. Density and velocity vary smoothly throughout the model, except at compositional boundaries (e.g., the core-mantle boundary) or phase transitions in the upper mantle (e.g., at depths of 410 km and 660 km). For 1-D models such as PREM, which vary only as a function of depth, seismograms are computed using semi-analytical techniques such as normal-mode summation or the reflectivity method. (B) Equatorial cross-section through the Pacific mantle of shear velocity model S20RTS (Ritsema et al. 1999). Shown are relative lateral variations in shear velocity $\delta v(r,\theta,\phi)/v(r)$, where r denotes the radius, θ colatitude, and ϕ longitude. These 3-D variations are superimposed on the velocity $v(r)$ in the 1-D reference model. Red colors denote lower than average velocity perturbations and blue colors denote higher than average wave velocities. For 3-D models, seismologists commonly use asymptotic methods such as ray theory (Cervený 2001) or the path-average approximation (Woodhouse & Dziewonski 1984) to construct seismograms.*

To be practical, a method for the simulation of global seismic wave propagation should accurately incorporate effects due to velocity heterogeneity, anisotropy, anelasticity, sharp velocity and density contrasts, crustal thickness variations, topography, ellipticity, rotation, self-gravitation, and the oceans, without intrinsic restrictions on the level of heterogeneity nor the applicable frequency range. The spectral-element method (SEM) is such a method, as has been demonstrated in the previous chapter. In this chapter, the effects of the ocean are incorporated based upon an equivalent surface load without having to actually mesh the water layer. Self-gravitation is introduced in the SEM in a fashion similar to the innovative work of Chaljub (2000) and Chaljub et al. (2003). We validate the implementation of self-gravitation and the oceans by comparison with normal-mode synthetic seismograms for the Preliminary Reference Earth Model (PREM) (Dziewonski & Anderson 1981).

3.2 Meshing the 3-D Earth

We use the mesh for a spherically symmetric Earth model developed in the previous chapter (Figure 2.4) as a starting point for a mesh for the 3-D Earth. Any reasonably smooth laterally heterogeneous shear-velocity, compressional-velocity, or density model may be used in the mantle. In this chapter we will use model S20RTS of Ritsema et al. (1999) (Figure 3.2). Lateral variations determined by this model are superimposed on the Preliminary Reference Earth Model (PREM) (Dziewonski & Anderson 1981). Variations in density are obtained by scaling the shear-wave velocity variations by a factor of 0.4, in accordance with mineral physics estimates.

Every phase observed in a seismogram is affected by the Earth's crust, so it is important to incorporate a detailed crustal model in the mesh. We use Crust 5.2, also known as Crust 2.0 (Bassin et al. 2000), which is a global $2^\circ \times 2^\circ$ crustal model (Figure 3.2). We do not incorporate the ice layer that is present in some regions of Crust 5.2, but we do include the sedimentary layers. The Moho depth in Crust 5.2 varies between 6.65 km (oceanic crust) and 75 km (underneath the Himalaya). The compressional-wave velocity at the surface of Crust 5.2, excluding the sedimentary layers, varies between 5.0 and 6.2 km.s^{-1}, the shear-wave velocity varies between 2.5 and 3.2 km.s^{-1}, and density varies between 2600

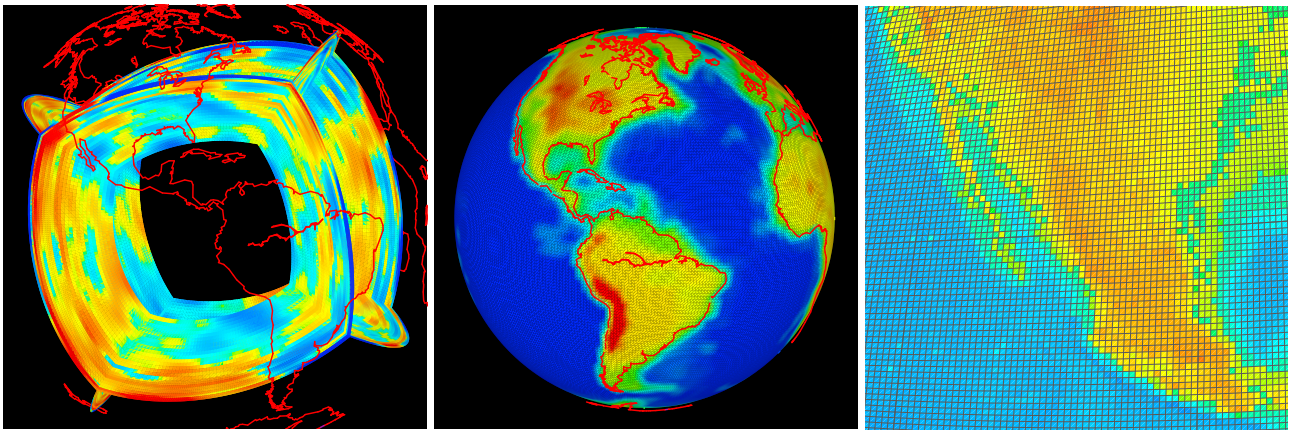

Figure 3.2 *(Right) Mantle model S20RTS (Ritsema et al. 1999) is superimposed on the mesh. A 3-D density model is obtained by scaling the shear-wave velocity variations by a factor of 0.4, in accordance with mineral physics estimates. The figure shows lateral variations in shear velocity projected onto the four sides of the six chunks that constitute the cubed sphere mesh. Blue colors denote faster than average shear-wave velocities, and red colors denote slower than average shear-wave velocities. (Middle) The* $2^\circ \times 2^\circ$ *crustal model Crust 5.2 (Bassin et al. 2000) is superimposed on the mesh. Because the model consists of blocks with constant properties, we smooth it by averaging over spherical caps with a* 2° *radius. The figure shows Moho depth (which varies between 6.65 km and 75 km in the model). Red represents thicker than average crust, and blue thinner than average crust. (Right) Topography and bathymetry of the Earth, obtained from the ETOPO5 model (NOAA 1988), is added to the mesh. We show a close-up of Mexico and the Southern United States representing the spectral elements in the mesh at the surface (gray squares). The color scale represents elevation with respect to the reference ellipsoid. In each spectral element we use a polynomial degree* $N = 4$*, therefore each surface mesh element contains* $(N+1)^2 = 25$ *grid points, which translates into an average grid spacing of approximately 10 km at the surface.*

and 2800 kg.m^{-3}. For comparison, PREM has an upper-crustal P-velocity of 5.8 km.s^{-1}, an S-velocity of 3.2 km.s^{-1} and a density of 2600 kg.m^{-3}.

Once the mantle and crustal models have been added, we make the Earth elliptical in shape. The ellipticity as a function of depth is determined by solving Clairaut's equation (Dahlen & Tromp 1998), and the mesh is stretched or squished accordingly. Free surface topography and bathymetry are also incorporated in the mesh (Figure 3.2). We use the global 5 minute $\times$ 5 minute ETOPO5 bathymetry and topography model (NOAA 1988). The bathymetry map is also used to define the thickness of the oceans at the surface of the mesh in order to take into account the effects of the oceans on global wave propagation. As will be explained in Section 3.3, the oceans are incorporated in the SEM by introducing an equivalent load at the ocean floor, without having to explicitly mesh the water layer. At this stage we therefore simply store a map of the thickness of the oceans.

3.3 The Spectral-Element Method

In this chapter we incorporate the oceans, which are mostly relevant for free surface reflected phases, such as PP, SS and SP, and for the dispersion of Rayleigh waves. We also include the effects of self-gravitation and rotation, which are mostly relevant in the context of long-period surface waves.

3.3.1 Hydrostatic equilibrium

Throughout this chapter we assume that the Earth is in hydrostatic equilibrium before the occurrence of an earthquake. For a rotating, self-gravitating Earth model this means that pressure gradients are balanced by gradients of the geopotential (e.g., Dahlen & Tromp 1998). Let P denote the initial pressure in the Earth model, let Φ denote the gravitational potential associated with the initial distribution of density ρ, and let ψ denote the centrifugal potential, which is defined in terms of the Earth's angular rotation vector $\mathbf{\Omega}$ by $\psi = -\frac{1}{2}[\Omega^2 r^2 - (\mathbf{\Omega} \cdot \mathbf{r})^2]$. Here $\mathbf{r}$ is the position vector, $r = |\mathbf{r}|$ denotes the radius, and $\Omega = |\mathbf{\Omega}|$ is the angular rotation rate. In what follows, we will ignore the non-hydrostatic prestress, in which case hydrostatic equilibrium is determined by $\boldsymbol{\nabla} P = -\rho \boldsymbol{\nabla}(\Phi + \psi)$. This equation implies that equal surfaces of initial pressure P, density ρ, and geopotential $\Phi + \psi$ coincide. As a result, these level surfaces are axially symmetric ellipsoids. Because we assume that we can neglect the non-hydrostatic prestress, there is no contradiction between this assumption and the fact that we use a 3-D density model in the mesh.

Suppose we start with a spherically symmetric, non-rotating Earth model. The gravitational potential Φ_0 of such an Earth model is determined by Poisson's equation: $\Phi_0'' + 2r^{-1}\Phi_0' = 4\pi G\rho_0$, where ρ_0 denotes the radial profile of density, G denotes the gravitational constant, and a prime denotes differentiation with respect to radius r. If we define the magnitude of the gravitational acceleration to be $g_0 = \Phi_0'$, then we have

$$g_0' + 2r^{-1}g_0 = 4\pi G\rho_0. \tag{3.4}$$

The gravitational potential Φ in a slowly rotating, ellipsoidal Earth model can be expressed as $\Phi = \Phi_0 + \frac{2}{3}(r\epsilon g_0 - \frac{1}{2}\Omega^2 r^2)P_2(\cos\theta)$, and the centrifugal potential ψ may be written in the form $\psi = -\frac{1}{3}\Omega^2 r^2[1 - P_2(\cos\theta)]$, where ϵ denotes the ellipticity as a function of radius, P_2 is the degree-2 Legendre function, and θ denotes colatitude. The associated gravitational acceleration $\mathbf{g}$ is defined in terms of the gradient of the geopotential by

$$\mathbf{g} = -\boldsymbol{\nabla}(\Phi + \psi) = -\left[g_0 + \tfrac{2}{3}(\epsilon g_0 + r\epsilon' g_0 + r\epsilon g_0')P_2 - \tfrac{2}{3}\Omega^2 r\right]\hat{\mathbf{r}} - \tfrac{2}{3}\,\epsilon g_0 \partial_\theta P_2\,\hat{\boldsymbol{\theta}}. \tag{3.5}$$

Here g_0' is determined by (3.4), and the radial derivative of ellipticity ϵ' is usually defined in terms of the auxiliary function $\eta = r\epsilon'/\epsilon$ (Dahlen & Tromp 1998).

In the weak formulation of the equations of motion in the mantle and inner core we shall need the gradient of the gravitational acceleration, $\mathbf{H} = \boldsymbol{\nabla}\mathbf{g}$, which is given by

$$\begin{aligned}
\mathbf{H} = \quad & - \left[g_0' + \tfrac{2}{3}(2\epsilon' g_0 + 2\epsilon g_0' + 2r\epsilon' g_0' + r\epsilon'' g_0 + r\epsilon g_0'')P_2 - \tfrac{2}{3}\Omega^2\right]\hat{\mathbf{r}}\hat{\mathbf{r}} \\
& - \tfrac{2}{3}(\epsilon' g_0 + \epsilon g_0')\,\partial_\theta P_2\,(\hat{\boldsymbol{\theta}}\hat{\mathbf{r}} + \hat{\mathbf{r}}\hat{\boldsymbol{\theta}}) \\
& - r^{-1}\left[g_0 + \tfrac{2}{3}(\epsilon g_0 + r\epsilon' g_0 + r\epsilon g_0')P_2 - \tfrac{2}{3}\Omega^2 r + \tfrac{2}{3}r^{-1}\epsilon g_0 \partial_\theta^2 P_2\right]\hat{\boldsymbol{\theta}}\hat{\boldsymbol{\theta}} \\
& - r^{-1}\left[g_0 + \tfrac{2}{3}(\epsilon g_0 + r\epsilon' g_0 + r\epsilon g_0')P_2 - \tfrac{2}{3}\Omega^2 r + \tfrac{2}{3}r^{-1}\epsilon g_0 \cot\theta \partial_\theta P_2\right]\hat{\boldsymbol{\phi}}\hat{\boldsymbol{\phi}}.
\end{aligned} \tag{3.6}$$

The second derivative of ellipticity with respect to radius is determined by Clairaut's equation, and the second derivative of the gravitational acceleration g_0'' may be obtained by differentiating (3.4).

In most cases, however, we can neglect the contribution of ellipticity and rotation, since ϵ is very small ($\epsilon \simeq 1/300$ at the surface) and so is the squared Earth's rotation rate. Under these assumptions, (3.5) and (3.6) reduce to

$$\mathbf{g} = -\,g_0\,\hat{\mathbf{r}} \tag{3.7}$$

and

$$\mathbf{H} = -\,g_0'\,\hat{\mathbf{r}}\hat{\mathbf{r}} - r^{-1}g_0\,(\hat{\boldsymbol{\theta}}\hat{\boldsymbol{\theta}} + \hat{\boldsymbol{\phi}}\hat{\boldsymbol{\phi}}), \tag{3.8}$$

respectively. These are the expressions that we will use in the rest of the chapter.

3.3.2 Mantle and Crust

In a rotating, self-gravitating Earth model, the elastic wave equation for the mantle and crust may be written in the form (Dahlen & Tromp 1998)

$$\rho(\partial_t^2\mathbf{s} + 2\boldsymbol{\Omega}\times\partial_t\mathbf{s}) = \boldsymbol{\nabla}\cdot\mathbf{T} + \boldsymbol{\nabla}(\rho\,\mathbf{s}\cdot\mathbf{g}) - \rho\boldsymbol{\nabla}\phi - \boldsymbol{\nabla}\cdot(\rho\,\mathbf{s})\mathbf{g} + \mathbf{f}. \tag{3.9}$$

Here $\mathbf{T}$ denotes the stress tensor, which is linearly related to the displacement gradient $\boldsymbol{\nabla}\mathbf{s}$ by Hooke's law (equation (2.6) in the previous chapter) in an elastic model, or by the generalization (2.9) in an anelastic model. The earthquake source is represented by the point force $\mathbf{f}$, which is given in terms of the moment tensor $\mathbf{M}$ by (2.14). The perturbed gravitational potential ϕ is determined by Poisson's equation within the Earth, $\nabla^2\phi = -\,4\pi G\,\boldsymbol{\nabla}\cdot(\rho\mathbf{s})$, and by Laplace's equation in the rest of space, $\nabla^2\phi = 0$.

Because Laplace's equation is defined in all of space, solving the momentum equation (3.9) in conjunction with Poisson's and Laplace's equations is rather daunting from a numerical perspective. The approach can be simplified considerably by making what is known as Cowling's approximation (Cowling 1941), as discussed by Valette (1987), Dahlen & Tromp (1998) and Chaljub (2000). In this approximation one ignores perturbations ϕ in the gravitational potential while retaining the unperturbed gravitational potential. Physically, this means that we ignore the effects of mass redistribution. Under this assumption the momentum equation (3.9) becomes

$$\rho(\partial_t^2\mathbf{s} + 2\boldsymbol{\Omega}\times\partial_t\mathbf{s}) = \boldsymbol{\nabla}\cdot\mathbf{T} + \boldsymbol{\nabla}(\rho\,\mathbf{s}\cdot\mathbf{g}) - \boldsymbol{\nabla}\cdot(\rho\,\mathbf{s})\mathbf{g} + \mathbf{f}. \tag{3.10}$$

The associated boundary conditions are that on the free surface the traction $\hat{\mathbf{n}}\cdot\mathbf{T}$, where $\hat{\mathbf{n}}$ denotes the unit outward normal to the free surface, needs to vanish. On the CMB the normal component of displacement $\hat{\mathbf{n}}\cdot\mathbf{s}$ needs to be continuous, and the traction $\hat{\mathbf{n}}\cdot\mathbf{T}$ at the bottom of the mantle needs to match the traction $-p\,\hat{\mathbf{n}}$ at the top of the outer core, where p denotes the perturbed pressure in the fluid.

The weak form of the equation of motion (3.10) is obtained by taking the dot product with an arbitrary test vector $\mathbf{w}$, integrating by parts over the volume M of the mantle and crust, and imposing the stress-free surface boundary condition. Using the definition (3.8), this gives

$$\begin{aligned}\int_{\mathrm{M}} \rho\,\mathbf{w}\cdot\partial_t^2\mathbf{s}\,\mathrm{d}^3\mathbf{r} + \int_{\mathrm{M}} 2\rho\,\mathbf{w}\cdot(\boldsymbol{\Omega}\times\partial_t\mathbf{s})\,\mathrm{d}^3\mathbf{r} = &- \int_{\mathrm{M}} \boldsymbol{\nabla}\mathbf{w} : (\mathbf{T}+\mathbf{G})\,\mathrm{d}^3\mathbf{r} + \mathbf{M} : \boldsymbol{\nabla}\mathbf{w}(\mathbf{r}_{\mathrm{s}})\,S(t)\\ &+ \int_{\mathrm{CMB}} p\,\hat{\mathbf{n}}\cdot\mathbf{w}\,\mathrm{d}^2\mathbf{r} - \int_{\mathrm{M}} \rho\,\mathbf{s}\cdot\mathbf{H}\cdot\mathbf{w}\,\mathrm{d}^3\mathbf{r},\end{aligned} \tag{3.11}$$

where we have used the continuity of traction at the CMB, and where we have defined the second-order tensor

$$\mathbf{G} = \rho[\mathbf{s}\mathbf{g} - (\mathbf{s}\cdot\mathbf{g})\mathbf{I}]. \tag{3.12}$$

Because of the non-symmetric nature of $\mathbf{G}$, we note that our definition of the double dot product between two second-order tensors $\mathbf{A}$ and $\mathbf{B}$ is $\mathbf{A} : \mathbf{B} = A_{ij}B_{ij}$. Let us mention that it is possible to obtain a symmetric weak formulation of the gravity terms (Chaljub 2000), but this is more expensive from a numerical perspective since one can show that the amount of computations is roughly doubled. This is not needed in finite-element or spectral-element methods, which can handle non-symmetric terms.

3.3.3 Outer core

In the fluid outer core, making the Cowling approximation, the equation of motion may be written in the form

$$\rho(\partial_t^2\mathbf{s} + 2\boldsymbol{\Omega}\times\partial_t\mathbf{s}) = \boldsymbol{\nabla}(\kappa\boldsymbol{\nabla}\cdot\mathbf{s} + \rho\,\mathbf{s}\cdot\mathbf{g}) - \boldsymbol{\nabla}\cdot(\rho\,\mathbf{s})\mathbf{g}, \tag{3.13}$$

where κ denotes the bulk modulus of the fluid. Under the assumption of hydrostatic equilibrium prior to the earthquake, the equation of motion in the fluid may be rewritten in the form

$$\partial_t^2\mathbf{s} + 2\boldsymbol{\Omega}\times\partial_t\mathbf{s} = \boldsymbol{\nabla}(\rho^{-1}\kappa\boldsymbol{\nabla}\cdot\mathbf{s} + \mathbf{s}\cdot\mathbf{g}) + \rho^{-1}g^{-2}\kappa(\boldsymbol{\nabla}\cdot\mathbf{s})N^2\mathbf{g}, \tag{3.14}$$

where $g = |\mathbf{g}|$ and

$$N^2 = (\rho^{-1}\boldsymbol{\nabla}\rho - \rho\kappa^{-1}\mathbf{g})\cdot\mathbf{g} \tag{3.15}$$

is the Brunt-Väisälä frequency (e.g., Valette 1986, 1987; Dahlen & Tromp 1998; Chaljub et al. 2003). Following the ideas of these authors, we assume that the fluid is stably stratified and isentropic, which means that $N^2 = 0$. In that case the equation of motion in the fluid outer core reduces to

$$\partial_t^2\mathbf{s} + 2\boldsymbol{\Omega}\times\partial_t\mathbf{s} = \boldsymbol{\nabla}(\rho^{-1}\kappa\boldsymbol{\nabla}\cdot\mathbf{s} + \mathbf{s}\cdot\mathbf{g}). \tag{3.16}$$

Next, we introduce a scalar potential χ such that the fluid pressure $p = -\kappa\boldsymbol{\nabla}\cdot\mathbf{s}$ may be written as

$$p = -\rho\partial_t\chi + \rho\mathbf{g}\cdot\mathbf{s}, \tag{3.17}$$

and a vector $\mathbf{u}$ such that

$$\partial_t\mathbf{s} = \boldsymbol{\nabla}\chi + \mathbf{u}. \tag{3.18}$$

Note that the scalar potential χ introduced in the previous chapter is a particular case of (3.17)-(3.18) in the absence of gravity and rotation. Upon differentiating (3.17) with respect to time and using (3.18) we obtain the scalar wave equation

$$\kappa^{-1}\rho\partial_t^2\chi = \boldsymbol{\nabla}\cdot(\boldsymbol{\nabla}\chi + \mathbf{u}) + \kappa^{-1}\rho\mathbf{g}\cdot(\boldsymbol{\nabla}\chi + \mathbf{u}). \tag{3.19}$$

Substitution of (3.18) and (3.17) in (3.16) yields a precession equation for $\mathbf{u}$:

$$\partial_t\mathbf{u} + 2\boldsymbol{\Omega}\times\mathbf{u} = -2\boldsymbol{\Omega}\times\boldsymbol{\nabla}\chi. \tag{3.20}$$

Let us write the angular rotation vector $\boldsymbol{\Omega}$ as $\boldsymbol{\Omega} = \Omega\hat{\mathbf{z}}$. Then the solution to (3.20) may be written in the form

$$\mathbf{u} = [A\cos(2\Omega t) + B\sin(2\Omega t)]\,\hat{\mathbf{x}} + [-A\sin(2\Omega t) + B\cos(2\Omega t)]\,\hat{\mathbf{y}}, \tag{3.21}$$

where the coefficients A and B are determined by

$$\begin{aligned} \partial_t A &= 2\Omega \left[\cos(2\Omega t)\partial_y \chi + \sin(2\Omega t)\partial_x \chi\right] , \\ \partial_t B &= 2\Omega \left[\sin(2\Omega t)\partial_y \chi - \cos(2\Omega t)\partial_x \chi\right] . \end{aligned} \tag{3.22}$$

Note that the vector $\mathbf{u}$ has no z-component, i.e., $\hat{\mathbf{z}} \cdot \mathbf{u} = 0$.

The weak form of (3.19) is obtained by multiplying by an arbitrary test function w and integrating by parts, using the continuity of the normal component of velocity:

$$\begin{aligned} \int_{\mathrm{OC}} \kappa^{-1} \rho w \partial_t^2 \chi \, d^3\mathbf{r} = & - \int_{\mathrm{OC}} (\boldsymbol{\nabla} w) \cdot (\boldsymbol{\nabla}\chi + \mathbf{u}) \, d^3\mathbf{r} + \int_{\mathrm{OC}} \kappa^{-1} \rho w \mathbf{g} \cdot (\boldsymbol{\nabla}\chi + \mathbf{u}) \, d^3\mathbf{r} \\ & + \int_{\mathrm{CMB}} w \hat{\mathbf{n}} \cdot \partial_t \mathbf{s} \, d^2\mathbf{r} - \int_{\mathrm{ICB}} w \hat{\mathbf{n}} \cdot \partial_t \mathbf{s} \, d^2\mathbf{r}. \end{aligned} \tag{3.23}$$

In the domain decomposition between the fluid outer core and the solid inner core and mantle, we match the normal component of velocity by taking $\hat{\mathbf{n}} \cdot \partial_t \mathbf{s}$ at the bottom of the mantle and using it in the surface integral over the CMB in (3.23), and by taking $\hat{\mathbf{n}} \cdot \partial_t \mathbf{s}$ from the top of the inner core and using it in the surface integral over the ICB in (3.23). This is identical to the fluid/solid domain decomposition approach adopted in the previous chapter. The continuity of traction is honored by calculating the fluid pressure p from (3.17) based upon $\partial_t \chi$ in the fluid and the normal component of displacement $\hat{\mathbf{n}} \cdot \mathbf{s}$ taken from the solid at the bottom of the mantle (CMB) or at the top of the inner core (ICB). This fluid pressure is then used in the surface integral over the CMB in (3.11) and in the surface integral over the ICB in (3.24).

3.3.4 Inner core

The weak form of the equation of motion in the solid inner core is similar to (3.11):

$$\begin{aligned} \int_{\mathrm{IC}} \rho \, \mathbf{w} \cdot \partial_t^2 \mathbf{s} \, \mathrm{d}^3\mathbf{r} + \int_{\mathrm{IC}} 2\rho \, \mathbf{w} \cdot (\boldsymbol{\Omega} \times \partial_t \mathbf{s}) \, \mathrm{d}^3\mathbf{r} = & - \int_{\mathrm{IC}} \boldsymbol{\nabla}\mathbf{w} : (\mathbf{T} + \mathbf{G}) \, \mathrm{d}^3\mathbf{r} \\ & - \int_{\mathrm{ICB}} p \, \hat{\mathbf{n}} \cdot \mathbf{w} \, \mathrm{d}^2\mathbf{r} - \int_{\mathrm{IC}} \rho \, \mathbf{s} \cdot \mathbf{H} \cdot \mathbf{w} \, \mathrm{d}^3\mathbf{r}. \end{aligned} \tag{3.24}$$

Note that the inner core-outer core interactions, represented by the surface integrals over the ICB in (3.23) and (3.24), also honor continuity in traction and continuity of the normal component of displacement and velocity.

3.3.5 Complications owing to the oceans

Those areas of the Earth that are covered by a water layer (oceans or large lakes) are subject to a slightly more complicated weak formulation of the problem. The weak form of the equations of motion in the solid Earth (mantle and crust) covered by water is

$$\begin{aligned} \int_{\mathrm{M}} \rho \, \mathbf{w} \cdot \partial_t^2 \mathbf{s} \, \mathrm{d}^3\mathbf{r} + \int_{\mathrm{M}} 2\rho \, \mathbf{w} \cdot (\boldsymbol{\Omega} \times \partial_t \mathbf{s}) \, \mathrm{d}^3\mathbf{r} = & - \int_{\mathrm{M}} \boldsymbol{\nabla}\mathbf{w} : (\mathbf{T} + \mathbf{G}) \, \mathrm{d}^3\mathbf{r} \; + \; \mathbf{M} : \boldsymbol{\nabla}\mathbf{w}(\mathbf{r}_{\mathrm{s}}) \, S(t) \\ & + \int_{\mathrm{CMB}} p \, \hat{\mathbf{n}} \cdot \mathbf{w} \, \mathrm{d}^2\mathbf{r} - \int_{\mathrm{OCB}} p \, \hat{\mathbf{n}} \cdot \mathbf{w} \, \mathrm{d}^2\mathbf{r} \\ & - \int_{\mathrm{M}} \rho \, \mathbf{s} \cdot \mathbf{H} \cdot \mathbf{w} \, \mathrm{d}^3\mathbf{r}, \end{aligned} \tag{3.25}$$

where OCB denotes the ocean-crust boundary (i.e., the ocean floor). What we need is an expression for the fluid pressure p at the OCB. In the oceans, the waves satisfy the fluid wave equation (3.16), which can be rewritten as:

$$\partial_t^2 \mathbf{s} + 2\boldsymbol{\Omega} \times \partial_t \mathbf{s} = -\boldsymbol{\nabla}(p - \mathbf{s} \cdot \mathbf{g}). \tag{3.26}$$

We shall assume that the oceans are incompressible, which means that the entire water column moves as a whole as a result of the normal displacement $\hat{\mathbf{n}} \cdot \mathbf{s}$ of the sea floor. This is a good approximation for periods of typically 20 seconds and above, as will be demonstrated in Section 3.4, because the thickness of the oceans is small compared to the wavelength of the seismic waves we are interested in (this would cease to be true at very short periods). We only wish to reproduce the effect of the load at the ocean floor, not phases that actually propagate in the oceans themselves (e.g., the tsunami).

Suppose that the water column has a local thickness h. Upon integrating (3.26) over the water column, taking into account the variations of gravity with radius according to (3.4), we obtain the local result

$$p = \rho_w \, h \, \hat{\mathbf{n}} \cdot \partial_t^2 \mathbf{s} + 2\rho_w \, h \, \hat{\mathbf{n}} \cdot (\mathbf{\Omega} \times \partial_t \mathbf{s}) + 4\pi G \rho_w^2 \, h \, \hat{\mathbf{n}} \cdot \mathbf{s}, \tag{3.27}$$

where ρ_w denotes the density of sea water ($\rho_w \simeq 1020$ kg.m^{-3}). As a result, the weak form of the equations of motion in the crust and mantle (3.25) becomes

$$\begin{aligned} \int_{\mathrm{M}} \rho \, \mathbf{w} \cdot \partial_t^2 \mathbf{s} \, \mathrm{d}^3\mathbf{r} \quad &+ \quad \int_{\mathrm{OCB}} \rho_w h \, (\mathbf{w} \cdot \hat{\mathbf{n}})(\hat{\mathbf{n}} \cdot \partial_t^2 \mathbf{s}) \, \mathrm{d}^2\mathbf{r} + \int_{\mathrm{M}} 2\rho \, \mathbf{w} \cdot (\mathbf{\Omega} \times \partial_t \mathbf{s}) \, \mathrm{d}^3\mathbf{r} \\ &+ \quad \int_{\mathrm{OCB}} 2\rho_w h \, (\mathbf{w} \cdot \hat{\mathbf{n}})[\hat{\mathbf{n}} \cdot (\mathbf{\Omega} \times \partial_t \mathbf{s})] \, \mathrm{d}^2\mathbf{r} \\ = \quad - \quad &\int_{\mathrm{M}} \boldsymbol{\nabla} \mathbf{w} : (\mathbf{T} + \mathbf{G}) \, \mathrm{d}^3\mathbf{r} \;+\; \mathbf{M} : \boldsymbol{\nabla} \mathbf{w}(\mathbf{r}_{\mathrm{s}}) \, S(t) \;-\; \int_{\mathrm{M}} \rho \, \mathbf{s} \cdot \mathbf{H} \cdot \mathbf{w} \, \mathrm{d}^3\mathbf{r} \\ &+ \quad \int_{\mathrm{CMB}} p \, \hat{\mathbf{n}} \cdot \mathbf{w} \, \mathrm{d}^2\mathbf{r} - \int_{\mathrm{OCB}} 4\pi G \rho_w^2 h (\hat{\mathbf{n}} \cdot \mathbf{w})(\hat{\mathbf{n}} \cdot \mathbf{s}) \, \mathrm{d}^2\mathbf{r} \, . \end{aligned} \tag{3.28}$$

In practice, the ocean load represents a small effect, and the gravity and rotation terms in (3.27) involve additional small corrections which can be safely neglected. Hence we solve the following equation in the mantle, moving the Coriolis term to the right-hand side:

$$\begin{aligned} \int_{\mathrm{M}} \rho \, \mathbf{w} \cdot \partial_t^2 \mathbf{s} \, \mathrm{d}^3\mathbf{r} \quad &+ \quad \int_{\mathrm{OCB}} \rho_w h \, (\mathbf{w} \cdot \hat{\mathbf{n}})(\hat{\mathbf{n}} \cdot \partial_t^2 \mathbf{s}) \, \mathrm{d}^2\mathbf{r} \\ = \quad - \quad &\int_{\mathrm{M}} 2\rho \, \mathbf{w} \cdot (\mathbf{\Omega} \times \partial_t \mathbf{s}) \, \mathrm{d}^3\mathbf{r} - \int_{\mathrm{M}} \boldsymbol{\nabla} \mathbf{w} : (\mathbf{T} + \mathbf{G}) \, \mathrm{d}^3\mathbf{r} \;+\; \mathbf{M} : \boldsymbol{\nabla} \mathbf{w}(\mathbf{r}_{\mathrm{s}}) \, S(t) \\ - \quad &\int_{\mathrm{M}} \rho \, \mathbf{s} \cdot \mathbf{H} \cdot \mathbf{w} \, \mathrm{d}^3\mathbf{r} + \int_{\mathrm{CMB}} p \, \hat{\mathbf{n}} \cdot \mathbf{w} \, \mathrm{d}^2\mathbf{r} \, . \end{aligned} \tag{3.29}$$

The local thickness of the oceans, h, is taken from a bathymetry map, as explained in Section 3.2. Note that this means that we can very efficiently take into account the effects of the oceans by a simple modification of the mass matrix for the points (more precisely the degrees of freedom) located at the ocean floor, as can be concluded from the second term on the left-hand side of (3.29), which is a mere surface integral along the OCB. Note also that the compressional-wave velocity in the oceans does not appear in (3.28)-(3.29).

3.3.6 Discretization of the weak formulation and time marching

Most of the terms in the weak formulations (3.11), (3.23) and (3.24) were presented in the previous chapter. In this section we give explicit expressions for the elemental form of the terms that arise as a result of the Earth's rotation and self-gravitation.

The weak form of the Coriolis term in (3.11) and (3.24) for an element Ω_e is

$$\int_{\Omega_e} 2\rho \, \mathbf{w} \cdot (\mathbf{\Omega} \times \partial_t \mathbf{s}) \, \mathrm{d}^3\mathbf{r} \approx 2\Omega \sum_{\alpha,\beta,\gamma=0}^{n} \omega_\alpha \omega_\beta \omega_\gamma J^{\alpha\beta\gamma} \rho^{\alpha\beta\gamma} \sum_{i,j=1}^{3} w_i^{\alpha\beta\gamma} \epsilon_{i3j} \dot{s}_j^{\alpha\beta\gamma}. \tag{3.30}$$

Here ϵ_{ijk} is the alternating tensor, and we have used the expansions (2.31) and (2.32) of the previous chapter for the displacement field $\mathbf{s}$ and the test vector $\mathbf{w}$. Note that the Coriolis matrix (3.30) is diagonal and has no contribution in the z-direction.

Self-gravitation contributes two terms to (3.11) and (3.24). The first contribution can be incorporated in the calculation of the stiffness matrix by making the substitution $\mathbf{T} \rightarrow \mathbf{T} + \mathbf{G}$, remembering that $\mathbf{G}$ is non-symmetric. The second gravity contribution has the weak form

$$\int_{\Omega_e} \rho \, \mathbf{s} \cdot \mathbf{H} \cdot \mathbf{w} \, \mathrm{d}^3\mathbf{r} \approx \sum_{\alpha,\beta,\gamma=0}^{n} \omega_\alpha \omega_\beta \omega_\gamma J^{\alpha\beta\gamma} \rho^{\alpha\beta\gamma} \sum_{i,j=1}^{3} w_i^{\alpha\beta\gamma} H_{ij}^{\alpha\beta\gamma} s_j^{\alpha\beta\gamma}. \tag{3.31}$$

Note that this gravity term is diagonal.

The only new fluid term that arises in the context of self-gravitation and rotation is

$$\int_{\Omega_e} \kappa^{-1} \rho w \mathbf{g} \cdot (\boldsymbol{\nabla}\chi + \mathbf{u})\, d^3\mathbf{r} \approx \sum_{\alpha,\beta,\gamma=0}^{n} \omega_\alpha \omega_\beta \omega_\gamma J^{\alpha\beta\gamma} w^{\alpha\beta\gamma} (\kappa^{-1}\rho)^{\alpha\beta\gamma} \sum_{i=1}^{3} g_i^{\alpha\beta\gamma} [(\partial_i \chi)^{\alpha\beta\gamma} + u_i^{\alpha\beta\gamma}], \tag{3.32}$$

where $(\partial_i \chi)^{\alpha\beta\gamma}$ is given by (2.45) in the previous chapter.

Schematically, the global system of equations we need to solve may be written in the form

$$M\ddot{U} + W\dot{U} + KU + BU = F, \tag{3.33}$$

where U denotes the displacement vector at all grid points in the global mesh, M the global diagonal mass matrix, W the global Coriolis matrix, K the global stiffness matrix, B the boundary interactions at the CMB and the ICB, and F the source term.

The presence of an ocean layer, in the context of the equivalent ocean load formulation introduced above, only affects the normal component of displacement at the ocean floor, i.e., at the top of the mesh. All that needs to be done for these points is to replace the mass matrix M by $M + m$, where m denotes the 'surface mass' which represents the ocean load. This modified mass matrix remains globally diagonal, and inverting it involves a simple division.

In the previous chapter, the momentum equation (3.33) was marched using a classical explicit second-order finite-difference scheme, which is a particular case of the general Newmark scheme for hyperbolic equations (e.g., Hughes 1987). In order to perform the coupling between solid and fluid regions in the domain decomposition approach, the scheme is implemented in practice in a staggered predictor-multicorrector format, following the ideas of Park & Felippa (1980) and Felippa & Deruntz (1984). In addition, in the previous chapter the memory variable equations used to mimic attenuation with a constant quality factor Q were marched separately using a modified second-order Runge-Kutta scheme. In this chapter, we still make use of these two schemes, but in addition we need to march the precession equation (3.22) to solve for rotation in the fluid outer core. A second-order Runge-Kutta scheme could be used for this purpose, but considering that the rotation rate of the Earth is slow compared to the time scale of wave propagation, we instead use a simple Euler time-integration scheme. The properties of the time schemes, as well as the value of the time step Δt, are unchanged with respect to the previous chapter.

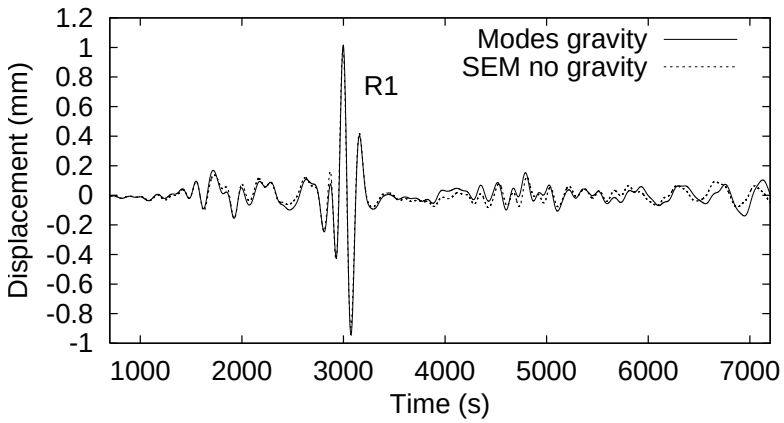

Figure 3.3 *Vertical component of displacement of the normal-mode solution for the shallow Irian Jaya event with the full implementation of gravity (solid line) and the SEM solution without gravity (dotted line) at an epicentral distance of 100°. The results have been lowpass-filtered at a corner period of 120 s. The total duration of the simulation is two hours in order to show R_1.*

3.4 Numerical results

In this section we first carefully benchmark the implementations of self-gravitation and the oceans for spherically-symmetric model PREM by comparing the SEM results to the normal-mode solution (e.g., Dahlen & Tromp 1998). We then combine the effects of self-gravitation, the oceans, rotation, anisotropy and attenuation with a 3-D mantle model, a 3-D crustal model, ellipticity, topography and bathymetry to simulate a real earthquake in Vanuatu.

All the calculations in this section incorporate an anisotropic asthenosphere as in PREM (the upper 220 km of the Earth's mantle). Attenuation is included in the Vanuatu calculations, but not in the tests for self-gravitation and the oceans, in order to validate these effects individually. Anisotropy and attenuation in the context of the SEM were validated in the previous chapter. The normal-mode and SEM calculations also include self-gravitation based upon the Cowling approximation, unless explicitly stated otherwise. We use the same time integration and mesh parameters as in the previous chapter, i.e.,

$N = 240$ spectral elements at the surface in each direction of each of the six chunks of the cubed sphere mesh, a time step of $\Delta t = 0.20$ s, and a Heaviside source time-function. The results are subsequently convolved with a Gaussian function with a half-duration of 18 s. The full mesh contains roughly 180 million global points (corresponding to approximately 483 million degrees of freedom, since we solve for the three components of displacement at each grid point, except in the fluid outer core, where we solve for the scalar potential), and the calculations are performed on a 150-processor PC cluster with 75 Gigabytes of memory.

3.4.1 Validation of self-gravitation in the Cowling approximation

First, let us illustrate the magnitude of the gravitational contributions. We compare the results of an SEM calculation without gravity to the normal-mode solution with the full implementation of self-gravitation. Because the influence of gravity is mainly noticeable at long periods (typically greater than 100 s), for this test we convolve the synthetic seismograms with a Gaussian function with a half-duration of 18 s and lowpass the results at a corner period of 120 s using a six-pole two-pass Butterworth filter. We choose a record length of two hours in order to include Rayleigh wave R_1 and Love waves G_1-G_2. In Figure 3.3 we show the results at an epicentral distance of 100° for a large shallow $M_w = 8.2$ event at a depth of 15 km (the Irian Jaya earthquake presented in the previous chapter). At these long periods there is a large effect associated with gravity on the vertical and longitudinal components, whereas the transverse component (not shown here) is unaffected.

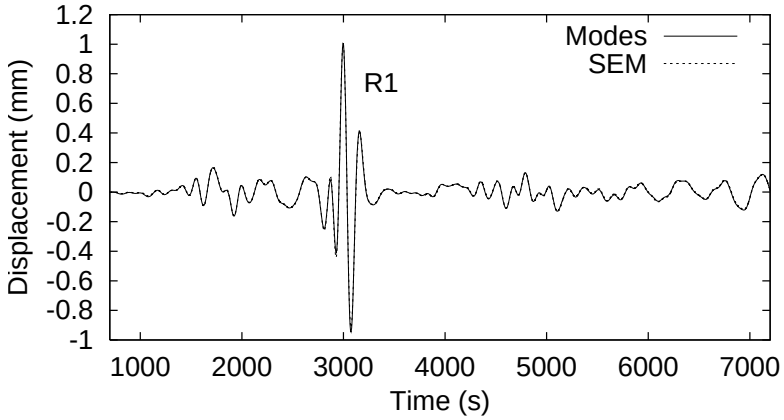

Figure 3.4 *Vertical component of the PREM normal-mode solution in the Cowling approximation (solid line) and the SEM displacement (dotted line) for the shallow Irian Jaya event at an epicentral distance of 100°. We have lowpass filtered the results at a corner period of 120 s. Compared to Figure 3.3 we fit the large gravitational signal very well.*

Next, we show that the implementation of self-gravitation in the SEM based upon the Cowling approximation (3.11), (3.23) and (3.24) is accurate. As mentioned earlier, the implementation of self-gravitation in the context of the SEM was studied by Chaljub (2000). We adopt a similar approach here, except that we use a simpler non-symmetric form as explained in Section 3.3. In Figure 3.4 we compare the SEM results to the normal-mode solution in the Cowling approximation for the shallow Irian Jaya event at an epicentral distance of 100°. Compared to Figure 3.3, we fit the large signal due to gravity very well. This result confirms that the implementation of self-gravitation in the SEM in the context of the Cowling approximation is accurate.

3.4.2 Effect of the oceans

The presence of the oceans is mostly relevant for the dispersion of Rayleigh waves in the case of shallow events, as well as for free surface reflected phases, such as PP, SS and SP. To illustrate the magnitude of the effect of the oceans on wave propagation, Figure 3.5 shows results of an SEM calculation for PREM without the ocean layer (therefore using an Earth radius of 6368 km instead of 6371 km), compared to the PREM normal-mode solution computed with the ocean layer. The event is the shallow Irian Jaya earthquake, and the station is located at the ocean floor at an epicentral distance of 60°. The Gaussian source has a half-duration of 25 s. The oceans have a small effect on P and S multiples and a large effect on the Rayleigh wave, which is slowed down significantly. The dispersion of the Rayleigh wave also changes dramatically. The Love wave is not affected by the presence of the oceans.

The most intuitive way to incorporate the effect of the oceans in the SEM is by defining a mesh of fluid elements, just as we do for the outer core. In principle, we can couple the ocean and crustal regions in the SEM based upon a domain-decomposition algorithm, as we do for the outer core at the ICB and the CMB (see the previous chapter for details). Unfortunately, closer examination reveals that the problem is much more challenging than it appears. First, the compressional-wave velocity in the oceans ($\simeq 1.45$ km.s^{-1}) is much smaller than the smallest shear-wave velocity in the

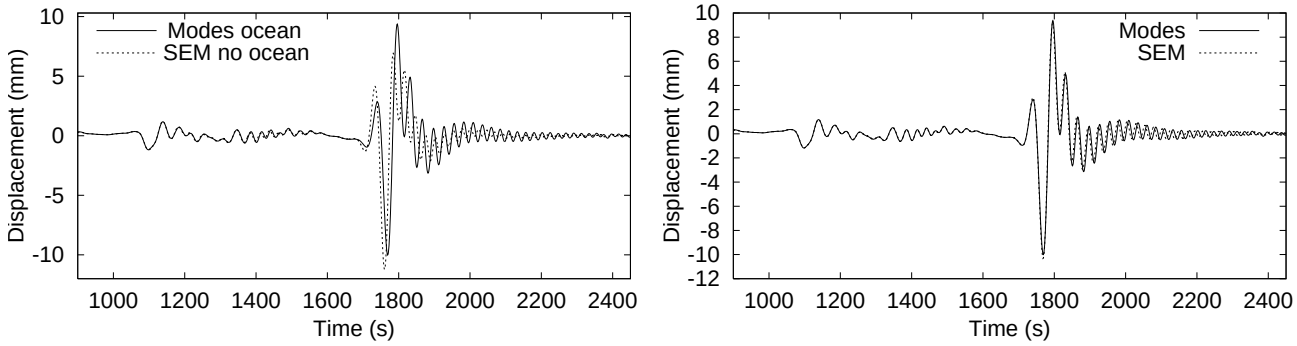

Figure 3.5 *(Left) Vertical component of displacement for a PREM normal-mode calculation with a 3 km-thick ocean layer (solid line), and for the SEM without the ocean layer (dotted line). The results are for the shallow Irian Jaya earthquake recorded at an epicentral distance of 60°. The Gaussian source has a half-duration of 25 s. The oceans have a small effect on P and S multiples and a large effect on the Rayleigh wave, which is slowed down considerably. The dispersion of the Rayleigh wave also changes dramatically. The Love wave is not affected by the presence of the oceans, and is therefore not shown here. (Right) Same vertical component of displacement for the PREM normal-mode calculation with a 3 km-thick ocean layer (solid line) compared to the SEM results with the same ocean layer (dotted line). Compared to the left figure, we fit the small effect of the oceans on P and S multiples perfectly, and most of the large effect on the Rayleigh wave, which is slowed down significantly and has a different dispersion. The small discrepancy in the coda of the Rayleigh wave is mainly attributed to the approximate ocean load formulation of equation (3.29).*

PREM crust ($\simeq 3.2$ km.s^{-1}). Therefore, in order to maintain a similar number of grid points per wavelength throughout the mesh, we would need to have far more points in the lateral direction in the oceans than in the crust (typically twice as many since $3.2/1.45 \simeq 2$). Because the crust is already the region of the mesh that has the highest density of elements (see the previous chapter), adding ocean elements would be very expensive in terms of memory and CPU requirements. Additionally, as at the ICB and the CMB, we would need to iterate the time scheme to couple the oceans and the crust in the domain decomposition (see the previous chapter), thereby increasing the CPU requirements even more. Because the oceans are very thin compared to the rest of the model (an average ocean thickness of 3 km compared to an average crustal thickness of 21 km and an Earth radius of 6371 km), the aspect ratio (i.e., the ratio of the lateral to the radial dimensions of the elements) of these ocean elements would be very large. This often induces stability problems in the time scheme in finite-element methods (e.g., Hughes 1987). Another drawback of meshing the oceans explicitly is that we would need to impose a minimum radial size (i.e., thickness) for the elements, typically 3 km, in order to avoid stability problems (the time step Δt tends to zero when the element size tends to zero), and therefore we could not handle shallow oceans.

In Section 3.3 we mentioned that by assuming an incompressible ocean, which is a reasonable approximation considering the fact that the thickness of the oceans is always much smaller than the wavelengths under consideration, we can avoid explicitly meshing the oceans (this would cease to be true at very short periods). Instead, the effect of the oceans is represented by a mere surface integral. In order to assess the validity of this approximation, in Figure 3.5 we perform a comparison between the PREM normal-mode solution with an ocean and a SEM simulation with a 3 km ocean introduced as an equivalent load. We fit the small effect on P and S multiples perfectly, and we correctly reproduce most of the effect on the Rayleigh wave, which is slowed down significantly by the oceans. The Love wave, which is not affected by the presence of the oceans, is not shown. There is a small phase shift in the coda of the Rayleigh wave in the SEM results. We attribute this effect to the fact that the ocean load formulation of equation (3.29) is approximate. Let us mention that a slight mesh subsampling which induces numerical dispersion in the SEM results might play a role as well. Note also that some of the discrepancies observed might come from the normal-mode solution itself, which is not perfect since it does not include the tsunami branch.

3.4.3 3-D simulations for a real event

As a final application of the SEM, we combine all the complications of a full 3-D Earth model. The simulations presented in this section include anisotropy, attenuation, self-gravitation, the oceans, rotation, ellipticity, topography and bathymetry, a 3-D mantle model and a 3-D crustal model. We model an event with a moment magnitude $M_w = 7.4$ that occurred on November 26, 1999 in Vanuatu at a depth of 15 km. The source has a half-duration of 18 s. This event gives us the opportunity to study the effects of the thin oceanic crust ($\sim$ 7 km) and the water layer on surface waves traveling across the Pacific. Reference Earth model PREM includes a 3 km thick water layer and has a peculiar crust with a thickness of 21.4 km, therefore we expect a 3-D SEM simulation to fit the data much better. Figure 3.6 shows displacement convolved with the instrument response (which effectively gives ground velocity) and lowpass filtered at a corner frequency of 40 s

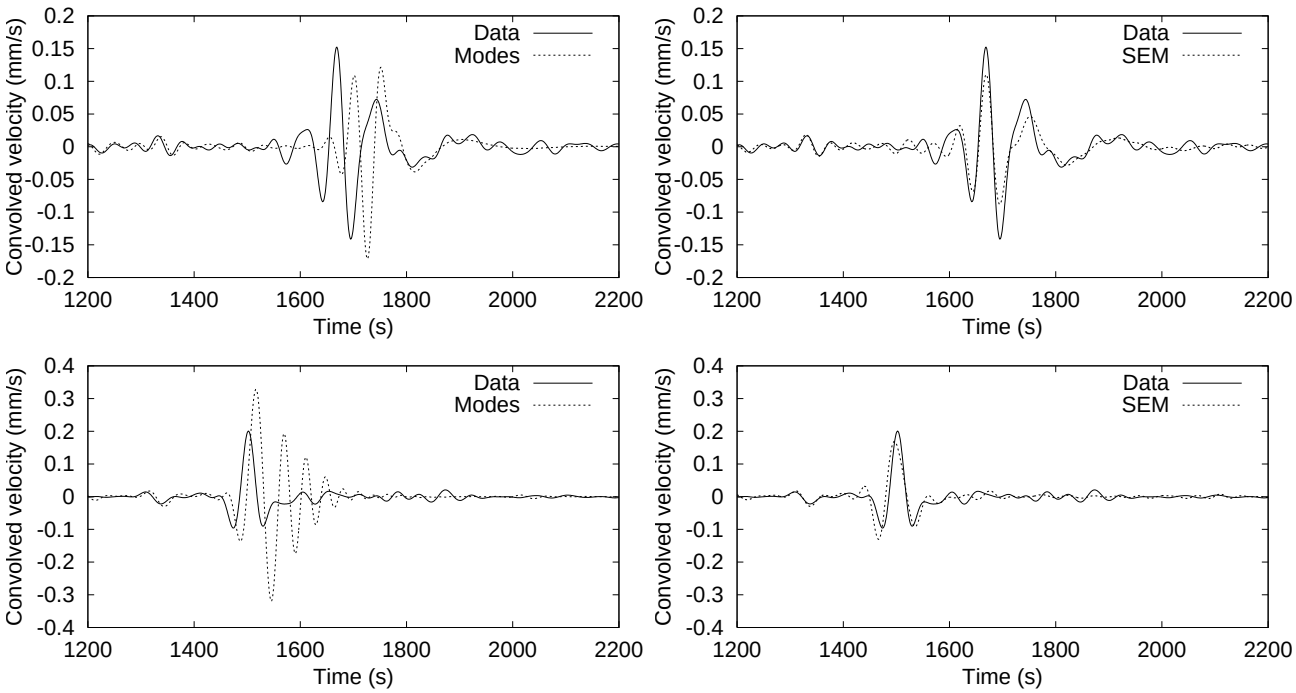

Figure 3.6 *Vertical (top) and transverse (bottom) components of displacement convolved with the instrument response and lowpass filtered at a corner frequency of 40 s at station MAJO in Japan, for the PREM normal-mode solution (left, dotted line) and a fully 3-D SEM simulation (right, dotted line) compared to real data (solid line). The event is located in Vanuatu and the path is therefore mostly oceanic. The epicentral distance is 60°. Note how the PREM normal-mode synthetic seismograms predict a Love wave whose duration is much too long, and a Rayleigh wave which arrives much too late. The SEM synthetic seismograms incorporate the thin oceanic crust and predict the arrival time of the Rayleigh wave, as well as the short duration of the Love wave.*

at station MAJO in Japan, at an epicentral distance of 60°. We use a six-pole two-pass Butterworth filter. Note how the normal-mode synthetic seismograms for PREM predict a Love wave whose duration is much too long, and a Rayleigh wave which arrives much too late. The SEM synthetic seismograms incorporate the thin oceanic crust and predict the arrival time of the Rayleigh wave much better, as well as the short duration of the Love wave (although it arrives a bit too early). An even more spectacular example of a fast Rayleigh wave is shown in Figure 3.7 for the vertical component of the Pasadena, California, TriNet station PAS, at an epicentral distance of 86°, where the Rayleigh wave arrives 85 s earlier than in PREM. Note that the 3-D SEM synthetic matches this early arrival very nicely and tracks the phase of the Rayleigh wave quite well.

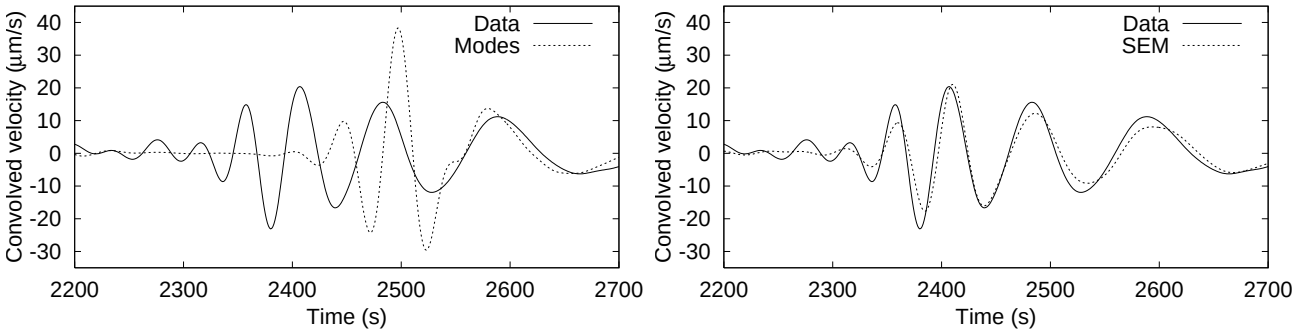

Figure 3.7 *Vertical component of displacement convolved with the instrument response and lowpass filtered at a corner frequency of 40 s at TriNet station PAS in Pasadena, California, for the PREM normal-mode solution (left, dotted line), and a fully 3-D SEM simulation (right, dotted line), compared to real data (solid line). The event is located in Vanuatu and the path is therefore mostly oceanic. The epicentral distance is 86°. The Rayleigh wave arrives 85 s earlier than in PREM. Note that the 3-D SEM synthetic matches this early arrival very nicely and tracks the phase of the Rayleigh wave quite well.*

Troisième partie

Modélisation à l'échelle régionale dans les bassins sédimentaires

Chapitre 4

Simulations des mouvements forts du sol dans le bassin de Los Angeles

Résumé

Dans ce chapitre, nous montrons comment nous pouvons simuler les mouvements forts du sol à l'échelle locale ou régionale en utilisant la méthode des éléments spectraux introduite dans les chapitres précédents. Le problème est sensiblement différent des simulations à l'échelle globale introduites précédemment : l'équation des ondes est plus simple, parce qu'à cette échelle il n'y a pas d'effet lié à la gravité ni à la rotation, et il n'y a aucune région liquide telle que le noyau externe couplée avec le modèle solide. Cependant, le modèle lui-même est beaucoup plus hétérogène qu'à l'échelle globale, en raison de la complexité de la géologie du bassin, et notamment de la forme fortement variable de la surface de contact entre les sédiments et le substratum formé de roches cristallines rapides. Par conséquent, la création du maillage est un facteur crucial et plus difficile qu'à l'échelle globale. Nous montrons comment résoudre le problème, et simulons ensuite les mouvements forts du sol produits par deux petits tremblements de terre récents et bien enregistrés dans le bassin de Los Angeles. Les simulations sont exécutées en utilisant un nouveau modèle du bassin sédimentaire qui est contraint par des centaines de logs de vitesse de compression dans des puits, provenant de l'industrie pétrolière, et par plus de 20000 kilomètres de profils de sismique réflexion. Les simulations numériques prennent en compte les variations tridimensionnelles des modèles de vitesse et de densité, la topographie, la bathymétrie et atténuation. Les simulations pour le tremblement de terre de Hollywood du 9 septembre 2001 ($M_w = 4.2$) et celui de Yorba Linda du 3 septembre 2002 ($M_w = 4.2$) démontrent que l'utilisation conjointe d'un modèle détaillé du bassin sédimentaire et d'une technique numérique précise permet la simulation des mouvements forts du sol jusqu'à des périodes de 2 secondes pour les trois composantes du déplacement. Une carte de l'accélération maximale du sol illustre également que des effets 3-D importants d'amplification se produisent dans le bassin.

Abstract

In this chapter, we illustrate how to simulate strong ground motion at the local or regional scale based upon the spectral-element method introduced at the global scale in the previous chapters. The problem is significantly different from global scale simulations introduced previously: the wave equation itself is simpler, because at this scale there is no effect related to self-gravitation or rotation, and there is no fluid region, such as the outer core, coupled with the solid region; however, the model is much more heterogeneous than at the global scale, because of the complex and rapidly-varying shape of the contact between the sediments and the crystalline basement. As a consequence, mesh design is a crucial and more difficult issue than at the global scale. We illustrate how to solve the problem, and subsequently simulate strong ground motion generated by two recent and well-recorded small earthquakes in the Los Angeles basin. Simulations are performed using a new sedimentary basin model that is constrained by hundreds of petroleum industry well logs and more than 20,000 kilometers of seismic reflection profiles. The calculations account for three-dimensional variations of seismic wave speeds and density, topography and bathymetry, and attenuation. Simulations for the 9 September, 2001 $M_w = 4.2$ Hollywood earthquake and the 3 September, 2002 $M_w = 4.2$ Yorba Linda earthquake demonstrate that the combination of a detailed sedimentary basin model and an accurate numerical technique facilitates the simulation of strong ground motion at periods of 2 seconds and longer. A peak ground acceleration map illustrates that significant amplification occurs in the basin.

4.1 Introduction

Accurate prediction of hazardous ground shaking generated by large earthquakes requires the ability to numerically simulate seismic wave propagation in realistic geological models. In this chapter we demonstrate that strong ground motion can be accurately modeled down to a period of 2 seconds using a detailed model of the Los Angeles, California, basin (Figure 4.1) and a very accurate numerical technique.

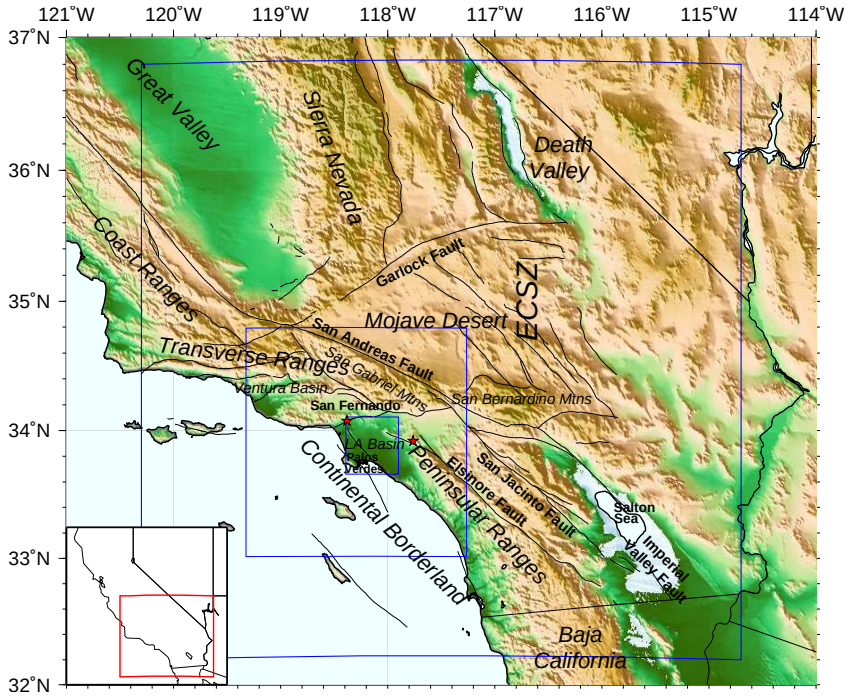

Figure 4.1 *Topographic map of southern California showing the Los Angeles region. The small California map in the lower-left corner shows the location of the area represented (red rectangle). The main late Quaternary faults (Jennings 1975) are also displayed. ECSZ denotes the Eastern California Shear Zone. TriNet stations are indicated by white triangles. The large blue rectangle shows the edges of the computer grid that we use to perform our three-dimensional strong ground motion calculations. The two smaller blue rectangles are the edges of the medium-resolution and high-resolution Los Angeles basin models, respectively. The epicenters of the Hollywood and Yorba Linda earthquakes studied in this chapter are denoted by red stars.*

The Los Angeles basin developed in the Neogene as a result of regional crustal extension associated with the opening of the California Borderlands and rotation of the Transverse Ranges (Luyendyk & Hornafius 1987; Wright 1991). Since the early Pliocene, the basin has been deformed by numerous strike-slip, reverse, and blind-thrust faults that accommodate oblique convergence between the Pacific and North American plates (e.g., Davis et al. 1989; Hauksson 1990; Wright 1991; Shaw & Suppe 1996; Schneider et al. 1996; Shaw & Shearer 1999; Fuis et al. 2003). This tectonic history, combined with varied depositional and diagenetic processes involving the basin sediments, have yielded complex three-dimensional (3-D) wave-speed and density structures in the Los Angeles basin (e.g., Süss & Shaw 2003).

Regional studies initially focused on developing average one-dimensional (1-D) models (e.g., Hadley & Kanamori 1977; Dreger & Helmberger 1990). Three-component broadband records of small earthquakes were used in Dreger & Helmberger (1990) to study the sensitivity of synthetic seismograms to perturbations of the crustal model, and to construct an average 1-D layered model of crustal structure. More recently, taking advantage of the large number of broadband seismic stations and the related wealth of high-quality data, regional tomographic V_p and V_p/V_s models have been constructed (e.g., Hauksson & Haase 1997; Hauksson 2000) based upon P and S-P travel times from local earthquakes and controlled artificial sources. The 3-D shape of the Southern California Moho has also been imaged (e.g., Ichinose et al. 1996; Lewis et al. 2000; Zhu & Kanamori 2000). Based upon the teleseismic receiver function technique, Zhu & Kanamori (2000) show that very significant variations of Moho depth exist in the region, from 21 km to 37 km, with a regional average of 29 km. A deep Moho is found under the eastern Transverse Range, the Peninsular Range and the Sierra Nevada Range. To the contrary, the central Transverse Range does not have a deep continental root. The crust is much thinner (typically 21 km to 22 km) in the Inner California Borderland and the Salton Trough. In the past few years, the Southern California Earthquake Center (SCEC) has focused on creating 3-D wave-speed models of the region (e.g., Magistrale et al. 1996; Graves 1999; Magistrale et al. 2000). The SCEC model is a rule-based wave-speed description, calibrated with seven sonic logs, that relates V_p to the age and depth of strata. In contrast, the model we use for our simulations is interpolated from more than 150 sonic logs and 7,000 stacking velocities derived from petroleum industry reflection profiles (Süss & Shaw 2003). The two models have similar average velocity functions, but our model describes more detailed lateral and vertical wave-speed structure that is observed in borehole and stacking velocity data.

Accurate numerical techniques are needed in order to understand strong ground motion in complex 3-D structures, and to study past large earthquakes or hypothetical earthquake scenarios and their impact in terms of seismic hazard, building

codes, disaster prevention and emergency planning. Numerical simulations of strong ground motion in complex heterogeneous structures have previously been performed based upon techniques that can handle highly heterogeneous 3-D models, such as the finite-difference (e.g., Boore 1972; Frankel & Vidale 1992; Frankel & Leith 1992; McLaughlin & Day 1994; Olsen et al. 1995; Pitarka & Irikura 1996a; Antolik et al. 1996; Larsen et al. 1997; Kristek et al. 1999; Stidham et al. 1999; Ji et al. 2000; Satoh et al. 2001) and finite-element methods (e.g., Lysmer & Drake 1972; Bao et al. 1998; Bielak et al. 1999; Garatani et al. 2000; Aagaard et al. 2001).

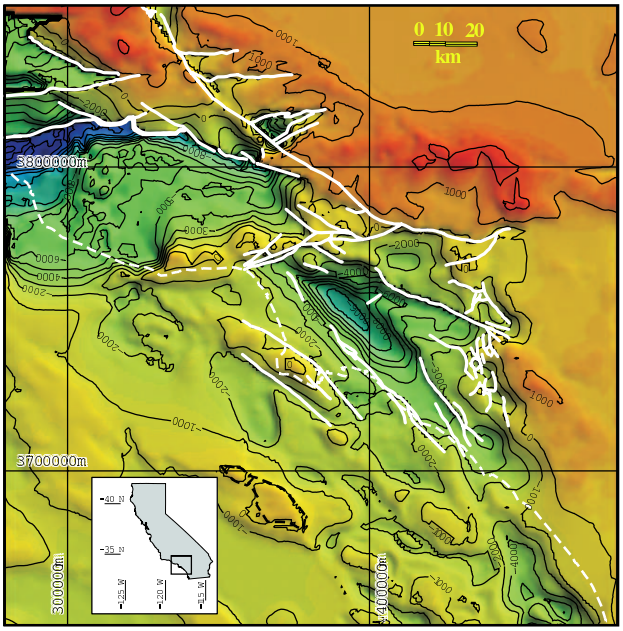

Figure 4.2 *Top view of the surface defining the top of the crystalline basement in the Los Angeles basin model. The coastline is indicated by the white dashed line, and major faults by white solid lines. Red regions denote shallow sediments or no sediments at all, and green and blue the deepest sediments. One can clearly see the deep sedimentary pocket underneath Los Angeles, as well as the very sharp Ventura escarpment.*

Several studies have focused more specifically on Southern California and the Los Angeles basin (e.g., Frankel 1993; Olsen & Archuleta 1996; Pitarka & Irikura 1996b; Olsen et al. 1997; Wald & Graves 1998; Graves 1999; Olsen 2000; Peyrat et al. 2001; Eisner & Clayton 2002). The complexity of the seismic response of the Los Angeles basin has been analyzed by many authors in recent years, e.g., Hartzell et al. (1996), Wald & Graves (1998), Hartzell et al. (1998) and Olsen (2000). Detailed reviews are available in particular in Wald & Graves (1998) and Olsen (2000). There is evidence that very significant amplification (factors of 3, 4 or more) can occur between basin sites and hard rock sites. It has also been shown that site effects caused by topography or local geological features, such as poorly consolidated sediments, can result in very significant amplification of the wave field (e.g., Gaffet & Bouchon 1989; Frankel & Leith 1992; Stevens et al. 1993). Such phenomena have been observed in the Los Angeles region, e.g., very large accelerations (up to 1.8 g) at Tarzana Hill during the 1994 Northridge earthquake (e.g., Bouchon & Barker 1996; Spudich et al. 1996; Rial 1996; Catchings & Lee 1996; Komatitsch & Vilotte 1998). Localization effects can also cause very significant damage, as illustrated in Santa Monica during the 1994 Northridge earthquake (e.g., Gao et al. 1996; Alex & Olsen 1998; Davis et al. 2000). Such effects are intrinsically 3-D, and therefore further illustrate the need for detailed basin models and accurate and flexible numerical techniques.

In this chapter, we present simulations based on a detailed model of the Los Angeles basin (Süss & Shaw 2003) and the powerful spectral-element method (SEM) introduced for the global Earth in the previous chapters. Using two recent well-recorded small ($M_w = 4.2$) earthquakes in the basin, we show that strong ground motion can be accurately modeled down to a period of 2 seconds. The spectral-element method has several distinct advantages over more classical numerical techniques mentioned above.

4.2 Basin model

Creating a high-resolution wave-speed model of the Los Angeles basin (Figure 4.1) has been the focus of significant attention in recent years. Collaborative efforts in the context of the Southern California Earthquake Center (SCEC) have led to the development of models that are now widely used in the geophysical community (e.g., Magistrale et al. 1996; Hauksson & Haase 1997; Graves 1999; Magistrale et al. 2000). In this chapter, we use an extension of the more recent model of Süss & Shaw (2003), which describes a complex, heterogeneous three-dimensional (3-D) wave-speed structure (Figures 4.2 and 4.3) based on more than 85,000 direct measurements from petroleum industry boreholes and seismic reflection profiles. The model contains a description of the sedimentary basin shape as defined by the contact between

lower wave-speed sediments and higher wave-speed crystalline basement. Wave speeds within the sedimentary sequence were interpolated from sonic log and stacking velocity measurements using geostatistical kriging techniques (Süss & Shaw 2003). The resultant wave-speed structure is highly complex, reflecting sedimentary, diagenetic, and structural controls, and is substantially different from previous descriptions mentioned above. While the original model (Süss & Shaw 2003) covered only parts of the San Fernando Valley, the improved model used in this chapter includes the San Fernando, Ventura, Soledad and Ridge basins, and extends northwards beyond the Ventura Basin. We constructed a surface defining the top of the crystalline basement for this area, and wave-speeds east of the San Andreas Fault were taken from the tomographic model of Hauksson (2000). The top of the crystalline basement in the Ventura Basin was constructed based upon reference surfaces taken from the SCEC-2 model (Magistrale et al. 2000) as well as cross-sections from Yeats et al. (1994) and Huftile & Yeats (1995). The geometry of the Ridge basin and Soledad basin were approximated based upon cross-sections in Namson & Davis (1992).

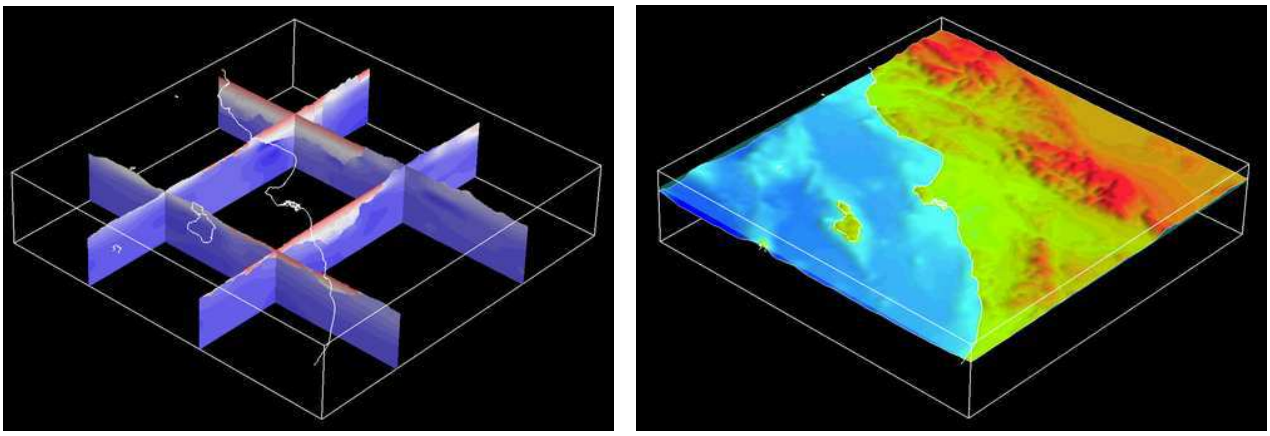

Figure 4.3 *View from the South-East upon the Los Angeles basin model. (Left) North-South and East-West cross-sections showing P-wave speed in the basin model, with blue denoting fast bedrock, and white and red slower deep and shallow sediments, respectively. The coastline is shown by the white line. The maximum depth of the basin is 8.5 km underneath downtown Los Angeles. The basin model is embedded into the regional tomographic model of Hauksson (2000) (not shown here). (Right) Surface topography and bathymetry. One can clearly see the San Gabriel Mountains toward the North, Palos Verdes along the coast, as well as the Ventura, San Fernando, and Los Angeles basins.*

The model and supporting data constrain compressional-wave (P-wave) speed (V_p). Shear-wave (S-wave) speed (V_s) and density (ρ) models, which are also needed for the simulations, were derived from the V_p model using simple empirical relations. More specifically, S-wave speed V_s is defined by dividing V_p by a coefficient that varies linearly from 1.732 in the deepest part of the basin (i.e., a Poisson's ratio of 0.25) to 2 in the shallow sediments near the surface (i.e., a Poisson's ratio of 0.33). Based upon well-log information, density is defined by $\rho = V_p/3 + 1280$ (McCulloh 1960; Stidham et al. 2001), imposing a minimum of 2000 kg.m^{-3}.

The basin model is embedded in the regional tomographic model of Hauksson (2000), which gives P- and S-wave speeds in Southern California. Density has to be defined independently based upon mineral physics estimates; we scale lateral variations in S-wave speed by a factor of 0.4 to obtain lateral variations in density. In addition, we use the one-dimensional (1-D) background regional model of Dreger & Helmberger (1990). Little is known about attenuation in the Los Angeles basin, but low values of the shear quality factor Q_μ have been observed (Hauksson et al. 1987). Based upon this article and trial-and-error numerical tests, we decided to use a constant value of $Q_\mu = 90$ in the sediments, and no attenuation in the bedrock. Lateral variations in crustal thickness are incorporated based upon the regional Moho model of Zhu & Kanamori (2000). Topography and bathymetry are obtained from a USGS digital elevation map (USGS 2003), as illustrated in Figure 4.3.

4.3 Numerical technique

We use the SEM, introduced in the previous chapters for modeling seismic wave propagation in the full Earth, to simulate strong ground motion in the basin based upon the linear anelastic wave equation. As mentioned previously, the main advantage of the SEM is that it combines the flexibility of the finite-element method (e.g., Lysmer & Drake 1972; Moczo et al. 1997; Bao et al. 1998; Bielak et al. 1999; Garatani et al. 2000) with the accuracy of pseudospectral techniques (e.g., Tessmer et al. 1992; Carcione & Wang 1993; Igel 1999). It is more accurate than widely-used classical techniques such

as the finite-difference method (e.g., Boore 1972; Virieux 1986; Graves 1996; Olsen et al. 1997), in particular for surface waves (e.g., Komatitsch & Tromp 1999, 2002a), which play an important role in strong ground motion seismology.

In the SEM, it is relatively straightforward to densify the mesh near the surface of the model in the low wave-speed sediments, using mesh doubling as a function of depth, as illustrated in Figure 4.4, assuming that the surfaces do not exhibit large local variations (i.e., that they are smooth enough). Using a coarser mesh in depth significantly reduces the memory requirements and facilitates an increase in the value of the time step, thus enabling larger simulations for a similar computational cost. Due to the geometrical flexibility that the SEM shares with the finite-element method, the mesh can be adapted to topography and bathymetry as well as the shape of the basement surface and the Moho (Figure 4.4). Even in the presence of substantial topography, the traction-free boundary condition at the Earth's free surface is satisfied automatically in a SEM (e.g., Komatitsch & Vilotte 1998; Komatitsch & Tromp 1999, 2002a).

In this chapter, we incorporate 3-D variations in P- and S-wave speeds, density, and attenuation. The mesh covers 516 km $\times$ 507 km, from 120.3°W to 114.7°W and from 32.2°N to 36.8°N, incorporates most of the roughly 140 broadband seismographic stations in the TriNet network (`www.trinet.org`) in Southern California, and extends to a depth of 60 km. It is important to honor the major discontinuities in the wave-speed model when creating a mesh of the structure, to avoid numerical diffraction by a staircase discretization of the complex-shaped interfaces (e.g., Zahradník et al. 1993). Therefore, the basin mesh honors the shape of the Moho (Zhu & Kanamori 2000), the lower part of the sedimentary basin underneath Los Angeles (Süss & Shaw 2003), as well as topography and bathymetry (USGS 2003), as illustrated in Figure 4.4.

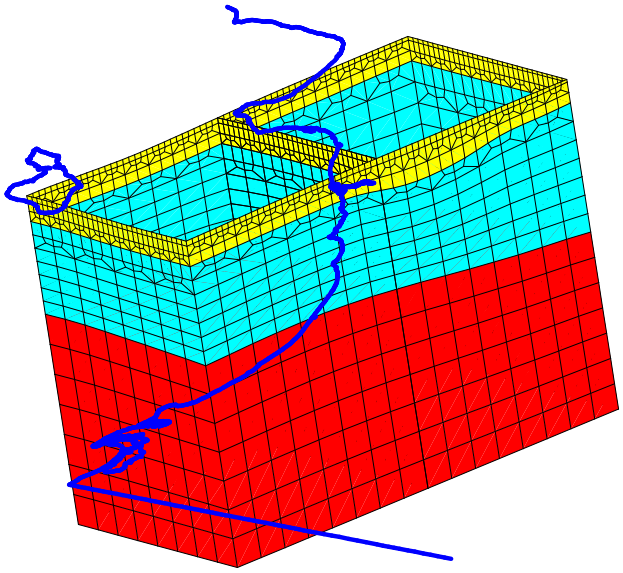

Figure 4.4 *North-South cross-section through the mesh of the Los Angeles basin region. For clarity only the vertical edges of the mesh slices are represented. The blue line shows the Mexican border, the coastline, Palos Verdes and Santa Catalina Island. The mesh is adapted to the deepest part of the basement surface and to the shape of the Moho taken from Zhu & Kanamori (2000). It is doubled in size twice: first below the low wave-speed surface layer and a second time below the basement. Red represents elements located below the Moho, cyan elements between the Moho and the bottom of the sedimentary pocket, and yellow elements in the upper part of the model honoring the shape of the surface and the bottom of the sedimentary pocket.*

There are several seismographic stations on the offshore Channel Islands; for this reason the effect of the oceanic water layer is incorporated in the modeling based upon an equivalent load formulation that takes into account the weight of the water column (see Section 3.3.5 of Chapter 3 for details). Paraxial absorbing conditions (Clayton & Engquist 1977) are used on the vertical edges and the bottom of the grid to simulate a semi-infinite regional medium. More accurate absorbing boundary conditions, such as the Perfectly Matched Layer (PML) (e.g., Bérenger 1994; Chew & Liu 1996; Collino & Tsogka 2001; Komatitsch & Tromp 2003), could be used instead, but, because we use a large mesh, the simpler paraxial conditions are sufficient. The PML absorbing condition for seismic wave propagation will be presented in Chapter 6.

As in previous chapters, the method is implemented on our Beowulf PC cluster computer, using parallel programming based upon a message-passing technique (the Message-Passing Interface - MPI). To take advantage of the parallel machine architecture, the mesh is divided into 144 slices that are distributed over 144 processors using a regular mesh partitioning topology. The mesh contains 672,768 spectral elements. We use a polynomial degree $N = 4$ to sample the wave field, therefore each spectral element contains $(N + 1)^3 = 125$ Gauss-Lobatto-Legendre points. Counting points on common spectral element edges and corners only once, the mesh therefore contains a total of 45.4 million grid points (i.e., 136 million degrees of freedom, because we solve for the three components of displacement at each grid point). The average distance between grid points at the surface is roughly 335 m. One needs to use roughly 5 points per wavelength to correctly sample the wave field in the SEM (e.g., Seriani & Priolo 1994), therefore the mesh resolves waves with a shortest period of about 2 seconds. The calculations require 14 gigabytes of distributed memory. On our cluster it takes about 6.5 hours to compute seismograms with a duration of 3 minutes. We use a time step of 9 ms, i.e., a total of 20,000 time steps.

4.4 Simulations of the 9 September 2001 $M_w = 4.2$ Hollywood earthquake

To assess the quality of the 3-D basin model and the 3-D SEM simulations, we simulated strong ground motion for the 9 September 2001 $M_w = 4.2$ Hollywood earthquake. This event is located right inside the basin and was well recorded by TriNet, and therefore provides an excellent test of the 3-D basin model and the numerical method. Complications associated with source complexity and directivity for larger events (e.g., Wald et al. 1996; Ji et al. 2002) are avoided. To obtain the source mechanism for this event we performed a 3-D centroid-moment tensor inversion based upon the basin model and the SEM. We calculated the required 3-D Fréchet derivatives numerically (Liu et al. 2004). The solution is in excellent agreement with first-motion and surface-wave estimates.

Figure 4.5 shows snapshots of the simulation. The vertical component of velocity at the surface is represented. If the basin model were 1-D one would see concentric circles centered on the epicenter. The highly distorted wave fronts are due to substantial 3-D variations in the model. Note that energy gets trapped in the Los Angeles and San Fernando basins due to the low wave-speed sediments.

In Figure 4.6 we compare the results of 3-D SEM simulations to three-component displacement data recorded by TriNet stations. Both data and synthetic seismograms are bandpass-filtered between 6 and 35 seconds with a 4-pole 2-pass Butterworth filter. We focus our attention on the Los Angeles region, where the detailed Harvard basin model is defined and in which the event took place. Notice that at these periods we can fit the data very well on all three components. The model captures the strong amplifications and resonance associated with the Los Angeles basin, e.g., transverse components at LAF, STS, LGB and PDR, and radial components are PDR, WTT and LLS. Note that station DJJ, which is very close to the epicenter, is nicely fit on all three components. Notice also that stations in the San Gabriel mountains, e.g., CHF, BFS, TA2 and MWC have relatively small displacements on all three components that are well fit by the synthetic seismograms. The good fit to the data demonstrates that the SEM wavefront distortions in Figure 4.5 capture actual facets of the data.

Figure 4.7 illustrates that even at periods between 2 and 35 seconds we can fit the data reasonably well on all three components. Because the model is a P-wave speed model and the largest signals in the seismograms are surface waves predominantly sensitive to S-wave speed, we allow for a small station correction in our SEM simulations. This stems from the fact that the S-wave speed (V_s) model is based upon a simple scaling relation to P-wave speed (V_p). For simplicity, rather than trying to determine an optimal scaling relation, or an independent S-wave speed model, we choose to use such a simple scaling, but allow for deficiencies in the V_s model by introducing a station correction. To find the station correction, we calculate the cross-correlation between the data and the synthetic seismograms and use this to determine the phase shift between the data and synthetic seismograms as well as the associated amplitude anomaly. In Figure 4.8 we plot the value of the cross-correlation, the time shift, and the associated amplitude anomaly. Note that the corrections are generally small, typically less than plus or minus two seconds for stations within 200 km of the epicenter.

Figure 4.9 shows peak ground acceleration in the basin region. Notice the strong amplification in the San Fernando Valley toward the north, in particular near its eastern edge. A hard rock site, such as Palos Verdes along the coast, shows no significant amplification. The same is true in the mountains, most of the energy being trapped in the two basins. Maps such as these can be used to construct synthetic ShakeMaps that would complement the empirically derived ShakeMaps depicting the intensity of ground motion produced automatically by the United States Geological Survey (`www.trinet.org/shake`).

4.5 Simulations of the 3 September 2002 $M_w = 4.2$ Yorba Linda earthquake

Next, we simulate strong ground motion for a second event, the 3 September 2003 $M_w = 4.2$ Yorba Linda earthquake. Again we performed a 3-D CMT inversion for this event, which is in excellent agreement with first-motion and long-period surface-wave mechanisms. Figure 4.10 illustrates that for this event we can also fit the data very well at periods between 6 and 35 seconds. We show the transverse component of displacement for stations in the Los Angeles area. To illustrate the magnitude of the basin resonance, in Figure 4.10 we also show the same transverse component displacement data compared to SEM synthetic seismograms for the 1-D Southern California average regional model of Dreger & Helmberger (1990). Note that at basin sites, such as LAF and BRE, the observed amplitudes can be 20 times larger that the 1-D predictions, even at long periods. Of course one could attempt to determine the best 1-D model for each event-station pair, but this figure illustrates that such models are meaningless because of very large local variations in response pattern. For example, stations BRE, STS and RPV trend along the same direction, and yet they have entirely different responses. Note from Figure 4.10 that the 3-D model captures all three stations very nicely. We note that the 1-D model of Dreger & Helmberger (1990) was developed to fit regional long-period waveforms, not basin sites.

4.6 Discussion

Our analyses of the Hollywood and Yorba Linda earthquakes demonstrate that it is feasible to fit three-component seismic data accurately down to a period of 2 seconds, thereby validating the basin model of Süss & Shaw (2003) and the SEM. Signals with a very wide dynamic range are well-captured by the model, and, in particular, stations within the Los Angeles and San Fernado basins are fit remarkably well on all three components. The full complexity of the 3-D model is included in the simulations, in particular the effect of attenuation, topography, and the oceans.

There are, however, some limitations to the model. Figure 4.11 illustrates that in the Salton Sea area, for instance at stations SAL, ERR and WES, and at shorter periods in the Mojave Desert, e.g., at station ADO, there is substantial low wave-speed sediment cover that is not included in our model. This causes resonance in the data that is not correctly reproduced. As can be seen in Figure 4.1, this region is not covered by our basin model, but rather by the regional model of Hauksson (2000). These limitations in the background model can be addressed by incorporating low wave-speed layers in selected areas, and by expanding our high-resolution model to encompass these problematic areas.

Another issue is the fact that the geotechnical layer, i.e., the first tens of meters of sediments which are highly heterogeneous and often significantly modify strong ground motion and local amplification (e.g., Anderson et al. 1996), is currently not included in our basin model. This layer will be incorporated in a future version of the model. However, it will be difficult to take into account in our numerical simulations, due to the very low S-wave speeds that are involved, which require a very fine grid. Using our current mesh, we are limited to minimum S-wave speeds of about 670 m.s^{-1}. (Our simulations are designed to be accurate down to a period of 2 seconds, the grid spacing at the surface is 335 m, and in the SEM one needs to sample the wave field using approximately 5 points per minimum wavelength, as mentioned previously.)

An additional difficulty in basin simulations is the lack of detailed knowledge of attenuation. We have used a constant shear quality factor $Q_\mu = 90$ in the sediments, no bulk Q, and no attenuation in the bedrock; this model is, of course, not realistic. However, it is difficult to improve, because very few available data sets constrain attenuation.

With present-day computer hardware, it is technically feasible to simulate strong ground motion for a given wave-speed model at much higher frequencies (at least 2 Hz or more). As is often the case in regional or local seismology (e.g., Graves 1999), we are presently limited by our knowledge of the 3-D model, not by the accuracy or the cost of the calculations. Our current basin model is largely based upon P-wave speed information. Strong motions in the basin are to a large extent determined by S-wave speeds, which we estimate based upon a simple scaling relationship. Therefore, the basin model could be improved by adding constraints on the S-wave speed and density structure, for instance based upon borehole data (Stidham et al. 2001), as well as more precise P-wave speed constraints in sub-regions of the model. In a related effort, we are planning to use surface-wave phase delays, such as those shown in Figure 4.8, as the starting point for an inversion for an improved S-wave model.

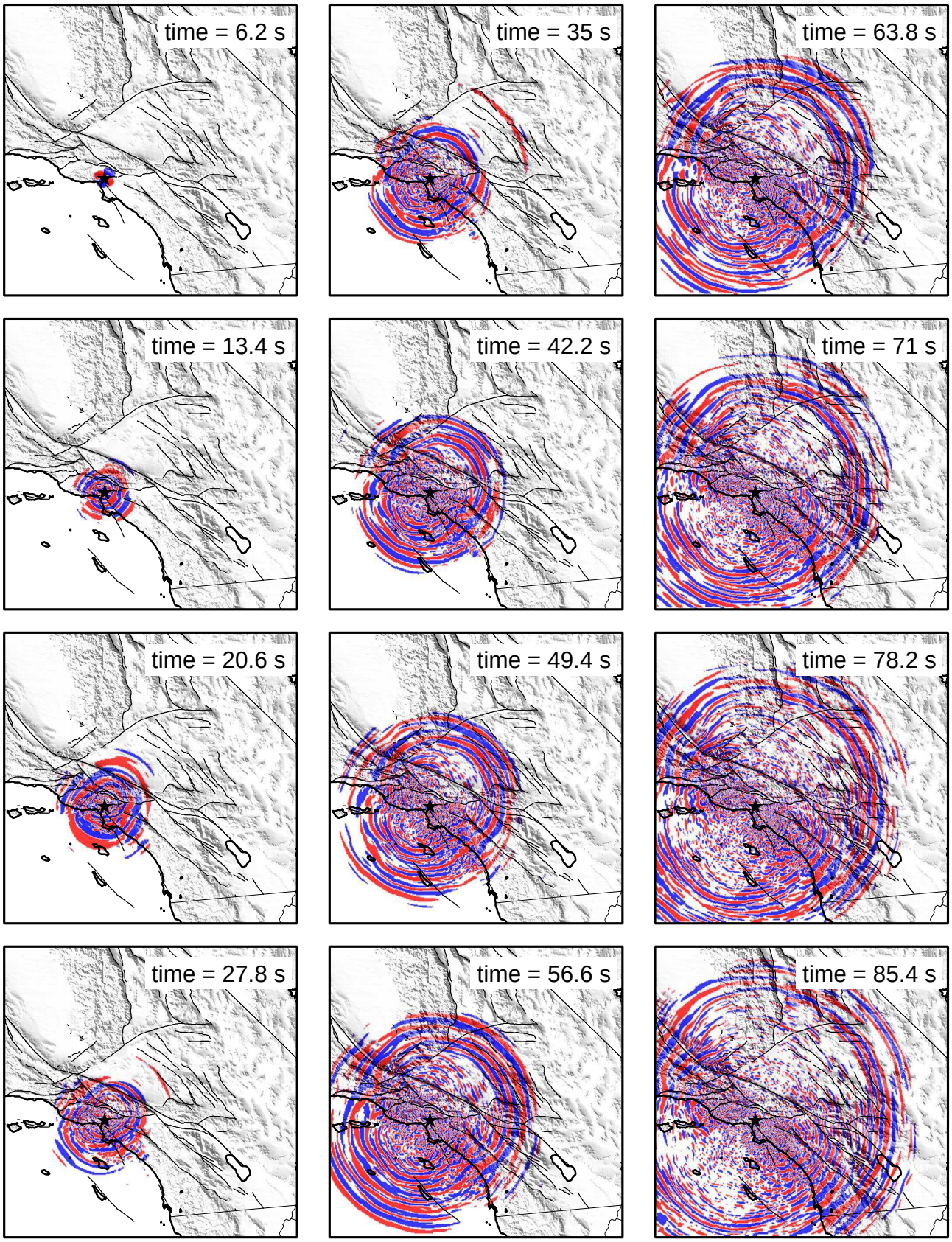

Figure 4.5 *Snapshots of the wave field simulated for the 9 September 2001 $M_w = 4.2$ Hollywood earthquake. The vertical component of velocity is displayed, with red colors denoting positive values and blue negative values. In a 1-D model the wave field would consist of concentric circles centered on the epicenter. The wavefront distortions are due to the presence of low wave-speed sediments in the Los Angeles and San Fernando sedimentary basins. Note in particular how ground motion lasts much longer in and around the basin, where energy is trapped because of the presence of sediments.*

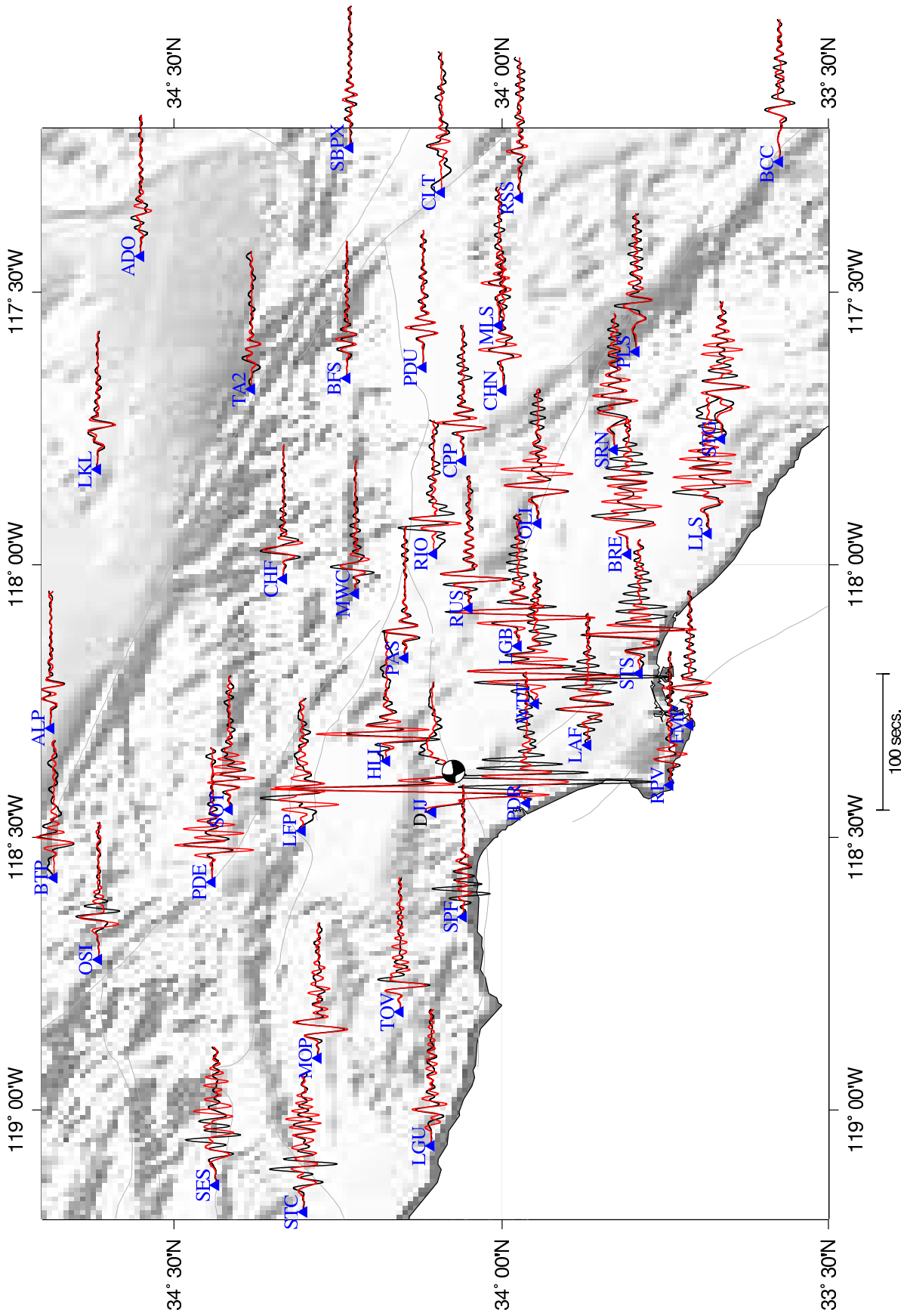

Figure 4.6 **Part A of Figure.** *Data (black) and 3-D SEM synthetic seismograms (red) for the 9 September, 2001, Hollywood event are plotted on a map of the Los Angeles area. We display the vertical (A), radial (B) and transverse (C) component of displacement. The mechanism and location of the event are indicated by the black-and-white beach ball. The time scale is indicated by the scale bar at the bottom. Stations are denoted by blue triangles. The instrument response was deconvolved from the data to obtain ground displacement. Both the data and the synthetic seismograms were subsequently bandpass filtered between 6 and 35 seconds with a 4-pole 2-pass Butterworth filter.*

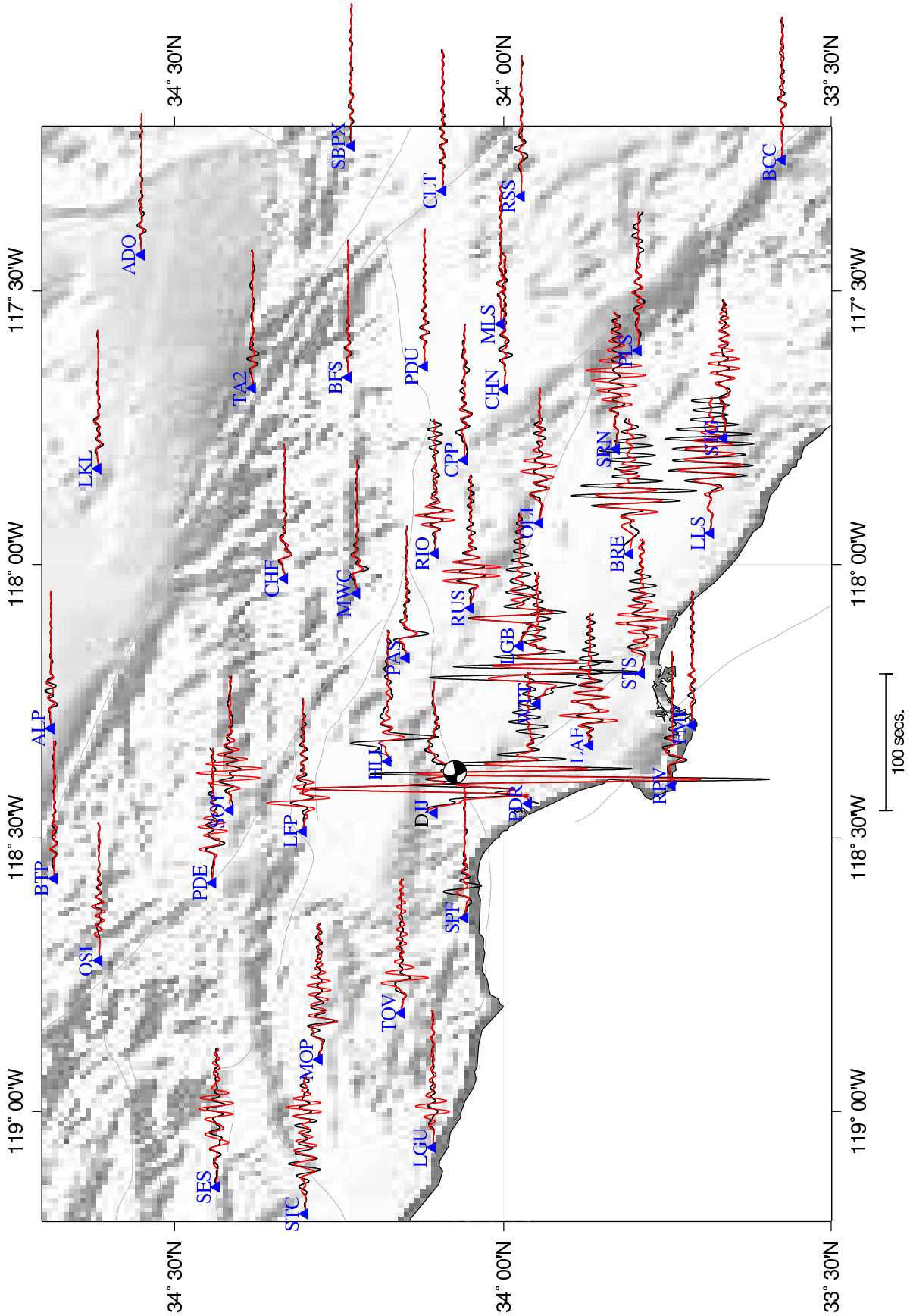

FIG. 4.6 **Part B of Figure.** Radial component of displacement.

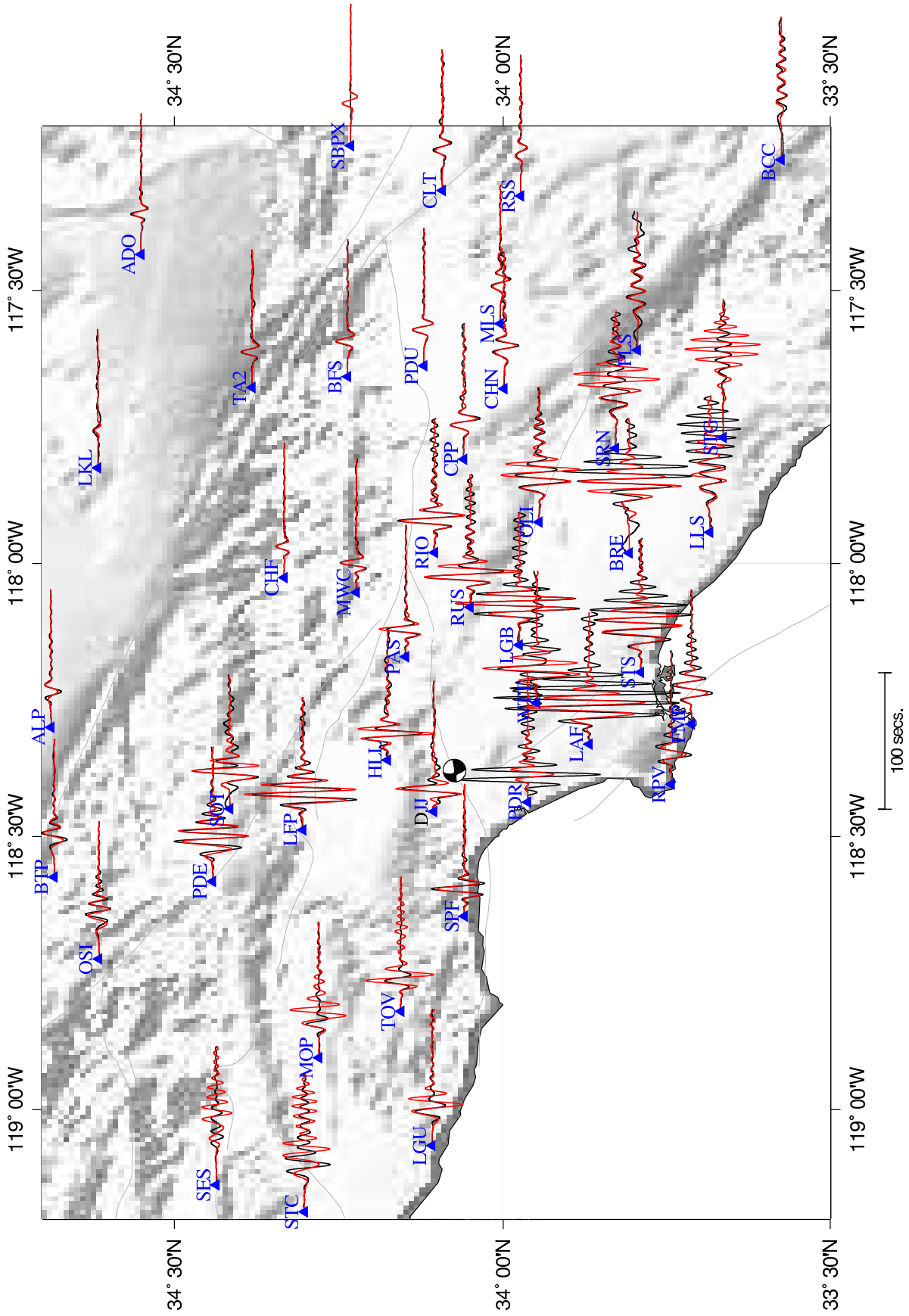

FIG. 4.6 **Part C of Figure.** Transverse component of displacement.

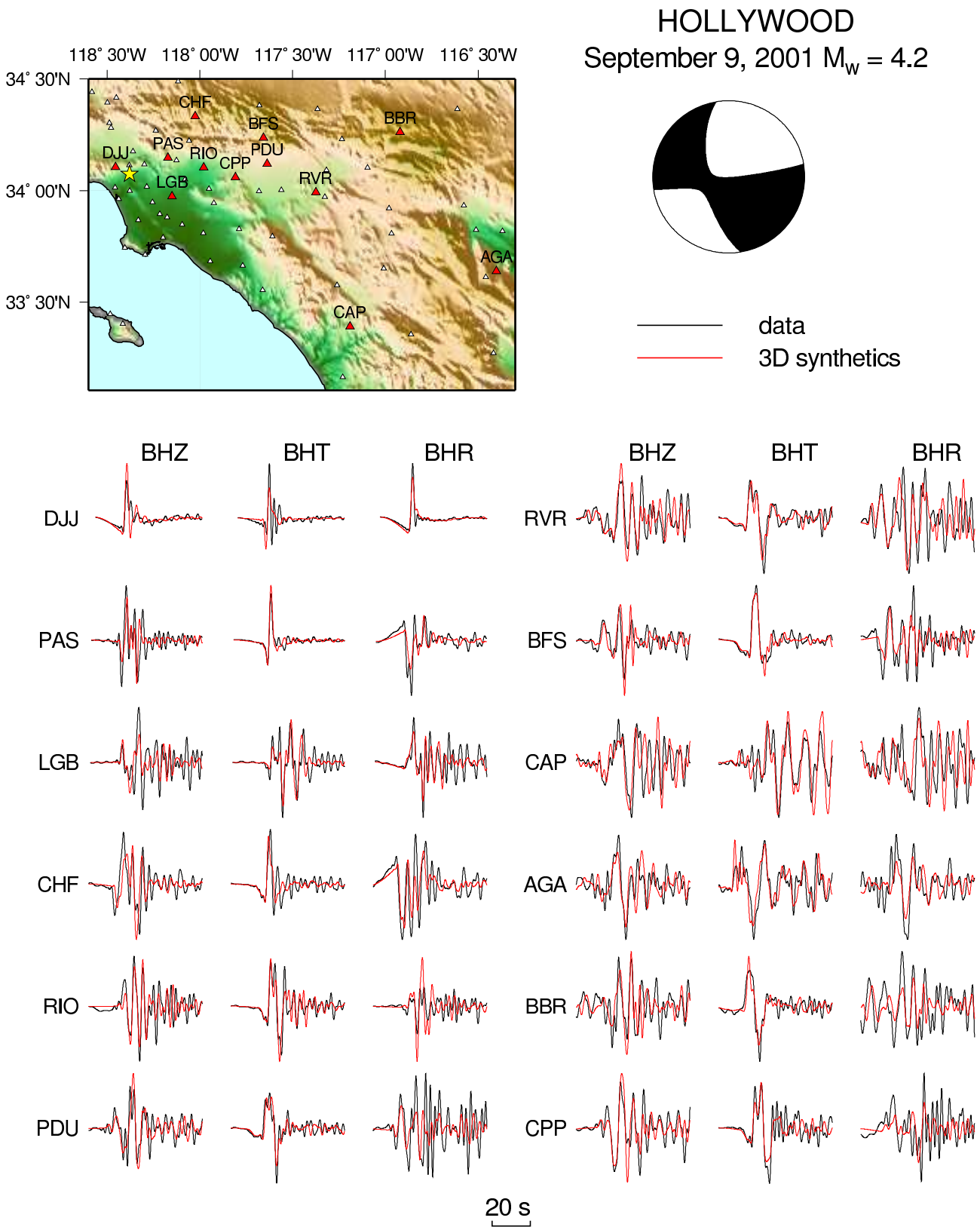

Figure 4.7 *(Top left) Map showing the epicenter (yellow star) and stations (red triangles with black labels) for which data and synthetic seismograms bandpass filtered between 2 and 35 seconds with a 4-pole 2-pass Butterworth filter are plotted in the bottom panel. The source mechanism of the 9 September 2001 $M_w = 4.2$ Hollywood earthquake is shown in the top right. Vertical (left columns), transverse (middle columns) and radial (right columns) components of displacement at 12 stations are shown in the bottom panel. SEM results are in red and data in black. The time scale is indicated by the scale bar at the bottom. We selected 12 among the stations where the best fit is obtained. Fit is determined by calculating the cross-correlation and the amplitude difference between data and synthetic seismograms.*

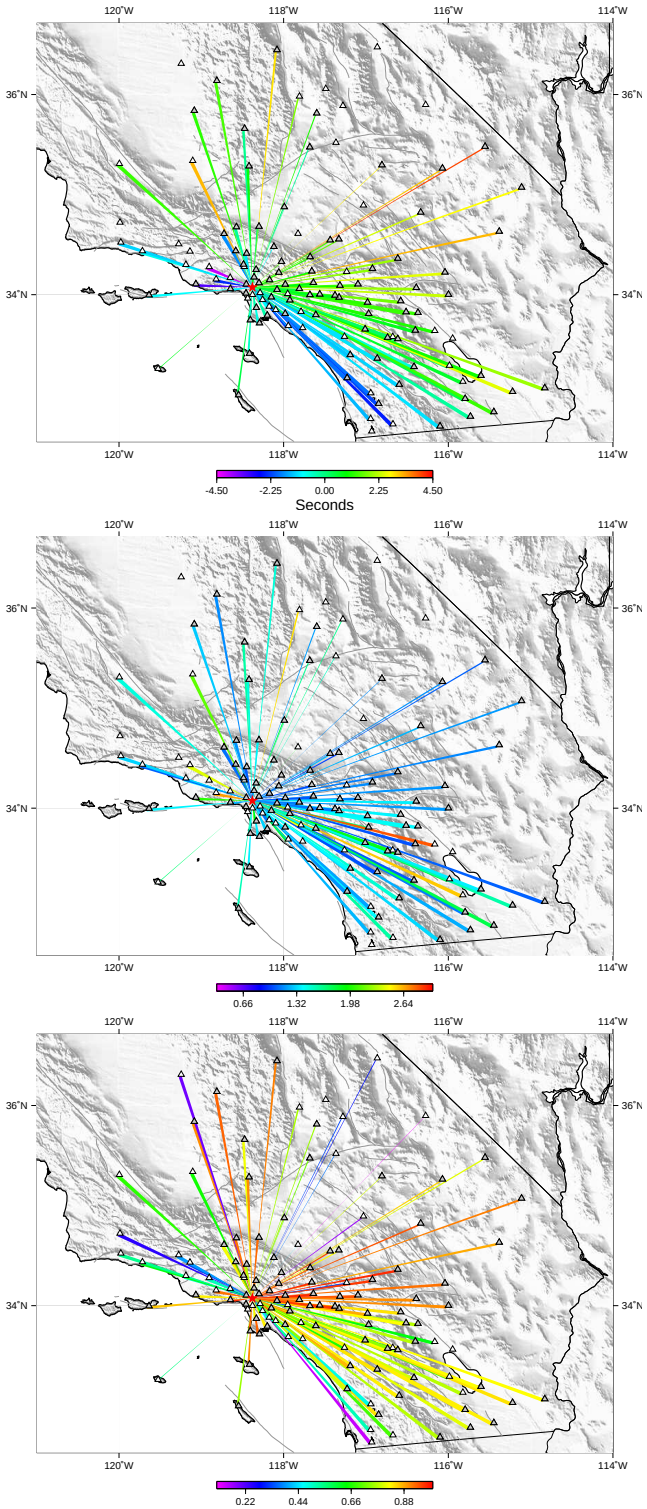

Figure 4.8 *We use cross-correlation to determine the time shift between the data and the synthetic seismograms. We show the results for the transverse component of displacement for the Hollywood event bandpass filtered between 6 and 35 seconds with a 4-pole 2-pass Butterworth filter. (Top) Time shifts are plotted as color-coded lines between event-station pairs, and are typically between* $+2$ *and* -2 *seconds. A positive (red) anomaly indicates that the synthetic seismograms are faster than the data, whereas negative (blue) values indicate that the synthetic seismograms arrive slower than the data. (Middle) Associated amplitude anomalies between the data and 3-D SEM synthetic seismograms. Color-coded lines between event-station pairs indicate the amplitude ratio between data and synthetic seismograms. An amplitude ratio greater than one (red) indicates the SEM amplitude is larger than the data, whereas a ratio smaller than one (blue) denotes SEM amplitudes smaller than the data. These amplitude anomalies are due to effects related to focusing and defocusing, attenuation, and the source. (Bottom) Correlation between the data and synthetic seismograms. Color-coded lines between event-station pairs indicate the correlation coefficients, with red denoting the highest correlations and blue lower correlations. The stations selected for this figure have a correlation coefficient of 0.6 or larger.*

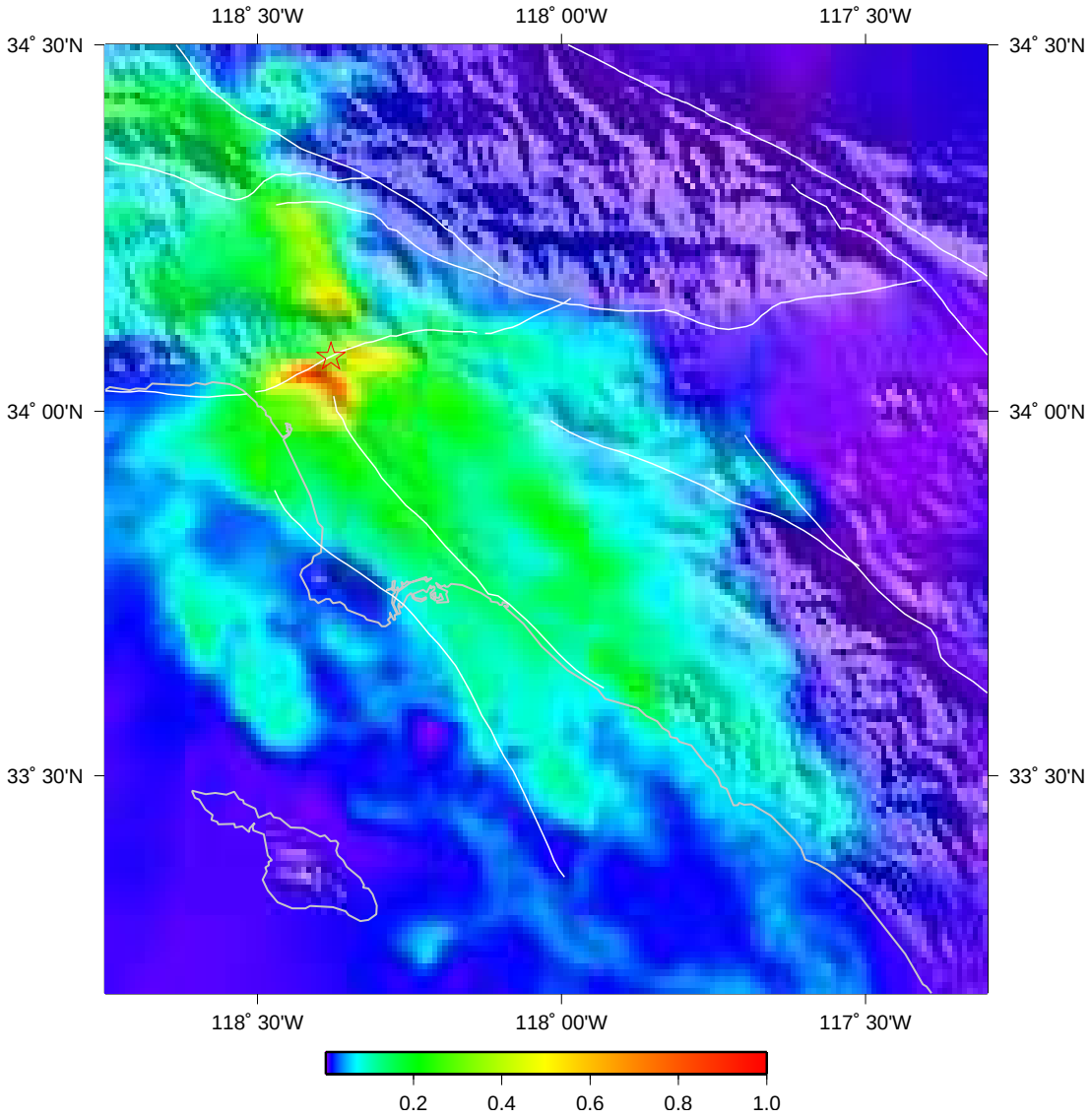

Figure 4.9 *Close-up of peak ground acceleration for the Hollywood earthquake in the Los Angeles basin. A value of 1 on the color scale corresponds to a maximum of 2.15 mm.s^{-2} for the norm of acceleration at the surface. One can notice that strong amplification occurs in the basin, where most of the energy is trapped, while hard rock sites such as Palos Verdes, or the mountains surrounding the Los Angeles and San Fernando basins, show little acceleration. Significant amplification occurs in the San Fernando valley, north of the epicenter, in particular near its eastern edge.*

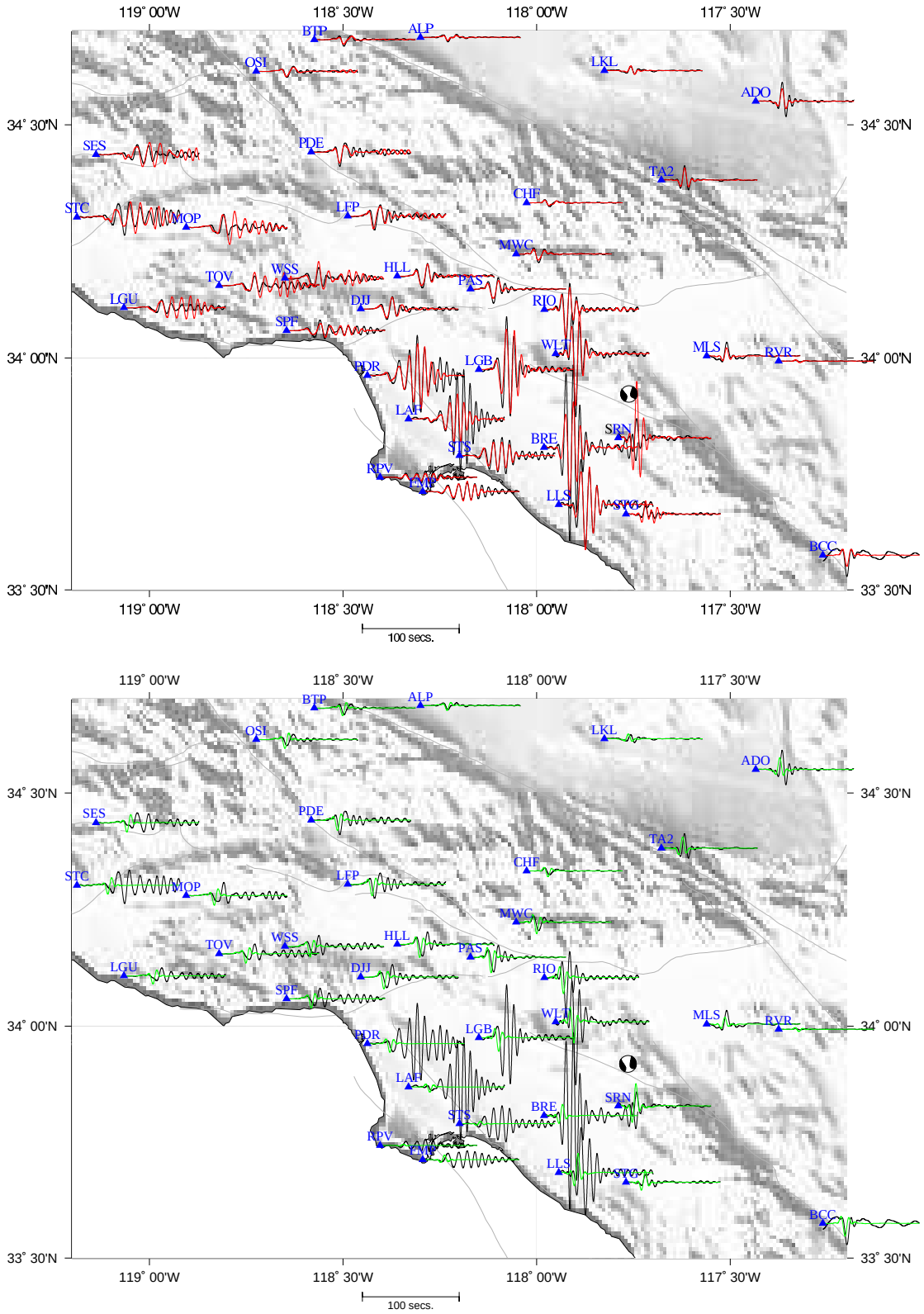

Figure 4.10 *(Top) Transverse component data (black) and 3-D SEM synthetic seismograms (red) for the 3 September, 2002, Yorba Linda event are plotted on a map of the Los Angeles area. Stations are denoted by blue triangles and labeled by their station codes. The instrument response was deconvolved from the data to obtain ground displacement. Both the data and the synthetic seismograms were subsequently bandpass filtered between 6 and 35 seconds with a 4-pole 2-pass Butterworth filter. The mechanism and location of the event are indicated by the black-and-white beach ball. The time scale is indicated by the scale bar at the bottom. (Bottom) Same figure, but showing 1-D SEM synthetic seismograms (green) instead of 3-D results. The average regional 1-D model is that of Dreger & Helmberger (1990). Attenuation was not included in this 1-D calculation. Resonance at basin stations is not correctly modeled, which clearly illustrates the importance of 3-D effects.*

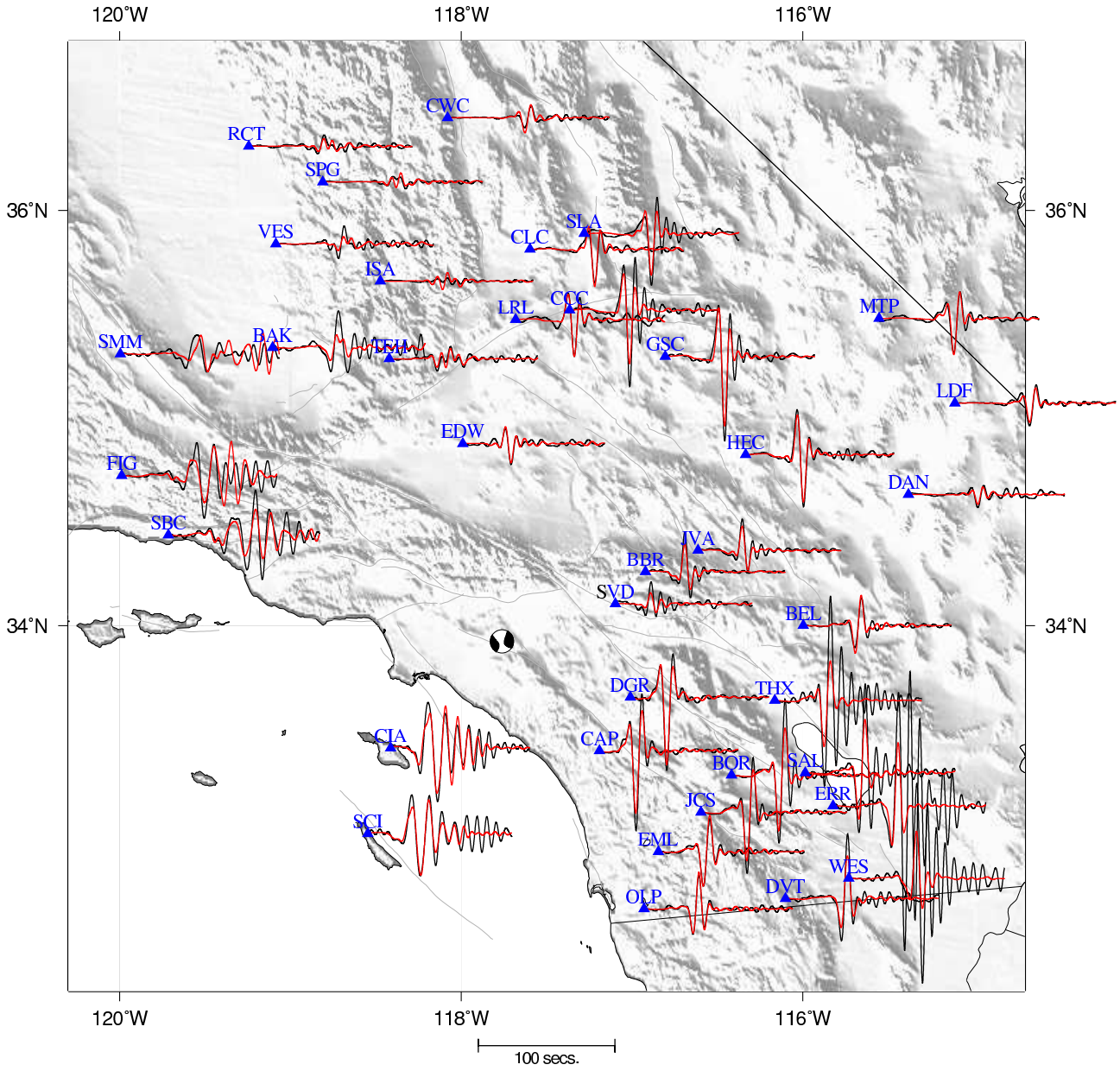

Figure 4.11 *Transverse component data (black) and 3-D SEM synthetic seismograms (red) for the 3 September, 2002, Yorba Linda event are plotted on a map of Southern California. Stations are denoted by blue triangles and labeled by their station codes. The instrument response was deconvolved from the data to obtain ground displacement. Both the data and the synthetic seismograms were subsequently bandpass filtered between 6 and 35 seconds with a 4-pole 2-pass Butterworth filter. The abrupt termination of the Ventura basin in our current basin model (Süss & Shaw 2003) produces very large amplitudes not observed in the data, e.g., at stations FIG, SYP, and SBC. In the Salton Sea area, for instance at stations SAL, ERR and WES, and in the Mojave Desert, e.g., at station ADO, there is substantial low wave-speed sediment cover that is not yet included in our model, which causes resonance in the data that is not correctly reproduced.*

Quatrième partie

Calcul massivement parallèle et vectoriel

Chapitre 5

Simulation du tremblement de terre de Denali, Alaska, sur le Earth Simulator

Résumé

Dans les chapitres précédents, nous avons montré comment la méthode des éléments spectraux peut être employée pour simuler de façon précise la propagation des ondes sismiques résultant de tremblements de terre à deux échelles différentes : locale et régionale (par exemple pour modéliser le risque sismique dans des bassins sédimentaires fortement peuplés), et globale (par exemple pour faciliter l'étude de la structure de la Terre globale dans le contexte de la tomographie sismique). Cependant, ces simulations ont été exécutées sur un cluster de PCs, et étaient donc intrinsèquement limitées par les ressources informatiques disponibles. Dans ce chapitre, nous nous affranchissons de ces limitations en employant la méthode des éléments spectraux sur l'ordinateur le plus rapide du monde (en 2003), le 'Earth Simulator' au Japon, pour simuler sur une large bande de fréquence la propagation des ondes sismiques produites par le tremblement de terre de Denali en Alaska en novembre 2002. Le tremblement de terre est bien décrit d'un point de vue géométrique par une rupture sur 5 segments de faille dominée par une rupture sur 220 kilomètres le long de la faille dextre de Denali. Nous exécutons des simulations numériques tridimensionnelles à une résolution sans précédent et mettons en évidence les forts effets de directivité observés en Amérique du Nord. Nous utilisons un maillage de très grande taille contenant 5.5 milliards de points de grille (soit 14.6 milliards de degrés de liberté). Nous effectuons les calculs sur 1944 processeurs (243 noeuds), en utilisant un total de 2.5 teraoctets de mémoire, avec un niveau de performance total de 5 teraflops. La très haute résolution du maillage nous permet de montrer pour la première fois des calculs dans un modèle 3-D à des périodes sismiques allant jusqu'à 5 secondes, c'est-à-dire des périodes qui vont au-delà des solutions quasi-analytiques classiques de modes normaux pour des modèles 1-D à symétrie sphérique, qui sont ordinairement limitées à des périodes de 8 secondes. Notre implémentation est basée exclusivement sur MPI, avec vectorisation de toutes les boucles internes sur chaque processeur. D'excellents taux de parallélisation et de vectorisation sont obtenus.

Abstract

In previous chapters, we illustrated how the highly-accurate spectral-element method can be used to simulate seismic wave propagation resulting from earthquakes at two different scales: local and regional (e.g., to model seismic hazard in densely-populated sedimentary basins), and global (e.g., to help to study the structure of the full Earth based upon seismic tomography). However, such simulations were performed on a Beowulf PC cluster, and were therefore intrinsically limited by available computer resources. In this chapter, we circumvent these limitations by using the spectral-element method on the world's fastest computer (as of 2003), the Earth Simulator in Japan, to simulate broadband seismic waves generated by the November 2002 Denali, Alaska, earthquake. The earthquake is well characterized by a 5-segment fault geometry dominated by right-lateral rupture along 220 km of the Denali fault. We perform the three-dimensional numerical simulations at unprecedented resolution and reveal significantly enhanced ground motions (directivity) toward the conterminous United States. We use a very large mesh with 5.5 billion grid points (14.6 billion degrees of freedom). We perform the calculations on 1944 processors (243 nodes), i.e., 38 % of the machine, using a total of 2.5 terabytes of memory, and achieving a total performance level of 5 teraflops. The very high resolution of the mesh allows us to show for the first time fully 3-D calculations at seismic periods as low as 5 seconds, i.e., periods that go beyond usual quasi-analytical normal-mode solutions for 1-D spherically-symmetric Earth models, which are classically limited to periods of 8 seconds. Our implementation is purely based upon MPI, with loop vectorization on each processor. Excellent parallel (more than 99%) and vectorization (99.3%) ratios are obtained.

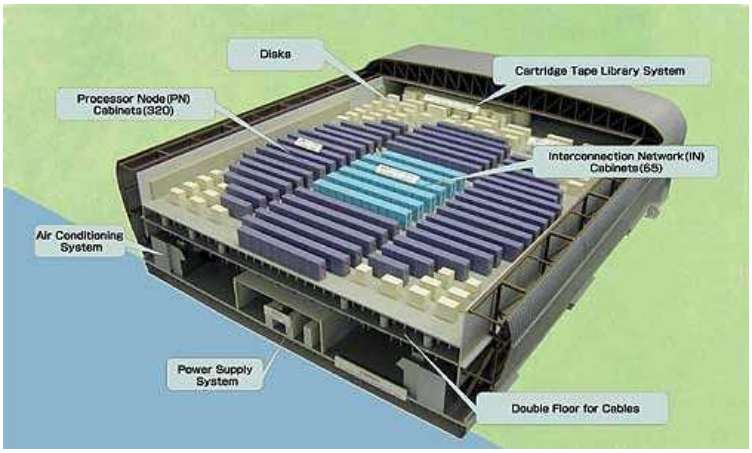

Figure 5.1 *The 'Earth Simulator' in Yokohama (Japan) is currently the largest parallel computer in the world (as of 2003). It has 5120 vectorial processors, structured in 640 nodes of 8 processors each. Each node has 16 gigabytes of memory, for a total of 10000 gigabytes. We use 1944 processors (i.e., 38%) of the machine for our SEM simulations. Pictures taken from the Earth Simulator Web site,* `www.es.jamstec.go.jp`.

5.1 Introduction

Detailed mapping of the three-dimensional (3-D) seismic velocity structure of the Earth is traditionally performed using a combination of short-period body and long-period surface waves. Modeling the rupture process during an earthquake also involves the analysis of both body and surface waves. Thus, the validation of 3-D Earth models and finite-source models requires the ability to calculate accurate broadband seismograms, i.e., synthetic seismograms that contain both short-period body waves and long-period surface waves. Here we use the world's fastest supercomputer (as of 2003), the Earth Simulator (Figure 5.1), which opened in 2002 at the Japan Marine Science & Technology Center (JAMSTEC) in Yokohama, Japan (see the Top500 list of supercomputers for details, `www.top500.org`), to model effects caused by the rupture propagating along a finite-size fault on the amplitude of seismic waves in the case of large earthquakes. We simulate broadband seismic waves generated by the large recent Denali, Alaska, earthquake that occurred on November 3, 2002 (magnitude 7.9, at a depth of 15 km). This event is the largest strike-slip earthquake in North America since the very destructive April 18, 1906 San Francisco earthquake. It ruptured 220 km of the Denali fault in Central Alaska, in five distinct fault segments (Figure 5.2). As a comparison, the 1906 San Francisco earthquake also had a magnitude of approximately 7.9, and ruptured 430 km of the San Andreas fault from northwest of San Juan Bautista to Cape Mendocino.

The main rupture for this Alaska earthquake occurred on the dextral Denali fault, which has been active since the late Cretaceous in response to the oblique convergence between the North American plate and the Pacific plate (Page et al. 1995). This tectonic setting dictates that the motion is dominated by right-lateral strike-slip. We constructed a five-segment fault geometry using observed surface offsets (Eberhart-Phillips et al. 2003) and teleseismic body-wave recordings as constraints (Ji et al. 2004) (Figure 5.2). The body waves are used to reconstruct the slip history, slip vector, rupture initiation time, and width of an analytic slip-rate function on each sub-fault, and are inverted simultaneously with the observed surface offsets using a recently developed finite-fault inversion procedure (Ji et al. 2002). Ours (Ji et al. 2004) and other studies (Kikuchi & Yamanaka 2002) indicate that the rupture initiated as a thrust event before traveling southeast along 220 km of the Denali fault. Slip along this segment increased from 6 m in the northwest to more than 10 m in the southeast. During the later part of the earthquake the rupture branches off the Denali fault onto the Totichunda fault, where it continues in strike-slip fashion. To use the finite fault model in our numerical simulations we approximate it by a set of 475 sub-events of size 4 km $\times$ 5 km; these sub-events represent the distribution of the moment-density tensor.

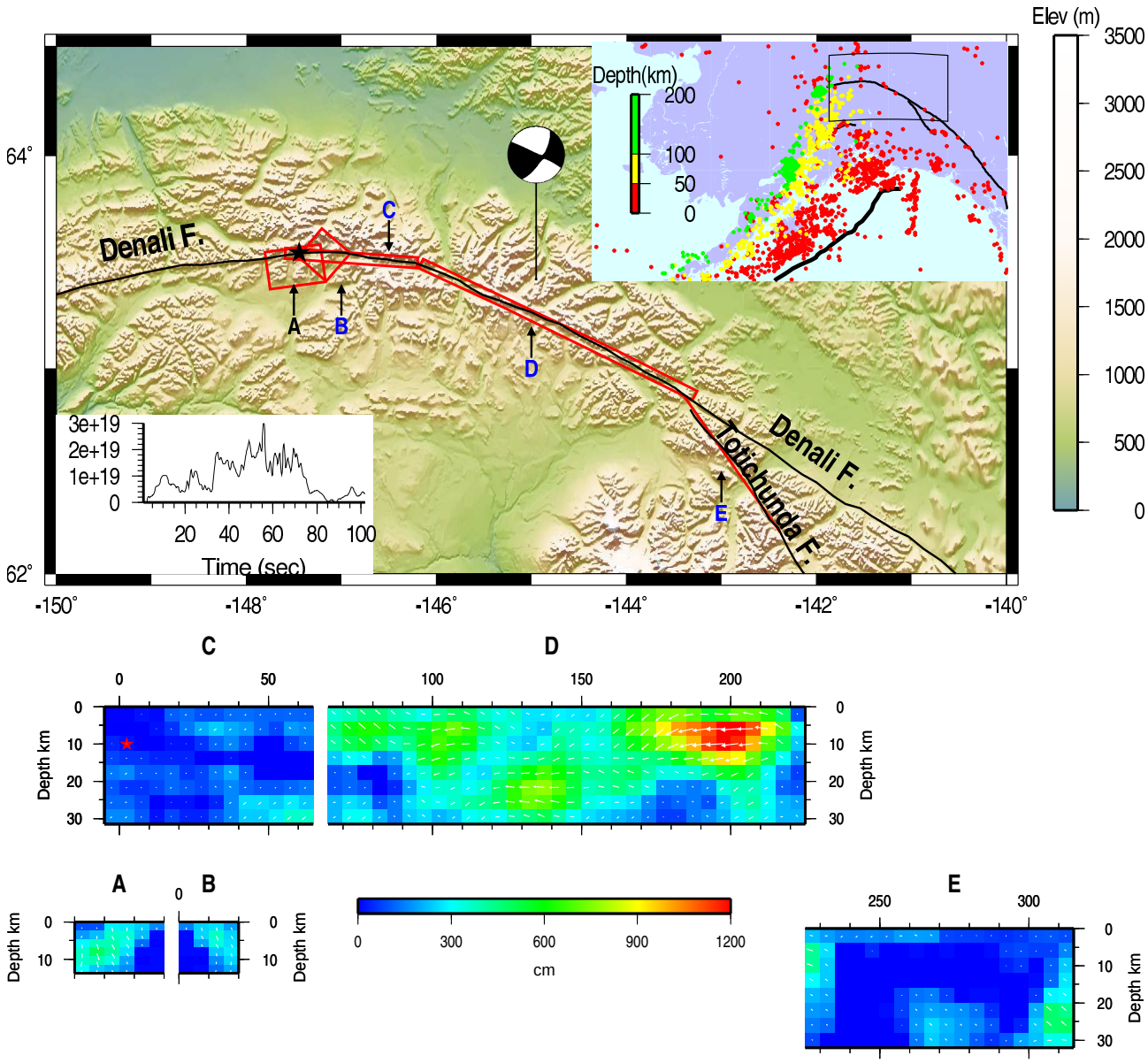

Figure 5.2 *Top: Fault geometry of the November 3, 2002, Denali, Alaska, earthquake. The top-right inset shows a map on which relocated seismicity determined by the International Seismological Center (Engdahl et al. 1998) is color-coded according to hypocentral depth. The thick black line off the coast denotes the location of the Aleutian trench. The black box denotes the area of detail shown in the larger map, on which the Denali and Totichunda faults are labeled. The Harvard Centroid-Moment Tensor solution (*`www.seismology.harvard.edu`*) is shown by the black-and-white beach ball. The five red boxes labeled A–E denote the surface projections of the five fault segments that were involved in the rupture. The earthquake started at the black star with a thrust event represented by fault planes A and B, which both have a 32-degree dip to the North, and Northwest, respectively. The rupture then proceeded as strike-slip motion along the nearly vertical fault planes C, D and E. Segments C and D represent the main rupture along the Denali fault, whereas segment E represents the rupture along the Totichunda fault. The average moment-rate function is plotted as a function of time in the bottom left corner of the map. Bottom: Slip distribution along the five fault segments A–E shown in the top. The red star on segment C denotes the point of rupture initiation. This point is shared with fault planes A and B. The white arrows on the fault plane denote the slip direction, and their length is proportional to the amount of slip.*

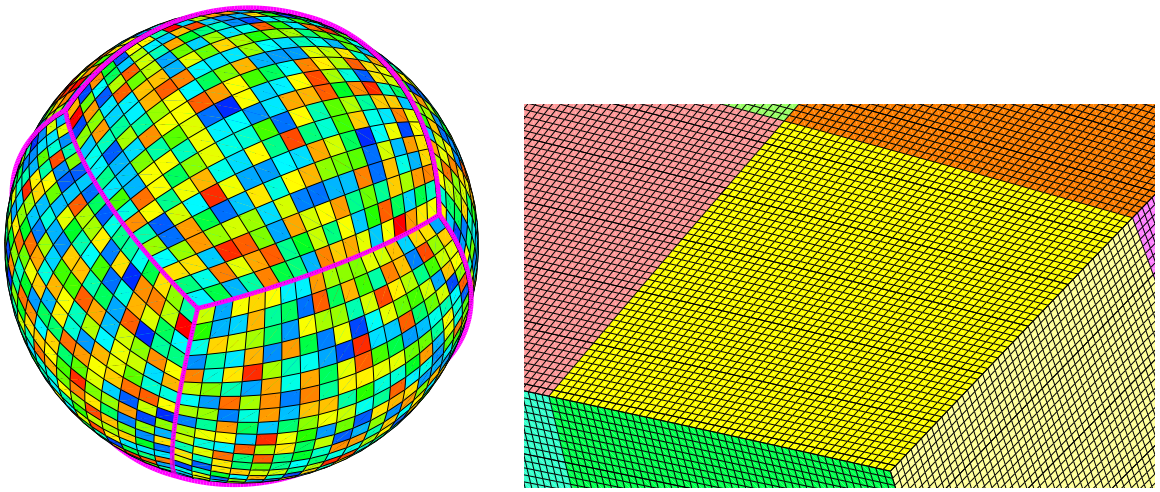

Figure 5.3 *The SEM uses a mesh of hexahedral finite elements on which the wave field is interpolated by high-degree Lagrange polynomials on Gauss-Lobatto-Legendre (GLL) integration points. The left figure shows a global view of the mesh at the surface, illustrating that each of the six sides of the so-called 'cubed sphere' mesh (Sadourny 1972; Chaljub 2000; Komatitsch & Tromp 2002a) is divided into 18 × 18 slices, shown here with different colors, for a total of 1944 slices. The right figure shows a close-up of the mesh of 48 × 48 spectral-elements at the surface of each slice. Within each surface element we use 5 × 5 = 25 GLL points, which translates into an average grid spacing of 2.9 km (or 0.026 degrees).*

The field of numerical modeling of seismic wave propagation in 3-D structures has significantly evolved in the last few years because of the introduction of the spectral-element method (SEM), as illustrated in previous chapters. However, until recently at the global scale available computer resources intrinsically limited such calculations. For instance on a PC Beowulf Cluster with 150 processors, Komatitsch & Tromp (2002a) reached a minimum seismic period of 18 seconds (i.e. 1/18 Hz). Such a minimum period is not short enough to capture important effects on wave propagation related to smaller-scale 3-D heterogeneity in the Earth. Here we show that on 38 % of the Japanese Earth Simulator we can simulate seismic waveforms accurately down to a minimum period of 5 seconds, i.e., almost a factor of 4 better than on our Beowulf cluster. (Note that one pays a factor of 16 in terms of numerical cost every time one wants to improve the resolution by a factor of 2, because the mesh needs to be doubled in the three directions of space, and in addition the time step needs to be divided by two in the fully-explicit conditionally-stable time integration scheme used in the SEM). In other words, the SEM on the Japanese Earth Simulator allows us to simulate global seismic wave propagation in fully 3-D Earth models at periods shorter than current seismological practice for simpler 1-D spherically-symmetric models, since quasi-analytical normal-mode calculations for such models are classically limited to periods of 8 seconds.

5.2 The spectral-element method on the Earth Simulator

As illustrated in Chapter 3, our SEM incorporates 3-D variations in compressional wave speed, shear-wave speed and density, attenuation, anisotropy, ellipticity, topography and bathymetry, and crustal thickness (Komatitsch & Vilotte 1998; Chaljub 2000; Komatitsch et al. 2002; Komatitsch & Tromp 2002a,b). We use model S20RTS of the mantle (Ritsema et al. 1999), model CRUST2.0 of the crust (Bassin et al. 2000), and topography and bathymetry model ETOPO5 (from the U.S. National Oceanic and Atmospheric Administration).

The Earth Simulator (Figure 5.1) has 640 8-processor compute nodes, for a total of 5120 processors. Each node has 16 gigabytes of shared memory, for a total of 10 terabytes of memory. Peak performance per node is approximately 64 gigaflops and total peak performance is approximately 40 teraflops. Because of the vector processor architecture, measured peak and sustained performance in the Top500 list of supercomputers (`www.top500.org`) are very close to theoretical performance, with measured $R_{\rm peak} = 41$ teraflops and $R_{\rm max}$ = 35.9 teraflops for the LINPACK benchmark.

Figure 5.3 shows a global view of the spectral-element mesh at the surface of the Earth. The sphere is meshed using hexahedra only, based upon the 'cubed sphere' analytical mapping from the six sides of a unit cube to a six-block decomposition of the surface of the sphere (e.g., Sadourny 1972; Ronchi et al. 1996; Chaljub 2000; Komatitsch & Tromp 2002a), as illustrated in Chapter 2. The figure illustrates that each of the six sides of the 'cubed sphere' mesh is divided into 18 × 18 slices, shown with different colors, for a total of 1944 slices. We use 38 % of the Earth Simulator (1944 processors, i.e., 243 nodes out of 640) and allocate one processor per slice. The figure also shows a close-up of the mesh

of 48 $\times$ 48 spectral-elements at the surface of each slice. Within each surface element we use 5 $\times$ 5 = 25 GLL grid points, which translates into an average grid spacing of 2.9 km (i.e., 0.026 degrees) at the surface. The total number of spectral-elements in this mesh is 82 million, which corresponds to a total of 5.47 billion global grid points, since each spectral element contains 5 $\times$ 5 $\times$ 5 = 125 grid points, but with points on its faces shared by neighboring elements. This in turns corresponds to 14.6 billion degrees of freedom (the total number of degrees of freedom is slightly less than 3 times the number of grid points, because we solve for the three components of displacement everywhere in the mesh, except in the liquid outer core of the Earth, where we solve for a scalar potential, as mentioned above).

Using this mesh, we can calculate synthetic seismograms that are accurate down to seismic periods of 5 seconds. Such simulations use a total of approximately 2.5 terabytes of memory. As a comparison, we can simulate global wave propagation only down to seismic periods of 18 seconds on a two-and-a-half-year-old PC cluster computer with 150 processors (733 MHz Pentium-III) and 75 gigabytes of memory at Caltech, as mentioned previously. The mesh files, created once and for all by our in-house parallel mesh generator, are stored on the Earth Simulator's large capacity tape system, to avoid having to recreate the mesh every time we start a new simulation (mesh creation and file saving takes of order 1 hour on 1944 processors, mainly because of the sorting routine needed to create a global numbering from the local numbering of grid points in each elements, and to remove multiple entries in the list of common points between neighbors).

Our SEM solver is based upon a pure MPI implementation, combined with loop vectorization on the Earth Simulator. We initially implemented a mixed MPI – OpenMP solution, using MPI between nodes (i.e., between blocks of 8 processors with shared memory), and using OpenMP inside each node. However, in the context of initial tests, in practice CPU time was almost identical to a pure MPI run on a small number of processors, therefore we decided to permanently switch to an MPI implementation. We do not claim that this conclusion is general on the machine; it might well be specific to our SEM algorithm, in particular we did not try the mixed OpenMP – MPI solution on a very large configuration. Other groups have successfully implemented algorithms based upon mixed OpenMP – MPI models on the Earth Simulator.

The SEM algorithm is not 'embarrassingly parallel', because of the need to assemble internal force contributions between neighboring slices, and because of the pattern of communications needed to assemble such slices on the edges and corners of the six blocks of the cubed-sphere mesh, as can be seen in Figure 5.3 (for instance the valence of most surface points is 4, but it is only three at the corners of the six block). However, because the mass matrix is exactly diagonal, processors spend most of their time performing actual computations, and the amount of communications is comparatively reasonably small (but not negligible). Because of the regular mesh pattern in each of the six blocks of the cubed sphere, load balancing is also very good in our SEM algorithm. Historically, our SEM code was first developed starting in 1996 on a Thinking Machine CM-5, then ported to a Sun Enterprise using shared memory with compilation directives, and then ported to MPI on a Linux PC cluster. Therefore, it took no effort to parallelize the code on the Earth Simulator, because we already had a portable MPI implementation. Before we ran simulations on 1944 processors, we benchmarked the MPI code using smaller meshes on 96 and 384 processors, and got an excellent measured parallelization ratio of more than 99 %.

Loop vectorization was a more difficult issue to address. Performance critically depends on vectorization on the Earth Simulator. Unfortunately, our existing Fortran90 MPI source code could not be fully vectorized automatically by the compiler because of the fact that the main routines consist of matrix-vector products in each spectral element, but these elements, and therefore the related matrices and vectors, are very small (5 $\times$ 5 $\times$ 5 grid points as mentioned above). Therefore, these matrix operations are too small to be efficiently replaced by calls to a standard optimized library such as BLAS, because the overhead would be large. We therefore had to manually restructure and inline most of these loops (in particular critical inner loops). Fortunately, only one or two small routines had to be rewritten (the code spends 80 to 90 percent of the CPU time in these critical routines, which fortunately are small in terms of source code size). After manual loop inlining, all critical loops in the SEM code were fully vectorized, and we reached an excellent vectorization ratio of 99.3 % (measured using standard system tools provided by the Earth Simulator Center).

I/O was not an issue in the context of our wave propagation simulation project, because we only output a small number of time series to record seismic motion (the three components of the displacement vector) at a small number of points at the surface of the mesh (the existing seismic recording stations). These time series (called 'seismograms') are then compared to recorded data from real earthquakes, as will be illustrated in the next section. This means that the amount of data saved by our SEM is negligible.

Using 1944 processors, a simulation of 60 minutes of actual seismic wave propagation accurate down to a period of 5 seconds requires about 15 hours of wall-clock time (using 50000 time steps of 72 ms each for the explicit time integration scheme of the SEM algorithm). Total performance of the code (measured using standard system tools provided by the Earth Simulator Center) was about 5 teraflops, which is about one third of expected peak performance for this number of nodes (243 nodes $\times$ 64 gigaflops = 15 teraflops). Because the batch management system limits wall-clock time to 6 hours when using more than 1/3rd of the machine, we ran the total simulation in three different steps of 5 wall-clock hours each, based upon restart files saved to the large-capacity tape system.

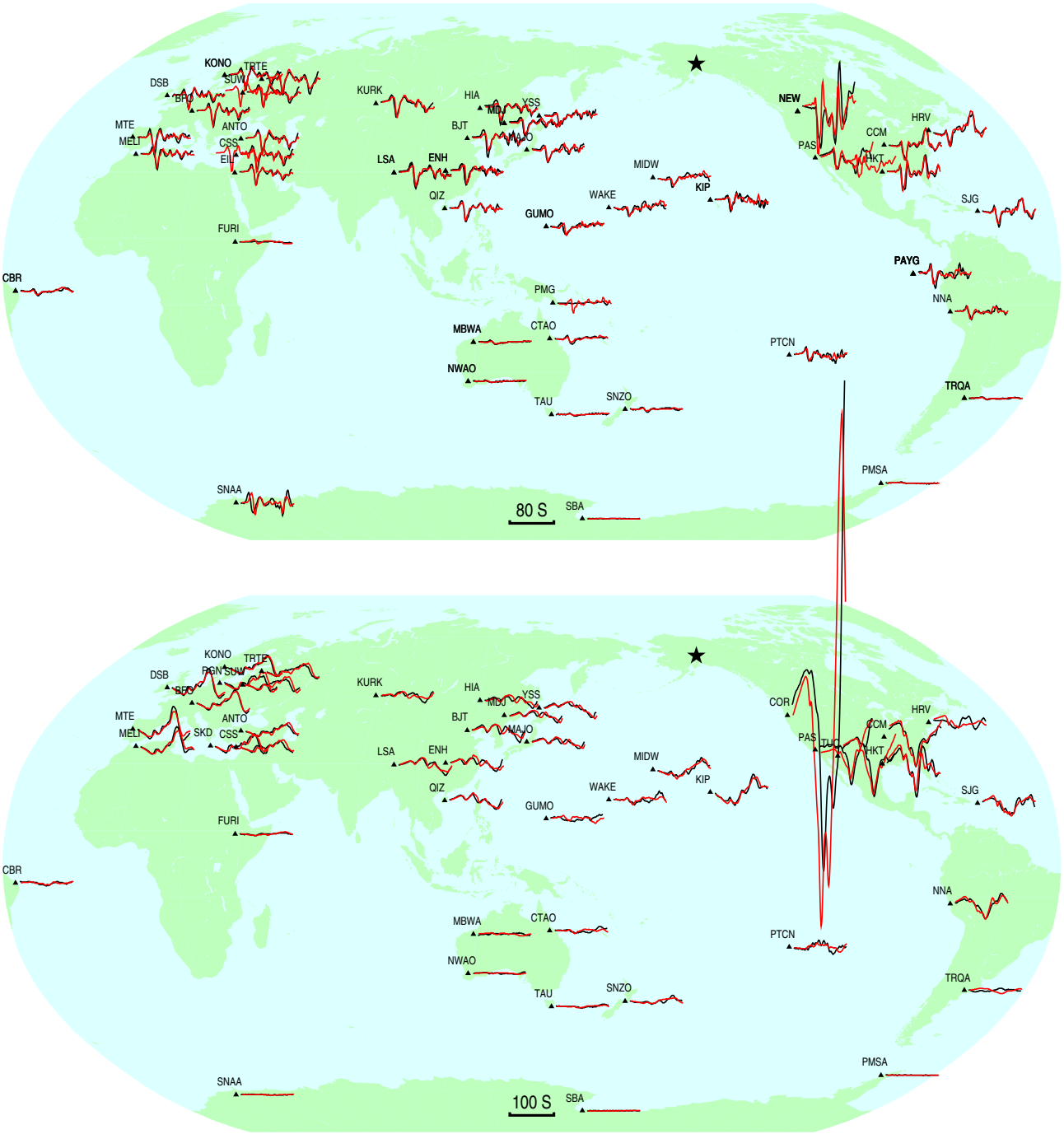

Figure 5.4 *Maps on which stations in the Global Seismographic Network are labeled and denoted by black triangles. To the right of each station the data are shown in black and the 3-D SEM synthetic seismograms in red. Both data and synthetic seismograms are bandpass-filtered with a two-pass six-pole Butterworth filter between periods of 5 and 150 seconds. The black star denotes the epicenter, and the black bar at the bottom denotes the time scale. Both data and synthetic seismograms are multiplied by the inverse of the body-wave geometrical spreading factor in an attempt to remove effects associated with epicentral distance. Top: P wave displacement on the vertical component. Bottom: S wave displacement on the transverse component. To compare the P- and S-wave amplitudes in the two figures the S waves need to be multiplied by a factor of four.*

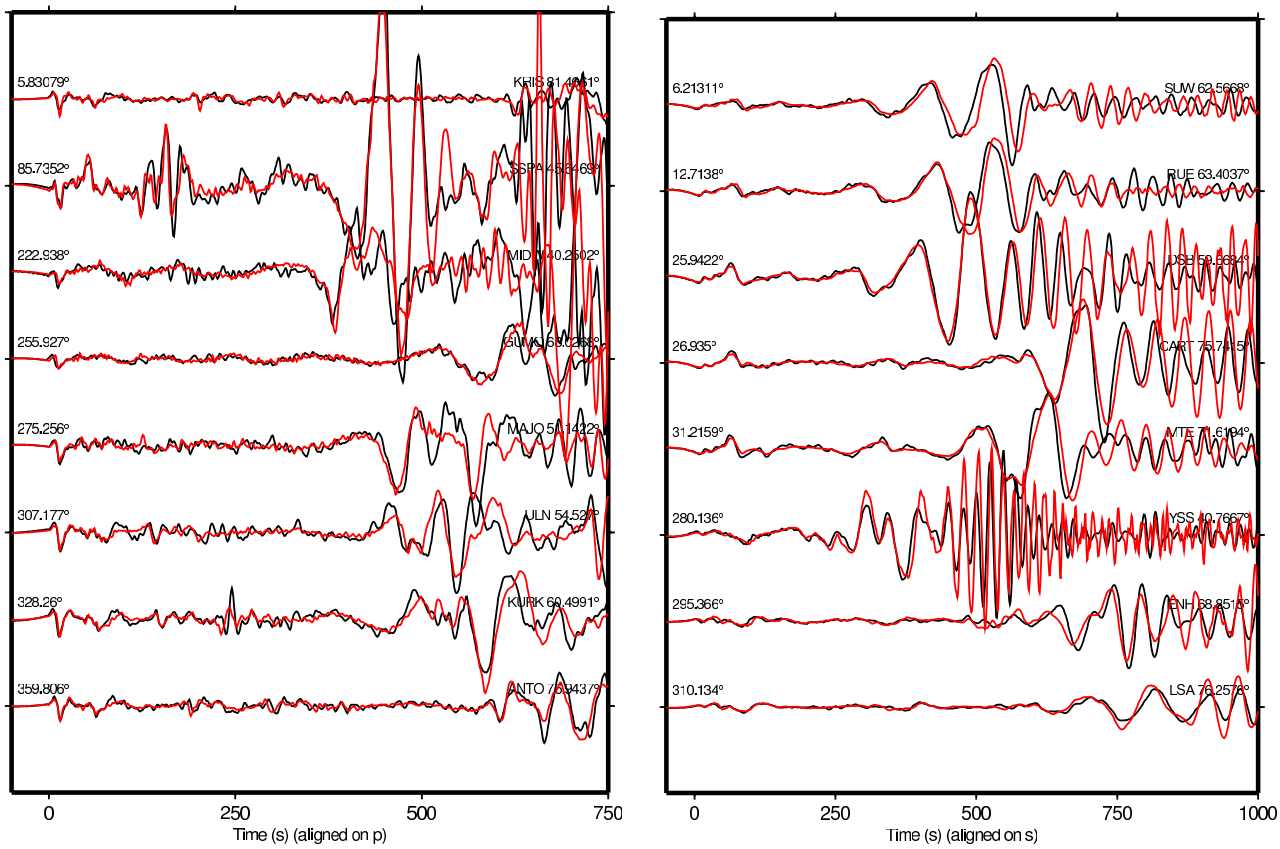

Figure 5.5 *Broadband data and synthetic displacement seismograms bandpass-filtered with a two-pass four-pole Butterworth filter between periods of 5 and 150 seconds. Left: vertical component data (black) and synthetic (red) displacement seismograms aligned on the arrival time of the P wave. Right: transverse component data (black) and synthetic (red) displacement seismograms aligned on the arrival time of the S wave. For each set of seismograms the azimuth is plotted above the records to the left, and the station name and epicentral distance are plotted to the right. The transverse component seismograms need to be multiplied by a factor of ten to compare them directly with the vertical component seismograms in terms of amplitude.*

5.3 Modeling of the Denali, Alaska, earthquake

In Figure 5.4 we show the results of the simulation for compressional (P) and shear (S) waves at periods between 5 and 150 seconds. The largest P and S wave arrivals are observed in North America; this is due to the fact that the main rupture is in a south-easterly direction. The duration of the rupture is about 100 seconds (Figure 5.2). The initial portion of the P waveforms, in particular at European stations, reflects the thrust event that initiated the earthquake. The importance of 3-D structure is illustrated by comparing the results in Figure 5.4 with those in Figure 5.6, which shows P and S wave data and synthetic seismograms for the one-dimensional (1-D) spherically- symmetric Preliminary Reference Earth Model (PREM) (Dziewonski & Anderson 1981). The finite source model is the same for the 3-D and PREM synthetic seismograms, so the differences are due to 3-D heterogeneity. The overall P and S waveforms for PREM have the right shape, but the arrival times are off, which is an imprint of 3-D heterogeneity in the mantle. In particular, P waveforms recorded at Pacific stations, such as MIDW (Midway), KIP (Kipapa, Hawaii), WAKE (Wake Island), GUMO (Guam, Mariana Islands), and PTCN (Pitcairn Island), are fit much better by the 3-D model. The same is true for S waveforms recorded in Eurasia. S waveforms in Europe, e.g., stations DSB (Dublin, Ireland), BFO (Black Forest, Germany), MTE (Manteigas, Portugal), and MELI (Melilla, Spain), clearly illustrate significant moment release toward the end of the rupture, a reflection of the moment release plotted in Figure 5.2. Notice that both P and S waveforms are nearly nodal in Australia, something that is well captured by the finite source model. The huge S wave at station COR (Corvallis, Oregon, USA) arrives 8 seconds too early in the 3-D simulations. Apparently, the highly heterogeneous path along the west coast of North America is not slow enough in the 3-D mantle model to explain the observed arrivals. Note in Figure 5.6 that the situation is worse for spherically symmetric model PREM, in which the S wave arrives 11 seconds too early at COR.

To illustrate the broadband nature of the seismograms, Figure 5.5 shows 12 minutes of vertical component displacement seismograms starting at the arrival time of the P wave, and 17 minutes of transverse component displacement seismograms starting at the arrival time of the S wave. The transverse component of displacement has an amplitude that is ten times

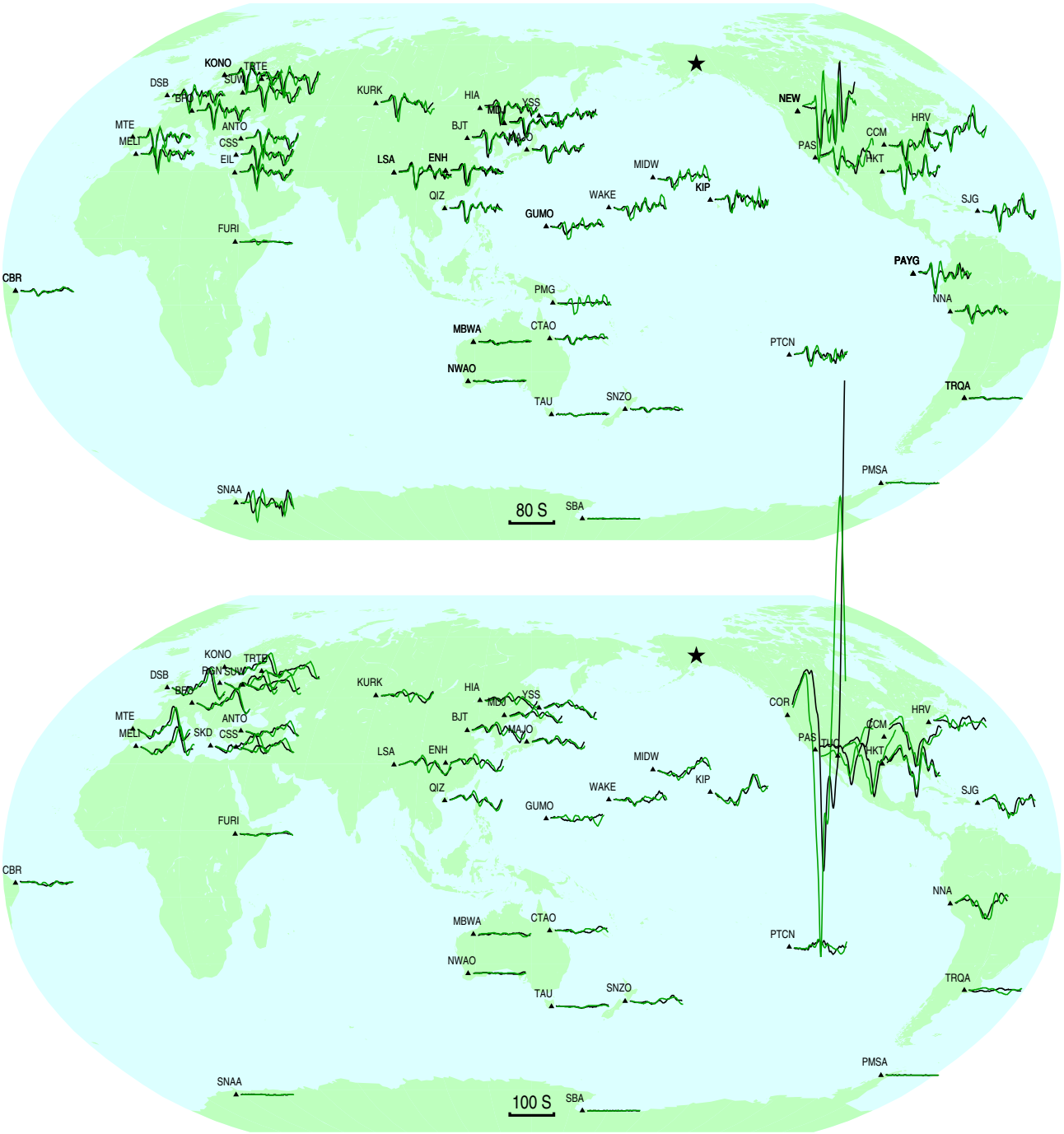

Figure 5.6 *Same as Figure 5.4, except that the SEM synthetic seismograms, shown in green, are for the spherically symmetric 1-D Earth model PREM (Dziewonski & Anderson 1981). Generally, PREM synthetic seismograms are calculated based upon normal-mode summation (Dahlen & Tromp 1998), which is a semi-analytical technique valid only for spherically symmetric Earth models. Because of the short periods involved in the calculations presented here, mode catalogs are neither practical nor available, and thus the PREM synthetic seismograms were also calculated on the Earth Simulator based upon the SEM. Top: P-wave displacement on the vertical component. Bottom: S-wave displacement on the transverse component. To compare the P- and S-wave amplitudes in the two figures the S waves need to be multiplied by a factor of four.*

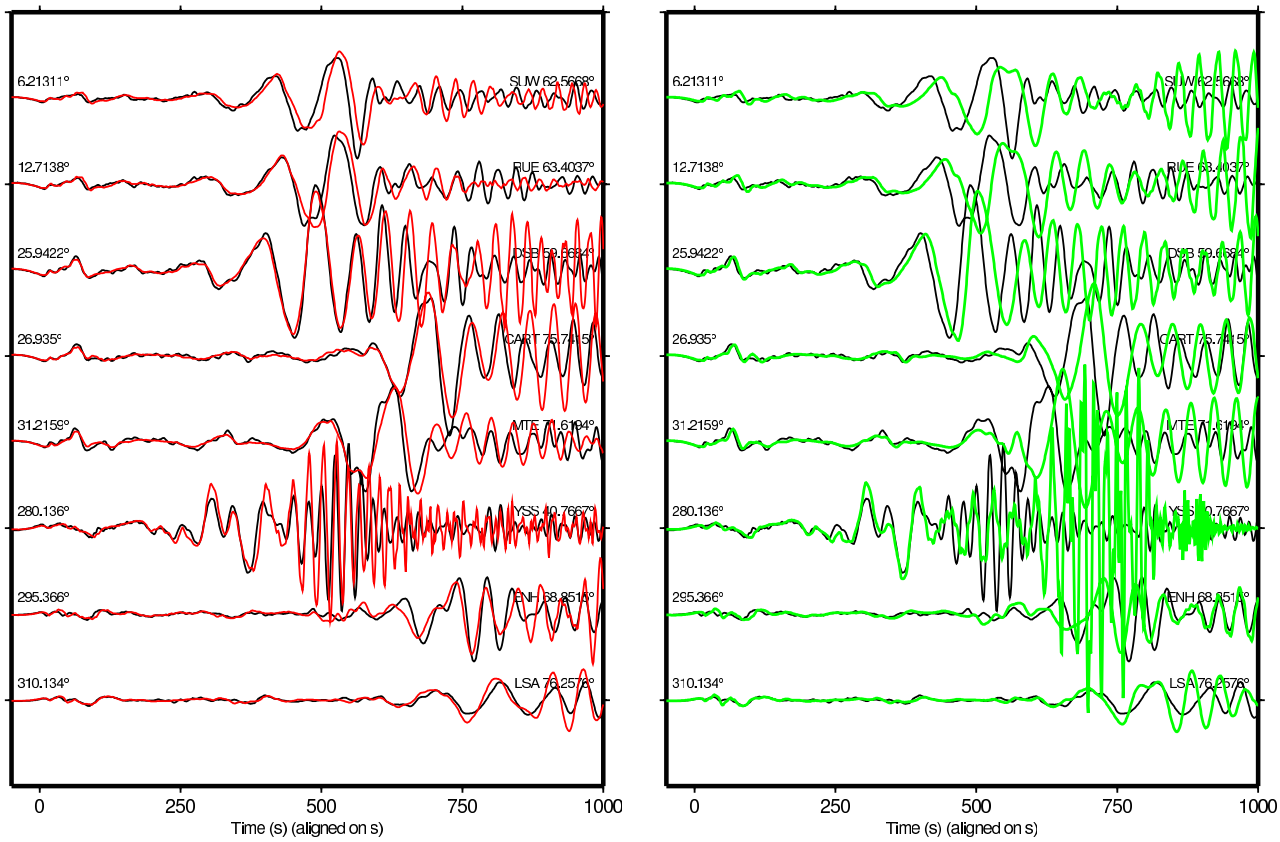

Figure 5.7 *Broadband data and synthetic seismograms bandpass-filtered with a two-pass four-pole Butterworth filter between periods of 5 and 150 seconds. The transverse component of displacement is displayed. Left: data (black) and 3-D SEM synthetic seismograms (red) aligned on the arrival time of the S wave. Right: data (black) and 1-D (PREM) synthetic seismograms (green). The fit is significantly improved by the 3-D model. For each set of seismograms the azimuth is plotted above the records to the left, and the station name and epicentral distance are plotted to the right.*

larger than the vertical component. This reflects the predominantly strike-slip nature of the event. For reference, the same transverse component data are compared against SEM synthetic seismograms for 1-D model PREM in Figure 5.7. The fit is significantly improved by the 3-D model.

Cinquième partie

Conditions parfaitement absorbantes, approximation de surface

Chapitre 6

Conditions parfaitement absorbantes PML au second ordre

Résumé

La simulation de la propagation des ondes sismiques en domaine non borné est un sujet difficile, parce que l'on doit introduire des bords fictifs dans le modèle numérique, sur lesquels des conditions absorbantes doivent être imposées. Dans le Chapitre 4 par exemple, nous avons utilisé de tels bords absorbants pour simuler la propagation des ondes sismiques dans le bassin de Los Angeles. Classiquement, de telles conditions absorbantes sont introduites en utilisant des couches absorbantes (zones "éponges") ou des équations paraxiales (traitement "one-way"). Cependant, ces dernières années ce thème de recherche a progressé de manière très sensible en raison de l'introduction de couches absorbantes parfaitement adaptées (Perfectly Matched Layer - PML), qui ont la propriété d'absorber parfaitement les ondes avec n'importe quel angle d'incidence et n'importe quel contenu fréquentiel avant discrétisation (c'est-à-dire que le coefficient de réflexion est analytiquement nul avant discrétisation ; malheureusement cette propriété est perdue pendant le processus de discrétisation). Dans de nombreuses études précédentes, la condition PML s'est avérée très efficace pour l'équation des ondes élastiques écrite sous la forme d'un système du premier ordre en vitesse et contraintes. Nous démontrons ici comment utiliser cette condition pour la même équation écrite sous la forme d'un système du second ordre en déplacement. Ceci permet d'utiliser cette condition dans le contexte d'algorithmes numériques basés sur un tel système, comme par exemple les méthodes classiques d'éléments finis, la méthode des éléments spectraux, et certaines méthodes de différences finies. Nous illustrons l'efficacité de cette formulation PML de second ordre à l'aide d'un test bidimensionnel avec des ondes de surface et de volume, possédant une solution analytique.

Abstract

Simulating seismic wave propagation in an unbounded domain is a challenging issue, because one needs to introduce fictitious model edges on which absorbing boundary conditions must be imposed. In Chapter 4 for instance, we used such absorbing boundaries to model seismic wave propagation in the Los Angeles basin. Classically, such absorbing conditions are introduced based upon either approximate damping layers ('sponge zones') or paraxial equations ('one-way treatment'). However, in recent years this topic has improved significantly based upon the introduction of the so-called 'Perfectly Matched Layer' (PML) absorbing condition, which has the property of perfectly absorbing waves with any angle of incidence and any frequency content before discretization (i.e., it has an analytically zero reflection coefficient before discretization; unfortunately this property is lost during the discretization process). In numerous previous studies, the PML condition has proven to be very efficient for the elastic wave equation written as a first-order system in velocity and stress. We demonstrate here how to use this condition for the same equation written as a second-order system in displacement. This facilitates use in the context of numerical schemes based upon such a system, e.g., the finite-element method, the spectral-element method, and some finite-difference methods. We illustrate the efficiency of this second-order Perfectly Matched Layer formulation based upon a two-dimensional benchmark with body and surface waves.

6.1 Introduction

In the context of numerical modeling of seismic wave propagation in unbounded media, energy needs to be absorbed at the artificial boundaries of the finite model domain. Such absorbing conditions are relevant for modeling strong ground

motion, and for local, regional and continental-scale simulations. In the last three decades, numerous techniques have been developed for this purpose: damping layers or 'sponge zones' (e.g., Cerjan et al. 1985; Sochacki et al. 1987), paraxial conditions (e.g., Engquist & Majda 1977; Clayton & Engquist 1977; Stacey 1988; Higdon 1991; Quarteroni et al. 1998), optimized conditions (e.g., Peng & Töksoz 1995), exact absorbing conditions on a spherical contour (e.g., Grote 2000), or asymptotic local or non-local operators (e.g., Givoli 1991; Hagstrom & Hariharan 1998). Unfortunately, all of the local conditions behave poorly under some circumstances, e.g. typically reflect a large amount of spurious energy at grazing incidence or low-frequency energy at all angles of incidence. On the other hand, non-local conditions are difficult to implement and numerically expensive. In the context of electromagnetics, Bérenger (1994) introduced a new condition called the Perfectly Matched Layer (PML), which has the remarkable property of having a zero reflection coefficient for all angles of incidence and all frequencies before discretization (hence the name 'perfectly matched'). This formulation has proven to be extremely efficient compared to classical conditions, and has become very popular. The formulation has been extended to three-dimensional problems (e.g., Chew & Weedon 1994; Bérenger 1996) and reformulated in a simpler manner in terms of a split field with complex coordinate stretching (e.g., Chew & Weedon 1994; Collino & Monk 1998b). The PML has become very successful in many other fields, e.g., linearized Euler equations (Hesthaven 1998), eddy-current problems (Kosmanis et al. 1999), and wave propagation in poroelastic media (Zeng et al. 2001).

In the context of wave propagation, the PML has been applied to both acoustic (e.g., Liu & Tao 1997; Qi & Geers 1998) and elastic problems (e.g., Hastings et al. 1996; Chew & Liu 1996; Collino & Monk 1998a; Collino & Tsogka 2001; Basu & Chopra 2003; Cohen & Fauqueux 2005). Collino & Tsogka (2001) demonstrated the high efficiency of the condition compared to the paraxial treatment of Higdon (1991), even though the PML reflection coefficient is not zero after discretization (e.g., Collino & Monk 1998a). All of these articles use the PML in the context of the elastic wave equation formulated as a first-order system in velocity and stress. Unfortunately, this means that this classical PML cannot be used in a straightforward manner in the context of numerical schemes that are based on the wave equation written as a second-order system in displacement, such as most finite-element methods (e.g., Bao et al. 1998), the spectral-element method (e.g., Komatitsch & Vilotte 1998; Komatitsch & Tromp 1999), and some finite-difference methods (e.g., Moczo et al. 2001). The goal of this chapter is to reformulate the classical PML condition in order to use it in this context. We also confirm that the PML is highly efficient for the absorption of surface waves, as suggested by Collino & Tsogka (2001).

6.2 A PML formulation for second-order systems

The differential or 'strong' form of the elastic wave equation can be written as

$$\rho\partial_t^2\mathbf{s} = \boldsymbol{\nabla}\cdot(\mathbf{c}:\boldsymbol{\nabla}\mathbf{s}), \tag{6.1}$$

where $\mathbf{s}$ is the displacement vector, $\mathbf{c}$ the elastic tensor, and ρ the density. The frequency-domain form is

$$-\rho\omega^2\mathbf{s} = \boldsymbol{\nabla}\cdot(\mathbf{c}:\boldsymbol{\nabla}\mathbf{s}), \tag{6.2}$$

where ω denotes angular frequency. In a homogeneous, isotropic medium, this equation permits plane wave solutions of the form $\mathbf{A}\exp[i(\mathbf{k}\cdot\mathbf{x}-\omega t)]$, where $\mathbf{A}$ represents the amplitude and polarization of the plane wave, $\mathbf{k} = k_x\hat{\mathbf{x}}+k_y\hat{\mathbf{y}}+k_z\hat{\mathbf{z}}$ its wave vector with Cartesian components k_x, k_y, and k_z, and $\mathbf{x} = x\hat{\mathbf{x}} + y\hat{\mathbf{y}} + z\hat{\mathbf{z}}$ the position vector. and ω denotes angular frequency. For plane P waves $\mathbf{A}\times\mathbf{k} = \mathbf{0}$ and $k = (k_x^2 + k_y^2 + k_z^2)^{1/2} = \omega/\alpha$, where α denotes the P-wave velocity, whereas for plane S waves $\mathbf{A}\cdot\mathbf{k} = 0$ and $k = \omega/\beta$, where β denotes the S-wave velocity.

The objective of the PML method is to construct a new wave equation that permits plane wave solutions of the form $\mathbf{A}\exp[i(\mathbf{k}\cdot\mathbf{x}-\omega t)-\gamma x]$, $\gamma > 0$, i.e., plane waves that decay exponentially in the direction of increasing x, say, while ensuring a reflection coefficient between the medium and the PML region that is exactly zero for all angles of incidence and all frequencies before discretization. Following the discussion of Collino & Tsogka (2001), to which the reader is referred for more details, this may be accomplished by introducing a new variable $\tilde{x} = x - i\gamma$ and transforming the original Equation (6.1) in terms of variables x, y, z, to a new wave equation in terms of variables $\tilde{x}$, y, z, where we have defined the origin of coordinates $x = 0$ at the contact between the regular domain and the PML layer, and the PML region corresponds to $x > 0$ (see Figure 6.1). This new wave equation permits plane wave solutions of the desired form $\mathbf{A}\exp[i(k_x\tilde{x} + k_y y + k_z z - \omega t)] = \mathbf{A}\exp[i(\mathbf{k}\cdot\mathbf{x}-\omega t)-\gamma x]$. The key in this mapping is the choice of γ.

Suppose the normal to the interface between the model and the PML layer is given by $\hat{\mathbf{n}}$ (Figure 6.1). We define the coordinate in the direction of increasing $\hat{\mathbf{n}}$ to be n. The gradient operator $\boldsymbol{\nabla}$ can now be split in terms of components perpendicular and parallel to the interface:

$$\boldsymbol{\nabla} = \hat{\mathbf{n}}\,\partial_n + \boldsymbol{\nabla}^{\parallel}. \tag{6.3}$$

Here $\partial_n = \hat{\mathbf{n}}\cdot\boldsymbol{\nabla}$ and $\boldsymbol{\nabla}^{\parallel} = (\mathbf{I}-\hat{\mathbf{n}}\hat{\mathbf{n}})\cdot\boldsymbol{\nabla}$, where $\mathbf{I}$ is the 3×3 identity tensor, and $\mathbf{I}-\hat{\mathbf{n}}\hat{\mathbf{n}}$ is the projection operator onto the surface with normal $\hat{\mathbf{n}}$.

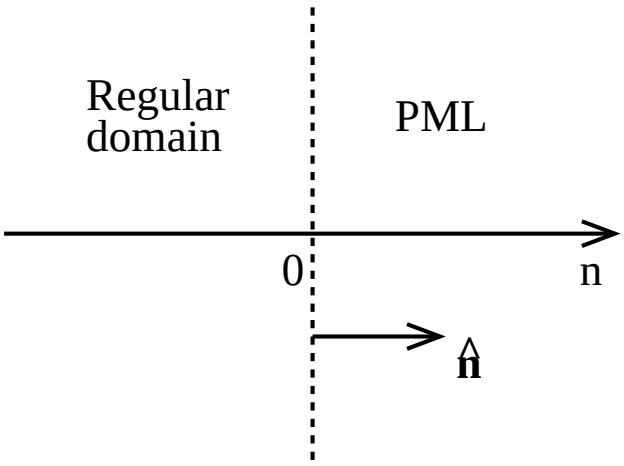

Figure 6.1 *Definition of the regular domain and the PML region. The PML layer starts at $n = 0$ and extends to $n > 0$. The local normal to the interface is denoted by $\hat{\mathbf{n}}$.*

6.2.1 Classical PML formulation for first-order systems

In the classical first-order velocity-stress formulation, one first rewrites Equation (6.1) as

$$\begin{aligned} \rho \partial_t \mathbf{v} &= \boldsymbol{\nabla} \cdot \boldsymbol{\sigma}, \\ \partial_t \boldsymbol{\sigma} &= \mathbf{c} : \boldsymbol{\nabla} \mathbf{v}, \end{aligned} \tag{6.4}$$

where $\mathbf{v}$ is the velocity vector, and $\boldsymbol{\sigma}$ the second-order stress tensor. The frequency-domain form is

$$\begin{aligned} i\omega\rho \mathbf{v} &= \boldsymbol{\nabla} \cdot \boldsymbol{\sigma}, \\ i\omega \boldsymbol{\sigma} &= \mathbf{c} : \boldsymbol{\nabla} \mathbf{v}. \end{aligned} \tag{6.5}$$

Using Equation (6.3), one obtains

$$\begin{aligned} i\omega\rho \mathbf{v} &= \hat{\mathbf{n}}\, \partial_n \cdot \boldsymbol{\sigma} + \boldsymbol{\nabla}^{\parallel} \cdot \boldsymbol{\sigma}, \\ i\omega \boldsymbol{\sigma} &= \mathbf{c} : \hat{\mathbf{n}}\, \partial_n \mathbf{v} + \mathbf{c} : \boldsymbol{\nabla}^{\parallel} \mathbf{v}. \end{aligned} \tag{6.6}$$

Next, one introduces a damping profile d across the PML region, such that $d = 0$ inside the medium and $d > 0$ in the PML, and a new complex coordinate $\tilde{n}$:

$$\tilde{n}(n) = n - \frac{i}{\omega} \int_0^n d(s) \mathrm{d}s \,, \tag{6.7}$$

or, equivalently, upon differentiating

$$\frac{\partial n}{\partial \tilde{n}} = \frac{i\omega}{i\omega + d(n)}. \tag{6.8}$$

One then replaces the wave equation (6.6) written in terms of n with a generalized wave equation written in terms of $\tilde{n}$:

$$\begin{aligned} i\omega\rho \mathbf{v} &= \hat{\mathbf{n}}\, \partial_{\tilde{n}} \cdot \boldsymbol{\sigma} + \boldsymbol{\nabla}^{\parallel} \cdot \boldsymbol{\sigma}, \\ i\omega \boldsymbol{\sigma} &= \mathbf{c} : \hat{\mathbf{n}}\, \partial_{\tilde{n}} \mathbf{v} + \mathbf{c} : \boldsymbol{\nabla}^{\parallel} \mathbf{v}. \end{aligned} \tag{6.9}$$

Inside the medium, both equations are identical because $d = 0$. But in the PML, this modified wave equation permits exponentially decaying plane wave solutions in the $\hat{\mathbf{n}}$ direction. Note that the choice of decay is $\gamma = \omega^{-1} \int_0^n d(s) ds$, and that it is inversely proportional to the angular frequency ω of the plane wave. One then uses the mapping (6.7) to rewrite the wave equation (6.9) in terms of n rather than $\tilde{n}$:

$$\begin{aligned} i\omega\rho \mathbf{v} &= \hat{\mathbf{n}}\, (\partial n / \partial \tilde{n}) \partial_n \cdot \boldsymbol{\sigma} + \boldsymbol{\nabla}^{\parallel} \cdot \boldsymbol{\sigma}, \\ i\omega \boldsymbol{\sigma} &= \mathbf{c} : \hat{\mathbf{n}}\, (\partial n / \partial \tilde{n}) \partial_n \mathbf{v} + \mathbf{c} : \boldsymbol{\nabla}^{\parallel} \mathbf{v}. \end{aligned} \tag{6.10}$$

Note that we have not had to assume that the interface is aligned with a coordinate axis, i.e., this PML formulation works in curvilinear coordinates (Collino & Monk 1998b). Next, using the split field technique (e.g., Chew & Weedon 1994; Collino & Monk 1998b), one splits the velocity and the stress into two parts, $\mathbf{v} = \mathbf{v}^1 + \mathbf{v}^2$ and $\boldsymbol{\sigma} = \boldsymbol{\sigma}^1 + \boldsymbol{\sigma}^2$, such that

$$\begin{aligned} i\omega\rho \mathbf{v}^1 &= (\partial n / \partial \tilde{n}) \hat{\mathbf{n}} \cdot \partial_n \boldsymbol{\sigma}, \\ i\omega\rho \mathbf{v}^2 &= \boldsymbol{\nabla}^{\parallel} \cdot \boldsymbol{\sigma}, \\ i\omega \boldsymbol{\sigma}^1 &= \mathbf{c} : \hat{\mathbf{n}}\, (\partial n / \partial \tilde{n}) \partial_n \mathbf{v}, \\ i\omega \boldsymbol{\sigma}^2 &= \mathbf{c} : \boldsymbol{\nabla}^{\parallel} \mathbf{v}. \end{aligned} \tag{6.11}$$

Substituting (6.8) in (6.11) and converting back to the time domain we obtain

$$\begin{aligned}(\partial_t + d)\rho\mathbf{v}^1 &= \hat{\mathbf{n}}\,\partial_n \cdot \boldsymbol{\sigma},\\ \partial_t\rho\mathbf{v}^2 &= \boldsymbol{\nabla}^{\parallel}\cdot\boldsymbol{\sigma},\\ (\partial_t + d)\boldsymbol{\sigma}^1 &= \mathbf{c}\!:\!\hat{\mathbf{n}}\,\partial_n\mathbf{v},\\ \partial_t\boldsymbol{\sigma}^2 &= \mathbf{c}\!:\!\boldsymbol{\nabla}^{\parallel}\mathbf{v}.\end{aligned} \tag{6.12}$$

Equation (6.12) permits the desired exponentially decaying plane wave solutions and governs wave propagation in the classical first-order PML.

6.2.2 Second-order systems

The key idea in this chapter is that we can apply the same concept to the wave equation formulated as a second-order system in displacement. Based upon the splitting of the gradient operator (6.3), Equation (6.2) can first be rewritten as

$$-\rho\omega^2\mathbf{s} = \hat{\mathbf{n}}\,\partial_n\cdot(\mathbf{c}\!:\!\hat{\mathbf{n}}\,\partial_n\mathbf{s}) + \hat{\mathbf{n}}\,\partial_n\cdot(\mathbf{c}\!:\!\boldsymbol{\nabla}^{\parallel}\mathbf{s}) + \boldsymbol{\nabla}^{\parallel}\cdot(\mathbf{c}\!:\!\hat{\mathbf{n}}\,\partial_n\mathbf{s}) + \boldsymbol{\nabla}^{\parallel}\cdot(\mathbf{c}\!:\!\boldsymbol{\nabla}^{\parallel}\mathbf{s}). \tag{6.13}$$

Introducing the new complex coordinate $\tilde{n}$ as defined by equation (6.7), we get:

$$-\rho\omega^2\mathbf{s} = \hat{\mathbf{n}}\,\partial_{\tilde{n}}\cdot(\mathbf{c}\!:\!\hat{\mathbf{n}}\,\partial_{\tilde{n}}\mathbf{s}) + \hat{\mathbf{n}}\,\partial_{\tilde{n}}\cdot(\mathbf{c}\!:\!\boldsymbol{\nabla}^{\parallel}\mathbf{s}) + \boldsymbol{\nabla}^{\parallel}\cdot(\mathbf{c}\!:\!\hat{\mathbf{n}}\,\partial_{\tilde{n}}\mathbf{s}) + \boldsymbol{\nabla}^{\parallel}\cdot(\mathbf{c}\!:\!\boldsymbol{\nabla}^{\parallel}\mathbf{s}). \tag{6.14}$$

Using the mapping (6.7), we now rewrite the wave equation (6.14) in terms of n rather than $\tilde{n}$:

$$\begin{aligned}-\rho\omega^2\mathbf{s} &= \hat{\mathbf{n}}\,\partial_n\cdot(\mathbf{c}\!:\!\hat{\mathbf{n}}\,\partial_n\mathbf{s})(\partial n/\partial\tilde{n})^2 + \hat{\mathbf{n}}\cdot(\mathbf{c}\!:\!\hat{\mathbf{n}}\,\partial_n\mathbf{s})(\partial n/\partial\tilde{n})\partial_n(\partial n/\partial\tilde{n})\\ &+ [\hat{\mathbf{n}}\,\partial_n\cdot(\mathbf{c}\!:\!\boldsymbol{\nabla}^{\parallel}\mathbf{s}) + \boldsymbol{\nabla}^{\parallel}\cdot(\mathbf{c}\!:\!\hat{\mathbf{n}}\,\partial_n\mathbf{s})](\partial n/\partial\tilde{n}) + \boldsymbol{\nabla}^{\parallel}\cdot(\mathbf{c}\!:\!\boldsymbol{\nabla}^{\parallel}\mathbf{s}).\end{aligned} \tag{6.15}$$

Next, we split the displacement into four parts

$$\mathbf{s} = \mathbf{s}^1 + \mathbf{s}^2 + \mathbf{s}^3 + \mathbf{s}^4\,, \tag{6.16}$$

such that

$$\begin{aligned}-\rho\omega^2\mathbf{s}^1 &= \hat{\mathbf{n}}\,\partial_n\cdot(\mathbf{c}\!:\!\hat{\mathbf{n}}\,\partial_n\mathbf{s})(\partial n/\partial\tilde{n})^2,\\ -\rho\omega^2\mathbf{s}^2 &= \hat{\mathbf{n}}\cdot(\mathbf{c}\!:\!\hat{\mathbf{n}}\,\partial_n\mathbf{s})(\partial n/\partial\tilde{n})\partial_n(\partial n/\partial\tilde{n}),\\ -\rho\omega^2\mathbf{s}^3 &= [\hat{\mathbf{n}}\,\partial_n\cdot(\mathbf{c}\!:\!\boldsymbol{\nabla}^{\parallel}\mathbf{s}) + \boldsymbol{\nabla}^{\parallel}\cdot(\mathbf{c}\!:\!\hat{\mathbf{n}}\,\partial_n\mathbf{s})](\partial n/\partial\tilde{n}),\\ -\rho\omega^2\mathbf{s}^4 &= \boldsymbol{\nabla}^{\parallel}\cdot(\mathbf{c}\!:\!\boldsymbol{\nabla}^{\parallel}\mathbf{s}).\end{aligned} \tag{6.17}$$

Upon differentiating (6.8) we find that

$$\frac{\partial}{\partial n}\left(\frac{\partial n}{\partial\tilde{n}}\right) = -\frac{i\omega}{(i\omega+d)^2}d'(n). \tag{6.18}$$

Substituting this and (6.8) in (6.17) and converting back to the time domain we obtain

$$\begin{aligned}&\rho(\partial_t + d)^2\mathbf{s}^1 = \hat{\mathbf{n}}\,\partial_n\cdot(\mathbf{c}\!:\!\hat{\mathbf{n}}\,\partial_n\mathbf{s}),\\ &\rho(\partial_t + d)^3\mathbf{s}^2 = -d'\,\hat{\mathbf{n}}\cdot(\mathbf{c}\!:\!\hat{\mathbf{n}}\,\partial_n\mathbf{s}),\\ &\rho\partial_t(\partial_t + d)\mathbf{s}^3 = \hat{\mathbf{n}}\,\partial_n\cdot(\mathbf{c}\!:\!\boldsymbol{\nabla}^{\parallel}\mathbf{s}) + \boldsymbol{\nabla}^{\parallel}\cdot(\mathbf{c}\!:\!\hat{\mathbf{n}}\,\partial_n\mathbf{s}),\\ &\rho\partial_t^2\mathbf{s}^4 = \boldsymbol{\nabla}^{\parallel}\cdot(\mathbf{c}\!:\!\boldsymbol{\nabla}^{\parallel}\mathbf{s}).\end{aligned} \tag{6.19}$$

Equation (6.19) also permits the desired exponentially decaying plane wave solutions and governs wave propagation in the PML formulated in displacement. Note that we have obtained a third-order system in time, contrary to the classical first-order velocity-stress formulation (6.12). In many numerical schemes, it is simpler to rewrite it as a second-order system using an intermediate variable

$$\mathbf{t} = (\partial_t + d)\mathbf{s}^2 \tag{6.20}$$

such that Equation (6.19) becomes

$$\begin{aligned}&\rho(\partial_t + d)^2\mathbf{s}^1 = \hat{\mathbf{n}}\,\partial_n\cdot(\mathbf{c}\!:\!\hat{\mathbf{n}}\,\partial_n\mathbf{s}),\\ &\rho(\partial_t + d)^2\mathbf{t} = -d'\,\hat{\mathbf{n}}\cdot(\mathbf{c}\!:\!\hat{\mathbf{n}}\,\partial_n\mathbf{s}),\\ &\rho\partial_t(\partial_t + d)\mathbf{s}^3 = \hat{\mathbf{n}}\,\partial_n\cdot(\mathbf{c}\!:\!\boldsymbol{\nabla}^{\parallel}\mathbf{s}) + \boldsymbol{\nabla}^{\parallel}\cdot(\mathbf{c}\!:\!\hat{\mathbf{n}}\,\partial_n\mathbf{s}),\\ &\rho\partial_t^2\mathbf{s}^4 = \boldsymbol{\nabla}^{\parallel}\cdot(\mathbf{c}\!:\!\boldsymbol{\nabla}^{\parallel}\mathbf{s}).\end{aligned} \tag{6.21}$$

The main drawback of Equation (6.21) is that one needs to modify existing numerical codes in order to handle the first-order system (6.20), i.e., an Euler or a Runge-Kutta time scheme has to be used, in addition to the classical explicit finite-difference time schemes used for the other variables $\mathbf{s}^1$, $\mathbf{s}^3$ and $\mathbf{s}^4$. For instance, the four terms in (6.21) can be marched based upon an explicit Newmark scheme (e.g., Hughes 1987), evaluating the terms on the right-hand side at the current time step, and discretizing the second-order time operators on the left-hand side $(\partial_t + d)^2$, $\partial_t(\partial_t + d)$ and ∂_t^2 explicitly. One can then use a first order scheme to march (6.20) explicitly as well by discretizing $(\partial_t + d)$ to get $\mathbf{s}^2$ from the known value of $\mathbf{t}$ computed in (6.21). The total displacement vector $\mathbf{s}$ can then be computed by summing the known values of $\mathbf{s}^1$, $\mathbf{s}^2$, $\mathbf{s}^3$ and $\mathbf{s}^4$ according to (6.16).

Another drawback of the PML in general (either as a first-order or as a second-order system) is that additional memory is required to store the split field arrays. However, this applies to the PML region only, which, because of the efficiency of the PML, is small compared to the main model, therefore in practice this problem is negligible. It is worth mentioning in this regard that in the context of electromagnetics an alternative 'anisotropic' PML formulation has been introduced to overcome this problem (e.g., Sacks et al. 1995; Zhao & Cangellaris 1996). How this formulation could be used in elastodynamics remains to be studied.

In order to use this PML system in the context of techniques such as the finite-element or spectral-element methods, one needs to write a variational formulation of the problem. The 'weak' or variational form of the classical wave equation (6.1) is obtained by dotting it with any test vector $\mathbf{w}$ and integrating by part over the volume V of the domain:

$$\int_{\mathrm{V}} \rho\, \mathbf{w} \cdot \partial_t^2 \mathbf{s}\, \mathrm{d}^3\mathbf{r} = -\int_{\mathrm{V}} (\boldsymbol{\nabla}\mathbf{w}) : \mathbf{c} : (\boldsymbol{\nabla}\mathbf{s})\, \mathrm{d}^3\mathbf{r}, \tag{6.22}$$

where we have used the free surface boundary condition and the fact that the match with the PML layer is 'perfect', i.e., on the boundary between the PML region and the regular domain the respective wave equations are identical. Similarly, the weak form of the PML system (6.21) is

$$\begin{aligned}
&\int_{\mathrm{V}} \rho(\partial_t + d)^2\mathbf{s}^1 \cdot \mathbf{w}\, \mathrm{d}^3\mathbf{r} = -\int_{\mathrm{V}} (\hat{\mathbf{n}}\partial_n \mathbf{w}) : \mathbf{c} : (\hat{\mathbf{n}}\, \partial_n \mathbf{s})\, \mathrm{d}^3\mathbf{r} + \int_{\Gamma} \hat{\mathbf{n}}\mathbf{w} : \mathbf{c} : (\hat{\mathbf{n}}\, \partial_n \mathbf{s})\, \mathrm{d}^2\mathbf{r}, \\
&\int_{\mathrm{V}} \rho(\partial_t + d)^2\mathbf{t} \cdot \mathbf{w}\, \mathrm{d}^3\mathbf{r} = -\int_{\mathrm{V}} d'\, \hat{\mathbf{n}}\mathbf{w} : \mathbf{c} : (\hat{\mathbf{n}}\, \partial_n \mathbf{s})\, \mathrm{d}^3\mathbf{r}, \\
&\int_{\mathrm{V}} \rho\partial_t(\partial_t + d)\mathbf{s}^3 \cdot \mathbf{w}\, \mathrm{d}^3\mathbf{r} = -\int_{\mathrm{V}} \left[(\hat{\mathbf{n}}\partial_n \mathbf{w}) : \mathbf{c} : (\boldsymbol{\nabla}^{\parallel}\mathbf{s}) + (\boldsymbol{\nabla}^{\parallel}\mathbf{w}) : \mathbf{c} : (\hat{\mathbf{n}}\, \partial_n \mathbf{s})\right] \mathrm{d}^3\mathbf{r} + \int_{\Gamma} \hat{\mathbf{n}}\mathbf{w} : \mathbf{c} : (\boldsymbol{\nabla}^{\parallel}\mathbf{s})\, \mathrm{d}^2\mathbf{r}, \\
&\int_{\mathrm{V}} \rho\partial_t^2\mathbf{s}^4 \cdot \mathbf{w}\, \mathrm{d}^3\mathbf{r} = -\int_{\mathrm{V}} (\boldsymbol{\nabla}^{\parallel}\mathbf{w}) : \mathbf{c} : (\boldsymbol{\nabla}^{\parallel}\mathbf{s})\, \mathrm{d}^3\mathbf{r}.
\end{aligned} \tag{6.23}$$

Again the match with the regular domain is assumed to be perfect. The boundary Γ denotes the surface of the PML that is not in contact with the regular domain.

We note that a very similar second-order PML system could be written for the acoustic wave equation formulated either in pressure or using a generalized potential (Komatitsch & Tromp 2002a). This would allow one to use the PML in the context of fluid-solid simulations.

6.3 Numerical validation

To illustrate the efficiency of the PML system (6.20)-(6.21), we simulate the propagation of P-SV waves in a two-dimensional elastic isotropic homogeneous medium. The medium is a block with P-velocity $\alpha = 2000$ m.s^{-1} and S-velocity $\beta = 1154.7$ m.s^{-1}, which corresponds to a value of 0.25 for Poisson's ratio, and density $\rho = 2200$ kg.m^{-3}. The size of the model is 30 m $\times$ 30 m. The source time function is a Ricker wavelet, i.e., the second-derivative of a Gaussian, with a dominant frequency of 1000 Hz.

We want to specifically validate the PML condition for surface waves, for which other classical absorbing conditions are known to behave poorly. Therefore we place the source, which is a vertical force, very close to the surface at a depth of 1.5 m and a horizontal distance of 3 m from the center of the block, in order to generate a large incident Rayleigh wave. A receiver is located on the surface at a horizontal distance of 10.5 m from the center of the block, and records the two components of displacement. On the two vertical edges of the finite-size medium, PML absorbing conditions are imposed in order to mimic a half-space. We do not use the PML at the bottom of the mesh for simplicity because we stop the simulation before waves can come back to the receiver.

We choose to compute synthetic seismograms based upon the spectral-element method because it has proven to be very precise in the context of elastic wave propagation, with very little numerical dispersion and anisotropy, and also because the free surface boundary condition is automatically taken into account, which means that surface waves are very accurately modeled (Komatitsch & Tromp 1999, 2002a), as illustrated in previous chapters.

The model is discretized using 60×60 spectral elements, and we use a polynomial degree $N = 5$ in each element, which means that the entire model contains a total of $(60N + 1)^2 = 90,601$ Gauss-Lobatto-Legendre grid points (for details on the spectral-element method, the reader is referred to the previous chapters). The PML region consists of two layers of spectral elements, and therefore contains $2N + 1 = 11$ Gauss-Lobatto-Legendre grid points in the damping direction. At the bottom of the PML, i.e., on the edge of the grid, we impose Dirichlet boundary conditions (zero displacement). The time step is 10 μs and the total duration of the simulation is 25 ms. In the PML, we use the empirical damping profile

$$d(x) = \frac{3\alpha}{2\delta} \log\left(\frac{1}{R}\right) \left(\frac{x}{\delta}\right)^2, \tag{6.24}$$

which is used by many authors, e.g., Collino & Tsogka (2001), where δ is the width of the PML layer, x is the horizontal coordinate with the origin chosen at the top of the PML layer, and R is the theoretical reflection coefficient after discretization, which can be chosen very small (typically 10^{-3}, which is the value used in this chapter).

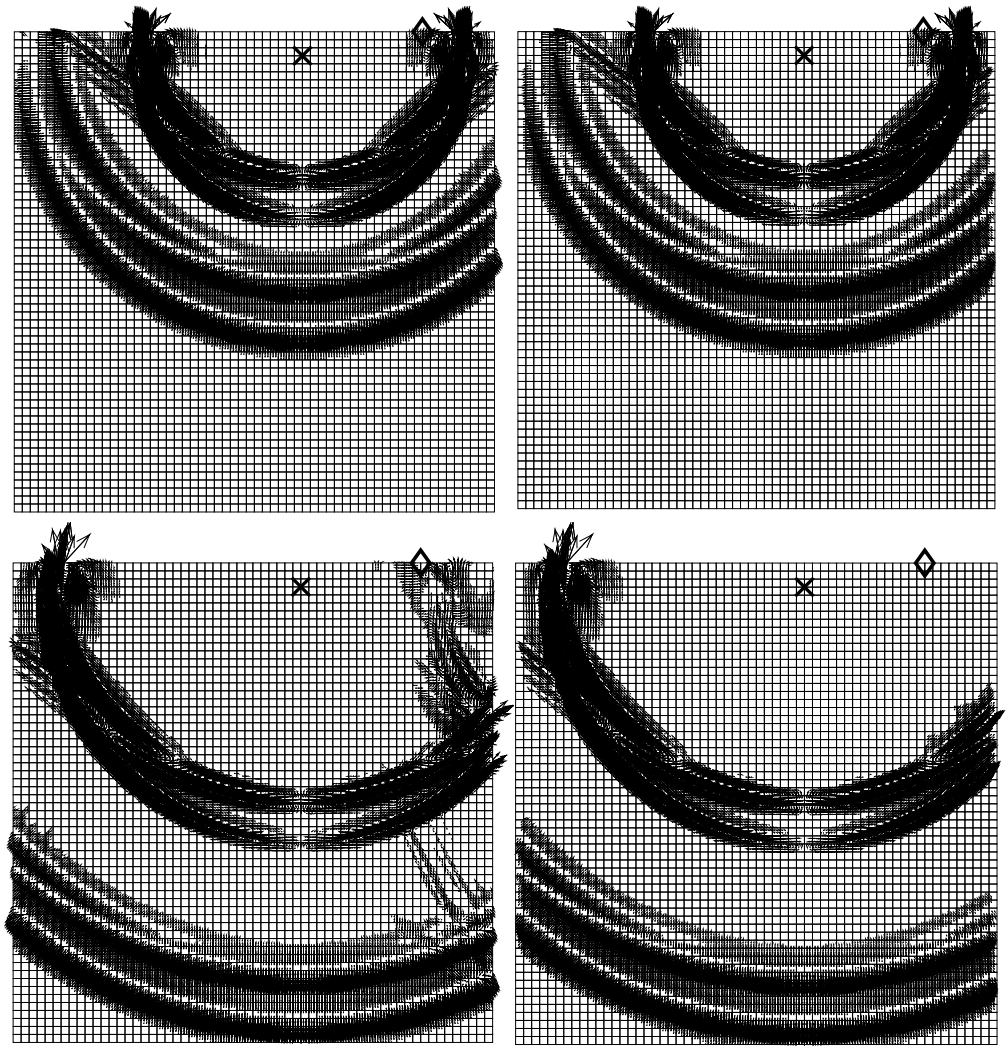

Figure 6.2 *Snapshots of a spectral-element simulation for surface waves at time $t = 10$ ms (top) and $t = 15$ ms (bottom), using the 'A1' paraxial treatment of Clayton & Engquist (1977) (left) and the PML (right). The small arrows represent the displacement vector. The grid cells represent the spectral elements. Each element contains $(N + 1)^2 = 36$ Gauss-Lobatto-Legendre grid points. The cross indicates the position of the vertical force and the diamond indicates the receiver. The display has been truncated below 1% of the maximum amplitude of the wave field, with the same graphical normalization factor used for both tests. One can clearly see that the PML condition is more efficient, in particular for the Rayleigh wave, as well as for body waves with non-normal incidence (bottom).*

In Figure 6.2, we compare snapshots obtained using the PML condition and the so-called 'A1' paraxial condition of Clayton & Engquist (1977). The large Rayleigh wave can easily be identified based upon its elliptical polarization. The

PML is clearly superior in terms of absorbing both body and surface waves, in particular in regions of the mesh where the waves are not incident close to the normal to the boundary. The efficiency of the paraxial condition for body waves is not satisfactory when the angle of incidence differs from 90 degrees, as can be seen in particular in the bottom part of the last snapshot; it also behaves poorly for surface waves, as expected from the fact that the polarization of the Rayleigh wave is elliptical, and a significant part of the incident energy is reflected back into the model. More sophisticated paraxial conditions could have been used as a reference, e.g., Higdon (1991) or Quarteroni et al. (1998), but Collino & Tsogka (2001) demonstrated than Higdon (1991) is far less efficient than the classical first-order PML.

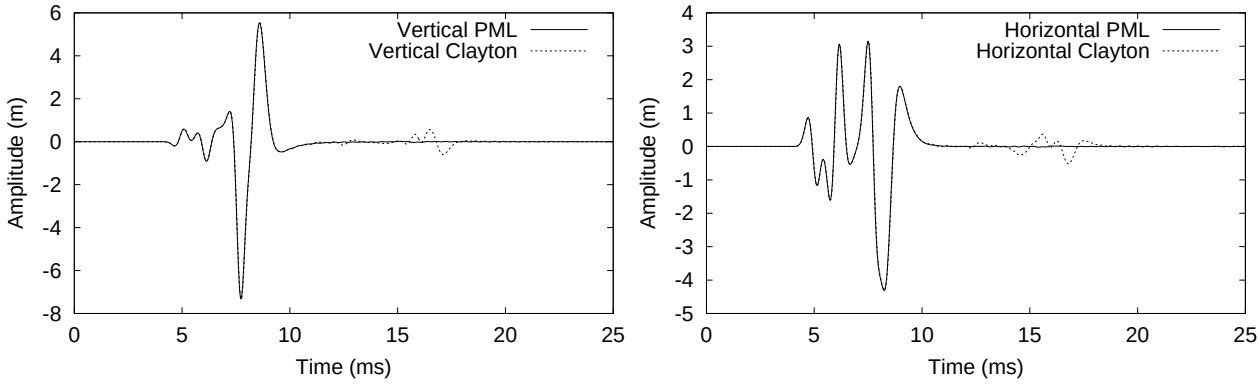

Figure 6.3 *Vertical (left) and horizontal (right) components of displacement recorded on the surface at the receiver denoted by the diamond in Figure 6.2, using the PML (solid line) and the 'A1' paraxial condition of Clayton & Engquist (1977) (dashed line). In the case of the PML, there is almost no spurious wave reflected off the boundary, while in the case of the paraxial treatment, a large signal is recorded.*

Figure 6.3 shows the seismogram recorded at the receiver at the surface. Because it is located on the surface, it mostly records a large-amplitude Rayleigh wave, in addition to the smaller direct body waves. In the case of the simulation with the Clayton & Engquist (1977) boundary condition, a large spurious signal is reflected off the boundary, while in the case of the PML, this unwanted reflection is almost completely suppressed. This again illustrates the efficiency of the PML absorbing condition.

To conclude, let us underline the fact that we did not change the basic idea behind the PML, but simply reformulated the classical first-order condition. Therefore, we expect to find the same properties as in the classical PML, i.e., use of the formulation for three-dimensional problems is straightforward (e.g., Bérenger 1996; Chew & Liu 1996), and the case of the corners of the model can be handled by combining different PMLs written along different grid axes (e.g., Bérenger 1994; Collino & Tsogka 2001).

However, we also find the same limitations as with the classical first-order PML. First, at grazing incidence the behavior of the discrete PML is poor, and the associated numerical reflection coefficient is high (Collino & Monk 1998a; Winton & Rappaport 2000). Following the work of these authors, one can numerically optimize the damping profile of Equation (6.24) in order to optimize the behavior at grazing incidence. Second, as noted by Bécache et al. (2003), for some anisotropic media intrinsic instabilities appear, even though it could seem from Equations (6.2) and (6.13) that any anisotropic elastic tensor could be used.

Chapitre 7

Approximation de surfaces géophysiques avec fortes variations

Résumé

Dans ce dernier chapitre, nous étudions l'approximation de surfaces présentant de fortes variations, et son application à la description de surfaces géophysiques. L'étude de certains problèmes géophysiques implique la description correcte de surfaces contenant de fortes variations locales. Ce problème est important dans de nombreux domaines de la géophysique, par exemple pour la description précise de la topographie lors de l'étude des effets de site liés à la propagation des ondes sismiques, ou l'écoulement de la lave ou des coulées pyroclastiques le long des pentes d'un volcan, ou pour la caractérisation de structures géologiques complexes contenant des failles. Cependant, l'ajustement de jeux de données présentant de fortes variations à l'aide de fonctions classiques telles que les splines est un problème difficile. Sans information sur la localisation des fortes variations dans le jeu de données, les méthodes d'approximation classiques produisent des instabilités ou des oscillations indésirables. Nous proposons une nouvelle méthode faisant appel à des changements d'échelle, et dont l'originalité consiste en l'utilisation d'un prétraitement et d'un post-traitement des données. Les variations de la fonction inconnue sont réduites en utilisant une transformation d'échelle dans la phase de prétraitement. Les données transformées ne présentant pas de fortes variations, nous pouvons utiliser un approximant classique qui ne crée pas d'oscillations significatives. Une transformation d'échelle inverse est ensuite appliquée. Nous discutons la convergence de la méthode quand le nombre de points de données tend vers l'infini. Nous montrons l'efficacité de cette technique en l'appliquant à un Modèle Numérique de Terrain du volcan du Piton de la Fournaise (île de la Réunion, France).

Abstract

In this final chapter, we study surface fitting of rapidly varying data, and its application to the approximation of geophysical surfaces. Addressing geophysical problems often implies the correct description of surfaces with large local variations. This problem is of interest in many areas of geophysics, for instance for the precise description of topography when studying site effects in seismic wave propagation, or the propagation of lava or pyroclastic flows along the slopes of a volcano, or in the presence of geological structures with faults. However, surface fitting of rapidly varying data using classical functions like splines is known to be difficult. Without information about the location of the large variations in the dataset, usual approximation methods lead to instabilities or undesirable oscillations. We propose a new approach that uses scale transformations, and whose originality consists in a pre-processing and a post-processing of the data. Variations of the unknown function are reduced using a scale transformation in the pre-processing phase. The transformed data do not exhibit large variations, and we can therefore use a usual approximant that does not create significant oscillations. An inverse scale transformation is subsequently applied. We discuss the convergence of the method when the number of data points tends to infinity. We demonstrate the efficiency of this technique by applying it to a Digital Elevation Model of the Piton de la Fournaise volcano (Réunion Island, France).

7.1 Introduction

In many problems of geophysical interest, when trying to describe surfaces, one has to deal with data that exhibit rapid local variations. This occurs for instance when describing the topography of mountain ranges, volcanoes, islands, or

the shape of geological entities, that can exhibit large and rapid variations due to the presence of faults in the structure. The correct description of such geological surfaces, by a fitting process from a given set of points, is therefore of great importance (Mallet 1992). This is particularly true when one needs to describe topographic models with good regularity, usually C^0 or C^1, from the knowledge of a given low or medium-resolution set of surface points, often called a digital elevation model (DEM). This is typically the case for instance when studying site effects and ground motion amplification related to topography in seismic wave propagation problems and earthquake hazard assessment (Frankel & Leith 1992; Bouchon et al. 1996; Komatitsch & Vilotte 1998; Komatitsch et al. 1999), or when studying the propagation of pyroclastic flows or lava flows along the slopes of a volcano (Ishihara et al. 1990).

Unfortunately, when applied to the approximation of surfaces from rapidly varying data, usual methods like splines lead to strong oscillations near steep gradients, as illustrated in Figure 7.1. When the location of the large variations in the dataset is known, Salkauskas (1974) and Foley (1987) have proposed methods that use a spline under tension with a non-constant smoothing parameter, and Hsieh & Chang (1994) have proposed a concept of virtual nodes inserted at the level of the large variations in the case of an approximant in the context of computer-aided geometric design. In the more general context when the location of the large variations in the dataset is not known a priori, Franke (1985) and Bouhamidi (1992) have proposed splines under tension belonging to more general spaces. These methods give good results in the case of curve fitting, but less accurate results in the case of surface fitting. Other approaches such as the Discrete Smooth Interpolation have also been used successfully to address the problem (Mallet 1992, 1997).

The new method we introduce here uses scale transformations, and is applied without any particular a priori knowledge of the data. The philosophy of the method is similar to interpolation methods based upon anamorphosed data commonly used in geostatistics (see for instance Issaks & Srivastava (1989)). In the first part of this chapter, a construction of the scale transformation families is presented. Results concerning the convergence of the approximation are given without proof. In the second part, we show the efficiency of this innovative approach by applying it to the topography of the summit of the Piton de la Fournaise volcano, located in the Réunion Island (Indian Ocean, France). This volcano exhibits large and rapid variations in steep river valleys in its south-western part, as well as in a caldera, where the behavior of the method is tested.

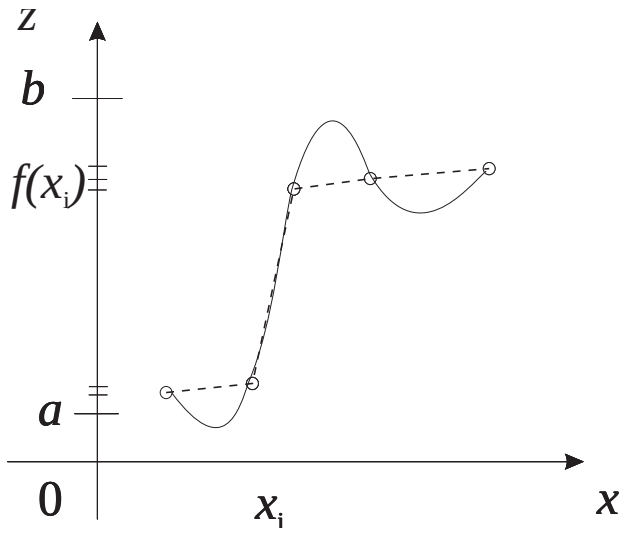

Figure 7.1 *When classical splines (for instance here a C^1 spline, solid line) are used to interpolate data points $(x_i, f(x_i))$ with large local variations (dashed line), strong spurious oscillations are generated near steep gradients.*

7.2 Description of the method

The method we propose uses two scale transformations, namely φ_d for the pre-processing and ψ_d for the post-processing. The first one, φ_d, is used to transform the z-values representing the height of the unknown surface f into values (u_i), regularly distributed in an interval chosen by the user, as illustrated in Figs. 7.2A and 7.2B. The preprocessing function φ_d is such that the transformed data do not exhibit large local variations, and therefore a usual spline operator T^d can subsequently be applied without generating significant oscillations, as shown in Figure 7.2C. The second scale transformation ψ_d is then applied to the approximated values to map them back and obtain the approximated values of z (Figure 7.2D). It is important to underline that the proposed scale transformations do not create spurious oscillations. Moreover, this method is applied without any particular knowledge of the location of the large variations in the dataset.

Let us consider a dataset $\left(x_i^d, z_i^d\right)_{i=1,..,N(d)}^d$ indexed with a real d, such that when d tends to 0, the number of data points $N(d)$ tends to infinity. For the purpose of a theoretical study of the convergence of the approximation, we introduce a

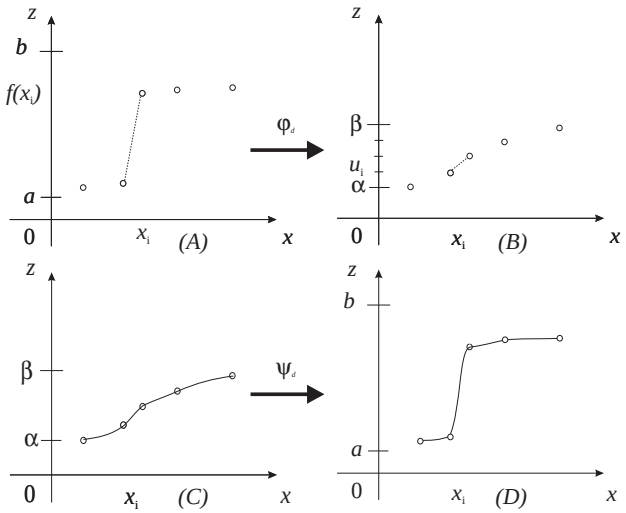

Figure 7.2 *The pre-processing phase (A and B) consists in transforming the values $f(x_i)$ using a scale transformation φ_d. After pre-processing (B), the local variations in the data have been drastically reduced. Therefore, it is possible to obtain a regular approximant with no significant oscillations using an usual C^1 spline operator, as shown in (C). A second scale transformation ψ_d is subsequently applied to the values of the approximant in a post-processing phase (D) to map them back and obtain the final approximant. It is important to mention that the scale transformations used do not create spurious oscillations, as illustrated in (D).*

function $f : \Omega \longrightarrow [a, b]$, such that the dataset becomes $\left(x_i^d, z_i^d = f(x_i^d)\right)_{i=1,..,N(d)}^d$. The functions introduced above have the following expression, for $m \in \mathbb{N}$:

- $\varphi_d : [a, b] \longrightarrow [\alpha, \beta] \subset \mathbb{R}$,

- $T^d : (\varphi_d \circ f) \in H^m(\Omega, [\alpha, \beta]) \rightarrow T^d(\varphi_d \circ f) \in H^m(\Omega, [\alpha, \beta])$,

- $\psi_d \circ \left(T^d(\varphi_d \circ f)\right) \in H^m(\Omega, [a, b])$,

where the pre-processing φ_d and the post-processing ψ_d are continuous scale transformations families, where T^d is an approximation operator, for instance a spline, and where $H^m(\Omega, .)$ denotes the usual Sobolev space. More precisely, we introduce a bounded non empty connected set Ω with a Lipschitz-continuous boundary of $\mathbb{R}^2$, and an unknown function $f \in H^{m'}(\Omega, [a, b])$ that we want to approximate, this hypothesis allowing to have $(\varphi_d \circ f)$ bounded in $C^m\left(\overline{\Omega}\right)$ (with $m' > m + 1$), a property that is used to establish the convergence of the approximation (Gout 1999). We also consider a subset A^d of $N = N(d)$ distinct points of $\overline{\Omega}$ such that

$$\sup_{x \in \overline{\Omega}} \delta\left(x, A^d\right) = d, \tag{7.1}$$

where δ is the Euclidean distance of $\mathbb{R}^2$; the index d represents the radius of the biggest sphere included in Ω that does not intersect with any point of A^d, and thus, when d tends to 0, the number of data points tends to infinity. We also introduce the set Z_1^d of $N = N(d)$ real numbers such that

$$\forall x_i^d \in A^d, f(x_i^d) \in Z_1^d, \tag{7.2}$$

and the sequence Z_2^d of $p(d)$ distinct z-values obtained from the ordering of Z_1^d, $\forall \tilde{z}_i^d \in Z_2^d, i = 1, ..., p(d)$,

$$a = \tilde{z}_1^d < \tilde{z}_2^d < \tilde{z}_3^d < ... < \tilde{z}_{p(d)-1}^d < \tilde{z}_{p(d)}^d = b, \tag{7.3}$$

where $[a, b] = \mathrm{Im}(f)$. The sequence Z_2^d will be used for the construction of the scale transformation families in the following section. In what follows, for convenience, we also write (z_i) instead of $\left(\tilde{z}_i^d\right)$.

7.2.1 Scale transformation families

In this section, we give a construction of the scale transformation families by generalizing the technique introduced by Apprato (1987) and Torrens (1991). These scale transformations are realistic in the sense that, as classical transformations, they are monotonous.

Pre-processing of the data: family (φ_d) of scale transformations

The goal of the scale transformation φ_d is to reduce the variations in the dataset. We first construct φ_d and, in order to study the convergence of the approximation, we then establish the convergence of φ_d to a function φ when the number

of data points tends to infinity (i.e. $d \to 0$). Let $[\alpha, \beta]$ be an interval of $\mathbb{R}$, and $\{u_i\}_{i=1,...,p(d)}$, the following regular subdivision, for $i = 1, ..., p(d)$,

$$\alpha = u_1 < u_2 < u_3 < ... < u_{p(d)-1} < u_{p(d)} = \beta \text{ and } u_{i+1} - u_i = \frac{\beta - \alpha}{p(d) - 1}. \tag{7.4}$$

These interval and subdivision are chosen by the user. When dealing with surface approximation from rapidly varying data, we choose the interval to be $[0, 1]$, and an even subdivision of the $\{u_i\}$ that is used to reduce the local variations of the (z_i). After applying φ_d, we obtain a new dataset (x_i, u_i) related to the initial data by $u_i = \varphi_d(z_i)$. When this technique is applied to other problems however, for instance in some applications in imaging, when one has an image with homogeneous gray levels, it can on the contrary be of interest to increase the variations between pixels values –the (z_i)–; in such a case, Gout (1997) showed that it is possible to choose a non-regular distribution in the interval $[\alpha, \beta]$ to generate variations, and therefore to enhance some features present in the image to facilitate its segmentation.

We introduce $\varphi : [a, b] \to [\alpha, \beta]$ the C^∞-diffeomorphism that transforms $[a, b]$ into $[\alpha, \beta]$ (such families of transformations are usually called anamorphosis in the geostatistics literature):

$$\varphi(z) = \frac{\beta - \alpha}{b - a}(z - a) + \alpha \tag{7.5}$$

We also introduce the function φ_d, for $i = 1, ..., p(d) - 1$, and for any $z \in [z_i, z_{i+1}]$,

$$\begin{aligned} \varphi_d(z) &= u_i q^0_{0m}\left(\frac{z - z_i}{z_{i+1} - z_i}\right) + u_{i+1} q^1_{0m}\left(\frac{z - z_i}{z_{i+1} - z_i}\right) + \alpha_1(z_i)(z_{i+1} - z_i) q^0_{1m}\left(\frac{z - z_i}{z_{i+1} - z_i}\right) \\ &+ \alpha_1(z_{i+1})(z_{i+1} - z_i) q^1_{1m}\left(\frac{z - z_i}{z_{i+1} - z_i}\right) \end{aligned} \tag{7.6}$$

where the q^i_{lm}, for $i = (0, 1)$, and $l = (0, 1)$ are the basis functions of the finite element of class C^m on $[0, 1]$ (Ciarlet 1978) and where, for any $i = 1, ..., p(d) - 1$,

$$\alpha_1(z_i) = \frac{u_{i+1} - u_i}{z_{i+1} - z_i} \text{ and } \alpha_1\left(z_{p(d)}\right) = \alpha_1\left(z_{p(d)-1}\right). \tag{7.7}$$

Using relations (7.3) to (7.6), we obtain the following results: φ_d implements the interpolation of the (u_i), and φ_d belongs to $C^m[a, b]$:

$$\begin{array}{lll} i) & \varphi_d(z_i) = u_i, & \text{for } i = 1, ..., p(d); \\ ii) & \varphi_d \in C^m[a, b]. & \end{array}$$

We now consider a *sufficient* convergence hypothesis, that implies that the distribution of the data (z_i) has an asymptotic regularity in the interval $[a, b]$ when d tends to 0, and which is used to establish the convergence of the approximation. This hypothesis is that there exists $C > 0$ and $m'' \in \mathbb{N}$ verifying $m'' \geq m \geq 2$ such that, for d small enough, and for any $i = 1, ..., p(d) - 2$, we have

$$\left|1 - \frac{z_{i+1} - z_i}{z_{i+2} - z_{i+1}}\right| \leq C\left(\frac{b - a}{p(d) - 1}\right)^{m''}. \tag{7.8}$$

We also suppose that the set A^d introduced above satisfies that there exists $C' > 0$ such that

$$p(d) \leq \frac{C'}{d^2}. \tag{7.9}$$

Equation (7.9), introduced by Arcangéli (1986), expresses a property of asymptotic regularity of the distribution of the dataset A^d in $\overline{\Omega}$. Using a compactness argument, Gout (1998) established that hypotheses (7.8) and (7.9) imply that there exists $C'' > 0$, such that $\|\varphi_d\|_{C^m[a,b]} \leq C''$ and

$$\lim_{d \to 0} \varphi_d = \varphi \text{ in } C^0([a, b]) \tag{7.10}$$

where φ_d is defined by Equation (7.6), and φ is defined by Equation (7.5).

One can notice that the construction of the scale transformations φ_d made in (7.6) uses a finite difference scheme of order 1 to construct, from the u_i, the first derivatives of φ_d at the points $\tilde{z}_i, i = 1, .., p(d)$. Moreover, the option retained in (7.6), which is to cancel the $l-$derivatives of φ_d at the points $\tilde{z}_i$ for any $l = 2, .., m$, could be substituted by the option consisting in using a finite difference scheme of order l to define these $l-$derivatives. Let us also mention that we have chosen to construct the scale transformations on a finite element basis in order to be able to study the convergence of the approximation.

Post-processing of the data: family (ψ_d) of scale transformations

Similar to the way we constructed the scale transformations φ_d, we now define a scale transformation family ψ_d that implements the post-processing of the calculation. We recall that after the pre-processing, the large local variations in the dataset have been drastically reduced, therefore it is possible to approximate the data using a usual spline operator T^d without generating significant oscillations. To map these values back and obtain the approximated values of z, we need to use a post-processing step, and therefore need to introduce a family (ψ_d), which is almost the inverse of (φ_d): as φ_d converges to φ, we construct ψ_d such that ψ_d converges to φ^{-1}. To do so, we define the C^∞-diffeomorphism $\varphi^{-1} : [\alpha, \beta] \longrightarrow [a, b]$ inverse of φ defined in Equation (7.5):

$$\varphi^{-1}(u) = \frac{(u-\alpha)(b-a)}{\beta-\alpha} + a \tag{7.11}$$

We also define ψ_d the function, for $i = 1, ..., p(d) - 1$, and for any $u \in [u_i, u_{i+1}]$,

$$\begin{aligned}\psi_d(u) \quad = \quad & z_i q^0_{0m}\left(\frac{u-u_i}{u_{i+1}-u_i}\right) + z_{i+1} q^1_{0m}\left(\frac{u-u_i}{u_{i+1}-u_i}\right) + (u_{i+1}-u_i)\,\beta_1(u_i)\, q^0_{1m}\left(\frac{u-u_i}{u_{i+1}-u_i}\right) \\ & + (u_{i+1}-u_i)\,\beta_1(u_{i+1})\, q^1_{1m}\left(\frac{u-u_i}{u_{i+1}-u_i}\right),\end{aligned} \tag{7.12}$$

where the q^i_{lm}, for $i = (0, 1)$, and $l = (0, 1)$ are the basis functions of the finite element of class C^m on $[0, 1]$ and where

$$\beta_1(u_i) = \frac{z_{i+1}-z_i}{u_{i+1}-u_i} \text{ and } \beta_1\left(u_{p(d)}\right) = \beta_1\left(u_{p(d)-1}\right). \tag{7.13}$$

Under hypotheses (7.8) and (7.9), Gout (1998) established the following relations

$$\begin{array}{ll} i) & \psi_d(u_i) = z_i, \qquad i = 1, ..., p(d); \\ ii) & \psi_d \in C^m[\alpha, \beta]; \\ iii) & \text{there exists } C > 0, \text{ such that } \|\psi_d\|_{C^m[\alpha,\beta]} \leq C; \\ iv) & \lim\limits_{d\to 0} \psi_d = \varphi^{-1} \text{ in } C^0([\alpha, \beta]). \end{array}$$

It is important to mention that (*i*) is one of the key points of the algorithm, that (*ii*) allows us to obtain approximants with high regularity, and that (*iii*) and (*iv*) are used to establish the convergence of the approximation.

7.2.2 The smoothing spline operator

Given a Lagrange dataset $(x_i, (\varphi_d \circ f)(x_i) = \varphi_d(z_i))$, we have to solve the classical problem of constructing an approximant T^d of class C^k (with $k = 1$ or 2 in practice). In this work, we use a smoothing D^m-spline, as defined in Arcangéli (1986) and Arcangéli (1989), which has many advantages: it is possible to implement a local refinement, the matrix of the linear system is banded, and it is possible to study the convergence of the approximation. We have chosen to use a smoothing D^m-spline and not an interpolation spline because we want to be able to work with large datasets of up to several hundreds of thousands of points, and in that case, a smoothing spline is far less expensive than an interpolation spline.

We consider the functional, for any $\Phi \in H^m(\Omega)$,

$$J^d_\varepsilon(\Phi) = \left\langle \rho^d(\Phi - \varphi_d \circ f)\right\rangle^2_d + \varepsilon\,|\Phi|^2_{m,\Omega} \tag{7.14}$$

where $\rho^d \in L\left(H^m(\Omega), \mathbb{R}^{p(d)}\right)$ is defined by $\rho^d f = (f(a))_{a\in A^d} \in \mathbb{R}^{p(d)}$, $|.|_{m,\Omega}$ is the usual semi-norm of $H^m(\Omega)$, $\langle . \rangle_d$ is the usual norm in $\mathbb{R}^{p(d)}$, and ε is a smoothing parameter. We call σ^d_ε the D^m-smoothing spline on Ω relative to $\rho^d(\varphi_d \circ f)$, which is the unique solution of the minimization problem: for any $\Phi \in H^m(\Omega)$, find $\sigma^d_\varepsilon \in H^m(\Omega)$ such that

$$J^d_\varepsilon(\sigma^d_\varepsilon) \leq J^d_\varepsilon(\Phi). \tag{7.15}$$

The solution σ^d_ε to this problem is also the unique solution of the variational problem: for any $\Phi \in H^m(\Omega)$, find $\sigma^d_\varepsilon \in H^m(\Omega)$ such that

$$\left\langle \rho^d\sigma^d_\varepsilon, \rho^d\Phi\right\rangle_d + \varepsilon\left(\sigma^d_\varepsilon, \Phi\right)_{m,\Omega} = \left\langle \rho^d(\varphi_d \circ f), \rho^d\Phi\right\rangle_d. \tag{7.16}$$

Uniqueness of the solution can be proved using the Lax-Milgram lemma and results by Necas (1967) to establish the equivalence of norms.

In order to compute σ_ε^d, we choose to discretize it on a finite element basis which enables us to obtain a small sparse linear system. We choose the generic Bogner-Fox-Schmit (BFS) rectangular finite element (Ciarlet 1978). In what follows, we use either the BFS of class C^0 or of class C^1 in order to obtain a C^0 or C^1 approximant. In the following, we write σ_ε^d instead of T^d.

7.2.3 Convergence of the approximation

We first give the convergence of the D^m-spline operator σ_ε^d related to the transformed data $(\varphi_d \circ f)$ to the function $\varphi \circ f$ when d tends to 0. We obtain this result using the convergence of φ_d to φ, using the fact that Arcangéli (1989) showed that, for any function g, we have $\lim_{d\to 0} \sigma_\varepsilon^d(g) = g$. Keeping the notation of the previous sections, and since $(\varphi_d \circ f)$ is bounded in $C^m(\overline{\Omega})$, Gout (1998) proved that

$$\lim_{d\to 0} \left(\sigma_\varepsilon^d(\varphi_d \circ f)\right) = \varphi \circ f \ \text{ in } C^0(\overline{\Omega}). \tag{7.17}$$

From this result, using a compactness argument, Gout (1999) established a theoretical result concerning the convergence of the approximation:

$$\lim_{d\to 0} \left\{\psi_d \circ \sigma_\varepsilon^d(\varphi_d \circ f)\right) = \varphi^{-1} \circ \varphi \circ f = f \text{ in } H^{m-\theta}(\Omega), \tag{7.18}$$

for any $\theta > 0$ such that $\theta < m - 1$ $\left(\Rightarrow H^{m-\theta}(\Omega) \hookrightarrow C^0(\overline{\Omega})\right)$. Note that if we take $n = 2$ and $m = 3$, the convergence takes place in $\mathrm{H}^{2-\theta}$ for any $\theta \in]0, 1[$.

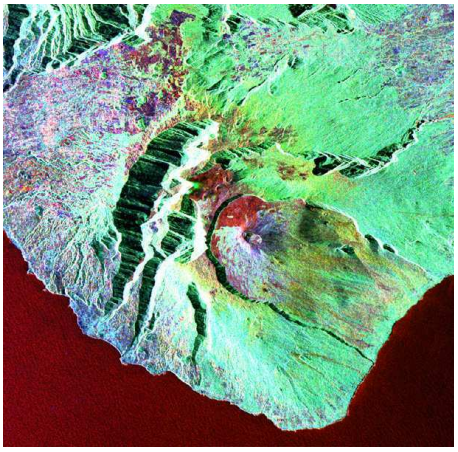

Figure 7.3 *Image of the Piton de la Fournaise volcano in the Réunion Island, Indian Ocean, France. One can clearly see the summital caldera, and the two steep valleys in the South-West. The size of the region represented is approximately* 40×35 *km. The height of the volcano is 2.6 km. Image taken as part of the Space Shuttle SIR-C/X-SAR radar missions, courtesy of Pete Mouginis-Mark, University of Hawaii.*

7.3 Application to a volcano

The Piton de la Fournaise is a volcano located in the Indian Ocean, in the Réunion Island, France. This volcano exhibits strong topographic variations near its summit, due to the presence of a caldera and of two steep river valleys in its south-western part, as can be seen on the picture of the volcano presented in Figure 7.3. The maximum height of the volcano is 2.6 km, and the depth of the valleys reaches more than 1000 m is several places.

Being able to describe the topography of such regions exhibiting rapid local variations with at least C^0 regularity, or even C^1 regularity, is important in many fields in geophysics. For example, this description of the topography can be an input to numerical modeling codes that study the propagation of pyroclastic flows or lava flows, and related hazard; other examples are seismic site effects and ground motion amplification due to topographic features. In both cases, to avoid creating numerical artefacts, it is very important not to introduce spurious oscillations in the description of the model itself. Otherwise, Komatitsch & Vilotte (1998) and Komatitsch et al. (1999) underlined in the context of curvilinear spectral-element modeling of elastic wave propagation that artificial diffraction points appear at the edges between elements, which significantly affects the behavior of surface waves.

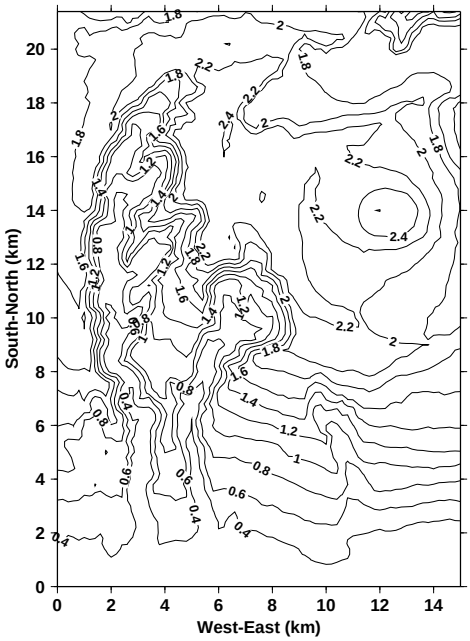

Figure 7.4 *Isocontours of the Digital Elevation Model (DEM) of the Piton de la Fournaise volcano. The DEM is given on a grid of* 76×108 *points, with a uniform grid spacing of 200 m. The isocontours represent the height of the topography every 0.2 km. The height of the summit is 2.6 km. One can clearly observe the slopes of the two steep valleys.*

To demonstrate the efficiency of our method, we create C^0 and C^1 approximants from a set of 8208 data points taken from a Digital Elevation Model (DEM) of the summit. The data points in the DEM have been obtained by digitizing a map of the area. In this DEM, the height is given on an evenly spaced grid of 76×108 points, with a grid spacing of 200 m. Therefore the region considered has a dimension of 15 km in the East-West direction, and 21.4 km in the North-South direction. This DEM is shown in Figure 7.4 using a top view with isocontours representing the height of the topography every 0.2 km.

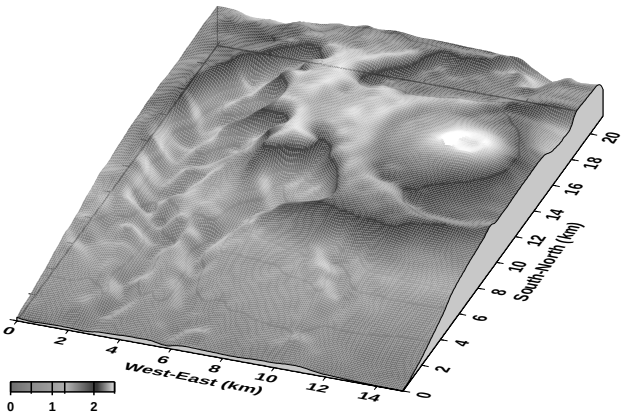

Figure 7.5 *3-D view of the* C^1 *approximant, after post-processing, obtained for the Piton de la Fournaise volcano from the Digital Elevation Model of Figure 7.4. The gray scale represents the height of the topography, from 0 to 2.6 km. The image has been generated with no vertical exaggeration. The approximant has been evaluated on an evenly spaced grid comprising* 200×200 *points. No significant oscillations can be observed, even in the difficult regions of the model, which are mainly the two valleys, and also the caldera. In this example, we have discretized the spline using* 15×20 *Bogner-Fox-Schmit finite elements, each having sixteen degrees of freedom.*

In the pre-processing, we choose a regular distribution of the $\{u_i\}$ in $[\alpha, \beta] = [0, 1]$ in order to reduce the large variations in the dataset. The approximants are subsequently obtained by discretizing the D_m-spline in a finite-element space. In the case of the C^0 approximant, we use 30×40 rectangular C^0-BFS finite elements, each having four degrees of freedom. In the case of the C^1 approximant, we use 15×20 rectangular C^1-BFS finite elements, each having sixteen degrees of freedom. In both cases, the smoothing parameter ε is taken to be 10^{-6}.

In Figure 7.5, we show a 3-D representation of the C^1 approximant after post-processing, evaluated on an evenly spaced grid comprising 200×200 points. The grid spacing in the East-West direction is therefore 107.54 m, and that in the North-South direction is 75.37 m. From the figure it is clear that the results do not exhibit strong oscillations, even though the use of such a dense grid for the evaluation of the approximant is expected to enhance the artefacts generated by the approximation method. To compare this approximant to the original dataset more precisely, in Figure 7.6 we present a top view of the approximated values, with isocontours representing the height every 0.2 km, in addition to the same plot for the original dataset, as in Figure 7.4. It is clear from these plots that the approximant is very close to the original data, with local variations smoothed as expected. One can notice that the approximant does not exhibit significant oscillations even in the difficult regions of the model, particularly the two valleys.

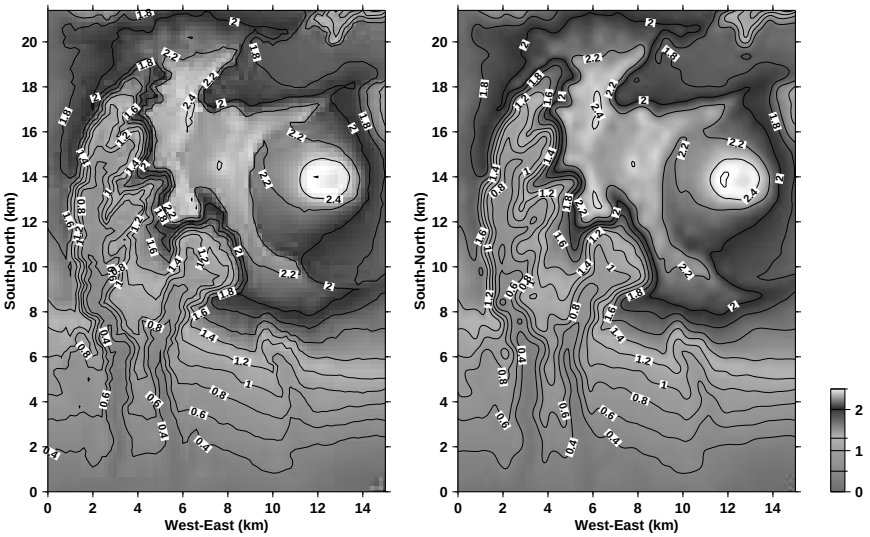

Figure 7.6 *Comparison between isocontours obtained from the original dataset of the Digital Elevation Model (left), as in Figure 7.4, and isocontours of the C^1 approximant after post-processing (right), as in the 3-D view of Figure 7.5. The general agreement is excellent, and it is important to notice that no significant oscillations can be observed, even in the two steep valleys. The isocontours represent the height of the topography every 0.2 km. The gray scale also indicates the height of the topography, from 0 to 2.6 km.*

To demonstrate this more quantitatively, we evaluate the quadratic error for the two approximants

$$\mathrm{Err}(\underset{i}{\cup} z_i) = \left(\sum_{i=1}^{8208} \left(\tilde{z}_i - z_i\right)^2 \Big/ \sum_{i=1}^{8208} z_i^2 \right)^{1/2} \tag{7.19}$$

where z_i represents the z-data value, and where $\tilde{z}_i$ is the z-approximant value for the same $(x_i, y_i) \in \Omega$. In the case of the C^0 approximant, we find that the error is 4.96 10^{-4}; in the case of the C^1 approximant it is 4.01 10^{-4}. Such values are considered very good in the context of surface approximation, and show the efficiency of the proposed approach for this case with rapidly varying data. In the entire dataset, the maximum error measured is 5.5 %, corresponding to an absolute error of 56 m. This maximum error occurs in a region located on the edge of the steep valleys, where the local variations are the strongest, as expected. More detailed studies of the approximation error, and evidence that the rate of convergence is higher in this method than in usual approaches with no pre-processing, such as splines under tension or thin plate splines, can be found in Gout (1997).

Sixième partie

Conclusions et perspectives

Chapitre 8

Conclusions et perspectives

Au cours de ce travail, nous avons montré comment la modélisation numérique tridimensionnelle avancée pouvait être utilisée en géophysique, en mettant plus particulièrement l'accent sur les applications dans le domaine de la sismologie. Ci-dessous, dans une première section nous récapitulons les conclusions principales que nous avons tirées de ces études, et dans une deuxième section, nous ouvrons quelques perspectives en termes de projets de recherche futurs.

8.1 Projets de recherche passés et actuels

8.1.1 Propagation des ondes sismiques dans la Terre globale 1-D

Dans le Chapitre 2, nous avons développé et appliqué une méthode d'éléments spectraux (SEM) pour la simulation de la propagation des ondes sismiques à l'échelle globale. La méthode a été validée par comparaison des sismogrammes synthétiques avec une solution quasi-analytique de référence calculée par sommation de modes normaux pour les versions élastiques et anélastiques du modèle de Terre de référence à symétrie sphérique PREM. Un excellent accord a été trouvé. Nous avons prouvé que le SEM peut incorporer avec précision les effets dus à la croûte peu épaisse et lente, à une asthénosphère transversalement isotrope, aux interfaces fluide-solide à la CMB et à l'ICB, à la valeur élevée du coefficient de Poisson dans la graine, et à l'atténuation. Nous avons également montré que le SEM est très bien adapté à l'architecture parallèle des supercalculateurs modernes. Afin de réduire le coût des simulations sur de très gros modèles, nous avons conçu et construit un réseau d'ordinateurs PCs sous Linux (Beowulf) avec 150 processeurs et 75 gigaoctets de mémoire.

8.1.2 Propagation des ondes sismiques dans la Terre globale 3-D

Dans le Chapitre 3, nous avons souligné que, pour un coût de calcul identique, le SEM peut simuler avec précision la propagation des ondes sismiques dans un modèle de Terre global entièrement 3-D. Nous avons étendu la méthode afin d'incorporer les effets du manteau 3-D et de modèles de croûte, des océans, de la gravité et de la rotation. Nous avons en particulier montré comment incorporer des variations transversales de vitesse P, de vitesse S et de densité dans le manteau, ainsi qu'un modèle 3-D de la croûte, et nous avons expliqué comment introduire l'ellipticité, la topographie et la bathymétrie de la Terre. L'effet des océans sur la propagation des ondes à l'échelle globale a été introduit de manière efficace à l'aide d'une intégrale de surface pour un chargement équivalent, qui permet de ne pas avoir à mailler les océans explicitement, ce qui simplifie considérablement la méthode et permet de réduire drastiquement le coût de calcul. Nous avons validé l'implémentation de la gravité et des océans en comparant les résultats du SEM à des sismogrammes synthétiques de référence calculés par sommation de modes normaux dans le modèle 1-D à symétrie sphérique PREM. Contrairement à ce que l'on suppose souvent, nous avons montré que pour certaines configurations de source et de récepteur les effets des océans et de la gravité peuvent être significatifs. Comme première application complètement 3-D, nous avons considéré un tremblement de terre peu profond dans la région de Vanuatu. Nous avons montré que les ondes de Rayleigh sur des trajets trans-Pacifique peuvent arriver plus de 85 s plus tôt que dans PREM, et que les ondes de Love ont une durée beaucoup plus courte que dans PREM.

Nous avons souligné le fait que par certains aspects la méthode SEM est en avance par rapport aux pratiques classiques actuelles en tomographie, du fait que des modèles entièrement anisotropes de la croûte, du manteau, et du noyau solide

peuvent d'ores et déjà être pris en compte. La méthode permet également d'étudier des modèles ayant des variations transversales de structure élastique et anélastique. Cependant, les techniques sismologiques classiques vont demeurer utiles pendant de nombreuses années encore, parce qu'elles fournissent une référence importante à laquelle l'ensemble de la communauté sismologique se réfère. Les anomalies de temps d'arrivée et d'amplitude continueront à être étudiées par rapport à cette référence. De même, les méthodes asymptotiques continueront à jouer un rôle important, parce qu'elles fournissent un moyen peu coûteux pour interroger un modèle 3-D. Le SEM fournit à la communauté sismologique des moyens complémentaires pour calculer des sismogrammes synthétiques très précis qui peuvent être employés pour améliorer les modèles 3-D.

8.1.3 Propagation des ondes sismiques à l'échelle locale et régionale

Dans le Chapitre 4, nous avons étudié la propagation des ondes à une échelle différente, dans le contexte de la sismologie locale et régionale. Nous avons mentionné que le problème est sensiblement différent de la modélisation sismique à l'échelle globale, parce que l'équation d'ondes elle-même est plus simple (les effets liés à la gravité et la rotation sont négligeables aux périodes concernées, et il n'y a aucune région liquide telle que le noyau externe couplée au modèle solide), mais le modèle lui-même est beaucoup plus hétérogène et a une structure beaucoup plus complexe présentant de fortes variations, parce que les évolutions tectoniques locales et régionales produisent habituellement une forme complexe de la surface de contact entre les sédiments et le sous-sol cristallin. Nous avons montré que les mouvements forts du sol dans le bassin de Los Angeles peuvent être modélisés avec précision en utilisant un nouveau modèle de bassin qui est contraint par des centaines de logs de vitesse P dans des puits forés par l'industrie pétrolière, et plus de 20000 kilomètres de profils de sismique réflexion. Les simulations numériques ont été à nouveau menées à bien en utilisant la méthode SEM, qui permet de prendre en compte des variations tridimensionnelles de vitesse des ondes sismique et de densité, la topographie et la bathymétrie, ainsi que l'atténuation.

Nous avons utilisé deux petits tremblements de terre récents et bien enregistrés pour valider le modèle de bassin et la technique numérique, tout en évitant les difficultés liées aux modèles de sources de taille finie et aux modèles de glissement sur la faille dans le cas de tremblements de terre de magnitude plus élevée. Les paramètres de source ont été inversés en calculant numériquement les dérivées de Fréchet (Liu et al. 2004). Puisqu'une inversion de tenseur de moment centroïde (Centroid Moment Tensor - CMT) nécessite de calculer les dérivées par rapport à une dizaine de paramètres, les simulations peuvent être réalisées aisément d'un point de vue du coût de calcul. Les résultats ont montré qu'il est possible de prévoir les mouvements forts du sol à des périodes de 2 secondes ou plus en utilisant un modèle réaliste de la complexité géologique de la région, ce qui améliore notre capacité à évaluer l'aléa sismique. Une carte d'accélération maximale du sol nous a permis de clairement illustrer le fait qu'une forte amplification intrinsèquement 3-D se produit dans le bassin.

8.1.4 Calcul massivement parallèle et vectoriel

Les calculs pour la Terre globale 3-D présentés dans le Chapitre 3 étaient précis jusqu'à une période minimum de 18 secondes, et nécessitaient l'utilisation de 150 processeurs et 50 gigaoctets de mémoire sur un cluster d'ordinateurs PCs sous Linux (Beowulf). Cependant, d'un point de vue théorique et numérique, il n'y a aucune limite supérieure à la gamme de fréquence sismique qui peut être simulée à l'aide de la technique SEM. C'est seulement la taille de notre cluster de PCs actuel qui limite la simulation de la propagation des ondes sismiques à des fréquences inférieures à 1/18 Hertz.

Dans le Chapitre 5, nous nous sommes affranchis de ces limitations en implémentant le SEM sur l'ordinateur le plus gros et le plus rapide du monde (en 2003), le 'Earth Simulator' au Japon. Une optimisation vectorielle et parallèle sophistiquée du code de SEM a été nécessaire pour mener à bien des simulations sur une machine de telle taille, mais le Earth Simulator nous a permis d'atteindre une résolution sans précédent pour la simulation de la propagation des ondes sismiques résultant d'un grand tremblement de terre dans la Terre globale 3- D. Les sismogrammes synthétiques large-bande calculés pour le grand tremblement de terre de Denali en Alaska ($M_w = 7.9$ en novembre 2002) ont montré qu'un modèle de source de taille finie peut être employé pour simuler la directivité des ondes de volume et de surface. De tels synthétiques pourraient ensuite être utilisés dans l'inversion de processus complexes de source pour de grands tremblements de terre. Les résultats ont illustré le fait que, étant donné un modèle détaillé de source du tremblement de terre, des modèles 3-D du manteau et de la croûte de la Terre, une technique numérique précise telle que le SEM, et un ordinateur de grande taille, des formes d'onde sismiques couvrant un intervalle d'amplitude de plusieurs ordres de grandeur et quelques décades en fréquence peuvent être modélisées avec précision.

Dans un proche avenir, l'outil de modélisation de sismogrammes synthétiques présenté dans le présent mémoire permettra aux sismologues d'étudier plus en détail et d'améliorer les modèles de Terre 3-D existants. Puisque les grands tremble-

ments de terre se produisent généralement dans des zones de subduction, où la structure de vitesse sismique est plus complexe en raison de la subduction d'une plaque océanique, cet outil devrait également être pertinent pour modéliser le processus de rupture de ces grands tremblements de terre. Puisque nos sismogrammes synthétiques 3-D fournissent une amélioration significative de l'ajustement aux données par rapport à des sismogrammes synthétiques pour des modèles 1-D, ils pourraient être calculés de manière systématique pour fournir un catalogue de sismogrammes synthétiques 3-D de référence. Les différences entre les données et ces sismogrammes synthétiques de référence pourraient être utilisées comme point de départ pour l'amélioration des modèles 3-D.

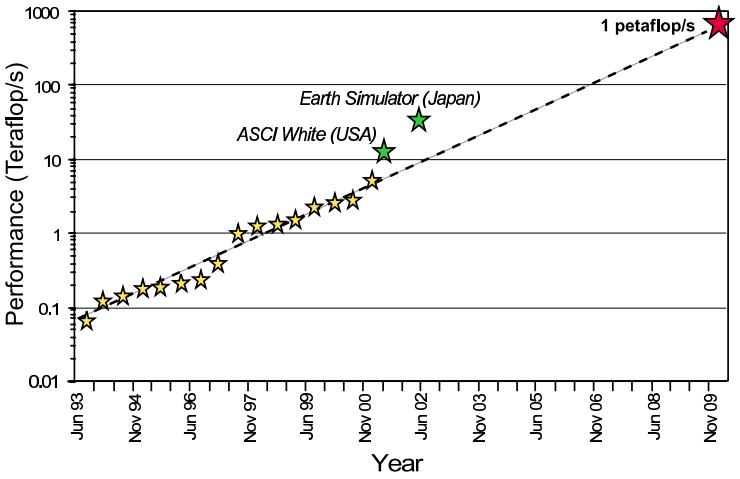

FIG. 8.1 *Extrapolation de 1993 jusqu'à 2010 de la vitesse de l'ordinateur le plus rapide du monde, prise dans la liste Top500 des supercalculateurs (Meuer et al. 2002). La courbe montre que nous pourrions atteindre un ordinateur ayant une vitesse de 1 Petaflop = 1 million de Gigaflops = 10^{15} flops aux environs de l'année 2010. On peut noter que les performances ont augmenté d'un facteur 100 entre 1993 et 2000, et il y a des raisons de penser qu'elles augmenteront d'un autre facteur de 100 ou plus au cours de la décennie actuelle. On notera également que les supercalculateurs actuels ASCI White aux États-Unis et Earth Simulator au Japon sont déjà significativement au-dessus de cette extrapolation linéaire en échelle logarithmique adaptée de Sterling (2000).*

Nous pensons que la méthode SEM est une technique idéale pour la simulation de la propagation des ondes sismiques à l'échelle globale dans des modèles de Terre entièrement 3-D. Jusqu'à présent, aucune autre technique ne s'est montrée capable d'incorporer avec précision toute la complexité liée à ce problème. L'inconvénient principal actuel de la méthode SEM est le coût de calcul relativement élevé des simulations 3-D pour des modèles de grande taille. Cependant, cette limitation technologique est provisoire : des supercalculateurs extrêmement puissants qui révolutionneront le calcul parallèle dans les années à venir sont actuellement en cours de développement. La Figure 8.1, adaptée de Sterling (2000), montre une extrapolation de 1993 à 2010 de la vitesse de l'ordinateur le plus rapide du monde, extraite de la liste Top500 des supercalculateurs (Meuer et al. 2002). La courbe montre que nous pourrions atteindre un ordinateur capable de calculer à une vitesse de 1 petaflop = 1 million de gigaflops = 10^{15} flops aux environs de l'année 2010 (ou même avant). Vu ces développements technologiques, nous sommes convaincus que dans un proche avenir le SEM sera utilisé de manière standard pour effectuer des calculs qui tiendront compte de la complexité 3-D de la Terre. Par exemple, on peut d'ores et déjà imaginer des inversions de tenseurs de moment centroïdes (Centroid Moment Tensor - CMT) dans la Terre 3-D, puisque le nombre d'inconnues à inverser est seulement de l'ordre de dix. Ces inversions de CMT entièrement 3-D devraient permettre de réduire le seuil de magnitude des tremblements de terre dans les catalogues globaux de manière significative, et de mieux contraindre leur localisation, leur durée et leur mécanisme. Dans un avenir plus lointain, nous pensons que la méthode SEM ouvrira la porte à des inversions de forme d'onde complète. Ceci exigera de simuler le problème direct plusieurs dizaines de milliers de fois pour des centaines de tremblements de terre. Sur des machines parallèles ayant une vitesse de l'ordre du petaflop, cela deviendra possible.

8.1.5 Conditions absorbantes parfaitement adaptées pour l'équation des ondes sismiques

Disposer de conditions absorbantes efficaces est un problème important et difficile dans le contexte de la modélisation des ondes sismiques en domaine non borné, par exemple dans le cas de la sismologie locale et régionale, ainsi que dans les expériences de sismique active effectuées dans l'industrie pétrolière. Ce domaine a considérablement évolué au cours des dernières années grâce à l'introduction de la condition absorbante parfaitement adaptée (PML - Perfectly Matched Layer), qui fut initialement développée pour les équations de Maxwell, et plus tard étendue à l'équation des ondes élastiques formulée comme un système du premier ordre en vitesse et contraintes. Malheureusement, une telle formulation du premier ordre n'est pas adaptée aux discrétisations classiques par éléments finis ou éléments spectraux, ces méthodes étant habituellement basées sur l'équation des ondes écrite comme un système du second ordre en déplacement. Dans le Chapitre 6, nous avons formulé une condition PML pour un tel système. Ceci permet d'utiliser cette condition PML dans le contexte de techniques numériques telles que la méthode des éléments finis, la méthode des éléments spectraux, et les méthodes de différences finies du second ordre. L'excellente efficacité de la condition a été démontrée en utilisant un test de validation bidimensionnel contenant des ondes de volume et de surface.

8.1.6 Approximation de surfaces géophysiques avec de fortes variations locales

Étudier certains phénomènes géophysiques implique la description précise de surfaces complexes contenant de fortes variations locales. Dans le Chapitre 7, nous avons présenté une nouvelle méthode d'approximation de données géophysiques présentant de fortes variations locales. Nous avons démontré sa capacité à supprimer, ou tout au moins à réduire de manière significative, les oscillations au voisinage des fortes variations de la surface. Les familles de transformation d'échelle introduites fournissent plus de contrôle sur le comportement de l'approximant, sans aucune connaissance détaillée a priori sur la localisation de ces fortes variations dans le jeu de données. La régularité obtenue, qui peut être C^0, C^1 ou plus, nous a permis de décrire la topographie d'une surface géophysique réelle de manière précise. Nous avons illustré les propriétés de cette méthode en l'appliquant au cas du volcan du Piton de la Fournaise dans l'île de la Réunion (France).

8.2 Projets de recherche futurs

Après avoir détaillé les principaux résultats de recherche obtenus jusqu'à présent, je vais exposer les projets que je suis actuellement en train de développer, ou que je compte développer au cours des prochaines années. L'idée principale est de parier sur le fait que la modélisation numérique 3-D va dans la décennie qui vient constituer un élément clé des progrès en géophysique, comme les améliorations en instrumentation et l'accumulation de données de haute qualité ont constitué un élément clé des progrès dans la décennie passée (et continuera bien entendu dans celle-ci).

8.2.1 Étude des effets de site

La connaissance des effets de site, c'est à dire de la réponse des sols à une excitation sismique, est une observation importante en milieu urbain pour pouvoir anticiper les dégâts sur les constructions et, le cas échéant, prévoir l'organisation des secours. C'est également un élément important de la définition des normes parasismiques. Les effets de site peuvent être déterminés de façon expérimentale, mais cela nécessite l'installation de stations pendant une durée suffisante pour enregistrer quelques dizaines d'événements. Une modélisation numérique permet d'éviter cette expérimentation souvent longue et difficile, à condition d'avoir une connaissance correcte de la structure géologique de la sub-surface dans la zone d'étude.

Des expériences de mesure des effets de site ont été conduites dans différentes villes de France, dans le cadre du développement de l'accélérométrie et de la redéfinition des normes parasismiques. À titre d'exemple, une expérience à Lourdes a révélé des variations d'amplitude d'un ordre de grandeur sur une échelle kilométrique. Une étude détaillée des données a été réalisée par Dubos et al. (2003) à l'Observatoire Midi-Pyrénées de Toulouse. De manière générale, les modélisations 1-D reproduisent très mal ces variations, car elles ne peuvent prendre en compte ni les importants changements latéraux de structure géologique dans la subsurface, ni la topographie. Seule une modélisation 3-D a vraiment un sens dans un tel contexte. Nous nous proposons donc d'utiliser les techniques numériques exposées dans le présent mémoire pour quantifier les effets de la topographie et des variations de structure. On utilisera la connaissance a priori des structures géologiques pour confronter quelques modèles simples avec des données expérimentales pour différents sites. On s'attachera en particulier à caractériser la réponse de structures telles que le fond des vallées, les collines et les zones de remplissage sédimentaire. Ces techniques numériques pourront être utilisées pour caractériser l'ensemble des stations du Réseau d'Accélérométrie Permanent (RAP) français.

8.2.2 Imagerie à haute résolution dans des milieux anisotropes, inversion de forme d'onde

Les mesures de splitting des ondes S sont couramment utilisées pour contraindre l'anisotropie du manteau supérieur. Les méthodes actuellement utilisées pour interpréter ces mesures sont toujours basées sur la théorie des rais. Cependant, nous savons depuis les travaux de Dahlen & Baig (2002) qu'il est important de considérer les noyaux de sensitivité ('sensitivity kernels') dès que nous utilisons des méthodes de rais. En effet, des résultats pouvant sembler peu intuitifs sont associés aux noyaux de sensitivité. Dans un milieu isotrope par exemple, certains noyaux sont nuls sur le rai lui-même et atteignent leur maximum en dehors du trajet géométrique du rai (les fameux noyaux 'banana-donut').

Le travail de Favier & Chevrot (2003) à l'Observatoire Midi Pyrénées a généralisé ce concept aux milieux anisotropes. À l'aide d'une approximation de Born de premier ordre, ils ont introduit une nouvelle observable, appelée 'intensité de splitting', et un calcul analytique des noyaux de sensitivité 2-D et 3-D. Nous avons plus récemment étudié ensemble la contribution des termes de champ proche à ces noyaux de sensitivité (Favier et al. 2004). Une telle étude a été motivée

par le fait qu'il est nécessaire d'inclure l'effet du champ proche dans le calcul de manière à obtenir une expression correcte du splitting des ondes S à faible profondeur. Nous avons appliqué cette théorie de splitting au cas d'un milieu constitué de deux blocs semi-infinis en contact par une interface verticale, chaque bloc ayant des paramètres anisotropes différents. Nous avons montré que, même dans un tel cas simple, des effets complexes et souvent peu intuitifs sont obtenus pour les mesures de splitting en surface. La méthode des éléments spectraux 3-D mentionnée dans le présent mémoire pouvant prendre en compte un tenseur d'anisotropie complet quelconque à 21 paramètres, nous avons pu calculer des sismogrammes synthétiques précis pour ce modèle à deux blocs. Nous souhaitons maintenant généraliser ce type de calcul à des milieux anisotropes plus complexes, par exemple des matériaux ne présentant pas d'axe de symétrie préférentiel.

Un objectif important dans le domaine de la sismologie est l'imagerie d'objets physiques à haute résolution, par exemple de la structure en profondeur d'une faille ou de la structure de l'anisotropie dans une zone de faille transformante. Nous chercherons donc dans le futur à généraliser les méthodes d'inversion basées sur une approximation de Kirchhoff pour les champs d'ondes télésismiques, et les techniques de type fonctions de récepteurs ('receiver functions'), telles que celles utilisées par exemple dans les travaux de Bostock & Rondenay (1999), Bostock et al. (2001) et Bostock (2002). Il est clair qu'il serait très intéressant d'introduire l'effet des noyaux de sensitivité dans les méthodes d'inversion, et à terme de pouvoir inverser des structures anisotropes. La prise en compte de la forme d'onde complète serait une amélioration très significative à cet égard. Une donnée essentielle de ce problème d'inversion sera de disposer d'un bon modèle de départ (Tarantola 1987), et un deuxième paramètre sera le coût du calcul numérique, étant donné la taille des problèmes à résoudre. Il faudra se demander si nous pourrons utiliser des techniques numériques de calcul du champ d'onde complet, telles que la méthode des éléments spectraux décrite dans le présent mémoire. Une alternative pour réduire le coût de calcul, tout au moins dans un premier temps, serait de faire appel à des méthodes plus rapides basées sur des approximations raisonnables, par exemple le calcul de l'amplitude en milieu hétérogène par la théorie des rais en utilisant une méthode d'éléments finis (Farra 1990).

Il est clair également qu'il serait intéressant d'utiliser les outils de calcul 3-D pour valider les méthodes d'inversion et de construction de modèles tomographiques globaux couramment utilisées actuellement. Nous pourrions par exemple prendre les modèles globaux classiquement utilisés de nos jours, et faire un calcul 3-D complet sur ces modèles pour estimer l'accord avec les données utilisées pour les construire. Ceci permettrait de justifier (ou non) les approximations et suppositions effectuées classiquement pour la construction de tels modèles.

8.2.3 Inversion de tenseurs de moment

La majorité des tremblements de terre se produisent dans des zones de subduction, qui comptent parmi les régions les plus hétérogènes du globe. Cependant, la plupart des méthodes de calcul des tenseurs de moment (Centroid-Moment Tensor - CMT) pour les catalogues globaux de tremblements de terre supposent que les ondes sismiques produites par ces événements se propagent dans des modèles de Terre 1-D à symétrie sphérique. Quand des corrections 3-D sont prises en compte, elles sont basées sur l'approximation dite de trajet moyen ('path average'), qui remplace la structure 3-D entre la source et le récepteur par une structure 1-D moyenne équivalente.

Dans le cas des techniques numériques 3-D mentionnées dans les chapitres précédents, il n'est plus nécessaire d'introduire de telles approximations, qui limitent la précision du calcul des CMTs. Il est possible de calculer numériquement les dérivées de Fréchet du CMT par rapport aux 10 paramètres de source (6 composantes du tenseur de moment symétrique, latitude, longitude, profondeur et durée) directement dans le modèle 3-D. Avec nos collègues Qinya Liu et Jeroen Tromp de Caltech, nous avons commencé à étudier de tels algorithmes d'inversion de CMTs dans le cas du bassin de Los Angeles étudié dans le Chapitre 4 (Komatitsch et al. 2004; Liu et al. 2004). La méthode utilisée est basée à la fois sur les ondes de surface et les ondes de volume, et utilise des critères de phase et de misfit d'enveloppe de la forme d'onde. Nous souhaitons dans le futur tester cette technique sur d'autres événements et d'autres régions du globe. Une telle méthode pourrait permettre de relocaliser les catalogues de tremblements de terre existants, et être appliquée de manière systématique aux événements futurs pour la construction de catalogues globaux ou la relocalisation plus précise de tremblements de terre à l'échelle locale ou régionale.

8.2.4 Étude de modèles globaux

Dans le contexte d'une collaboration avec Jeroen Ritsema et Jeroen Tromp (Caltech, USA), j'ai récemment comparé les effets de focalisation par des variations latérales des paramètres élastiques et d'atténuation sur l'amplitude des ondes. La plupart des modèles globaux de variations de vitesse de cisaillement et de compression sont contraints par le temps de trajet des ondes de volume, et les délais de phase des ondes de surface. Cependant, l'amplitude des ondes sismiques doit pouvoir fournir des contraintes supplémentaires importantes. Pour illustrer ce point, nous avons comparé le rapport des

amplitudes SS/S dans les données et dans un calcul dans la Terre 3-D par éléments spectraux. Nous avons montré qu'une part importante du rapport d'amplitude SS/S observé est due à des effets de focalisation élastique et non à l'atténuation (Komatitsch et al. 2002; Ritsema et al. 2002).

L'anélasticité implique également de la dispersion, ce qui signifie que des variations latérales d'atténuation peuvent se traduire par des anomalies de temps d'arrivée qui ne sont pas liées à des variations de vitesse dans le modèle. Inversement, la focalisation et la défocalisation associées aux hétérogénéités de propriétés élastiques créent des anomalies de forme d'onde qui ne sont pas liées à l'atténuation. Les méthodes numériques 3-D telles que la méthode des éléments spectraux pouvant prendre en compte des variations latérales du facteur de qualité en même temps que des variations latérales de vitesse et de densité, il sera intéressant de développer ce genre d'études dans les prochaines années afin d'analyser plus précisément les effets des hétérogénéités élastiques et anélastiques.

De ce point de vue, il serait également important d'étudier les effets de l'anisotropie à l'échelle globale sur les ondes de surface et sur les ondes S. L'influence d'une faible anisotropie sur la vitesse de phase des ondes de surface est bien comprise dans le cadre de la théorie développée par Smith & Dahlen (1973). Mais à nouveau, en tirant parti de la capacité des méthodes numériques 3-D à prendre en compte un tenseur anisotrope complet, nous pourrions étudier en détail le domaine de validité de la théorie asymptotique. L'anisotropie va créer des effets complexes sur la forme d'onde, par exemple des ondes de quasi-Love et quasi-Rayleigh, que la théorie asymptotique n'inclut pas, mais qui seront présents dans les résultats numériques 3-D. L'anisotropie produit également du splitting d'ondes S, de ce fait il serait intéressant de procéder à une étude systématique des effets de l'anisotropie sur les ondes de surface et sur les ondes S. Nous pourrions dans un premier temps considérer des modèles simples, puis à terme utiliser des modèles anisotropes globaux tels que ceux de Montagner (2002) ou Simons et al. (2002).

8.2.5 Optimisation des conditions de frontière absorbantes

Le Chapitre 6 a montré l'intérêt crucial de disposer de conditions de frontière absorbantes efficaces pour pouvoir augmenter la résolution des calculs 3-D. Disposer de telles conditions de frontière absorbantes serait d'un intérêt majeur en sismologie. En effet, cela permettrait d'étudier de manière très précise certaines régions du globe, par exemple à l'échelle d'un continent (futur réseau sismologique haute-résolution 'USArray' aux États-Unis, réseau SKIPPY en Australie) en utilisant un maillage de volume minimal parfaitement adapté à la taille et à la géométrie de la structure. Grâce à de telles conditions absorbantes, nous pourrions augmenter significativement la fréquence maximale des ondes pouvant être simulées, le but étant à terme de pouvoir étudier des ondes de volume dans des structures 3-D hétérogènes jusqu'à des périodes très courtes.

À cet égard, le fort potentiel de la condition absorbante parfaitement adaptée PML ('Perfectly Matched Layer') a été mentionné, et nous avons montré comment nous l'avions adaptée au cas des méthodes numériques d'éléments finis du second ordre et d'éléments spectraux classiques (Komatitsch & Tromp 2003). Cependant, des études sur l'équation de Maxwell ont montré qu'après discrétisation par un schéma numérique, la condition PML n'est plus parfaitement adaptée (le coefficient de réflexion numérique après discrétisation n'est plus exactement zéro), et ce coefficient discret devient élevé lorsque l'incidence des ondes sur le bord PML est rasante (Collino & Monk 1998a). De ce fait, si l'efficacité de la condition PML est excellente pour des ondes incidentes avec des angles proches de la normale au bord absorbant, ce n'est plus le cas pour des modèles 'étroits' (c'est à dire de forme rectangulaire très allongée), pour lesquels les ondes rasantes sont assez fortement réfléchies sur les bords du modèle. Ce problème a été étudié de manière détaillée par Collino & Monk (1998a) et Winton & Rappaport (2000) pour les équations de Maxwell, et des algorithmes d'optimisation pour améliorer l'efficacité de la condition à incidence rasante ont été proposés. Il serait intéressant d'aborder ce même problème dans le cas de la condition PML pour les ondes élastiques. Ceci permettrait d'étudier des modèles 3-D tels que des 'tranches' autour d'une partie du grand cercle dans la Terre, ou bien des récepteurs à offset lointain en sismologie locale, régionale ou pétrolière, avec une grande précision et un faible coût de calcul numérique.

Références

Aagaard, B. T., Hall, J. F., & Heaton, T. H., 2001, Characterization of near-source ground motions with earthquake simulations, *Earthquake Spectra*, **17**(2), 177–207.

Alex, C. M. & Olsen, K. B., 1998, Lens effect in Santa Monica ?, *Geophys. Res. Lett.*, **25**, 3441–3444.

Anderson, J. G., Lee, Y., Zeng, Y., & Day, S. M., 1996, Control of strong motion by the upper 30 meters, *Bull. Seismol. Soc. Am.*, **86**, 1749–1759.

Antolik, M., Larsen, S., Dreger, D., & Romanowicz, B., 1996, Modeling broadband waveforms in central California using finite differences, *Seis. Res. Lett.*, **67**, 30.

Apprato, D., 1987, *Approximation de surfaces paramétrées par éléments finis*, Ph.D. thesis, Université de Pau et des Pays de l'Adour, Pau, France, Thèse d'Etat, 142 p.

Apprato, D., Gout, C., & Komatitsch, D., 2002, A new method for C^k-surface approximation from a set of curves, with application to ship track data in the Marianas trench, *Math. Geol.*, **34**(7), 831–843.

Arcangéli, R., 1986, D^m-splines sur un domaine borné de R, Tech. Rep. 1986/2, UA 1204 CNRS, Université de Pau et des Pays de l'Adour, Pau, France, 47 p.

Arcangéli, R., 1989, Some applications of discrete D^m-splines, in *Mathematical Methods in Computer Aided Geometric Design*, edited by T. Lyche & L. L. Schumaker, pp. 35–44, Academic Press, New York.

Bao, H., Bielak, J., Ghattas, O., Kallivokas, L. F., O'Hallaron, D. R., Shewchuk, J. R., & Xu, J., 1998, Large-scale simulation of elastic wave propagation in heterogeneous media on parallel computers, *Comput. Methods Appl. Mech. Engrg.*, **152**, 85–102.

Bassin, C., Laske, G., & Masters, G., 2000, The current limits of resolution for surface wave tomography in North America, *EOS*, **81**, F897.

Basu, U. & Chopra, A. K., 2003, Perfectly matched layers for time-harmonic elastodynamics of unbounded domains : theory and finite-element implementation, *Comput. Methods Appl. Mech. Engrg.*, **192**, 1337–1375.

Bécache, E., Fauqueux, S., & Joly, P., 2003, Stability of Perfectly Matched Layers, group velocities and anisotropic waves, *J. Comput. Phys.*, **188**(2), 399–433.

Becker, T. W. & Boschi, L., 2002, A comparison of tomographic and geodynamic mantle models, *Geochem. Geophys. Geosyst.*, **3**(1), 1003.

Bérenger, J. P., 1994, A Perfectly Matched Layer for the absorption of electromagnetic waves, *J. Comput. Phys.*, **114**, 185–200.

Bérenger, J. P., 1996, Three-dimensional Perfectly Matched Layer for the absorption of electromagnetic waves, *J. Comput. Phys.*, **127**, 363–379.

Bermúdez, A., Hervella-Nieto, L., & Rodriguez, R., 1999, Finite element computation of three-dimensional elastoacoustic vibrations, *J. Sound Vibr.*, **219**, 279–306.

Bernardi, C., Debit, N., & Maday, Y., 1990, Coupling finite element and spectral methods : first results, *Mathematics of Computation*, **54**, 21–39.

Bernardi, C., Maday, Y., & Patera, A. T., 1994, A new nonconforming approach to domain decomposition : the Mortar element method, in *Nonlinear partial differential equations and their applications*, edited by H. Brezis & J. L. Lions, Séminaires du Collège de France, pp. 13–51, Pitman, Paris.

Bielak, J., Xu, J., & Ghattas, O., 1999, Earthquake ground motion and structural response in alluvial valleys, *J. Geotech. Geoenv. Eng.*, **125**, 413–423.

Boore, D. M., 1972, Finite difference methods for seismic wave propagation in heterogeneous materials, in *Methods in Computational Physics*, vol. 11, Academic Press, New York.

Bostock, M. G., 2002, Kirchhoff-approximate inversion of teleseismic wavefields, *Geophys. J. Int.*, **149**, 787–795.

Bostock, M. G. & Rondenay, S., 1999, Migration of scattered teleseismic body waves, *Geophys. J. Int.*, **137**, 732–746.

Bostock, M. G., Rondenay, S., & Shragge, J., 2001, Multiparameter two-dimensional inversion of scattered teleseismic body waves - 1. Theory for oblique incidence, *J. Geophys. Res.*, **106**, 30771–30782.

Bouchon, M. & Barker, J. S., 1996, Seismic response of a hill : the example of Tarzana, California, *Bull. Seismol. Soc. Am.*, **86**(1A), 66–72.

Bouchon, M., Schultz, C. A., & Töksoz, M. N., 1996, Effect of three-dimensional topography on seismic motion, *J. Geophys. Res.*, **101**, 5835–5846.

Bouhamidi, A., 1992, *Interpolation et approximation par des fonctions splines radiales à plusieurs variables*, Ph.D. thesis, Université de Nantes, Nantes, France, 190 p.

Canuto, C., Hussaini, M. Y., Quarteroni, A., & Zang, T. A., 1988, *Spectral methods in fluid dynamics*, Springer-Verlag, New-York, USA.

Capdeville, Y., 2000, *Méthode couplée éléments spectraux - solution modale pour la propagation d'ondes dans la Terre à l'échelle globale (A coupled method using spectral elements and normal modes for global wave propagation in the Earth)*, Ph.D. thesis, Université Paris VII Denis Diderot, Paris, France.

Capdeville, Y., Stutzmann, E., & Montagner, J., 2000, Effect of a plume on long-period surface waves computed with normal-mode coupling, *Phys. Earth Planet. Inter.*, **119**, 54–71.

Capdeville, Y., Chaljub, E., Vilotte, J. P., & Montagner, J. P., 2003, Coupling the spectral element method with a modal solution for elastic wave propagation in global Earth models, *Geophys. J. Int.*, **152**, 34–67.

Carcione, J. M., 1994, The wave equation in generalized coordinates, *Geophysics*, **59**, 1911–1919.

Carcione, J. M., 1996, A 2D Chebyshev differential operator for the elastic wave equation, *Comput. Methods Appl. Mech. Engrg.*, **130**, 33–45.

Carcione, J. M. & Wang, P. J., 1993, A Chebyshev collocation method for the wave equation in generalized coordinates, *Comp. Fluid Dyn. J.*, **2**, 269–290.

Carcione, J. M., Kosloff, D., & Kosloff, R., 1988, Wave propagation simulation in a linear viscoelastic medium, *Geophys. J. Int.*, **95**, 597–611.

Catchings, R. D. & Lee, W. H. K., 1996, Shallow velocity structure and Poisson's ratio at the Tarzana, California, strong-motion accelerometer site, *Bull. Seismol. Soc. Am.*, **86**, 1704–1713.

Cerjan, C., Kosloff, D., Kosloff, R., & Reshef, M., 1985, A nonreflecting boundary condition for discrete acoustic and elastic wave equation, *Geophysics*, **50**, 705–708.

Cervený, V., 2001, *Seismic Ray Theory*, Cambridge University Press, Cambridge, UK.

Chaljub, E., 2000, *Modélisation numérique de la propagation d'ondes sismiques en géométrie sphérique : application à la sismologie globale (Numerical modeling of the propagation of seismic waves in spherical geometry : application to global seismology)*, Ph.D. thesis, Université Paris VII Denis Diderot, Paris, France.

Chaljub, E. & Tarantola, A., 1997, Sensitivity of SS precursors to topography on the upper-mantle 660-km discontinuity, *Geophys. Res. Lett.*, **24**(21), 2613–2616.

Chaljub, E., Capdeville, Y., & Vilotte, J. P., 2003, Solving elastodynamics in a fluid-solid heterogeneous sphere : a parallel spectral-element approximation on non-conforming grids, *J. Comput. Phys.*, **187**(2), 457–491.

Chew, W. C. & Liu, Q., 1996, Perfectly Matched Layers for elastodynamics : a new absorbing boundary condition, *J. Comput. Acoust.*, **4**(4), 341–359.

Chew, W. C. & Weedon, W. H., 1994, A 3-D perfectly matched medium from modified Maxwell's equations with stretched coordinates, *Microwave Opt. Technol. Lett.*, **7**(13), 599–604.

Ciarlet, P. G., 1978, *The Finite Element Method for Elliptic Problems*, North Holland, Amsterdam, 530 p.

Clayton, R. & Engquist, B., 1977, Absorbing boundary conditions for acoustic and elastic wave equations, *Bull. Seismol. Soc. Am.*, **67**, 1529–1540.

Cohen, G. & Fauqueux, S., 2005, Mixed spectral finite elements for the linear elasticity system in unbounded domains, *SIAM Journal on Scientific Computing*, **26**(3), 864–884.

Cohen, G., Joly, P., & Tordjman, N., 1993, Construction and analysis of higher-order finite elements with mass lumping for the wave equation, in *Proceedings of the second international conference on mathematical and numerical aspects of wave propagation*, edited by R. Kleinman, pp. 152–160, SIAM, Philadelphia, Pennsylvania, USA.

Collino, F. & Monk, P., 1998, Optimizing the Perfectly Matched Layer, *Comput. Methods Appl. Mech. Engrg.*, **164**, 157–171.

Collino, F. & Monk, P., 1998, The Perfectly Matched Layer in curvilinear coordinates, *SIAM J. Sci. Comput.*, **19**(6), 2061–2090.

Collino, F. & Tsogka, C., 2001, Application of the PML absorbing layer model to the linear elastodynamic problem in anisotropic heterogeneous media, *Geophysics*, **66**(1), 294–307.

Cormier, V. F., 1999, Anisotropy of heterogeneity scale lengths in the lower mantle from pkikp precursors, *Geophys. J. Int.*, **136**, 373–384.

Cowling, T. G., 1941, The non-radial oscillations of polytropic stars, *Mon. Not. Roy. Astron. Soc.*, **101**, 369–373.

Dahlen, F. A. & Baig, A. M., 2002, Fréchet kernels for body-wave amplitudes, *Geophys. J. Int.*, **150**, 440–466.

Dahlen, F. A. & Tromp, J., 1998, *Theoretical Global Seismology*, Princeton University Press, Princeton, New-Jersey, USA.

Davis, P. M., Rubinstein, J. L., Liu, K. H., Gao, S. S., & Knopoff, L., 2000, Northridge earthquake damage caused by geologic focusing of seismic waves, *Science*, **289**, 1746–1750.

Davis, T. L., Namson, J., & Yerkes, R. F., 1989, A cross-section of the Los Angeles area : seismically active fold-and-thrust belt, the 1987 Whittier Narrows earthquake and earthquake hazard, *J. Geophys. Res.*, **94**, 9644–9664.

Day, S. M., 1998, Efficient simulation of constant Q using coarse-grained memory variables, *Bull. Seismol. Soc. Am.*, **88**, 1051–1062.

Dreger, D. S. & Helmberger, D. V., 1990, Broadband modeling of local earthquakes, *Bull. Seismol. Soc. Am.*, **80**, 1162–1179.

Dubos, N., Souriau, A., Ponsolles, C., Fels, J. F., & Sénéchal, G., 2003, Étude des effets de sites dans la ville de Lourdes (Pyrénées, France) par la méthode des rapports spectraux, *Bull. Soc. Géol. Fr.*, **174**(1), 33–44.

Dziewonski, A. M. & Anderson, D. L., 1981, Preliminary reference Earth model, *Phys. Earth Planet. Inter.*, **25**, 297–356.

Eberhart-Phillips, D., Haeussler, P. J., Freymueller, J. T., Frankel, A. D., Rubin, C. M., Craw, P., Ratchkovski, N. A., Anderson, G., Carver, G. A., Crone, A. J., Dawson, T. E., Fletcher, H., Hansen, R., Harp, E. L., Harris, R. A., Hill, D. P., Hreinsdottir, S., Jibson, R. W., Jones, L. M., Kayen, R., Keefer, D. K., Larsen, C. F., Moran, S. C., Personius, S. F., Plafker, G., Sherrod, B., Sieh, K., Sitar, N., & Wallace, W. K., 2003, The 2002 Denali fault earthquake, Alaska : a large magnitude, slip-partitioned event, *Science*, **300**, 1113–1118.

Eisner, L. & Clayton, R. W., 2002, A full waveform test of the southern California velocity model by the reciprocity method, *Pure Appl. Geophys.*, **159**, 1691–1706.

Emmerich, H. & Korn, M., 1987, Incorporation of attenuation into time-domain computations of seismic wave fields, *Geophysics*, **52**, 1252–1264.

Engdahl, E. R., van der Hilst, R., & Buland, R., 1998, Global teleseismic earthquake relocation with improved travel times and procedures for depth determination, *Bull. Seismol. Soc. Am.*, **88**, 722–743.

Engquist, B. & Majda, A., 1977, Absorbing boundary conditions for the numerical simulation of waves, *Math. Comp.*, **31**, 629–651.

Everstine, G. C., 1981, A symmetric potential formulation for fluid-structure interaction, *ASME J. Sound Vib.*, **79**(1), 157–160.

Faccioli, E., Maggio, F., Paolucci, R., & Quarteroni, A., 1997, 2D and 3D elastic wave propagation by a pseudo-spectral domain decomposition method, *J. Seismol.*, **1**, 237–251.

Farra, V., 1990, Amplitude computation in heterogeneous media by ray perturbation theory : a finite element approach, *Geophys. J. Int.*, **103**, 341–354.

Favier, N. & Chevrot, S., 2003, Sensitivity kernels for shear wave splitting in transverse isotropic media, *Geophys. J. Int.*, **153**(1), 213–228.

Favier, N., Chevrot, S., & Komatitsch, D., 2004, Near-field influences on shear wave splitting and traveltime sensitivity kernels, *Geophys. J. Int.*, **156**(3), 467–482.

Felippa, C. A. & Deruntz, J. A., 1984, Finite-element analysis of shock-induced hull cavitation, *Comput. Methods Appl. Mech. Engrg.*, **44**, 297–337.

Fischer, P. F. & Rønquist, E. M., 1994, Spectral-element methods for large scale parallel Navier-Stokes calculations, *Comput. Methods Appl. Mech. Engrg.*, **116**, 69–76.

Foley, T. A., 1987, Weighted bicubic spline interpolation to rapidly varying data, *ACM Trans. Graphics*, **6**, 1–18.

Franke, R., 1985, Thin plate spline with tension, *Computer Aided Geometric Design*, **2**, 87–95.

Frankel, A., 1993, Three-dimensional simulations of ground motions in the San Bernardino valley, California, for hypothetical earthquakes on the San Andreas fault, *Bull. Seismol. Soc. Am.*, **83**, 1020–1041.

Frankel, A. & Leith, W., 1992, Evaluation of topographic effects on *P* and *S* waves of explosions at the northern Novaya Zemlya test site using 3-D numerical simulations, *Geophys. Res. Lett.*, **19**, 1887–1890.

Frankel, A. & Vidale, J., 1992, A three-dimensional simulation of seismic waves in the Santa Clara valley, California, from the Loma Prieta aftershock, *Bull. Seismol. Soc. Am.*, **82**, 2045–2074.

Fuchs, K. & Muller, G., 1971, Computation of synthetic seismograms with the reflectivity method and comparison of observations, *Geophys. J. R. Astron. Soc.*, **23**, 417–433.

Fuis, G. S., Clayton, R. W., Davis, P. M., Ryberg, T., Lutter, W. J., Okaya, D. A., Hauksson, E., Prodehl, C., Murphy, J. M., Benthien, M. L., Baher, S. A., Kohler, M. D., Thygesen, K., Simila, G., & Keller, G. R., 2003, Fault systems of the 1971 San Fernando and 1994 Northridge earthquakes, Southern California : relocated aftershocks and seismic images from LARSE II, *Geology*, **31**, 171–174.

Furumura, T., Kennett, B. L. N., & Furumura, M., 1998, Seismic wavefield calculation for laterally heterogeneous whole Earth models using the pseudospectral method, *Geophys. J. Int.*, **135**(3), 845–860.

Gaffet, S. & Bouchon, M., 1989, Effects of two-dimensional topographies using the discrete wavenumber-boundary integral equation method in *P-SV* cases, *J. Acoust. Soc. Am.*, **85**, 2277–2283.

Gao, S., Liu, H., Davis, P. M., & Knopoff, L., 1996, Localized amplification of seismic waves and correlation with damage due to the Northridge earthquake : evidence for focusing in Santa Monica, *Bull. Seismol. Soc. Am.*, **86**(1B), S209–S230.

Garatani, K., Nakamura, H., Okuda, H., & Yagawa, G., 2000, Large-scale parallel wave propagation analysis by GeoFEM, *Lecture Notes in Computer Science*, **1823**, 445–453.

Geller, R. J. & Ohminato, T., 1994, Computation of synthetic seismograms and their partial derivatives for heterogeneous media with arbitrary natural boundary conditions using the Direct Solution Method, *Geophys. J. Int.*, **116**, 421–446.

Gilbert, F., 1970, Excitation of the normal modes of the Earth by earthquake sources, *Geophys. J. R. Astron. Soc.*, **22**, 223–226.

Givoli, D., 1991, Non-reflecting boundary conditions : review article, *J. Comput. Phys.*, **94**, 1–29.

Gout, C., 1997, *Etude de changements d'échelle en approximation - ajustement spline sur des morceaux de surfaces*, Ph.D. thesis, Université de Pau et des Pays de l'Adour, Pau, France, 203 p.

Gout, C., 1998, Approximation of curves and surfaces from rapidly varying data, Tech. Rep. 1001, Center for Pure and Applied Mathematics, University of California at Berkeley, USA, 36 p.

Gout, C., 1999, Approximation using scale transformations, in *Approximation Theory IX*, edited by C. K. Chui & L. L. Schumaker, vol. 1, pp. 151–158, Vanderbilt University Press, Nashville.

Gout, C. & Komatitsch, D., 2000, Surface fitting of rapidly varying data using rank coding : application to geophysical surfaces, *Math. Geol.*, **32**(7), 873–888.

Graves, R. W., 1996, Simulating seismic wave propagation in 3D elastic media using staggered-grid finite differences, *Bull. Seismol. Soc. Am.*, **86**(4), 1091–1106.

Graves, R. W., 1999, Three-dimensional computer simulations of realistic earthquake ground motions in regions of deep sedimentary basin, in *The Effects of Surface Geology on Seismic Motion*, edited by K. Irikura, K. Kudo, H. Okada, & T. Sasatani, vol. 1, pp. 103–120, Balkema, Rotterdam, The Netherlands.

Gropp, W., Lusk, E., & Skjellum, A., 1994, *Using MPI, portable parallel programming with the Message-Passing Interface*, MIT Press, Cambridge, USA.

Gropp, W., Lusk, E., Doss, N., & Skjellum, A., 1996, A high-performance, portable implementation of the MPI message passing interface standard, *Parallel Computing*, **22**(6), 789–828.

Grote, M. J., 2000, Nonreflecting boundary conditions for elastodynamics scattering, *J. Comput. Phys.*, **161**, 331–353.

Guo, B. & Babuška, I., 1986, The *h-p* version of the finite element method, *Comput. Mech.*, **1**, 21–41.

Hadley, D. & Kanamori, H., 1977, Seismic structure of the Transverse Ranges, California, *Geol. Soc. Am. Bull.*, **88**, 1469–1478.

Hagstrom, T. & Hariharan, S. I., 1998, A formulation of asymptotic and exact boundary conditions using local operators, *Appl. Num. Math.*, **27**, 403–416.

Hara, T., Tsuboi, S., & Geller, R., 1991, Inversion for laterally heterogeneous Earth structure using a laterally heterogeneous starting model : preliminary results, *Geophys. J. Int.*, **104**, 523–540.

Hartzell, S., Harmsen, S., Frankel, A., Carver, D., Cranswick, E., Meremonte, M., & Michael, J., 1998, First-generation site-response maps for the Los Angeles region based on earthquake ground motions, *Bull. Seismol. Soc. Am.*, **88**, 463–472.

Hartzell, S. H., Leeds, A., Frankel, A., & Michael, J., 1996, Site response for urban Los Angeles using aftershocks of the Northridge earthquake, *Bull. Seismol. Soc. Am.*, **86**(1B), S168–S192.

Hastings, F. D., Schneider, J. B., & Broschat, S. L., 1996, Application of the Perfectly Matched Layer (PML) absorbing boundary condition to elastic wave propagation, *J. Acoust. Soc. Am.*, **100**(5), 3061–3069.

Hauksson, E., 1990, Earthquakes, faulting, and stress in the Los Angeles basin, *J. Geophys. Res.*, **95**, 15365–15394.

Hauksson, E., 2000, Crustal structure and seismicity distribution adjacent to the Pacific and North America plate boundary in Southern California, *J. Geophys. Res.*, **105**, 13875–13903.

Hauksson, E. & Haase, J. S., 1997, Three-dimensional V_p and V_p/V_s velocity models of the Los Angeles basin and central Transverse Ranges, California, *J. Geophys. Res.*, **102**, 5423–5453.

Hauksson, E., Teng, T. L., & Henyey, T. L., 1987, Results from a 1500 m deep, three-level downhole seismometer array : site response, low Q values, and f_{max}, *Bull. Seismol. Soc. Am.*, **77**, 1883–1904.

Heaney, S., 2000, *Beowulf, a new verse translation, bilingual edition*, Farrar, Straus and Giroux Publishers, New York.

Hesthaven, J. S., 1998, On the analysis and construction of perfectly matched layers for the linearized Euler equations, *J. Comput. Phys.*, **142**(1), 129–147.

Higdon, R. L., 1991, Absorbing boundary conditions for elastic waves, *Geophysics*, **56**, 231–241.

Hsieh, H. C. & Chang, W. T., 1994, Virtual knot technique for curve fitting of rapidly varying data, *Computer Aided Geometric Design*, **11**, 71–95.

Huftile, G. J. & Yeats, R. S., 1995, Convergence rates across a displacement transfer zone in the western Transverse Ranges, Ventura basin, California, *J. Geophys. Res.*, **100**(2), 2043–2067.

Hughes, T. J. R., 1987, *The finite element method, linear static and dynamic finite element analysis*, Prentice-Hall International, Englewood Cliffs, New Jersey, USA.

Ichinose, G. A., Day, S. M., Magistrale, H., Prush, T., Vernon, F., & Edelman, A., 1996, Crustal thickness variations beneath the Peninsular Ranges, southern California, *Geophys. Res. Lett.*, **23**, 3095–3098.

Igel, H., 1999, Wave propagation in three-dimensional spherical sections by the Chebyshev spectral method, *Geophys. J. Int.*, **136**, 559–566.

Igel, H. & Geller, R., 2000, Numerical modeling of global seismic wave propagation : algorithms, accuracy, verification, *Phys. Earth Planet. Inter.*, **119**, 1–2.

Igel, H. & Weber, M., 1996, P-SV wave propagation in the whole mantle using high-order finite differences : application to lowermost mantle structure, *Geophys. Res. Lett.*, **23**, 415–418.

Ishihara, K., Iguchi, M., & Kamo, K., 1990, Numerical simulation of lava flows on some volcanoes in Japan, in *Lava flows and domes*, edited by J. H. Fink, pp. 174–207, Springer-Verlag, Berlin.

Issaks, E. H. & Srivastava, R. M., 1989, *An Introduction to Applied Geostatistics*, Oxford University Press, Oxford, 560 p.

Jennings, P., 1975, Fault map of California with volcanoes, thermal springs and thermal wells at 1 :750,000 scale, in *Geological Data Map 1*, California Division of Mines and Geology, Sacramento, California.

Ji, C., Helmberger, D. V., & Wald, D. J., 2000, Basin structure estimation by waveform modeling : forward and inverse methods, *Bull. Seismol. Soc. Am.*, **90**, 964–976.

Ji, C., Wald, D. J., & Helmberger, D. V., 2002, Source description of the 1999 Hector Mine, California earthquake ; Part I : Wavelet domain inversion theory and resolution analysis, *Bull. Seismol. Soc. Am.*, **92**, 1192–1207.

Ji, C., Helmberger, D. V., & Wald, D. J., 2004, A teleseismic study of the 2002 Denali fault, Alaska, earthquake and implications for rapid strong-motion estimation, *Earthquake Spectra*, **20**(3), 617–637.

Kallivokas, L. F. & Bielak, J., 1993, Time-domain analysis of transient structural acoustics problems based on the finite element method and a novel boundary element, *J. Acoust. Soc. Am.*, **94**(6), 3480–3492.

Kikuchi, M. & Yamanaka, Y., 2002, Source rupture process of the central Alaska earthquake of November 3, 2002, inferred from teleseismic body waves, ERI, University of Tokyo, Japan, wwweic.eri.u-tokyo.ac.jp/EIC/EIC_News/021103AL-e.html.

Komatitsch, D., 1997, *Méthodes spectrales et éléments spectraux pour l'équation de l'élastodynamique 2D et 3D en milieu hétérogène (Spectral and spectral-element methods for the 2D and 3D elastodynamics equations in heterogeneous media)*, Ph.D. thesis, Institut de Physique du Globe, Paris, France, 187 pages.

Komatitsch, D. & Tromp, J., 1999, Introduction to the spectral-element method for 3-D seismic wave propagation, *Geophys. J. Int.*, **139**(3), 806–822.

Komatitsch, D. & Tromp, J., 2002, Spectral-element simulations of global seismic wave propagation-I. Validation, *Geophys. J. Int.*, **149**(2), 390–412.

Komatitsch, D. & Tromp, J., 2002, Spectral-element simulations of global seismic wave propagation-II. 3-D models, oceans, rotation, and self-gravitation, *Geophys. J. Int.*, **150**(1), 303–318.

Komatitsch, D. & Tromp, J., 2003, A Perfectly Matched Layer absorbing boundary condition for the second-order seismic wave equation, *Geophys. J. Int.*, **154**(1), 146–153.

Komatitsch, D. & Vilotte, J. P., 1998, The spectral-element method : an efficient tool to simulate the seismic response of 2D and 3D geological structures, *Bull. Seismol. Soc. Am.*, **88**(2), 368–392.

Komatitsch, D., Vilotte, J. P., Vai, R., Castillo-Covarrubias, J. M., & Sánchez-Sesma, F. J., 1999, The spectral-element method for elastic wave equations : application to 2D and 3D seismic problems, *Int. J. Numer. Meth. Engng.*, **45**(9), 1139–1164.

Komatitsch, D., Barnes, C., & Tromp, J., 2000, Wave propagation near a fluid-solid interface : a spectral element approach, *Geophysics*, **65**(2), 623–631.

Komatitsch, D., Barnes, C., & Tromp, J., 2000, Simulation of anisotropic wave propagation based upon a spectral element method, *Geophysics*, **65**(4), 1251–1260.

Komatitsch, D., Ritsema, J., & Tromp, J., 2002, The spectral-element method, Beowulf computing, and global seismology, *Science*, **298**(5599), 1737–1742.

Komatitsch, D., Tsuboi, S., Ji, C., & Tromp, J., 2003, A 14.6 billion degrees of freedom, 5 teraflops, 2.5 terabyte earthquake simulation on the Earth Simulator, *Proceedings of the ACM/IEEE Supercomputing SC'2003 conference*, pp. 4–11, Gordon Bell Prize winner article.

Komatitsch, D., Liu, Q., Tromp, J., Süss, P., Stidham, C., & Shaw, J. H., 2004, Simulations of ground motion in the Los Angeles basin based upon the spectral-element method, *Bull. Seismol. Soc. Am.*, **94**(1), 187–206.

Kosmanis, T. I., Yioultsis, T. V., & Tsiboukis, T. D., 1999, Perfectly matched anisotropic layer for the numerical analysis of unbounded eddy-current problems, *IEEE transactions on Magnetics*, **35**(6), 4452–4458.

Kristek, J., Moczo, P., Irikura, K., Iwata, T., & Sekiguchi, H., 1999, The 1995 Kobe mainshock simulated by 3D finite differences, in *The Effects of Surface Geology on Seismic Motion*, edited by K. Irikura, K. Kudo, H. Okada, & T. Sasatani, vol. 3, pp. 1361–1368, Balkema, Rotterdam, The Netherlands.

Lahaye, D. J. P., Maggio, F., & Quarteroni, A., 1997, Hybrid finite element-spectral element approximation of wave propagation problems, *East-West J. Numer. Math.*, **5**(4), 265–289.

Larsen, S., Antolik, M., Dreger, D., Stidham, C., Schultz, C., Lomax, A., & Romanowicz, B., 1997, 3-D models of seismic wave propagation : Simulating scenario earthquakes along the Hayward fault, *Seis. Res. Lett.*, **68**, 328.

Lesieur, M., 1997, *Turbulence in fluids*, Kluwer Academic Publishers, Dordrecht.

Lewis, J., Day, S. M., Magistrale, H., Eakins, J., & Vernon, F. L., 2000, Crustal thickness of the Peninsular Ranges, southern California, from teleseismic receiver functions, *Geology*, **28**, 303–306.

Li, X. D. & Tanimoto, T., 1993, Waveforms of long-period body waves in a slightly aspherical Earth model, *Geophys. J. Int.*, **112**, 92–102.

Liu, H. P., Anderson, D. L., & Kanamori, H., 1976, Velocity dispersion due to anelasticity : implications for seismology and mantle composition, *Geophys. J. R. Astron. Soc.*, **47**, 41–58.

Liu, Q. & Tao, J., 1997, The perfectly matched layer for acoustic waves in absorptive media, *J. Acoust. Soc. Am.*, **102**(4), 2072–2082.

Liu, Q., Polet, J., Komatitsch, D., & Tromp, J., 2004, Spectral-element moment-tensor inversions for earthquakes in Southern California, *Bull. Seismol. Soc. Am.*, **94**(5), 1748–1761.

Lognonné, P. & Romanowicz, B., 1990, Modeling of coupled normal modes of the Earth : the spectral method, *Geophys. J. Int.*, **102**, 365–395.

Love, A. E. H., 1911, *Some problems of geodynamics*, Cambridge University Press, Cambridge.

Luyendyk, B. P. & Hornafius, J. S., 1987, Neogene crustal rotations, fault slip and basin development in southern California, in *Cenozoic basin development of coastal California*, edited by R. V. Ingersoll & W. G. Ernst, pp. 259–283, Prentice-Hall, Old Tappan, New Jersey.

Lysmer, J. & Drake, L. A., 1972, A finite element method for seismology, in *Methods in Computational Physics*, edited by B. Alder, S. Fernbach, & B. A. Bolt, vol. 11, chap. 6, pp. 181–216, Academic Press, New York, USA.

Maday, Y. & Patera, A. T., 1989, Spectral-element methods for the incompressible Navier-Stokes equations, in *State of the art survey in computational mechanics*, pp. 71–143, A. K. Noor and J. T. Oden editors.

Maday, Y., Meiron, D., Patera, A. T., & Rønquist, E. M., 1993, Analysis of iterative methods for the steady and unsteady Stokes problem : Application to Spectral Element discretizations, *SIAM J. Sci. Stat. Comput.*, **14**, 310–337.

Magistrale, H., McLaughlin, K., & Day, S., 1996, A geology based 3-D velocity model of the Los Angeles basin sediments, *Bull. Seismol. Soc. Am.*, **86**, 1161–1166.

Magistrale, H., Day, S., Clayton, R. W., & Graves, R., 2000, The SCEC Southern California reference three-dimensional seismic velocity model version 2, *Bull. Seismol. Soc. Am.*, **90**, S65–S76.

Mallet, J. L., 1992, Discrete smooth interpolation in geometric modeling, *Computer-Aided Design*, **24**, 178–191.

Mallet, J. L., 1997, Discrete modeling for natural objects, *Math. Geol.*, **29**, 199–219.

McCulloh, T. H., 1960, Gravity variations and the geology of the Los Angeles basin of California, *U.S. Geological Survey Professional Paper*, **400-B**, 320–325.

McLaughlin, K. L. & Day, S. M., 1994, 3-D elastic finite-difference seismic wave simulations, *Computers in Physics*, **8**(6), 656–663.

Meuer, H. W., Strohmaier, E., Dongarra, J. J., & Simon, H. D., 2002, Top500 list of supercomputer sites, Tech. rep., University of Mannheim, Mannheim, Germany, `www.top500.org`.

Moczo, P., Bystrický, E., Kristek, J., Carcione, J. M., & Bouchon, M., 1997, Hybrid modeling of *P-SV* seismic motion at inhomogeneous viscoelastic topographic structures, *Bull. Seismol. Soc. Am.*, **87**, 1305–1323.

Moczo, P., Kristek, J., & Bystrický, E., 2001, Efficiency and optimization of the 3-D finite-difference modeling of seismic ground motion, *J. Comput. Acoust.*, **9**(2), 593–609.

Montagner, J.-P., 1998, Where can seismic anisotropy be detected in the Earth's mantle ? in boundary layers ..., *Pure Appl. Geophys.*, **151**, 223–256.

Montagner, J. P., 2002, Upper mantle low anisotropy channels below the Pacific Plate, *Earth Planet. Sci. Lett.*, **202**, 263–274.

Namson, J. & Davis, T. L., 1992, Late Cenozoic thrust ramps of southern California, Tech. rep., Davis & Namson Consulting Geologists, Valencia, California, USA, unpublished report.

Necas, J., 1967, *Les méthodes directes en théorie des équations elliptiques*, Masson, Paris, 351 p.

NOAA, 1988, National Oceanic and Atmospheric Administration (NOAA) product information catalog - ETOPO5 Earth Topography 5-minute digital model, Tech. rep., U.S. Department of Commerce, Washington D.C., USA, 171 pages.

Nolet, G. & Dahlen, F. A., 2000, Wavefront healing and the evolution of seismic delay times, *J. Geophys. Res.*, **105**, 19,043–19,054.

Ohminato, T. & Chouet, B. A., 1997, A free-surface boundary condition for including 3D topography in the finite difference method, *Bull. Seismol. Soc. Am.*, **87**, 494–515.

Olsen, K. B., 2000, Site amplification in the Los Angeles basin from three-dimensional modeling of ground motion, *Bull. Seismol. Soc. Am.*, **90**, S77–S94.

Olsen, K. B. & Archuleta, R. J., 1996, 3-D simulation of earthquakes on the Los Angeles fault system, *Bull. Seismol. Soc. Am.*, **86**(3), 575–596.

Olsen, K. B., Pechmann, J. C., & Schuster, G. T., 1995, Simulation of 3-D elastic wave propagation in the Salt Lake basin, *Bull. Seismol. Soc. Am.*, **85**, 1688–1710.

Olsen, K. B., Madariaga, R., & Archuleta, R. J., 1997, Three-dimensional dynamic simulation of the 1992 Landers earthquake, *Science*, **278**, 834–838.

Page, R. A., Plafker, G., & Pulpan, H., 1995, Block rotation in east-central Alaska : a framework for evaluating earthquake potential ?, *Geology*, **23**, 629–632.

Paolucci, R., Faccioli, E., & Maggio, F., 1999, 3D response analysis of an instrumented hill at Matsuzaki, Japan, by a spectral method, *J. Seismol.*, **3**, 191–209.

Park, J., 1986, Synthetic seismograms from coupled free oscillations : the effects of lateral structure and rotation, *J. Geophys. Res.*, **91**, 6441–6464.

Park, J. & Yu, Y., 1992, Anisotropy and coupled free oscillations : simplified models and surface wave observations, *Geophys. J. Int.*, **110**, 401–420.

Park, K. C. & Felippa, C. A., 1980, Partitioned transient analysis procedures for coupled field problems : accuracy analysis, *J. Appl. Mech.*, **47**, 916–926.

Patera, A. T., 1984, A spectral element method for fluid dynamics : laminar flow in a channel expansion, *J. Comput. Phys.*, **54**, 468–488.

Peng, C. B. & Töksoz, M. N., 1995, An optimal absorbing boundary condition for elastic wave modeling, *Geophysics*, **60**, 296–301.

Peyrat, S., Olsen, K. B., & Madariaga, R., 2001, Dynamic modeling of the 1992 Landers earthquake, *J. Geophys. Res.*, **106**, 26467–26482.

Pitarka, A. & Irikura, K., 1996, Modeling 3D surface topography by a finite-difference method : Kobe-JMA station site, Japan, case study, *Geophys. Res. Lett.*, **23**, 2729–2732.

Pitarka, A. & Irikura, K., 1996, Basin structure effects on long period strong motions in the San Fernando valley and the Los Angeles basin from the 1994 Northridge earthquake and aftershocks, *Bull. Seismol. Soc. Am.*, **86**(1B), S126–S137.

Priolo, E., Carcione, J. M., & Seriani, G., 1994, Numerical simulation of interface waves by high-order spectral modeling techniques, *J. Acoust. Soc. Am.*, **95**(2), 681–693.

Qi, Q. & Geers, T. L., 1998, Evaluation of the Perfectly Matched Layer for computational acoustics, *J. Comput. Phys.*, **139**(1), 166–183.

Quarteroni, A., Tagliani, A., & Zampieri, E., 1998, Generalized Galerkin approximations of elastic waves with absorbing boundary conditions, *Comput. Methods Appl. Mech. Engrg.*, **163**, 323–341.

Rial, J. A., 1996, The anomalous seismic response of the ground at the Tarzana Hill site during the Northridge 1994 Southern California earthquake : a resonant, sliding block ?, *Bull. Seismol. Soc. Am.*, **86**, 1714–1723.

Ritsema, J., Van Heijst, H. J., & Woodhouse, J. H., 1999, Complex shear velocity structure imaged beneath Africa and Iceland, *Science*, **286**, 1925–1928.

Ritsema, J., Rivera, L. A., Komatitsch, D., Tromp, J., & van Heijst, H. J., 2002, The effects of crust and mantle heterogeneity on PP/P and SS/S amplitude ratios, *Geophys. Res. Lett.*, **29**(10), 1430.

Robertsson, J. O. A., 1996, A numerical free-surface condition for elastic/viscoelastic finite-difference modeling in the presence of topography, *Geophysics*, **61**, 1921–1934.

Romanowicz, B., 1998, Attenuation tomography of the Earth's mantle : a review of current status, *Pure Appl. Geophys.*, **153**, 257–272.

Ronchi, C., Ianoco, R., & Paolucci, P. S., 1996, The "Cubed Sphere" : a new method for the solution of partial differential equations in spherical geometry, *J. Comput. Phys.*, **124**, 93–114.

Sacks, Z. S., Kingsland, D. M., Lee, R., & Lee, J. F., 1995, A Perfectly Matched anisotropic absorber for use as an absorbing boundary condition, *IEEE transactions on Antennas and Propagation*, **43**(12), 1460–1463.

Sadourny, R., 1972, Conservative finite-difference approximations of the primitive equations on quasi-uniform spherical grids, *Monthly Weather Review*, **100**, 136–144.

Salkauskas, K., 1974, C^1 splines for interpolation of rapidly varying data, *Rocky Mountain J. Math.*, **14**, 239–250.

Satoh, T., Kawase, H., Sato, T., & Pitarka, A., 2001, Three-dimensional finite-difference waveform modeling of strong motions observed in the Sendai basin, Japan, *Bull. Seismol. Soc. Am.*, **91**, 365–380.

Schneider, C. L., Hummon, C., Yeats, R. S., & Huftile, G. J., 1996, Structural evolution of the northern Los Angeles basin, California, based on growth strata, *Tectonics*, **15**, 341–355.

Seriani, G., 1998, 3-D large-scale wave propagation modeling by a spectral element method on a Cray T3E multiprocessor, *Comput. Methods Appl. Mech. Engrg.*, **164**, 235–247.

Seriani, G. & Priolo, E., 1994, A spectral element method for acoustic wave simulation in heterogeneous media, *Finite Elements in Analysis and Design*, **16**, 337–348.

Seriani, G., Priolo, E., & Pregarz, A., 1995, Modelling waves in anisotropic media by a spectral element method, in *Proceedings of the third international conference on mathematical and numerical aspects of wave propagation*, edited by G. Cohen, pp. 289–298, SIAM, Philadephia, PA.

Shaw, J. H. & Shearer, P., 1999, An elusive blind-thrust fault beneath metropolitan Los Angeles, *Science*, **283**, 1516–1518.

Shaw, J. H. & Suppe, J., 1996, Earthquake hazards of active blind-thrust faults under the central Los Angeles basin, California, *J. Geophys. Res.*, **101**, 8623–8642.

Simons, F. J., van der Hilst, R. D., Montagner, J. P., & Zielhuis, A., 2002, Multimode Rayleigh wave inversion for heterogeneity and azimuthal anisotropy of the Australian upper mantle, *Geophys. J. Int.*, **151**(3), 738–754.

Smith, M. L. & Dahlen, F. A., 1973, The azimuthal dependence of Love and Rayleigh wave propagation in a slightly anisotropic medium, *J. Geophys. Res.*, **78**, 3321–3333.

Sochacki, J., Kubichek, R., George, J., Fletcher, W. R., & Smithson, S., 1987, Absorbing boundary conditions and surface waves, *Geophysics*, **52**(1), 60–71.

Spetzler, J., Trampert, J., & Snieder, R., 2001, Are we exceeding the limits of the great circle approximation in global surface wave tomography ?, *Geophys. Res. Lett.*, **28**, 2341–2344.

Spudich, P., Hellweg, M., & Lee, W. H. K., 1996, Directional topographic site response at Tarzana observed in aftershocks of the 1994 Northridge, California, earthquake : implications for mainshock motions, *Bull. Seismol. Soc. Am.*, **86**(1B), S193–S208.

Stacey, R., 1988, Improved transparent boundary formulations for the elastic wave equation, *Bull. Seismol. Soc. Am.*, **78**(6), 2089–2097.

Sterling, T. L., 2000, Petaflops computing : looking back at the future, Tech. rep., California Institute of Technology, Pasadena, California, presented at the Supercomputing'2000 conference, Dallas, Texas, Nov. 2000.

Sterling, T. L., Salmon, J., Becker, D. J., & Savarese, D. F., 1999, *How to build a Beowulf, a guide to the implementation and application of PC clusters*, MIT Press, Cambridge.

Stevens, J. L., McLaughlin, K. L., Shkoller, B., & Day, S. M., 1993, 2-D axisymmetric calculations of surface waves generated by an explosion in an island, mountain and sedimentary basin, *Geophys. J. Int.*, **114**, 548–560.

Stidham, C., Antolik, M., Dreger, D., Larsen, S., & Romanowicz, B., 1999, Three-dimensional structure influences on the strong motion wavefield of the 1989 Loma Prieta earthquake, *Bull. Seismol. Soc. Am.*, **89**, 1184–1202.

Stidham, C., Süss, M. P., & Shaw, J. H., 2001, 3D density and velocity model of the Los Angeles basin, in *Geological Society of America 2001 annual meeting abstracts*, vol. 33, p. 299, Geological Society of America.

Süss, M. P. & Shaw, J. H., 2003, P wave seismic velocity structure derived from sonic logs and industry reflection data in the Los Angeles basin, California, *J. Geophys. Res.*, **108**(B3), 2170.

Takeuchi, N., Geller, R., & Cummins, P., 2000, Complete synthetic seismograms for 3-D heterogeneous Earth models computed using modified DSM operators and their applicability to inversion for Earth structure, *Phys. Earth Planet. Inter.*, **119**, 25–36.

Tarantola, A., 1987, *Inverse problem theory : methods for data fitting and model parameter estimation*, Elsevier Science Publishers, Amsterdam, Netherlands.

Tarnow, N. & Simo, J. C., 1994, How to render second-order accurate time-stepping algorithms fourth-order accurate while retaining the stability and conservation properties, *Comput. Methods Appl. Mech. Engrg.*, **115**, 233–252.

Taubes, G., 1996, Do-it-yourself supercomputers, *Science*, **274**, 1840.

Taylor, M., Tribbia, J., & Iskandarani, M., 1997, The spectral element method for the shallow water equation on the sphere, *J. Comput. Phys.*, **130**, 92–108.

Tessmer, E., Kessler, D., Kosloff, D., & Behle, A., 1992, Multi-domain Chebyshev-Fourier method for the solution of the equations of motion of dynamic elasticity, *J. Comput. Phys.*, **100**, 355–363.

Thomas, C., Igel, H., Weber, M., & Scherbaum, F., 2000, Acoustic simulation of P-wave propagation in a heterogeneous spherical Earth : numerical method and application to precursor waves to PKPdf, *Geophys. J. Int.*, **141**, 6441–6464.

Thompson, L. L. & Pinsky, P., 1996, A space-time finite element method for structural acoustics in infinite domains. part 1 : formulation, stability and convergence, *Comput. Methods Appl. Mech. Engrg.*, **132**, 195–227.

Torrens, J. J., 1991, *Interpolación de superficies paramétricas con discontinuidades mediante, elementos finitos, aplicaciones*, Ph.D. thesis, Universidad de Zaragoza, Zaragoza, España, 186 p.

Tromp, J. & Komatitsch, D., 2000, Spectral-element simulations of wave propagation in a laterally homogeneous Earth model, in *Problems in Geophysics for the New Millennium*, edited by E. Boschi, G. Ekström, & A. Morelli, pp. 351–372, INGV, Roma, Italy.

Tsuboi, S., Komatitsch, D., Ji, C., & Tromp, J., 2003, Spectral-element simulations of the November 3, 2002, Denali, Alaska earthquake on the Earth Simulator, *Phys. Earth Planet. Inter.*, **139**(3-4), 305–313.

USGS, 2003, United States Geological Survey Southern California topography map, available online at www.usgs.gov.

Valette, B., 1986, About the influence of prestress upon the adiabatic perturbations of the Earth, *Geophys. J. R. Astron. Soc.*, **85**, 179–208.

Valette, B., 1987, *Spectre des oscillations libres de la Terre : aspects mathématiques et géophysiques (Spectrum of the free oscillations of the Earth : mathematical and geophysical aspects)*, Ph.D. thesis, Université Paris VI Jussieu, Paris, thèse d'état.

Virieux, J., 1986, *P-SV* wave propagation in heterogeneous media : velocity-stress finite-difference method, *Geophysics*, **51**, 889–901.

Wald, D. J. & Graves, R. W., 1998, The seismic response of the Los Angeles basin, California, *Bull. Seismol. Soc. Am.*, **88**, 337–356.

Wald, D. J., Heaton, T. H., & Hudnut, K. W., 1996, The slip history of the 1994 Northridge, California, earthquake determined from strong ground motion, teleseismic, GPS, and leveling data, *Bull. Seismol. Soc. Am.*, **86**, S49–S70.

Winton, S. C. & Rappaport, C. M., 2000, Specifying PML conductivities by considering numerical reflection dependencies, *IEEE transactions on Antennas and Propagation*, **48**(7), 1055–1063.

Woodhouse, J. H. & Dziewonski, A. M., 1984, Mapping the upper mantle : Three-dimensional modeling of Earth structure by inversion of seismic waveforms, *J. Geophys. Res.*, **89**, 5953–5986.

Wright, T. L., 1991, Structural geology and tectonic evolution of the Los Angeles basin, California, in *Active Margin Basins*, edited by K. T. Biddle, vol. 52, pp. 35–134, Am. Assoc. Pet. Geol. Memoir.

Yeats, R. S., Huftile, G. J., & Stitt, L. T., 1994, Late Cenozoic tectonics of the east Ventura basin, Transverse Ranges, California, *AAPG Bulletin*, **78**(7), 1040–1074.

Zahradník, J., Moczo, P., & Hron, F., 1993, Testing four elastic finite-difference schemes for behavior at discontinuities, *Bull. Seismol. Soc. Am.*, **83**, 107–129.

Zeng, X., 1996, *Finite difference modeling of viscoelastic wave propagation in a generally heterogeneous medium in the time domain, and a dissection method in the frequency domain*, Ph.D. thesis, University of Toronto, Canada.

Zeng, Y. Q., He, J. Q., & Liu, Q. H., 2001, The application of the perfectly matched layer in numerical modeling of wave propagation in poroelastic media, *Geophysics*, **66**(4), 1258–1266.

Zhao, L. & Cangellaris, A. C., 1996, GT-PML : generalized theory of Perfectly Matched Layers and its application to the reflectionless truncation of Finite-Difference Time-Domain grids, *IEEE transactions on Microwave Theory and Techniques*, **44**(12), 2555–2563.

Zhu, L. & Kanamori, H., 2000, Moho depth variation in southern California from teleseismic receiver functions, *J. Geophys. Res.*, **105**, 2969–2980.

Zienkiewicz, O. C., 1977, *The finite element method in engineering science*, McGraw-Hill, New York, 3rd edn.